

**FUNCTIONALIZED MULTIWALL CARBON NANOTUBES FOR ELECTRONIC  
AND MAGNETIC APPLICATIONS**

By

JAMES AYODELE OKE

submitted in accordance with the requirements for the degree of

DOCTOR OF PHILOSOPHY

in the subject

PHYSICS

at the

UNIVERSITY OF SOUTH AFRICA

SUPERVISOR: PROF. S. C. RAY

CO-SUPERVISOR: PROF. S. J. MOLOI

November, 2020

**DECLARATION**

Name: JAMES AYODELE OKE

Student No.: 64048691

I declare that “**FUNCTIONALIZED MULTIWALL CARBON NANOTUBES FOR ELECTRONIC AND MAGNETIC APPLICATIONS**” is my own work and that all the sources I have used or quoted have been indicated and acknowledged by means of complete references.

I further declare that I have not previously submitted this work for examination at University of South Africa or any other institution to obtain a research degree.



---

SIGNATURE

12 / 11 / 2020

---

DATE

## **DEDICATION**

This work is dedicated to the less privilege and above all to God Almighty.

## ACKNOWLEDGMENTS

I would like to express my earnest appreciation to my supervisor, Prof. Shekhar Chandra Ray for the opportunity given to me to pursue my Ph.D. degree under his direct supervision. I am grateful to him for his trust which encouraged and motivated me to work hard and achieve this success. He is indeed a great mentor and source of inspiration for me.

I would also like to show my immeasurable gratitude to my co-supervisor Prof. Sabata Jonas Moloi, for his encouragement and guidance throughout the research work. I dedicate this part of my thesis to him. Great thanks to Dr. Sarma Sweety and Mr. Idis David Omoefe for their impact on my research work. I also acknowledge Prof. Gaotsiwe Rampho (CoD) and Ms. Bongilele Hlela (Administrator) for their unconditional love throughout my stay in the Department. I say a big thanks to you all.

I take the authority to thank the National Research Foundation (NRF) for awarding me a doctoral fellowship through my co-supervisor (Grant no. 105292) from 2018 to 2020. I also appreciate the Department for sponsoring me for overseas Conference on Advance Energy Physics (AEM), Guildford, UK.

I am indeed grateful to my parents, who nurtured me from cradle up to this stage of my life, Mr. and Mrs. Samuel Babatunde Oke for their spiritual and moral support. May God give you long life to eat the fruit of your labor. I also appreciate the support of my siblings from the start, up to this point in my life. You are the best family on earth.

Finally, I would like to appreciate the effort of my cherished friends Oluwadamilola Bodunrin, Oluwadamilola Owoyemi, Sandy Mosia, Oliver Mnisi, Moses Okoro, Olufunsho Olotu, and to all my colleagues who contributed one way or the other to the successful completion of my Ph.D. programme. I appreciate your contributions. Thank you all.

**ABSTRACT**

In this work, SiO<sub>2</sub>, MWCNTs, MWCNTs:SiO<sub>2</sub>, MWCNTs-TiO<sub>2</sub>, and MWCNTs:TiO<sub>2</sub>:SiO<sub>2</sub> nanomaterials were synthesized and characterized by the use of different techniques to ascertain novelty of the nanomaterials and also to establish their suitability for several electrical, electronic and magnetic based device applications. The results, in general, indicate that the nanocomposites were well prepared and the properties of MWCNTs can be tuned by introducing SiO<sub>2</sub>, TiO<sub>2</sub>, and a composite of SiO<sub>2</sub> and TiO<sub>2</sub> in its matrix. This tunability of properties leading to the suitability of the material for various applications has been explained in this work.

**Key terms:** SiO<sub>2</sub>; TiO<sub>2</sub>; MWCNTs; MWCNTs:SiO<sub>2</sub>; MWCNTs-TiO<sub>2</sub>; MWCNTs:TiO<sub>2</sub>:SiO<sub>2</sub>; composites; synthesis; characterization; electrical; electronic; magnetic

**TABLE OF CONTENTS**

<b>DECLARATION</b> .....	<b>ii</b>
<b>DEDICATION</b> .....	<b>iii</b>
<b>ACKNOWLEDGMENTS</b> .....	<b>iv</b>
<b>ABSTRACT</b> .....	<b>v</b>
<b>TABLE OF CONTENTS</b> .....	<b>vi</b>
<b>LIST OF FIGURES</b> .....	<b>xii</b>
<b>LIST OF TABLES</b> .....	<b>xvii</b>
<b>LIST OF ACRONYMS</b> .....	<b>xix</b>
<b>LIST OF SYMBOLS</b> .....	<b>xxi</b>
<b>Chapter One</b> .....	<b>1</b>
<b>Introduction</b> .....	<b>1</b>
1. 1. Background.....	2
1.2. Motivation of the study .....	2
1.3. Aim and objectives .....	5
1.4. Structure of the thesis .....	6
References .....	7
<b>Chapter Two</b> .....	<b>10</b>
<b>Overview of CNTs</b> .....	<b>10</b>
2.1. A brief history of CNTs.....	11

2.2. Carbon nanotubes (CNTs).....	11
2.2.1. Synthesis of CNTs.....	12
2.2.2. Purification of CNTs .....	13
2.2.3. Structure of CNTs.....	14
<b>2.2.4. Properties of CNTs .....</b>	<b>17</b>
2.2.4.1. Electrical properties.....	17
2.2.4.2. Mechanical strength .....	17
2.2.4.3. Thermal conductivity .....	18
2.2.5. Functionalization of CNTs.....	18
2.2.5.1. Non-covalent modification of CNTs.....	19
2.2.5.2. Covalent modification of CNTs .....	20
2.3. Magnetic CNTs.....	21
2.3.1. Magnetic moment.....	22
2.3.2. Magnetic domains.....	22
2.3.3. Magnetic-hysteresis (M-H) loop .....	23
2.4. Electrical hysteresis loop and memristive behavior .....	24
References .....	25
<b>Chapter Three.....</b>	<b>33</b>
<b>Experimental .....</b>	<b>33</b>
3.1 Characterization Techniques.....	34

3.1.1.	Field emission-scanning electron spectroscopy (FE-SEM).....	34
3.1.2.	X-ray diffraction (XRD).....	35
3.1.3.	Raman spectroscopy.....	37
3.1.4.	X-ray photoelectron spectroscopy (XPS).....	37
3.1.5.	X-ray absorption near edge structure (XANES) spectroscopy.....	39
3.1.6.	Current-voltage (I-V) characteristic.....	39
3.1.7.	Superconducting quantum interference device (SQUID).....	41
3.1.8.	Electron spin resonance (ESR).....	41
	References.....	43
	<b>Chapter Four</b> .....	<b>44</b>
	<b>Electronic, Electrical and Magnetic Behavioural change of SiO<sub>2</sub>- NPs Decorated MWCNTs</b> .....	<b>44</b>
4.1.	Introduction.....	45
4.2.	Methodology.....	46
4.2.1	Preparation of MWCNTs.....	46
4.2.2	Preparation of SiO <sub>2</sub> and MWCNTs:Si nanocomposites.....	47
4.2.3	Characterization.....	47
4.3.	Result and discussion.....	48
4.3.1.	Field emission-scanning electron microscopy (FE-SEM).....	48
4.3.2.	X-Ray Diffraction (XRD) Patterns.....	49



4.3.3.	Raman spectroscopy .....	51
4.3.4.	X-ray photoelectron spectroscopy (XPS) .....	54
4.3.5.	X-ray absorption near edge structure (XANES) spectroscopy .....	59
4.3.6.	Current-voltage (I-V) measurement .....	63
4.3.7.	M-H loop and temperature-dependent magnetization measurement .....	66
4.3.8.	Electron spin resonance (ESR) .....	68
4.4.	Conclusion .....	71
	References .....	73
	<b>Chapter Five</b> .....	<b>79</b>
	<b>Tuning the Electronic and Electrical Behaviour of MWCNTs-TiO<sub>2</sub> Nanocomposites</b> .....	<b>79</b>
5.1.	Introduction .....	80
5.2.	Methodology .....	81
5.2.1.	Synthesis of MWCNTs .....	81
5.2.2.	Synthesis of MWCNTs-TiO <sub>2</sub> nanocomposites .....	82
5.2.3.	Characterization .....	82
5.3.	Result and discussion .....	83
5.3.1.	Field emission-scanning electron microscopy (FE-SEM) .....	83
5.3.2.	X-Ray diffraction (XRD) patterns .....	84
5.3.3.	Raman spectroscopy .....	85

5.3.4.	X-ray photoelectron spectroscopy (XPS).....	89
5.3.5.	X-ray absorption near edge structure (XANES) spectroscopy.....	94
5.3.6.	Current-voltage (I-V) measurement .....	98
5.4	Conclusion .....	101
References.....		102
<b>Chapter Six.....</b>		<b>108</b>
<b>Structural, Electronic and Electrical Behaviour of MWCNTs:(TiO<sub>2</sub>:SiO<sub>2</sub>) Nanocomposites.....</b>		<b>108</b>
6.1.	Introduction .....	109
6.2.	Methodology .....	111
6.2.1.	Synthesis of TiO <sub>2</sub> , SiO <sub>2</sub> , MWCNTs, and MWCNTs:Ti:Si.....	111
6.2.2.	Characterization.....	112
6.3.	Result and discussion .....	112
6.3.1.	Field emission-scanning electron microscopy (FE-SEM).....	112
6.3.2.	X-Ray Diffraction (XRD) Patterns.....	114
6.3.3.	Raman spectroscopy .....	115
6.3.4.	X-ray photoelectron spectroscopy (XPS).....	119
6.3.5.	X-ray absorption near edge structure (XANES) spectroscopy.....	126
6.3.6.	Current-voltage (I-V) measurement .....	130
6.4.	Conclusion .....	136

References.....	137
<b>Chapter Seven.....</b>	<b>145</b>
<b>Summary, Conclusions, Recommendations and Future work.....</b>	<b>145</b>
7.1 Thesis summary.....	146
7.2 Conclusions .....	152
7.3 Recommendations.....	153
7.4 Future work.....	154
<b>Appendix .....</b>	<b>155</b>
<b>Published Papers.....</b>	<b>155</b>
Appendix 1.....	156
Appendix 2.....	166
Appendix 3.....	174
Appendix 4.....	182
Appendix 5.....	194
Appendix 6.....	201

## LIST OF FIGURES

<b>Figure 2.1.</b> Setup technique (a) arc discharge, (b) laser ablation, (c) thermal CVD.....	13
<b>Figure 2.2.</b> Vector direction of chiralities of CNTs .....	15
<b>Figure 2.3.</b> Different structures chiralities of CNTs. (a) armchair (b) zigzag (c) chiral .....	15
<b>Figure 2.4.</b> (a) Single wall carbon nanotubes (SWCNTs) (b) Double wall and carbon nanotube (DWCNT) (c) Multiwall carbon nanotubes (MWCNTs) .....	16
<b>Figure 2.5.</b> Possible modification for CNTs: (A) defect modification, (B) wall-side modification, (C) bio- modification, (D) polymer modification, and (E) endohedral modification .....	20
<b>Figure 2.6.</b> Production of angular momentum ( $l$ ) and magnetic moment ( $m$ ) through current flowing a loop .....	22
<b>Figure 2.7.</b> (a) single-wall domain. (b) 180° wall domain. (c) 90° wall domain .....	23
<b>Figure 2.8.</b> M-H loop of a magnetic material .....	24
<b>Figure 3.1.</b> Schematic working principle of SEM. ....	35
<b>Figure 3.2.</b> Schematic diagram of the Bragg's Law in XRD.....	36
<b>Figure 3.3.</b> Schematic principle of XPS.....	38
<b>Figure 3.4.</b> Schematic diagram of a conducting I-V curve .....	40
<b>Figure 3.5.</b> Schematic diagram of a semiconducting I-V curve.....	40
<b>Figure 3.6.</b> Schematic diagram of ESR process.....	42

<b>Figure 4.1.</b> (a, b and c) SEM images for SiO <sub>2</sub> , MWCNTs, and MWCNTs:Si nanocomposites. (d) EDS spectra for MWCNTs:Si nanocomposites. ....	49
<b>Figure 4.2.</b> XRD pattern for SiO <sub>2</sub> , MWCNTs, and MWCNTs:Si nanocomposites.....	50
<b>Figure 4.3.</b> Raman spectra for SiO <sub>2</sub> , MWCNTs, and MWCNTs:Si nanocomposites.....	52
<b>Figure 4.4.</b> De-convolution Raman spectra for MWCNTs and MWCNTs:Si nanocomposites. .....	53
<b>Figure 4.5.</b> XPS spectra for SiO <sub>2</sub> , MWCNTs, and MWCNTs:Si nanocomposites.....	55
<b>Figure 4.6.</b> De-convolution of C1s and O1s XPS spectra for MWCNTs. ....	56
<b>Figure 4.7.</b> De-convolution of C1s, O1s, Si 2s and Si 2p XPS spectra for MWCNTs functionalized with 1.5 at % concentration of SiO <sub>2</sub> .....	57
<b>Figure 4.8.</b> De-convolution of C1s, O1s, Si 2s and Si 2p XPS spectra for MWCNTs functionalized with 5.75 at % concentration of SiO <sub>2</sub> .....	58
<b>Figure 4.9.</b> C <i>K</i> -edge XANES spectra of MWCNTs and MWCNTs:Si nanocomposites. ....	60
<b>Figure 4.10.</b> O <i>K</i> -edge XANES spectra of MWCNTs and MWCNTs:Si nanocomposites. ...	61
<b>Figure 4.11.</b> Si <i>L</i> <sub>3,2</sub> -edge XANES spectra of SiO <sub>2</sub> and MWCNTs:Si nanocomposites. ....	62
<b>Figure 4.12.</b> I-V curve for SiO <sub>2</sub> and MWCNTs.....	64
<b>Figure 4.13.</b> I-V curve for MWCNTs functionalized with 1.5 and 5.75 at % concentration of SiO <sub>2</sub> .....	64
<b>Figure 4.14.</b> I-V log plot for SiO <sub>2</sub> and MWCNTs.....	65

<b>Figure 4.15.</b> I-V log plot for MWCNTs functionalized with 1.5 and 5.75 at % concentration of SiO <sub>2</sub> .....	66
<b>Figure 4.16.</b> (a) Comparison of M-H loop for SiO <sub>2</sub> , MWCNTs, and MWCNTs:Si nanocomposites at different temperatures. (b) Field cooling (FC) and zero-field cooling (ZFC) for SiO <sub>2</sub> , MWCNTs, and MWCNTs:Si nanocomposites.....	67
<b>Figure 4.17.</b> ESR spectra for SiO <sub>2</sub> , MWCNTs, and MWCNTs:Si nanocomposites.....	70
<b>Figure 5.1.</b> (a), (b), (c) SEM images of TiO <sub>2</sub> , MWCNTs and MWCNTs-TiO <sub>2</sub> nanocomposite (d) EDS spectra for MWCNTs:TiO <sub>2</sub> nanocomposite. ....	84
<b>Figure 5.2.</b> XRD spectra for MWCNTs, TiO <sub>2</sub> , and MWCNTs-TiO <sub>2</sub> nanocomposites.....	85
<b>Figure 5.3.</b> Raman spectra for MWCNTs, TiO <sub>2</sub> and MWCNTs-TiO <sub>2</sub> nanocomposites.....	86
<b>Figure 5.4.</b> De-convolution of Raman spectra for MWCNTs, TiO <sub>2</sub> and MWCNTs-TiO <sub>2</sub> nanocomposites.....	87
<b>Figure 5.5.</b> XPS spectra for MWCNTs, TiO <sub>2</sub> , and MWCNTs-TiO <sub>2</sub> nanocomposites.....	90
<b>Figure 5.6.</b> De-convolution of C1s and O1s XPS spectra for MWCNTs and Ti 2p spectra for TiO <sub>2</sub> .....	91
<b>Figure 5.7.</b> De-convolution of C1s, O1s and Ti 2p XPS spectra for MWCNTs functionalized with 15 at % of TiO <sub>2</sub> . ....	92
<b>Figure 5.8.</b> De-convolution of C1s, O1s and Ti 2p XPS spectra for MWCNTs functionalized with 20 at % of TiO <sub>2</sub> . ....	93
<b>Figure 5.9.</b> C K-edge XANES spectra for MWCNTs and MWCNTs functionalized with 15 and 20 at % concentration of TiO <sub>2</sub> .....	95

<b>Figure 5.10.</b> O K-edge XANES spectra for TiO <sub>2</sub> , MWCNTs, and MWCNTs functionalized with 15 and 20 at % concentration of TiO <sub>2</sub> .....	96
<b>Figure 5.11.</b> Ti L <sub>2,3</sub> -edge XANES spectra for TiO <sub>2</sub> and MWCNTs functionalized with 15 and 20 at % concentration of TiO <sub>2</sub> .....	97
<b>Figure 5.12.</b> I-V curve for TiO <sub>2</sub> and MWCNTs.....	99
<b>Figure 5.13.</b> I-V curve for MWCNTs functionalized with 15 and 20 at % concentration of TiO <sub>2</sub> .....	99
<b>Figure 5.14.</b> I-V log plot for TiO <sub>2</sub> and MWCNTs. ....	100
<b>Figure 5.15.</b> I-V log plot for MWCNTs functionalized with 15 and 20 at % concentration of TiO <sub>2</sub> .....	100
<b>Figure 6.1.</b> (a, b, c, d and e) FESEM images for TiO <sub>2</sub> , SiO <sub>2</sub> , MWCNTs, and MWCNTs:Ti:Si nanocomposites. (d) EDS spectra for MWCNTs:Ti:Si nanocomposites.....	113
<b>Figure 6.2.</b> XRD spectra for TiO <sub>2</sub> , SiO <sub>2</sub> , MWCNTs, and MWCNTs:Ti:Si nanocomposites. ....	115
<b>Figure 6.3.</b> Raman spectra for TiO <sub>2</sub> , SiO <sub>2</sub> , MWCNT, and MWCNTs:Ti:Si nanocomposites. ....	117
<b>Figure 6.4.</b> De-convolution of Raman spectra for MWCNTs and MWCNTs:Ti:Si nanocomposites.....	118
<b>Figure 6.5.</b> XPS spectra for TiO <sub>2</sub> , SiO <sub>2</sub> , MWCNTs, and MWCNTs:Ti:Si nanocomposites.	120
<b>Figure 6.6.</b> XPS de-convolution of (a and b) C1s and O1s spectra for MWCNTs. (c) Ti 2p spectra for TiO <sub>2</sub> . (d and e) Si 2s and 2p spectra for SiO <sub>2</sub> . ....	123

<b>Figure 6.7.</b> De-convolution of C1s, O1s, Ti 2p, and Si 2p XPS spectra for MWCNTs:Ti:Si nanocomposites.....	124
<b>Figure 6.8.</b> Deconvolution of C1s, O1s, Ti 2p, and Si 2p XPS spectra for MWCNTs:Ti:Si nanocomposites.....	125
<b>Figure 6.9.</b> C <i>K</i> -edge XANES spectra of MWCNTs and MWCNTs:Ti:Si nanocomposites. ....	127
<b>Figure 6.10.</b> O <i>K</i> -edge XANES spectra of MWCNTs and MWCNTs:Ti:Si nanocomposites. ....	128
<b>Figure 6.11.</b> Si <i>L</i> <sub>3,2</sub> -edge XANES spectra of SiO <sub>2</sub> and MWCNTs:Ti:Si nanocomposites. ..	129
<b>Figure 6.12.</b> Ti <i>L</i> <sub>3,2</sub> -edge XANES spectra of TiO <sub>2</sub> and MWCNTs:Ti:Si nanocomposites...	130
<b>Figure 6.13.</b> I-V curve for SiO <sub>2</sub> and TiO <sub>2</sub> . ....	131
<b>Figure 6.14.</b> I-V curve for MWCNTs and MWCNTs:Ti:Si (6:6 at %) nanocomposite. ....	132
<b>Figure 6.15.</b> I-V curve for MWCNTs:Ti:Si (10:10 at %) nanocomposite.....	132
<b>Figure 6.16.</b> I-V log plot for TiO <sub>2</sub> and SiO <sub>2</sub> .....	134
<b>Figure 6.17.</b> I-V log plot for MWCNTs and MWCNTs:Ti:Si (6:6 at %) nanocomposite....	134
<b>Figure 6.18.</b> I-V log plot for MWCNTs:Ti:Si (10:10 at %) nanocomposite. ....	135



## LIST OF TABLES

<b>Table 4.1:</b> Different parameters obtained from the deconvolution of Raman spectra for MWCNTs and MWCNTs:Si nanocomposites.....	54
<b>Table 4.2:</b> XPS quantificational analysis of silicon (Si), carbon (C) and oxygen (O).....	55
<b>Table 4.3:</b> C 1s, O 1s, Si 2p and Si 2s XPS parameters obtained from the de-convoluted of SiO <sub>2</sub> , MWCNTs, MWCNTs:Si nanocomposites.....	59
<b>Table 4.4:</b> Parameters obtained from M-H loops [Retentivity (M <sub>R</sub> ) Coercivity (H <sub>C</sub> ), Magnetic and Saturation (M <sub>s</sub> ),] measured at 40 K and 300 K for SiO <sub>2</sub> , MWCNTs, MWCNTs:Si nanocomposites.....	68
<b>Table 4.5:</b> Parameters obtained from ESR of SiO <sub>2</sub> , MWCNTs, MWCNTs:Si nanocomposites at 300 K.....	71
<b>Table 5.1:</b> Parameters obtained from the deconvolution of Raman spectra for MWCNTs and MWCNTs-TiO <sub>2</sub> nanocomposites.....	88
<b>Table 5.2:</b> XPS compositional and quantificational analysis of silicon (Ti), carbon (C) and oxygen (O).....	89
<b>Table 5.3:</b> Parameters obtained from the de-convolution of C 1s, O 1s, and Ti 2p XPS spectra.....	94
<b>Table 6.1:</b> Parameters obtained from the deconvolution of Raman spectra for MWCNTs and MWCNTs:Ti:Si nanocomposites.....	119
<b>Table 6.2:</b> XPS quantificational analysis of titanium (Ti), silicon (Si), carbon (C) and oxygen (O).....	120

**Table 6.3:** Parameters obtained from the de-convolution of C 1s, O 1s, Ti 2p, and Si 2p XPS spectra ..... 121

**LIST OF ACRONYMS**

CCVD	Catalytic chemical vapor deposition
CNTs	Carbon nanotubes
CVD	Chemical vapor deposition
DWCNTs	Double walled carbon nanotubes
EDX	Energy dispersive X-ray analysis
ESR	Electron spin resonance
FC	Field cooling
FCNTs	Functionalized carbon nanotubes
FE-SEM	Field emission-scanning electron microscopy
GMR	Giant magneto-resistance
HFCVD	Hot-filament chemical vapor deposition
HRTEM	High resolution transmission electron microscope
I-V	Current-voltage
LA	Laser ablation
LED	Light emitting diode
M-H	Magnetization (M) - magnetic field (H)
MNMs	Magnetic nanomaterials

MPECVD	Microwave plasma enhanced chemical vapor deposition
MWCNTs	Multiwall carbon nanotubes
NPs	Nanoparticles
RF-CVD	Radiofrequency-chemical vapor deposition
SiO <sub>2</sub>	Silicon dioxide
SQUID	Superconducting quantum interference device
SWCNTs	Single walled carbon nanotubes
TiO <sub>2</sub>	Titanium dioxide
XANES	X-ray absorption near edge structure spectroscopy
XPS	X-ray photoelectron spectroscopy
XRD	X-ray diffraction
ZFC	Zero field cooling

**LIST OF SYMBOLS**

$r$	Radius
$H$	Magnetic field
$E$	Electric field
$B$	Magnetic induction
$M$	Magnetization
$M_r$	Remanence magnetization
$M_s$	Saturation magnetization
$H_c$	Coercive field
$I$	Electric current
$J$	Electric current density
$q$	Electric charge
$\omega$	Angular frequency
$A$	Area
$M$	Magnetic moment
$m_o$	Orbital magnetic moment
$m_s$	Spin magnetic moment
$l$	Orbital angular momentum

$v$	Velocity
$m_e$	Electron mass
$F$	Force
$\lambda$	Wavelength
$\sigma$	Electrical conductivity
$\nabla$	Curl
$E$	Exponential factor
$I_0$	Incident photon intensity
$\mu$	Absorption coefficient
$D$	Component concentrations
$V$	Volume of unit cell
$\sigma_i$	Absorption cross section
KE	Kinetic energy
$h$	Planck's constant,
$\nu$	Frequency of the incident radiation
$E_b$	Binding energy
$\phi$	Work function
$n$	Number of reflection

$d$	Distance of lattice
$\theta$	Angle of diffraction
$\beta$	Full width at half maximum
$\Delta H$	Line width
$h_u$	Upper peak height
$h_l$	Lower peak height
$P_{asy}$	Asymmetric factor
$N$	Number of spin
$I_{p-p}$	Peak to peak height
$H_r$	Resonance field
$g$	Lange gfactor

## List of published articles:

- Article 1:** **James A. Oke**, David O. Idisi, Sweety Sarma, S. J. Moloi, Sekhar C. Ray, K. H. Chen, A. Ghosh, A. Shelke, W. F Pong, (2019). Electronic, Electrical and Magnetic Behavioural change of SiO<sub>2</sub>-NPs decorated MWCNTs. *ACS Omega*, 4: 14589–14598.
- Article 2:** **James A. Oke**, David O. Idisi, Sweety Sarma, S. J. Moloi, Sekhar C. Ray, K. H. Chen, A. Ghosh, A. Shelke, S-H. Hsieh, W. F Pong, (2019). Tuning of Electronic and Electrical Behaviour of MWCNTs-TiO<sub>2</sub> Nanocomposite. *Diamond and Related Materials*, 100: 107570
- Article 3:** David O. Idisi, Hyder AAli, **J. A. Oke**, Sweety Sarma, S. J. Moloi, Sekhar C. Ray, H. T. Wang, Nikihil R., W. F. Pong, André M. Strydom, (2019). Electronic, Electrical and Magnetic Behaviour of reduced graphene-oxide functionalized with gold nanoparticles. *Journal of Applied Surface Science*, 483: 106-113.
- Article 4:** David O. Idisi, **James A. Oke**, Sweety Sarma, S. J. Moloi, Sekhar C. Ray, W. F. Pong, André M. Strydom, (2019). Tuning of electronic and magnetic properties of multifunctional reduced-graphene-oxide/Fe<sub>2</sub>O<sub>3</sub> nanocomposite for magnetic resonance imaging application. *Journal of Applied Physics*. 126: 035301.
- Article 5:** David O. Idisi, **James A. Oke**, Evans M. Benecha, Sabata Moloi, Sekhar Chandra Ray, (2020). Magnetic properties of graphene oxide functionalized with “Au” and “Fe<sub>2</sub>O<sub>3</sub>” nanoparticles: A comparative study. *Materials Today: Proceedings*. doi.org/10.1016/j.matpr.2020.02.869



**Article 6:** **James A. Oke**, David O. Idisi, S. J. Moloi, Sekhar C. Ray, Kuan Hung Chen, Anirudha Ghosh, Abhijeet Shelke, Way-Faung Pong, (2020). Structural, electronic, and electrical behaviour of MWCNTs:TiO<sub>2</sub>:(SiO<sub>2</sub>) nanocomposites. *Journal of Electron Spectroscopy and Related Phenomena*. 245, 147002.

# **Chapter One**

## **Introduction**

## **1. 1. Background**

The electronic and magnetic behavior of a material depends on the interaction of electrons in the material when subjected to an electric and magnetic field. The theory of electron explains electronic, magnetic, electrical, optical, and thermal properties of the material. This theory is important since new technology depends on it [1]. For example, electronic materials are used to fabricate devices for various applications such as light-emitting diode (LED), memories, and displays. Magnetic materials are utilized for transformers, electric generators, loudspeakers, motors, tapes, and tape recorders [1]. The current devices are unable to operate efficiently due to an increase or change in demand. It is therefore important that new materials with improved properties are developed to meet these technological challenges. The efforts in developing new materials have led to the search of materials that are ballistic with a weak spin-orbit coupling which yields long spin lifetime such as carbon nanotubes (CNTs) containing nano-magnetic materials [2]. In this work, properties of multiwall CNTs (MWCNTs) would be established and studied with the ultimate of improving its electrical and magnetic properties for various applications, particularly for nano-electronics devices.

## **1.2. Motivation of the study**

Understanding the interaction of spin electrons in nano-materials will enable avenue for novel electronic and magnetic devices. The technology is at advantage of producing a very fast, high density, less power consuming, non-volatile, and more versatile devices. The spin relaxation time is described as a time at which the electrons diffuse within the material without losing their coherence [3], which makes electronic and magnetic devices attractive for data processing and storage capabilities. The materials with long spin relaxation time are, therefore, reliable for electronic and magnetic applications.

An attempt has been made to improve the spin relaxation time of different materials. Jiang et al. [4] investigated the formation of a spin injection structure which is based on the crystalline MgO/CoFe tunnel barrier. Although, the structure showed long spin relaxation time at 100 K. The suggestion of sputter deposition fabrication of MgO by the author is still not understood, hence not reproducible. It was noted that the giant magneto-resistance (GMR) effect of MgO/CoFe was not studied. On the other hand, a material with long spin relaxation time corresponds to a large decrease or no GMR.

Morley et al. [5] worked on FeCo and NiFe spin-valve devices and showed that the material could have long spin relaxation time at room temperature. It was also observed that the thickness of the non-magnetic spacer increases with a decrease in GMR. The increase in the layer thickness will be a shortfall in the practical implementation of the structure. The reason being that the thickness of the layer needs to be at the nanoscale to control the coupling between the two ferromagnetic layers [6].

In-Mn:As and Ga-Mn:As [7,8] semiconductors have long spin lifetime and a Curie temperature of 35 K and 100 K, respectively. Despite the long spin relaxation time, the Curie temperature is low for practical implementation. The practical implementation of ferromagnetic materials requires a temperature range of at least  $\geq 300$  K, a temperature at which the devices would be expected to operate under. At this temperature, the materials however lose their permanent magnetism [9].

Similar work on improving properties of the materials for memory storage application was presented by Pramanik et al., Wang et al., and Park et al. [10-12]. In their work [10], nanowire spin valves based on tri-layer cobalt, an organic, Alq<sub>3</sub>, and nickel were fabricated. The result in this case showed a long spin relaxation time at 100 K. Despite the long spin relaxation time, the procedure seemed complex and there is a possibility of inter-dispersion of these materials

which could influence the results negatively. Furthermore, the long spin relaxation time discovered at a low temperature is still a shortfall.

Wang et al. [11] worked on Fe/Alq<sub>3</sub>/Co spin-valves. In this case, a long spin relaxation time and GMR approximately 5 % at 11 K were observed. GMR was also observed to vanish at 90 K. The GMR vanishing at a low temperature is a challenge for practical implementation, since it shows that the device would be unstable, hence, unreliable during its operation time. In a related study, Park et al. [12] studied the flow of electrons from an antiferromagnetic layer (IrMn) to a non-magnetic metallic layer (Pt) through a tunnel barrier. A large GMR of approximately 160 % at 4 K was detected. The effect of GMR later vanishes at 100 K. The low temperature observed will be a challenge for practical applications. It can be noticed that as the properties are being improved the temperature has been a challenge [13–15].

Hueso et al. [13] demonstrated an injection of spin currents from La<sub>0.7</sub> Sr<sub>0.3</sub> MnO<sub>3</sub> into CNT and transform the spin information into a large electrical signal. The direct action of the magnetic field on electric current calculated in their system was 61% at 5 K. This indicates long spin relaxation time still at low temperature.

In their study, Tsukagoshi et al. [14] found MWCNTs/Co to have long spin relaxation time and a decrease in GMR which later vanishes at 20 K. The vanishing of GMR at a low temperature is a setback. Similar work on CNT/Fe and CNT/(Ga, Mn) was presented by [15], the GMR vanishes at a low temperature, <30 K.

The interactions of spin electrons of some nano-composite materials have not been fully understood. These materials have shown the potential to be suitable for various applications [15]. The current study involves MWCNTs materials which are more cost-effective and promising materials compared with those used in previous studies [4,5,7,8,10-12]. These

materials are most suitable due to their perfect spin-transport medium. MWCNTs also have spin electron transport in one-dimensional and ballistic with a weak spin-orbit coupling which yields a long spin relaxation time [16]. MWCNTs are diamagnetic material because they lack a magnetic moment. Also, they are conducting in nature and are low-density materials [17,18]. Based on this fact, properties of MWCNTs need to be improved by functionalizing them with some nanoparticle materials to establish their magnetic moment, semiconducting behaviour with high storage density, and to vary its magnetization for different electronic, electrical and magnetic applications.

Silicon and Titanium dioxide were used to functionalize MWCNTs due to the fact that Silicon and Titanium are cheaper and abundant in nature. Also, silicon is a semiconducting material that can act as an insulating as well as a conducting material depending on the operating condition. Titanium, on the other hand, has excellent physical properties such as lightweight, corrosion resistance, and high strength which can be oxidized to produce titanium dioxide ( $\text{TiO}_2$ ) [19].  $\text{TiO}_2$  could be considered as a supporting nanomaterial due to its semiconducting properties, nontoxic, and possibility of charge transfer characteristic [20]. It is of these reasons silicon, titanium dioxide, and the composition of the two (Si and  $\text{TiO}_2$ ) were used to tune the properties of MWCNTs to establish the feasibility of the material to be used for electronic, electrical and magnetic device applications.

### **1.3. Aim and objectives**

The aim is to develop reliable functionalized MWCNTs for efficient electronic and magnetic material-based devices.

The specific objectives are to:

1. Synthesize MWCNTs materials using spray pyrolysis and chemical vapor decomposition methods;
2. Functionalize MWCNTs materials with different concentrations of SiO<sub>2</sub>-NPs, TiO<sub>2</sub>-NPs, and TiO<sub>2</sub>:SiO<sub>2</sub> using different methods;
3. Characterize the unfunctionalized and functionalized materials with different techniques;
4. Study the electronic, electrical, and magnetic properties of unfunctionalized and functionalized MWCNTs materials.

## 1.4. Structure of the thesis

**Chapter one** presents information on a general introduction to the electronic and magnetic properties of MWCNTs, motivation, problems, aim, and objectives of the research. **Chapter Two** consists of the overview, properties, synthesis, structure, functionalization, magnetism, and applications of CNTs. **Chapter Three** consists of the experimental details, which involve characterization techniques. **Chapter Four** studies the electronic, electrical, and magnetic behavioral change of MWCNTs-SiO<sub>2</sub>-NPs with the aim of developing a material with improved properties for different electronic/magnetic applications. **Chapter Five** investigates the electronic and electrical behavior of MWCNTs-TiO<sub>2</sub> nanocomposites material with the help of different techniques used in this article for electrical/electronic devices, particularly for memristive devices. **Chapter Six** examines the electronic, electrical, and bonding properties of MWCNTs:Ti:Si materials and explains the chemical bonding, electrical, and electronic structure of the material. **Chapter Seven** contains a summary of chapter One to Six, general conclusion, recommendations, and future work. The published papers to peer-review journals are contained in the **Appendix**.

## References

- [1] Rolf E Hummel, *Electronic properties of materials. Springer Science & Business Media*, 2011.
- [2] S. C. Ray, S. Sitha, and P. Papakonstantinou, “Change of magnetic behaviour of nitrogenated carbon nanotubes on chlorination/oxidation,” *Int. J. Nanotechnol.*, vol. 14, no. 1–6, pp. 356–366, 2017.
- [3] S. Das Sarma, J. Fabian, X. Hu, and I. Žutić, “Spintronics: Electron spin coherence, entanglement, and transport,” *Superlattices Microstruct.*, vol. 27, no. 5, pp. 289–295, 2000.
- [4] X. Jiang *et al.*, “Highly spin-polarized room-temperature tunnel injector for semiconductor spintronics using MgO(100),” *Phys. Rev. Lett.*, vol. 94, no. 5, pp. 1–4, 2005.
- [5] N. A. Morley, A. Rao, D. Dhandapani, M. R. J. Gibbs, M. Grell, and T. Richardson, “Room temperature organic spintronics,” *J. Appl. Phys.*, vol. 103, no. 7, pp. 101–104, 2008.
- [6] F. J. Ferraro, “Magnetic anisotropies and exchange bias in ultrathin cobalt layers for the tunnel anisotropic magnetoresistance,” *PhD Thesis*, 1-159, 2015.
- [7] H. Akai, “Ferromagnetism and its stability in the diluted magnetic semiconductor (In, Mn) As,” *Phys. Rev. Lett.*, vol. 81, no. 14, pp. 3002–3005, 1998.
- [8] F. Matsukura, H. Ohno, A. Shen, and Y. Sugawara, “Transport properties and origin of ferromagnetism in (Ga,Mn)As,” *Phys. Rev. B*, vol. 57, no. 4, pp. 2037–2040, 1998.



- [9] S. J. Pearton *et al.*, “Advances in wide bandgap materials for semiconductor spintronics,” *Mater. Sci. Eng. R Reports*, vol. 40, no. 4, pp. 137–168, 2003.
- [10] S. Pramanik *et al.*, “Observation of extremely long spin relaxation times in an organic nanowire spin valve,” *Nat. Nanotechnol.*, vol. 2, no. 4, pp. 216–219, 2007.
- [11] F. J. Wang, Z. H. Xiong, D. Wu, J. Shi, and Z. V. Vardeny, “Organic spintronics: The case of Fe/Alq<sub>3</sub>/Co spin-valve devices,” *Synth. Met.*, vol. 155, no. 1, pp. 172–175, 2005.
- [12] B. G. Park *et al.*, “A spin-valve-like magnetoresistance of an antiferromagnet-based tunnel junction,” *Nat. Mater.*, vol. 10, no. 5, pp. 347–351, 2011.
- [13] L. E. Hueso *et al.*, “Transformation of spin information into electrical signals using carbon nanotubes,” *Nature*, vol. 445, p. 410, 2007.
- [14] S. Tsukagoshi, B. W. Alphenaar, and H. Ago, “Coherent transport of electron spin in a ferromagnetically contacted carbon nanotubes,” *Nature*, vol. 401, no. October, pp. 572–574, 1999.
- [15] A. Jensen, J. R. Hauptmann, J. Nygård, and P. E. Lindelof, “Magnetoresistance in ferromagnetically contacted single-wall carbon nanotubes,” *Phys. Rev. B - Condens. Matter Mater. Phys.*, vol. 72, no. 3, pp. 1–5, 2005.
- [16] R. H. Baughman, “Carbon Nanotubes — the Route Toward,” *Science (80-. )*, vol. 297, no. 787, pp. 787–792, 2002.
- [17] M. S. . Shaffer, T. Prasse, A. . Windle, J. Sandler, K. Schulte, and W. Bauhofer, “Development of a dispersion process for carbon nanotubes in an epoxy matrix and the resulting electrical properties,” *Polymer (Guildf.)*, vol. 40, no. 21, pp. 5967–5971, 2002.

- [18] W. Shi *et al.*, “High pressure study of nitrogen doped carbon nanotubes using Raman spectroscopy and synchrotron X-ray diffraction,” *Arab. J. Chem.*, Vol. 13, no. 1, 3008-3016, 2018.
- [19] W. L. Johnson, A. Kahl, G. Duan, M. L. Lind, and A. Wiest, “Lightweight Ti-based bulk metallic glasses excluding late transition metals,” *Scr. Mater.*, vol. 58, no. 6, pp. 465–468, 2007.
- [20] S. Delpeux, A. Jitianu, S. Bonnamy, R. Benoit, T. Cacciaguerra, and F. Béguin, “Synthesis and characterization of carbon nanotubes–TiO<sub>2</sub> nanocomposites,” *Carbon N. Y.*, vol. 42, no. 5–6, pp. 1147–1151, 2004.

## **Chapter Two**

### **Overview of CNTs**

## 2.1. A brief history of CNTs

Carbon nanotubes (CNTs) have been discovered as carbon filament decades ago (1952) by Russian scientists Lukyanovich and Radushkevich. It was quite unfortunate that their discovery was not recognized by western scientists due to the cold war at that time. Access to their article was limited and most of the Russian papers didn't appear in the database of literature [1]. In the 1970s, throughout oxygen combustion, carbon nanofilaments were formed as a by-product alongside carbon fibers. Thereafter, Iijima used HRTEM (high-resolution transmission electron microscopy) to investigate these nanofilaments, which brought about CNTs discovery in 1991 [2] and was given credit for making CNTs known to the science community. Iijima [3] and Bethune [4] also reported single-wall carbon nanotubes (SWCNTs) in 1993. The discovery of CNTs opened ways for novel electronics due to their characteristics, which was proven experimentally in 1998 [5].

## 2.2. Carbon nanotubes (CNTs)

Carbon materials exist in amorphous, diamond, and graphite structures. The well-known allotropes of carbon are graphite and diamond [6]. Research methods have expanded the existing knowledge about carbonaceous materials and more allotropes have been identified [6]. These allotropes include [7]: graphene, fullerene, and carbon nanotubes. Most research in material science has been about the allotropes (graphitic carbon) due to their exceptional electrical [7–9], thermal [7,9,10], and mechanical [7,9,11] properties for several applications such as electronics, communication, storage, medical and composite materials [9,12]. Research about nanotubes has accelerated over the last decade due to their better properties and have begun to find several commercial applications [7]. After the discovery of CNT by Iijima [13], most research has been about synthesis, properties [7], and applications [12,14]. CNTs can be synthesized and purified using different techniques. The most common techniques used in

synthesizing CNTs are arc discharge, laser ablation (LA), and chemical vapor deposition (CVD) [15]. The techniques used in purifying CNTs are oxidation, ultrasonication, acid treatment, annealing, micro filtering, and functionalization techniques [12].

### **2.2.1. Synthesis of CNTs**

Arc discharge method makes use of two graphite electrodes (cathode and anode), which were steamed by 100 A DC current through a separation of 1 to 2 mm between the cathode and anode in a helium atmosphere of 400 mbar. After this process, the cathode experiences a build-up of the carbon rod. This method is mostly used in the production of MWCNTs and also, with the introduction of catalysts like Mo, Ni, Co, or Fe, SWCNTs can be produced. Parameters like metal concentration, temperature, type of gas used and inert gas pressure determined the quality and quantity of the purity, lengths, and diameters of the obtained nanotubes. Thereafter, another method was successfully introduced in 1996 by Smalley called laser ablation (LA), which produces SWCNT in large quantities [16]. In the LA method, a composite of graphite-metal (target) is placed in a furnace of high temperature up to 1200°C. A laser beam is then focused on the target which scans through the surface for vaporization. There is some dirt produced during this process, which is been cleaned by Ar gas flowing through the system from a very high-temperature region into a water-cooled collector made of copper situated outside the furnace. The LA method utilizes 1.2 percent of nickel/cobalt and 98.8 percent of the target, the metal act as a catalyst in growing the SWCNTs [17]. Arc discharge and laser ablation are techniques used in synthesizing CNTs with high quality. They, however, have the disadvantage of being costly and low scale production. The purification of the obtained CNT is difficult due to the mixture of unwanted carbon impurities and metal species. CVD is another well-known technique used in synthesizing CNTs on a large scale, which has the degree of control over length, diameter, and morphology. It also has a higher potential for industrial production [12],

[15]. In the CVD process, nitrogen and hydrocarbon gas (methane, acetylene, and ethylene) are disintegrated under atmospheric pressure on a catalytic metal hot substrate inside a reactor at approximately  $1000^{\circ}\text{C}$  to maintain the growth of CNT on the metallic catalyst. Different substrate can be used such as glass,  $\text{SiO}_2$ , or Si for the deposition of solid catalyst, or injected gas [18,19]. The morphology of CNTs can be controlled using a high magnetic field (10 T) [20]. Types of CVD are radiofrequency (RF-CVD), microwave plasma (MPECVD), catalytic chemical (CCVD) (thermal or plasma-enhanced (PE) oxygen assisted CVD) and hot-filament (HFCVD) or water-assisted CVD. Nowadays, among the CVD techniques, CCVD is the most used technique for synthesizing CNTs. In comparison with arc discharge and laser ablation, using CCVD is more economical and has the advantage of large-scale production of pure CNTs [21].

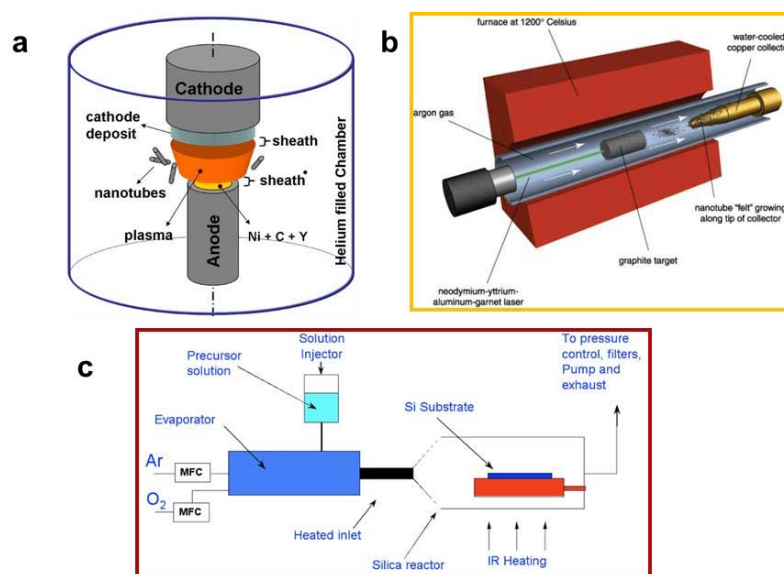


Figure 2.1. Setup technique (a) arc discharge, (b) laser ablation, (c) thermal CVD [15].

### 2.2.2. Purification of CNTs

Oxidation technique is a process of removing carbonaceous impurities using oxidizing agents such as  $\text{H}_2\text{O}_2$  and  $\text{H}_2\text{SO}_4$ . The main disadvantage of this technique is that the impurities are not

only oxidized but also the CNTs. In the ultrasonication technique, vibration is used to obtain a pure CNTs in which the nanoparticles are separated and become more dispersed due to the introduction of vibration. The separation of the particles depends on the reagent, solvent, and surfactant used. Acid treatment is another well-known technique, which is used to remove impurities such as metal catalysts from CNTs. The surface of the metal must be exposed by oxidation or sonication before exposure to acid and solvated. The treatment has an effect on the metal catalyst but little or no effect on the pure CNTs obtained. Annealing method also involves the use of a very high temperature ranging from 873 to 1873 K to obtain a pure CNTs. The high temperature causes the graphitic carbon to decompose. When using high-temperature treatment of 1873 K, the metal will melt and can be separated from pure CNTs. Microfiltration is also a purification technique that is based on particle size separation. In this technique, CNTs are then trapped in a filter and other impurities are passing through the filter to obtain pure CNTs. Another most used technique is the functionalization of CNTs, in this process, other groups are been attached to the wall of CNTs, which makes them more soluble than the impurities. This attachment makes easy separation of CNTs from the insoluble impurities (metal) with filtration [12].

### **2.2.3. Structure of CNTs**

CNT is a cylindrical fullerene or a wrapped graphene sheet (single layer of graphite atoms) and consists of  $sp^2$  hybrid carbon atom [12,22]. It exists in a single wall CNTs (SWCNTs), double-wall CNTs (DWCNTs) and multiwall CNTs (MWCNTs) [12]. CNTs are arranged in a hexagonal shape (honeycomb arrangement) with each carbon atom covalently bonded to the other three carbon atoms. Nanotubes can either be an armchair, zigzag and chiral structures, depending on the folding of graphene sheet [23]. The structures of CNTs are shown in Figures 2.2 and 2.3.

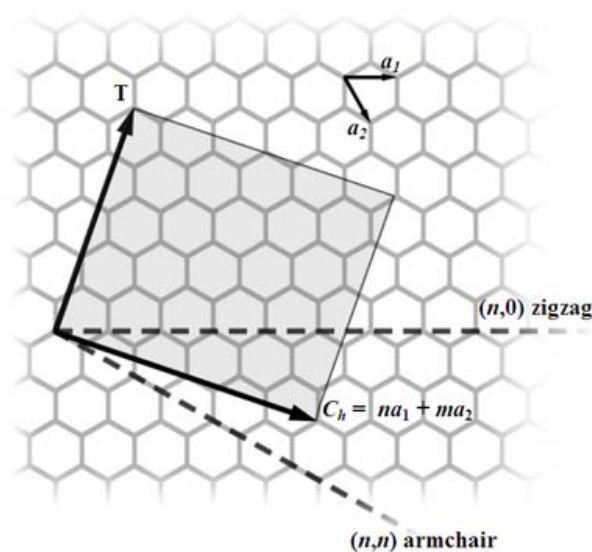


Figure 2.2. Vector direction of chiralities of CNTs [12].

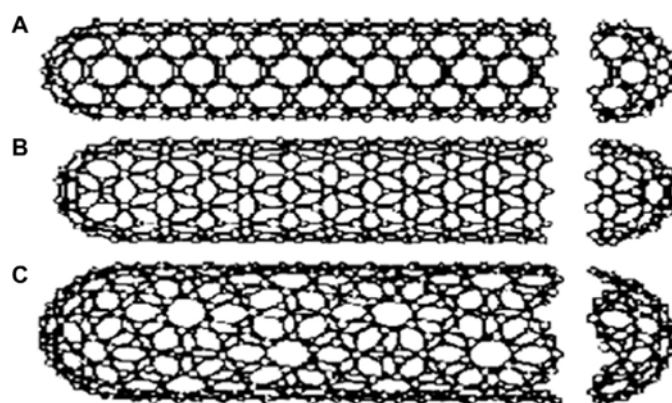


Figure 2.3. Different structures chiralities of CNTs. (a) armchair (b) zigzag (c) chiral [12].

In SWCNT, the carbon nanotube is a sheet of graphene wrapped into a cylinder (one-atom thick-layer of graphite) with open or closed ends with a definite size in a definite direction. Putting the cylinder symmetric into consideration, the graphene sheet have several atoms, and two out of these atoms are chosen, in which one serves as the origin. This sheet is wrapped till the two atoms overlap. The tube circumference is equal to the length of the vector which is pointing from one atom to the other and it is called a chiral vector (Figure 2.2). The axis of the tube's direction and the chiral vector are perpendicular to each other. The difference in chiral



vectors of SWCNTs has different electrical conductivity, mechanical strength, and optical properties, while in DWCNTs, there are two SWCNTs with one nested within the other with different diameters. MWCNTs, on the other hand, consist of multiple concentric SWCNTs where the interlayers are held together by Van der Waal's forces [22]. Two models used in describing the MWCNTs structures are Russian Doll and Parchment models. In the Russian Doll model, the sheets of graphite are arranged in concentric cylinders, while in the Parchment model, a single sheet of graphite is wrapped in around itself, like a rolled newspaper. The diameter of the outermost layer varies between a few nanometers (nm) and hundreds of nanometers, while the length can be as long as 100  $\mu\text{m}$ . These forms of CNTs are shown in Figure 2.3.

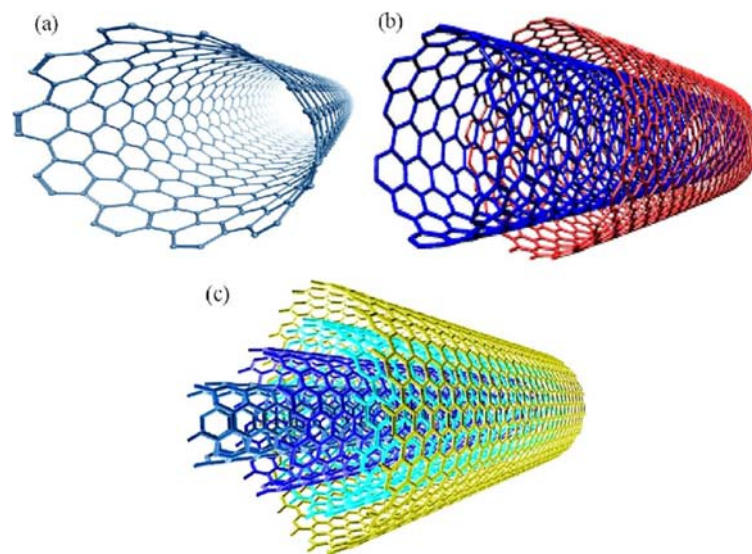


Figure 2.4. (a) Single wall carbon nanotubes (SWCNTs) (b) Double wall and carbon nanotube (DWCNT) (c) Multiwall carbon nanotubes (MWCNTs) [24].

MWCNTs are more attractive than SWCNTs because of their relatively low-cost production and availability in large quantities [24]. However, because of their chemical inertness, carbon nanotubes have to be functionalized to establish additional physical and chemical properties for electronic applications [24].

## 2.2.4. Properties of CNTs

Owing to one dimensional structure of CNTs, their electrical, thermal, and mechanical properties have been established to a huge extent. Their significant properties are been highlighted below.

### 2.2.4.1. Electrical properties

The electrical properties of CNTs depend on how the graphene sheet is been wrapped. Also, tube diameters and chirality ( $n, m$ ) have an effect on their electrical properties. Owing to the direction in which CNTs is wrapped, they can either be semiconductor or metallic in nature with large and small energy gap [25]. For example; CNTs with the zigzag and Armchair structure are semiconducting and metallic material, respectively, while chiral has a unique structure [26]. The name of the structures initiated from the shape of the cross-sectional ring. The armchair structure has the chiral ( $n, n$ ) direction at angle  $30^\circ$  with metal-like conductivity [27] with pseudo forbidding gap ranging from 2 to 50 meV and diameter range of 3.0 to 0.7 nm [28], respectively. The zigzag structure has a chiral ( $n, 0$ ) direction at angle  $0^\circ$  with semiconducting properties [27]. They have forbidding gap associated to their diameter, which range from  $< 0.4$  to 2 eV with diameter  $> 3.0$  and 0.4 nm [29], respectively. Chiral structure has chiral ( $n, m$ ) direction at angle  $30^\circ > \theta > 0^\circ$  [27]. Naturally, CNTs have electrical resistivity like a metal ( $10^{-4}$  to  $10^{-3} \Omega \text{ cm}$ ) [30] with a current flow a thousand times higher than that of copper ( $10^9 \text{ A cm}^{-2}$ ) [31].

### 2.2.4.2. Mechanical strength

The honeycomb-like lattice of graphite in which its single layer makes up graphene with several atoms are held together chemically by strong bonds [32]. Due to these bonds, graphite is known as the largest basal-plane elastic modulus. Based on this fact, CNTs have been predicted to have great high strength fibers. SWCNTs for example, are harder than steel and

are damage resistant to physical forces. The tip of CNTs bends when pressed but tends to return to its original state when the force is removed without causing any damage to the tip. This uniqueness of CNTs makes them useful for high-resolution scanning microscopy [33]. CNTs have superior mechanical properties with large surface area and less density of  $200\text{-}900\text{ m}^2\text{g}^{-1}$ , and  $1\text{-}2\text{ g cm}^{-3}$ , respectively. A high Young's modulus and tensile strength have been reported for MWCNTs to be 1.8 TPa and 150 GPa and 1.0 TPa and 100 GPa for SWCNTs, respectively [31,34].

#### **2.2.4.3. Thermal conductivity**

As wrapped graphene structures, CNTs are smaller in size. The quantum effects are of significant and thermal conductivity and the low-temperature specific heat shows evidence of 1-D quantization of phonon band structure in CNTs [32]. Due to the uniqueness in structures or shapes of CNTs, made their longitudinal thermal conductivity exceptionally greater than that of graphite of range  $1750\text{-}5800\text{ W m}^{-1}\text{ K}^{-1}$  at 300 K which is following the thermal conductivity of pure diamond [25]. CNTs also have high thermal stability up to  $\sim 750$  and  $\sim 2800$  °C in air and vacuum respectively [34,35].

#### **2.2.5. Functionalization of CNTs**

Functionalization of CNTs is a deliberate introduction of impurity atoms or molecules into the lattice of CNTs, either by physisorption or chemical bonding [26]. CNTs are functionalized to modify their electrical, chemical, physical, and magnetic properties for various applications [36]. As a result, functionalization could be a route to modify the properties of material towards the desired application [26]. Attaching or restraining chemical or biological atoms or molecules onto the surface of CNTs can also give room for biochemical sensors [26,37]. Functionalizing CNTs with ferromagnetic nanoparticles or the adsorption of oxygen atoms transform their diamagnetic to ferromagnetic behavior. When CNTs are wrapped into zigzag chirality, they

act as a semiconducting material and are diamagnetic in nature, although, coating them with titanium establish their conductivity and magnetization [26]. The two main methods used to functionalize CNTs are covalent and non-covalent modification [12,36]. Covalent and non-covalent modification attaches functional groups to the CNTs. The attachment of the functional group can be on the ends or sidewall [36]. Furthermore, CNTs tend to agglomerate due to their hydrophobic nature deterring their dispersion in the solvent. To disperse CNTs in a solvent, the surface needs to be modified to decrease the hydrophobicity and improve the interfacial bond to other material through chemical attachment [15]. Due to this uniqueness and the possibility of modifying its surface, CNT becomes promising material for other many technological applications [22] particularly for nanoelectronics devices [38]. It is mainly of these reasons that the study is about CNTs.

#### **2.2.5.1. Non-covalent modification of CNTs**

Non-covalent functionalization does not disrupt the natural configuration of the CNTs with the cost of stability [36]. Different techniques were used in carrying out non-covalent functionalization. These techniques include metal, polymer biological, and Endohedral functionalization. Metal functionalization involves the use of nanoparticles like Ni, Au, or Ag to be decorated on the surface of CNTs [30]. Functionalizing CNTs with polymer energizes the Van Der Waals forces to roll CNTs with polymer chains as seen in Figure 2.5 (D) [39]. The conjugation of protein and DNA are attached to the wall of CNTs by biological functionalization (Figure 2.5 (E)) to produce bioactive CNTs for drug carriers and bio-sensing [30], [40]. Endohedral functionalization is a method whereby molecules are captured within CNTs by the effect of a capillary tube [39] (Figure 2.5 (E)).

### 2.2.5.2. Covalent modification of CNTs

The covalent process is very stable and the  $sp^2$  hybridization is disrupted due to  $\sigma$ -bond formed. During mechanical loading and production, the  $\sigma$ -bond formed normally contains defect sites, which disrupt local bonds [26]. For example, functionalizing CNTs with  $HNO_3$  [41–43],  $H_2SO_4 / HNO_3$  [44–46],  $H_2O_2 / H_2SO_4$  [42,47] induced the formation of  $C=O$ ,  $C-OH$  and  $COOH$  bonds [48,49], which are connected covalently to the structure of CNTs. Furthermore, the attachment of nanoparticles (NPs) can also form a covalent bond directly by transforming the carbon atom from  $sp^2$  to  $sp^3$  hybridization. This technique provides a strong covalent bond and wide destruction which leads to a huge defect [30,39]. The different types of covalent and non-covalent functionalization are presented in figure 2.5.

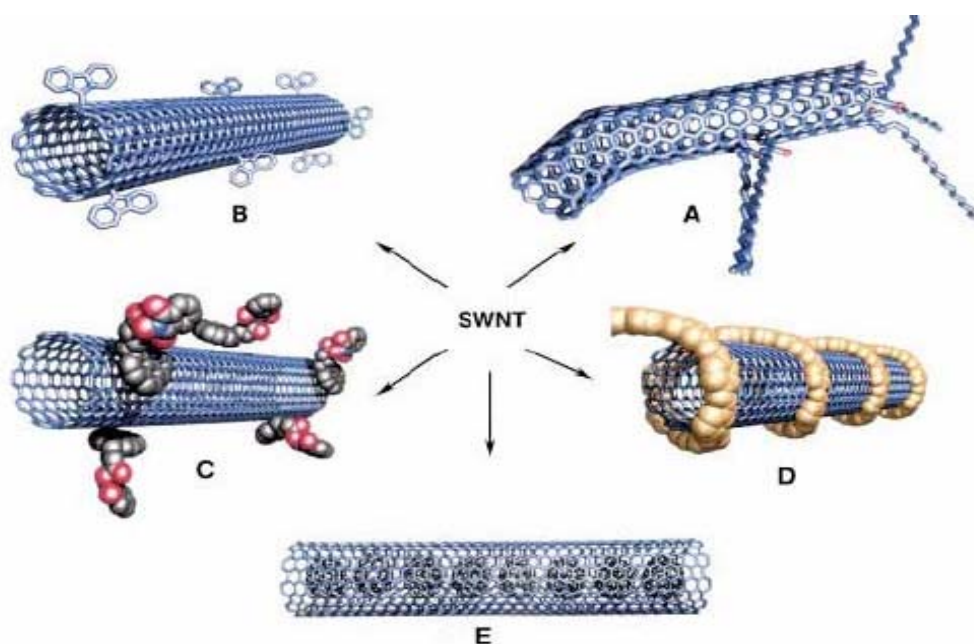


Figure 2.5. Possible modification for CNTs: (A) defect modification, (B) wall-side modification, (C) bio- modification, (D) polymer modification, and (E) endohedral modification [30].

### 2.3. Magnetic CNTs

Elements of the periodic table are classified base on their positive and negative relative permeability into ferromagnetic, antiferromagnetic, diamagnetic, and paramagnetic materials. Ferromagnetic materials are iron, cobalt, and nickel with high permeability of  $10^2$  to  $10^5$ , which makes magnetic moments in them parallel and equal. In Antiferromagnetic materials, the reverse is the case whereby their magnetic moments are equal and antiparallel, which produces nearly zero net magnetization. This only occurs in chromium [27]. Paramagnetic materials are material (oxygen) with positive and low relative permeability. Diamagnetic materials like noble gases and carbon are the weakest form of a magnetic material due to their very weak negative relative permeability.

CNTs are diamagnetic materials, but the attachment of magnetic nanomaterials (MNMs) onto its surface either by covalent or non-covalent modification makes them a potential material for magnetic applications. The incorporation of MNMs to a diamagnetic material with high relative permeability induce a composite material with transitional magnetic behavior. The attachment of MNMs is an appropriate way to control and align CNTs when exposed to an external magnetic field [50,51]. This functionalized (F)CNTs surface also offers different surfaces that match well with dispersing mediums. The FCNT's surface is used to overwhelm the high connected electric resistance that occurs owing to their anisotropic behavior. Also, the functionalization of the CNTs surface improves their mechanical properties by helping with mechanical load transfer [52]. Due to nature (quasi-one-dimensional) of CNTs, making them parallel alongside their longitudinal axes are best exploited [53]. Magnetic CNTs are used in several applications such as biomedical applications [54], phase separation [55], microwave absorbers [56,57], drug carriers [40,58], and wastewater treatment [59,60].

### 2.3.1. Magnetic moment

Modifying CNTs with MNMs can be achieved by utilizing the techniques discussed above. MNMs are materials that possess magnetic moment which can be used to manipulate CNTs in several dispersing medium using an external magnetic field. When an electric current is flowing through a wire it produces a magnetic field ( $H$ ). The current density ( $J$ ) is equal to the curl of the magnetic field ( $\nabla \times H$ ) with a stable electric field [27]. Also, when a current ( $I$ ) is introduced into a finite loop of area ( $A$ ) with angular velocity ( $\omega$ ) and charge ( $q$ ), produces a magnetic moment ( $m$ ). Likewise, the electrons in a circular path moving with  $q = -e$ , velocity ( $v = \omega \times r$ ), and mass ( $m_e$ ) as shown in figure 2.6 produced an orbit  $m$  ( $m_o$ ) and orbit  $l$  [27].

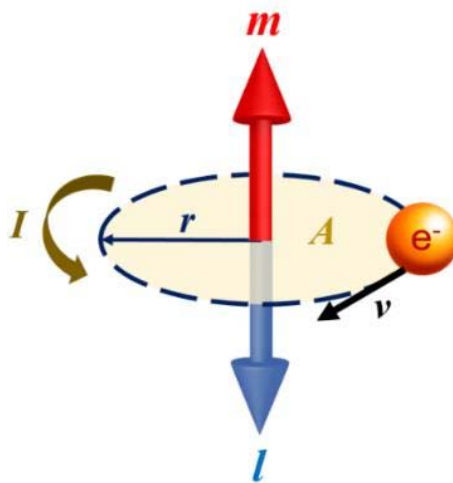


Figure 2.6. Production of angular momentum ( $l$ ) and magnetic moment ( $m$ ) through current flowing a loop [27].

### 2.3.2. Magnetic domains

A region in a magnetic material can be regarded as a magnetic domain when the magnetization is in a homogenous direction. This indicates a single domain where the magnetic moments are aligned pointing in the same direction. When the material is cooled beyond Curie temperature, the region is then divided into smaller regions known as multi-domains. These multi-domains

are separated by domain walls in which the magnetization in one domain is parallel to the other or in a different direction [27]. The structure of the magnetic domain determines the magnetic behavior of the material. The magnetization in each domain can be in different angles and are categorized into single,  $180^\circ$ ,  $90^\circ$  wall domains [61] as displayed in figure 2.7.

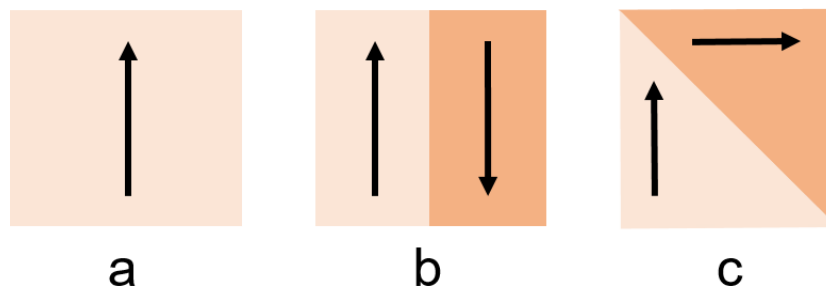


Figure 2.7. (a) single-wall domain. (b)  $180^\circ$  wall domain. (c)  $90^\circ$  wall domain [61].

### 2.3.3. Magnetic-hysteresis (M-H) loop

The magnetization of a material can be determined by using the M-H loop, which shows the level of magnetization and demagnetization of that material as presented in figure 2.8. When the magnetic field is applied, the domain walls accelerate in contrary to the crystal defects. This is to direct the magnetic moment into the crystal axis, which is closely aligned to the direction of the field. Therefore, making the material a single domain. The single-domain can then be rotated from the easy direction to a parallel direction by an increase in the strength of the magnetic field. The magnetization in the material reaches a magnetic saturation ( $M_s$ ) and the field applied is been removed, the material still retains its magnetization. This is known as remanence magnetization ( $M_r$ ). Furthermore, the retained magnetization needs to be reduced to zero, which involves the reversal of the process, and the required field needed to do so is known as a coercive field ( $H_c$ ) [27]. This mechanism is analogous to the electrical hysteresis loop. The figure below represents the M-H loop of a magnetic material.



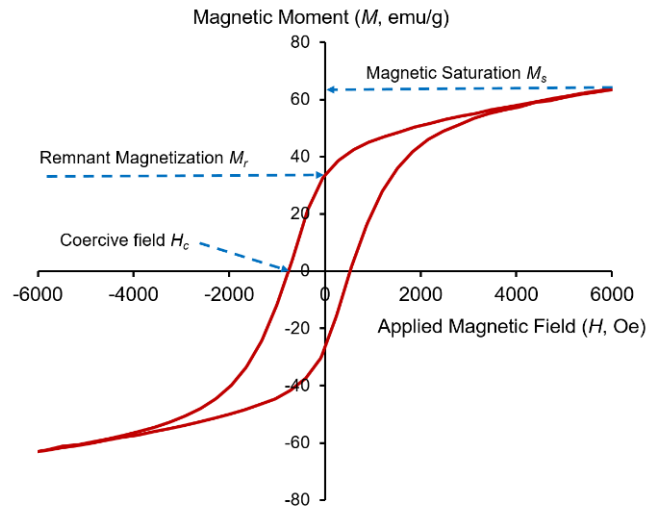


Figure 2.8. M-H loop of a magnetic material [27].

## 2.4. Electrical hysteresis loop and memristive behavior

Most CNTs are conducting material in nature but when functionalized with semiconducting NPs using the methods discussed earlier, its electrical structure can be transformed into a semiconducting material. It has been confirmed that most types of semiconductor spintronic systems have memristive behavior [62]. The mechanism is based on a convenient control of electron spin degree of freedom in nanostructures. If the external voltage (control parameter) is changed, the tuning of electron spin polarization is deferred because of the relaxation and diffusion processes, thereby causing hysteresis [63].

## References

- [1] P. J. F. Harris, "Transmission Electron Microscopy of Carbon : A Brief History," *C—Journal of Carbon Research*, vol 4, no. 1, 1-17, 2018.
- [2] S. Iijima, "Helical microtubules of graphitic carbon," *Nature*, vol. 354, no. 6348, pp. 56–58, 1991.
- [3] T. I. S Iijima, "Single-shell carbon nanotubes of 1-nm diameter," *Nature*, vol. 362, no. 6430, pp. 603-605, 1993.
- [4] D. S. Bethune *et al.*, "Cobalt-catalysed growth of carbon nanotubes with single-atomic-layer walls," *Nature*, vol. 363, no. 6430, pp. 605–607, 1993.
- [5] S. B. Sinnott, R. Andrews, and S. B. Sinnott, "Carbon Nanotubes : Synthesis , Properties , and Applications Carbon Nanotubes : Synthesis, Properties and Applications," *Critical Rev. in Solid State and Mater. Sci.*, vol. 26, no. 3, 145-249, 2001.
- [6] M. I. Katsnelson, "Graphene: Carbon in two dimensions," *Graphene Carbon Two Dimens.*, vol. 9780521195, no. 1, pp. 1–351, 2012.
- [7] S. K. Tiwari, V. Kumar, A. Huczko, R. Oraon, A. De Adhikari, and G. C. Nayak, "Magical Allotropes of Carbon: Prospects and Applications," *Crit. Rev. Solid State Mater. Sci.*, vol. 41, no. 4, pp. 257–317, 2016.
- [8] S. Park and R. S. Ruoff, "Chemical methods for the production of graphenes," *Nat. Nanotechnol.*, vol. 4, no. 4, pp. 217–224, 2009.
- [9] G. Lalwani and B. Sitharaman, "Multifunctional Fullerene- and Metallofullerene-Based Nanobiomaterials," *Nano Life*, vol. 3, no. 3, pp. 1-22, 2013.

- [10] A. A. Balandin *et al.*, “Superior thermal conductivity of single-layer graphene,” *Nano Lett.*, vol. 8, no. 3, pp. 902–907, 2008.
- [11] I. W. Frank, D. M. Tanenbaum, A. M. van der Zande, and P. L. McEuen, “Mechanical properties of suspended graphene sheets,” *J. Vac. Sci. Technol. B Microelectron. Nanom. Struct.*, vol. 25, no. 6, p. 2558, 2007.
- [12] M. Daenen, R. D. de Fouw, B. Hamers, P. G. A. Janssen, K. Schouteden, and M. A. J. Veld, “The Wondrous World of Carbon Nanotubes,” *Eindhoven Univ. Technol.*, no. 2, pp. 1–35, 2003.
- [13] S. Iijima, P. M. Ajayan, and T. Ichihashi, “Growth model for carbon nanotubes,” *Phys. Rev. Lett.*, vol. 69, no. 21, pp. 3100–3103, 1992.
- [14] M. Bansal, C. Lal, R. Srivastava, M. N. Kamalasanan, and L. S. Tanwar, “Comparison of structure and yield of multiwall carbon nanotubes produced by the CVD technique and a water assisted method,” *Phys. B Condens. Matter*, vol. 405, no. 7, pp. 1745–1749, 2010.
- [15] and D. T. Karousis, Nikolaos, Nikos Tagmatarchis, “Current progress on the chemical modification of carbon nanotubes,” *Chem. Rev.*, vol. 110, no. 9, pp. 5366–5397, 2010.
- [16] H. Dai, A. G. Rinzler, P. Nikolaev, A. Thess, D. T. Colbert, and R. E. Smalley, “Single-wall nanotubes produced by metal-catalyzed disproportionation of carbon monoxide,” *Chem. phys. lett.*, vol. 260, no. 4, pp. 471-475, 1996.
- [17] A. Mostofizadeh, Y. Li, B. Song, and Y. Huang, “Synthesis , Properties , and Applications of Low-Dimensional Carbon-Related Nanomaterials,” *J of nanomater.*, vol. 2011, no. 685081, 1-21, 2011.

- [18] J. Prasek *et al.*, “Chemical vapor depositions for carbon nanotubes synthesis,” *Carbon Nanotub. Synth. Prop.*, pp. 87–106, 2012.
- [19] M. L. Terranova, V. Sessa, and M. Rossi, “The World of Carbon Nanotubes : An Overview of CVD Growth Methodologies,” *Chem.l Vapor Deposit.*, vol 12. no. 6, pp. 315–325, 2006.
- [20] H. Yokomichi, M. Ichihara, S. Nimori, and N. Kishimoto, “Morphology of carbon nanotubes synthesized by thermal CVD under high magnetic field up to 10 T,” *Vacuum*, vol. 83, no. 3, pp. 625–628, 2008.
- [21] A. Eatemadi, H. Daraee, H. Karimkhanloo, M. Kouhi, and N. Zarghami, “Carbon nanotubes : properties , synthesis , purification , and medical applications,” vol. 9, no. 1, pp. 1–13, 2014.
- [22] L. Stobinski *et al.*, “Multiwall carbon nanotubes purification and oxidation by nitric acid studied by the FTIR and electron spectroscopy methods,” *J. Alloys Compd.*, vol. 501, no. 1, pp. 77–84, 2010.
- [23] A. Aqel, K. M. M. A. El-Nour, R. A. A. Ammar, and A. Al-Warthan, “Carbon nanotubes, science and technology part (I) structure, synthesis and characterisation,” *Arab. J. Chem.*, vol. 5, no. 1, pp. 1–23, 2012.
- [24] A. Hirsch, “Functionalization of single-walled carbon nanotubes,” *Angew. Chemie - Int. Ed.*, vol. 41, no. 11, pp. 1853–1859, 2002.
- [25] J. M. Wernik and S. A. Meguid, “Recent developments in multifunctional nanocomposites using carbon nanotubes,” *Appl. Mech. Rev.*, vol. 63, no. 5, pp. 1–40, 2010.

- [26] S. Ciraci, S. Dag, T. Yildirim, O. Gülseren, and R. T. Senger, “Functionalized carbon nanotubes and device applications,” *J. Phys. Condens. Matter*, vol. 16, no. 29, 901-960, 2004.
- [27] A. Ahmed, “Synthesis and characterization of magnetic carbon nanotubes,” *Dr. Diss.*, pp. 1–181, 2017.
- [28] C. Zhou, J. Kong, and H. Dai, “Intrinsic electrical properties of individual single-walled carbon nanotubes with small band gaps,” *Phys. Rev. Lett.*, vol. 84, no. 24, pp. 5604–5607, 2000.
- [29] G. R. A. Jamal, M. S. Arefin, and S. M. Mominuzzaman, “Empirical prediction of bandgap in semiconducting single-wall carbon nanotubes,” *7th Int. Conf. Electr. Comput. Eng. ICECE*, pp. 221–224, 2012.
- [30] L. Meng, C. Fu, and Q. Lu, “Advanced technology for functionalization of carbon nanotubes,” *Prog. Nat. Sci.*, vol. 19, no. 7, pp. 801–810, 2009.
- [31] M. F. L. De Volder, S. H. Tawfick, R. H. Baughman, and A. J. Hart, “Carbon Nanotubes : Present and Future Commercial Applications,” *science*, vol. 339, no. 6119, pp. 535–540, 2013.
- [32] K. S. Ibrahim, “Carbon nanotubes-properties and applications: a review,” *Carbon Lett.*, vol. 14, no. 3, pp. 131–144, 2013.
- [33] L. Ebert, “Science of fullerenes and carbon nanotubes By M. S. Dresselhaus, G. Dresselhaus and P. C. Eklund, Academic Press, 1996, 965 pages, \$130.00. ISBN 0-12-221820-5,” *Carbon N. Y.*, vol. 35, no. 3, pp. 437–438, 1997.
- [34] K. Varshney, “Carbon Nanotubes : A Review on Synthesis , Properties and Applications,” vol. 2, no. 4, pp. 660–677, 2014.

- [35] C. Wang *et al.*, “Heusler nanoparticles for spintronics and ferromagnetic shape memory alloys,” *J. Vac. Sci. Technol. B, Nanotechnol. Microelectron. Mater. Process. Meas. Phenom.*, vol. 32, no. 2, p. 020802, 2014.
- [36] N. Karousis, N. Tagmatarchis, and D. Tasis, “Current progress on the chemical modification of carbon nanotubes,” *Chem. Rev.*, vol. 110, no. 9, pp. 5366–5397, 2010.
- [37] R. J. Chen *et al.*, “Noncovalent functionalization of carbon nanotubes for highly specific electronic biosensors,” *Proceedings of the National Academy of Sciences*, vol. 100, no. 9, pp. 4984-4989, 2003.
- [38] S. C. Ray, S. Sitha, and P. Papakonstantinou, “Change of magnetic behaviour of nitrogenated carbon nanotubes on chlorination/oxidation,” *Int. J. Nanotechnol.*, vol. 14, no. 1–6, pp. 356–366, 2017.
- [39] P. Ma, N. A. Siddiqui, G. Marom, and J. Kim, “Composites : Part A Dispersion and functionalization of carbon nanotubes for polymer-based nanocomposites : A review,” *Compos. Part A*, vol. 41, no. 10, pp. 1345–1367, 2010.
- [40] F. Yang, C. Jin, D. Yang, Y. Jiang, J. Li, and Y. Di, “Magnetic functionalised carbon nanotubes as drug vehicles for cancer lymph node metastasis treatment,” *European journal of cancer*, vol. 7, no. 12 pp. 1873–1882, 2011.
- [41] M. A. Atieh, “Effect of Functionalized Carbon Nanotubes with Carboxylic Functional Group on the Mechanical and Thermal Properties of Styrene Butadiene Rubber Effect of Functionalized Carbon Nanotubes with Carboxylic Functional Group on the Mechanical and Thermal Proper,” *Fullerenes, Nanotubes and Carb. Nanostruct.*, vol. 19, no. 7, 617-627, 2011.

- [42] D. S. Ahmed, A. J. Haider, and M. R. Mohammad, "Comparision of Functionalization of multi  $\check{G}$  walled carbon nanotubes treated by oil olive and nitric acid and their characterization," *Energy Procedia*, vol. 36, no. 1, pp. 1111–1118, 2013.
- [43] Y. Kanai, V. R. Khalap, P. G. Collins, and J. C. Grossman, "Atomistic Oxidation Mechanism of a Carbon Nanotube in Nitric Acid," *Phys. rev. lett.*, vol. 104, no 6, pp. 1–4, 2010.
- [44] H. Zhang, H. Guo, X. Deng, and P. Gu, "Functionalization of multi-walled carbon nanotubes via surface unpaired electrons," *Nanotech.*, vol 21, no. 8, 1-7, 2010.
- [45] A. Baykal, M. Senel, B. Unal, E. Karaog, and H. So, "Acid Functionalized Multiwall Carbon Nanotube / Magnetite ( MWCNT ) -COOH / Fe <sub>3</sub> O <sub>4</sub> Hybrid : Synthesis , Characterization and Conductivity Evaluation," *J of Inorg. and Organomet. Polym. and Mater.*, vol 23, no. 3, 726-735, 2013.
- [46] A. Sánchez, R. C. Sampedro, L. Peña-parás, and E. Palacios-aguilar, "Functionalization of Carbon Nanotubes and Polymer Compatibility Studies," *J of Mater. Sci. Research*, vol. 3, no. 1, pp. 1–12, 2014.
- [47] V. Datsyuk *et al.*, "Chemical oxidation of multiwalled carbon nanotubes," *Carbon N. Y.*, vol. 46, no. 6, pp. 833–840, 2008.
- [48] D. Tasis, N. Tagmatarchis, A. Bianco, and M. Prato, "Chemistry of Carbon Nanotubes," *Chem. rev.*, vol 106, no. 3, pp. 1105-1136 2006.
- [49] B. S. Banerjee, T. Hemraj-benny, and S. S. Wong, "Covalent Surface Chemistry of Single-Walled Carbon Nanotube," *Advanced materials*, vol. 17, no. 1, pp. 17–29, 2005.
- [50] S. Ghosh and I. K. Puri, "Soft polymer magnetic nanocomposites: Microstructure

- patterning by magnetophoretic transport and self-assembly,” *Soft Matter*, vol. 9, no. 6, pp. 2024–2029, 2013.
- [51] S. Ghosh, M. Tehrani, M. S. Al-haik, and I. K. Puri, “Patterning the Stiffness of Elastomeric Nanocomposites by Magnetophoretic Control of Cross-linking Impeder Distribution,” *Mater.*, vol 8, no. 2, pp. 474–485, 2015.
- [52] M. Jagannatham, S. Sankaran, and H. Prathap, “Electroless nickel plating of arc discharge synthesized carbon nanotubes for metal matrix composites,” *Appl. Surf. Sci.*, vol. 324, no. 1, pp. 475–481, 2015.
- [53] P. S. Goh, A. F. Ismail, and B. C. Ng, “Directional alignment of carbon nanotubes in polymer matrices: Contemporary approaches and future advances,” *Compos. Part A Appl. Sci. Manuf.*, vol. 56, no. 1, pp. 103–126, 2014.
- [54] C. Y. Chen, M. J. Fu, C. Y. Tsai, F. H. Lin, and K. Y. Chen, “Functionalization and magnetization of carbon nanotubes using Co-60 gamma-ray irradiation,” *J. Magn. Magn. Mater.*, vol. 367, no. 10, pp. 47–52, 2014.
- [55] G. Daneshvar Tarigh and F. Shemirani, “Magnetic multi-wall carbon nanotube nanocomposite as an adsorbent for preconcentration and determination of lead (II) and manganese (II) in various matrices,” *Talanta*, vol. 115, no. 10, pp. 744–750, 2013.
- [56] Z. Wang, L. Wu, J. Zhou, W. Cai, B. Shen, and Z. Jiang, “Magnetite nanocrystals on multiwalled carbon nanotubes as a synergistic microwave absorber,” *J. Phys. Chem. C*, vol. 117, no. 10, pp. 5446–5452, 2013.
- [57] D. Sarkar, A. Bhattacharya, P. Nandy, and S. Das, “Enhanced broadband microwave reflection loss of carbon nanotube ensheathed Ni – Zn – Co-ferrite magnetic



- nanoparticles,” *Mater. Lett.*, vol. 120, no. 4, pp. 259–262, 2014.
- [58] Y. Huang, Y. Yuan, Z. Zhou, J. Liang, Z. Chen, and G. Li, “Optimization and evaluation of chelerythrine nanoparticles composed of magnetic multiwalled carbon nanotubes by response surface methodology,” *Appl. Surf. Sci.*, vol. 292, no. 2, pp. 378–386, 2014.
- [59] J. L. Gong *et al.*, “Removal of cationic dyes from aqueous solution using magnetic multi-wall carbon nanotube nanocomposite as adsorbent,” *J. Hazard. Mater.*, vol. 164, no. 3, pp. 1517–1522, 2009.
- [60] H. Fazelirad, M. Ranjbar, M. Ali, and G. Sargazi, “Preparation of magnetic multi-walled carbon nanotubes for an efficient adsorption and spectrophotometric determination of amoxicillin,” *J. Ind. Eng. Chem.*, vol. 21, no. 1, pp. 889–892, 2015.
- [61] V. L. M. Calculated and P. Press, *References 1.*, vol. 4130, no. 1997. 2004.
- [62] M. Kang *et al.*, “Memristive devices and systems,” *Proc. IEEE*, vol. 64, no. 2, pp. 209–223, 1976.
- [63] Y. V. Pershin and M. Di Ventra, “Spin memristive systems: Spin memory effects in semiconductor spintronics,” *Phys. Rev. B - Condens. Matter Mater. Phys.*, vol. 78, no. 11, pp. 5–8, 2008.

## **Chapter Three**

### **Experimental**

### 3.1 Characterization Techniques

The working principle of the equipment used in characterizing the synthesized nanomaterials utilized for this study has been described in this section. Field emission scanning electron microscopy (FE-SEM), X-ray diffraction (XRD), Raman spectroscopy, X-ray photoemission spectroscopy (XPS), X-ray absorption near-edge spectroscopy (XANES), current-voltage (I-V), superconducting quantum interference device (SQUID) and electron spin resonance (ESR) techniques were used to characterize TiO<sub>2</sub>, SO<sub>2</sub>, MWCNTs, MWCNTs:SO<sub>2</sub>, MWCNTs-TiO<sub>2</sub>, and MWCNTs:TiO<sub>2</sub>:SO<sub>2</sub> nanomaterials. All characterizations were carried out at room temperature, except SQUID which was also measured at 40 K.

#### 3.1.1. Field emission-scanning electron spectroscopy (FE-SEM)

FE-SEM spectroscopy is an image characterization method to study a microstructure and morphology of nanomaterial. FE-SEM utilized a speed of beams to scan through the surface of a material, as a result, sequences of radiations will be emitted, which is exploited and then form images [1]. Such radiations emitted are:

1. Characteristic X-rays which arise from the energy difference between two electrons;
2. Secondary electrons less than 50 eV energy ejected from the outer orbital of the atoms of the sample due to multiple inelastic scattering effects; and
3. Electrons that are scattered backward above 50 eV energy reflected out of the contact volume of the specimen due to the elastic scattering effect.

The working principle of SEM is shown in figure 3.1 [1].

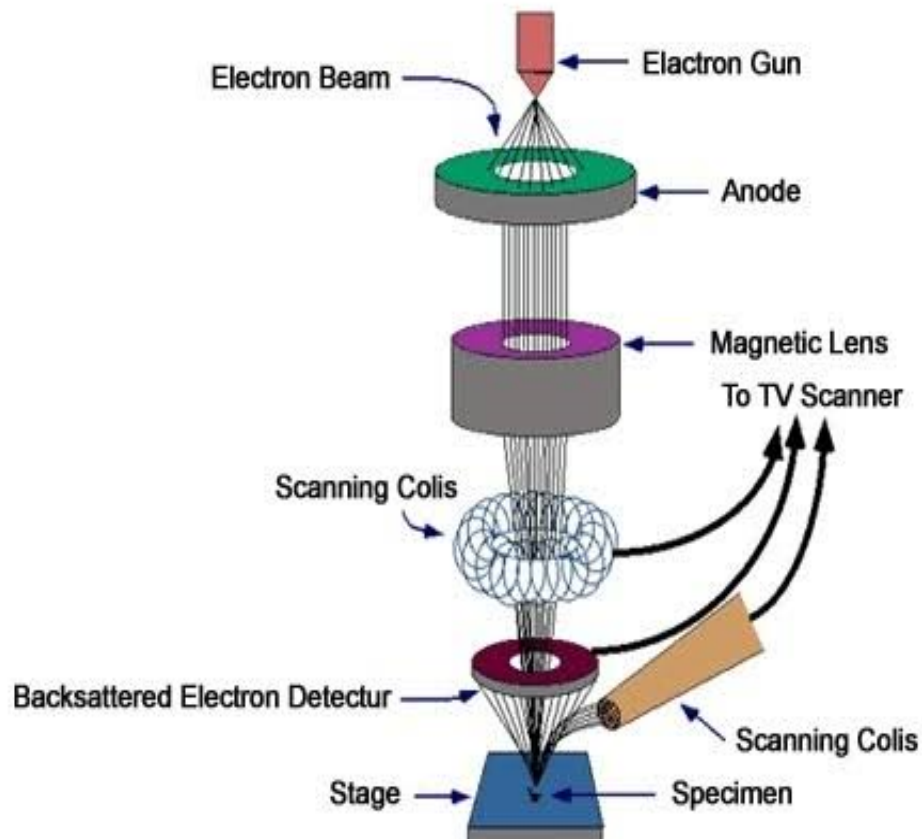


Figure 3.1. Schematic working principle of SEM.

FE-SEM supplied by Jeol JEM of model 2100 was used to study the morphology of the nanomaterial, which operates at a voltage range of 0.5 to 30 kV.

### 3.1.2. X-ray diffraction (XRD)

XRD is an essential technique which is used to characterize different materials and gives information about:

1. Crystal structure;
2. Crystalline phases; and
3. Crystallite size.

XRD depends on the constructive interference of X-ray monochromatic and crystalline materials. Also, the X-ray monochromatic created in cathode ray tube depends on the bombardment of energetic electrons and filtered to yield radiation, which is focused on the material. Constructive interference is produced due to the interaction of the incident rays with the material, i.e the interaction gives diffracted rays by obeying Bragg's Law [2] and is given as:

$$n\lambda = 2d \sin \theta \quad (3.1)$$

where  $n$  is the reflection number,  $\lambda$  is the X-ray wavelength,  $d$  is the lattice distance and  $\theta$  is the diffracted angle. Figure 3.2 shows the schematic diagram of Bragg's Law in XRD [2].

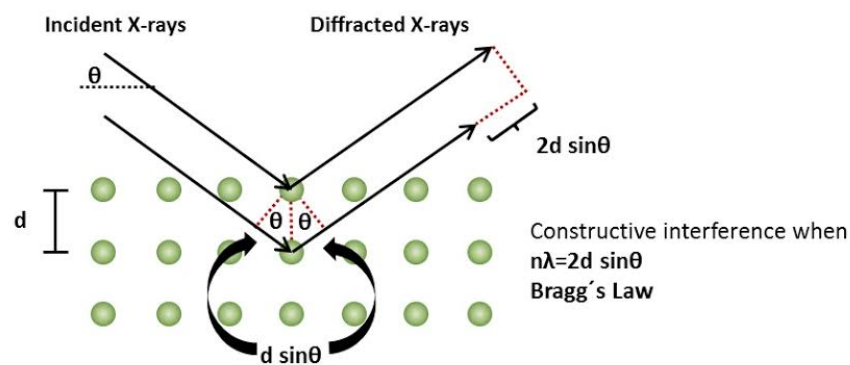


Figure 3.2. Schematic diagram of the Bragg's Law in XRD.

Moreover, Scherrer's equation [3] below was used to calculate the crystallite size of the nanocomposites materials.

$$D = k\lambda/\beta\cos\theta \quad (3.2)$$

where  $D$  is the crystallite size,  $k$  is  $\sim 0.9$ ,  $\lambda$  is the wavelength of x-ray ( $1.54 \text{ \AA}$ ),  $\beta$  is the full width at half maximum and  $\theta$  is the Bragg's angle.

In this work, X-ray diffractometer supplied by Rigaku Smartlab was used to characterize the samples with XRD technique. The wavelength ( $\lambda$ ) used was 0.154 nm with Cu  $K_{\alpha}$ -line radiation.

### **3.1.3. Raman spectroscopy**

Raman spectroscopy is a characterization technique based on the scattering of inelastic monochromatic light from the laser source which is focused on the sample. There is a transition in the monochromatic light when interacting with the sample due to the rate of photons in the laser. The sample absorbed and reemitted these photons from the laser light and gives information concerning the defect in the sample. When compared with the monochromatic frequency, there is a shift up or down in the speed of the reemitted photons. This shift is known as the Raman effect. The rotation and vibration effect also depends on this shift [4].

Raman spectroscopy supplied by Horiba scientific XploRA with Laser light excitation energy ( $E_{\text{ex}} = 2.41 \text{ eV}$ ) at 532 nm was used to study the defect in the nanomaterials.

### **3.1.4. X-ray photoelectron spectroscopy (XPS)**

XPS technique is used to examine the elemental composition of a material. Also to determine the material's chemical and electronic state. The principle of XPS is based on photoelectron spectroscopy which involves high energy radiation to eject core electrons from a sample [5, 6]. The diagram shown in figure 3.3 provides information on how core electrons are being ejected from a sample.

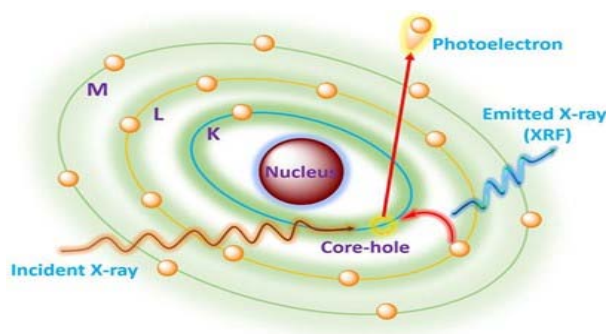


Figure 3.3. Schematic principle of XPS [5].

The kinetic energy used to ejecting the core electrons is given as:

$$KE = h\nu - E_b - \phi \quad (3.2)$$

where KE is the kinetic energy of the electron,  $h$  is Planck's constant,  $\nu$  is the frequency of the incident radiation,  $E_b$  is the binding energy and  $\phi$  is the work function.

The kinetic energy of the ejected electron can also be determined using equation 3.2. XPS is a powerful tool with monochromatic Al  $K_\alpha$  radiation possessing excitation energy,  $h\nu = 1486.6$  eV, and base pressure  $1.2 \times 10^{-9}$  Torr in which the presence and relative quantities of elements can be detected in a sample. Afterward, high-resolution scans of the peaks give information about the state and environment (hybridization, bonding, and functionalities) of atoms in the sample, which makes it easy to understand the surface structure of the material. Thus, XPS technique is used to determine the purity of the material. Furthermore, XPS spectra give evidence of functionalization and can provide insight into the identity of the functional groups.

The core levels C  $1s$ , O  $1s$ , Si  $2p$ , Si  $2s$ , and Ti  $2p$  of the nanomaterials were studied using XPS KRATOS-SUPRA spectrometer with a base pressure of  $1.2 \times 10^{-9}$  Torr, monochromatic Al  $K_\alpha$  and radiation possessing excitation energy of  $h\nu = 1486.6$  eV.

### 3.1.5. X-ray absorption near edge structure (XANES) spectroscopy

XANES techniques is an essential tool for characterizing CNTs materials. It gives information about the local electronic structure of a material in the form of bond hybridization ( $sp^2$  and  $sp^3$ ). In XANES spectroscopy, the photon beam exponential decay is measured with a specified source of energy. The energy source of the photon beam can be increased randomly, which is a key factor in which the X-ray absorption depends on. An edge is been created due to the increase in the X-ray absorption of molecules or atoms. As the photon beam passes through the material their energy is been measured [7]. This principle is based on Beer's law and the photon beam passing through the sample is given as:

$$I = I_0 e^{-\mu D} \quad (3.3)$$

where  $I_0$  is the incident photon intensity,  $\mu$  is the absorption coefficient and  $D$  is the component concentrations in the material. The symmetry crystalline solid for  $\mu$  value is calculated using:

$$\mu = \frac{1}{V} \sum_{i=1}^n \sigma_i \quad (3.4)$$

where  $V$  is the unit cell volume,  $\sigma_i$  is the absorption cross-section and it is related to unit cell and n elements.  $\sigma_i$  is in the order of  $1M\text{barn} = 10^{-18} \text{cm}^2$  [7].

The XANES of the nanocomposites materials were investigated using Taiwan Light Source (TLS) to study their electronic structures.

### 3.1.6. Current-voltage (I-V) characteristic

I-V technique is an essential tool to determine the electrical properties and conductivity of a material. Metals are known to be conducting materials due to the fact that the interacting force among electrons in them is very strong. This strong interaction results in the elimination of the forbidden gap, which allows the easy flow of free electrons from the valence to conduction band when heat or electric current is been introduced. Therefore, the electrical conductivity of



a material depends on the easy flow and numbers of free electrons that can move to the conduction band [8].

The I-V curves below are examples of the conducting and semiconducting structure of a material.

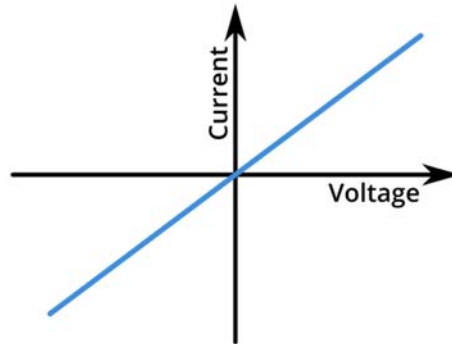


Figure 3.4. Schematic diagram of a conducting I-V curve

A typical I-V curve has current flowing in a positive and negative path (forward and reverse biased) with a voltage in the same direction. From figure 3.4, the curve cutting across the positive and negative path, indicating a linear curve and ohmic behavior. From the curve, the relationship between current and voltage can be written as  $1/R$ , which is known as a constant slope.

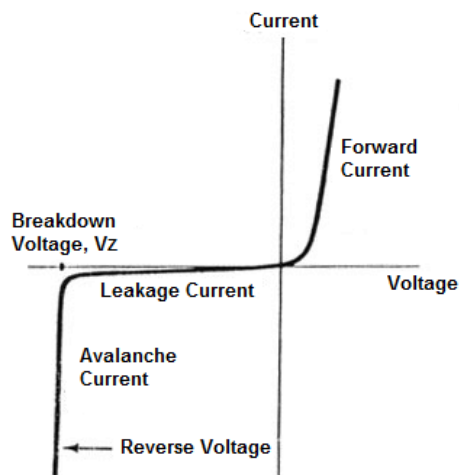


Figure 3.5. Schematic diagram of a semiconducting I-V curve

A semiconducting I-V curve is non-ohmic and nonlinear in nature as depicted in figure 3.5. From the figure, the current flowing through the positive path increases constantly until the positive voltage reaches an internal voltage barrier limit and thereby forming a nonlinear curve. On the other hand, the reverse-biased act as a diode. In the reverse-biased, there is a leakage current, which is as a result of the generation of a diode blocking the flow of current. As this process continues, the negative voltage becomes higher than the breakdown voltage. This result in the superposition of the voltage breakdown and diode voltage provides a rapid increase in the development of reverse current.

In this study, the electrical conductivity of the nanomaterials was studied using silver paste as a conducting electrode and measured using Keithley 6487 with voltage sweep in the range of -1 to 1 and steps of 0.01 V.

### **3.1.7. Superconducting quantum interference device (SQUID)**

The magnetic behavior of a material can be measured using a superconducting quantum interference device (SQUID). Though, the transition in magnetic fluxes of material in extreme cases can be measured using this technique. Also, the technique is used in measuring the magnetic properties of a material at a wide range of temperatures, which gives information concerning the zero-field cooling (ZFC) and field cooling (FC) of the material.

SQUID type magnetometer with sensitivity less than  $5 \times 10^{-8}$  emu was used to measure the magnetic properties of the studied nanomaterials at 40 K and 300 K.

### **3.1.8. Electron spin resonance (ESR)**

ESR is a technique used in investigating samples with unpaired electrons and it is based on the photon energy absorbed or emitted by the unpaired electrons in the material when subjected to a magnetic field. When a material is inserted into the ESR system, microwaves and static

magnetic field were two key factors used in observing the behavior of the unpaired electrons in the studied material. The behavioral study of the electrons in the material provides information concerning the condition of the material. Figure 3.6 shows the schematic diagram of ESR process

In this work, ESR supplied by Bruker EMX at 9.45 GHz was used to study the defect arising from ferromagnetism in the nanomaterials.

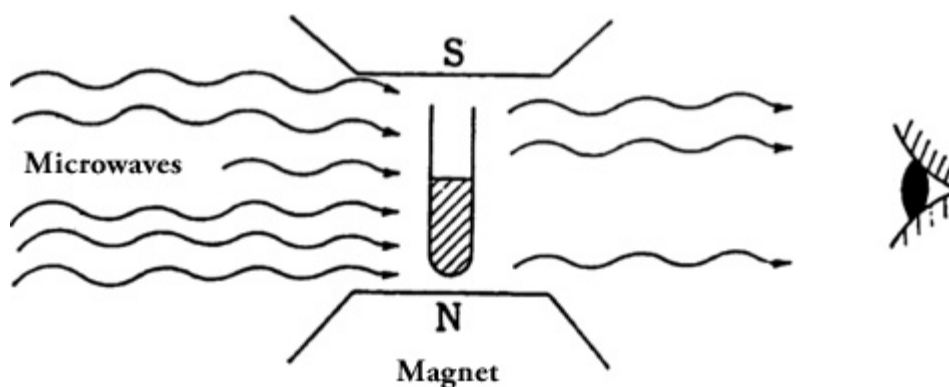


Figure 3.6. Schematic diagram of ESR process.

## References

- [1] P. J. Goodhew and J. Humphreys. Electron microscopy and analysis. *CRC Press*; 2000.
- [2] P. M. Chaikin and T. C. Lubensky. Principles of condensed matter physics. *Cambridge: Cambridge university press*; 2000.
- [3] L. A. Rodriguez and D. N. Travessa, “Core/Shell Structure of TiO<sub>2</sub>-Coated MWCNTs for Thermal Protection for High-Temperature Processing of Metal Matrix Composites,” *Adv. Mater. Sci. Eng.*, 2018.
- [4] S. Y. Lin and C. W. Dence, editors. Methods in lignin chemistry. *Springer Science & Business Media*; 2012.
- [5] J. F. Watts. X-ray photoelectron spectroscopy. Surface science techniques. 1994.
- [6] C. Defosse and P. G. Rouxhet. Introduction to X-ray photoelectron spectroscopy. Advanced chemical methods for soil and clay minerals research, *Springer*, Dordrecht, 1980
- [7] Van Bokhoven, A. Jeroen and Carlo Lamberti, eds. X-ray absorption and X-ray emission spectroscopy: theory and applications, *John Wiley & Sons*, 2016.
- [8] J. R. Hook and E. H. Henry. "Solid state physics." 1991.

## **Chapter Four**

### **Electronic, Electrical and Magnetic Behavioural change of SiO<sub>2</sub>- NPs Decorated MWCNTs**

## 4.1. Introduction

Carbon nanotubes (CNTs) such as single-wall carbon nanotubes (SWCNTs) and multiwall carbon nanotubes (MWCNTs) are man-made carbon allotrope which is consist of  $sp^2$  hybridized carbon atoms. After the discovery of CNTs by Iijima in 1991 [1], different techniques (arc discharge, laser ablation, and chemical vapor deposition (CVD)) [2] have been used to synthesize CNTs. CVD is the most used technique in synthesizing CNTs on a large scale in the presence of a catalyst, which has the degree of control over length, diameter, and morphology. SWCNTs are graphene sheet rolled into a cylindrical shape and MWCNTs are multiple SWCNTs nested into the other.

MWCNTs have been a material of focus due to their unique properties (electrical, thermal, and mechanical strength) and has been known for future potential applications in electronic, electrical, optical, and magnetic devices [3], depending on their structure and the form in which they are applied. An increased non-linearity current-voltage (I-V) relationship was displayed by different MWCNTs when connected under gold electrodes. On the other hand, nearly decreased if the contact was placed at the top of the inscribed CNTs. CNTs also demonstrated a promising application in electrochemical sensing due to their electrochemical stability, large surface area, and rapid electron transfer [4]. Despite the uniqueness of CNTs, there is still a need to transform its electronic, electrical, and magnetic properties to be tailored towards different applications. Efforts have been made to transform their properties, an example is a nitrogen and boron been introduced into the matrix of MWCNTs [5].

Silicon (Si) was used to functionalized MWCNTs in this research due to its high reactive centre which made the enhancement of their properties possible compared to boron and nitrogen. This possibility could give room to novel electronic, electrical, and magnetic nano-device applications. It was proven theoretically that the  $sp^3$  bond formed when Si is incorporated into

CNTs relaxed outward [6]. The formation of  $sp^3$  bond in the CNTs matrix is expected to transform and enhance its electrical/electronic/magnetic behavior. Also, there are formation of dangling bonds due to the chemical absorption of Si on the CNTs surface, which enables the modification into a changed material. From the theoretical calculation of important theory, it was observed that Si-doped CNTs behaved as a binding site for more functionalization of CNTs with exceptional contact of several nanoparticles [7]. Silicon displayed an important role in modifying the host structure compared to several elements of group IV due to its larger size. On Si doping, the distinct energy level increases in the forbidden gap and thus reducing the mobility of Si due to defect scattering. CNTs mobility has a minute negative effect when doped with Si owing to the strong contact between carbon (C) and Si atoms. Therefore, the arrangement of atoms and  $sp^3$  formation in MWCNTs:SiO<sub>2</sub> structure was studied using different techniques.

## **4.2. Methodology**

### **4.2.1 Preparation of MWCNTs**

Spray pyrolysis [8] technique was used to synthesize MWCNTs. In this process, a mixture of Fe(C<sub>5</sub>H<sub>5</sub>)<sub>2</sub> (ferrocene-catalyst) and C<sub>7</sub>H<sub>8</sub> (toluene-carbon source) were prepared. Thereafter, the mixture was atomized and fed into a quartz tube, which acts as a substrate in a horizontal hot-wall reactor at 850°C-900°C. The argon flow was sustained for almost 40 minutes for the completion of the growth of MWCNTs. Furthermore, the MWCNTs were purified using the mixture of nitric and hydrochloric acid in the ratio of 1:1 and was stirred for 90 minutes. The MWCNTs were filtered and washed with distilled water to remove any waste from the acids.

#### 4.2.2 Preparation of SiO<sub>2</sub> and MWCNTs:Si nanocomposites

The thermal decomposition method [9] was adopted to synthesize Si-NPs. The process involves the thermal decomposition of chloro(dimethyl) octadecylsilane in a 1,3,5-trimethyl benzene solvent at ~140 °C. Chloro(dimethyl) octadecylsilane was used due to its uniqueness under low-temperature degradation compared to octadecylsilane which requires a high-temperature degradation of greater than 200 °C and trichlorovinylsilane which evaporate at low-temperature degradation greater than 90 °C due to lower boiling points. The synthesis was carried out in an open atmosphere, which makes the oxidation of Si-NPs possible. SiO<sub>2</sub> and MWCNTs were used at different concentrations of Si-1.5 at % and Si-5.75 at %, which were suspended in toluene at >100°C and MWCNTs:SiO<sub>2</sub> nanocomposites were obtained. The samples were dropped cast on a silicon wafer and were left to dry for several hours.

#### 4.2.3 Characterization

Different techniques were utilized to characterize SiO<sub>2</sub>, MWCNTs, and MWCNTs:Si nanocomposites. The different techniques are Field emission scanning electron microscopy (FE-SEM) (Jeol JEM 2100) with Energy-dispersive X-ray spectroscopy (EDS) for the study of morphology and chemical impurities, X-ray diffraction (XRD) (Rigaku Smartlab X-ray diffractometer and wavelength ( $\lambda$ ) of 0.154 nm with Cu  $K_{\alpha}$ -line radiation) for the study of crystalline structure, Raman spectroscopy (Horiba scientific XploRA with laser light excitation energy ( $E_{ex}$  = 2.41 eV) at 532 nm) for the study of the degree of graphitization, X-ray photoemission spectroscopy (XPS) (KRATOS-SUPRA spectrometer with a base pressure of  $1.2 \times 10^{-9}$  Torr, monochromatic Al  $K_{\alpha}$  and radiation possessing excitation energy of  $h\nu = 1486.6$  eV) and X-ray absorption near-edge spectroscopy (XANES) (carried out at Taiwan Light Source (TLS), Hsinchu, Taiwan) for the study of electronic and chemical bonding properties. The current-voltage (I-V) was measured using Keithley 6487 with voltage sweep ranging from



-1 to 1 for the study of electrical behavior. Silver paste was used to necessitate contacts between the sample and electrical test probes. The stability of the contact was confirmed by the continuity of the acquired I–V trends. A superconducting quantum interference device (SQUID) (magnetometer with a sensitivity of  $<5 \times 10$ ) magnetometer was used to obtain the hysteresis loop and the field-dependent magnetization. The electron spin resonance (ESR) (Bruker EMX spectrometer at 9.45 GHz) of the samples were also measured for the concentration of electron spin. All characterizations were carried out at room temperature, except SQUID which was also measured at 40 K.

### **4.3. Result and discussion**

#### **4.3.1. Field emission-scanning electron microscopy (FE-SEM)**

The FE-SEM images of SiO<sub>2</sub>, MWCNTs, and MWCNTs:Si nano-composites are shown in figure 4.1 (a, b and c). (a) shows the morphology of SiO<sub>2</sub> in a spherical image. (b) shows a usual tube-like image. In (c), MWCNTs show a rough surface that confirms the deposition and no agglomeration of SiO<sub>2</sub>. It can also be seen from the figure that SiO<sub>2</sub>-NPs are well-dispersed and bounded to the surface of MWCNTs. The attachment and anchoring of SiO<sub>2</sub> to the surface of MWCNTs is important for the variation of the electrical conductivity of MWCNTs. This variation of conductivity is shown later in the text. The EDS spectrum of MWCNTs:Si nanocomposites is presented in figure 3 (d). Carbon (C), oxygen (O), and silicon (Si) peaks were observed without any impurity. The O peak observed could be from the MWCNTs O-functional group.

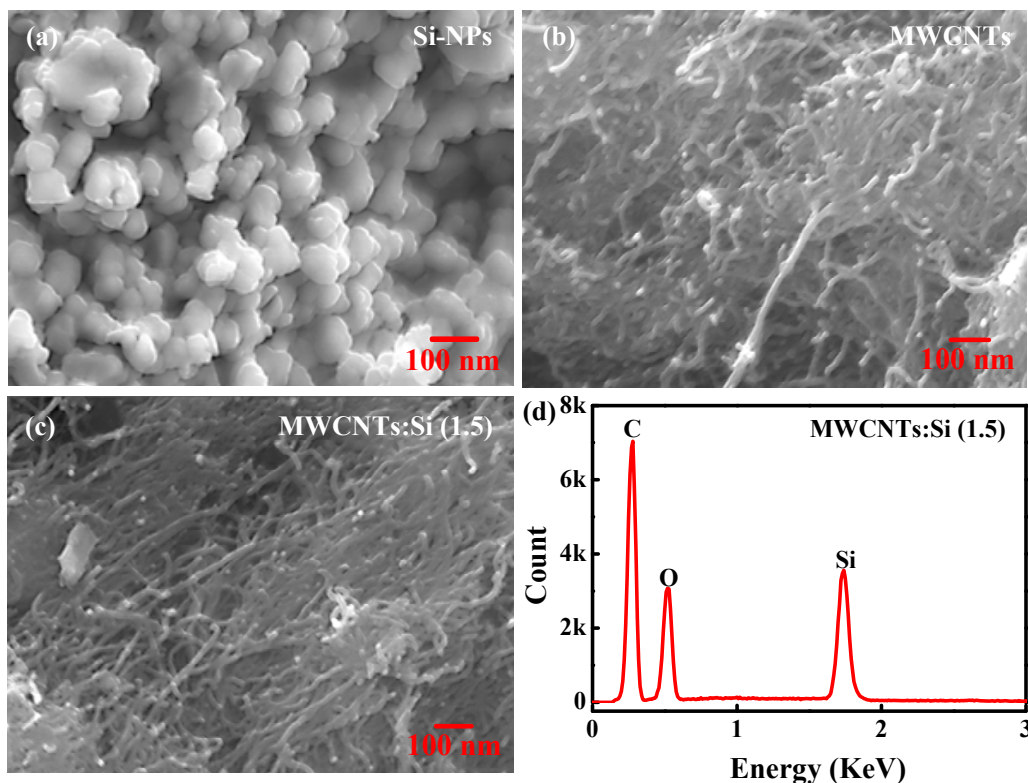


Figure 4.1. (a, b and c) SEM images for SiO<sub>2</sub>, MWCNTs, and MWCNTs:Si nanocomposites. (d) EDS spectra for MWCNTs:Si nanocomposites.

#### 4.3.2. X-Ray Diffraction (XRD) Patterns

The crystal structure of MWCNTs, SiO<sub>2</sub>, and MWCNTs:Si nanocomposites are identified by XRD patterns. Figure 4.2 shows the XRD patterns of SiO<sub>2</sub>, MWCNTs, and MWCNTs functionalized with different concentrations (~1.5 and ~5.75 at %) of SiO<sub>2</sub>. A broad diffraction peak  $2\theta$  is observed at approximately 25.9° corresponding to a plane (002) of graphitic carbon. Other peaks  $2\theta$  are observed at 43.6° and 53.6° corresponding to planes (100) and (004), respectively for MWCNTs (JCPD 75-1621) [11]. In the same Figure, SiO<sub>2</sub> shows a broad peak with low intensity at 22.7° indicating the crystalline phase of SiO<sub>2</sub> [10,12]. Another peak at 7° assigned to Si (111) [13]. MWCNTs functionalized with 1.5 at % of SiO<sub>2</sub> show the same peaks as MWCNTs with additional peak  $2\theta$  at 78.1° assigned to (110) plane, indicating that the structure of MWCNTs was not destroyed. MWCNTs functionalized with ~5.75 at % of SiO<sub>2</sub>

shows two peaks  $2\theta$  at  $7^\circ$  and at  $21.6^\circ$  which is of very low intensity towards low  $2\theta$  degree. The observed carbon planes in the pattern of MWCNTs functionalized with  $\sim 1.5$  at % of  $\text{SiO}_2$ , which may be due to lower concentration of  $\text{SiO}_2$  in MWCNTs suspension. These changes were not observed with the higher concentration of  $\text{SiO}_2$ , indicating that the increased concentration of  $\text{SiO}_2$  has impacted the crystal structure of MWCNTs.

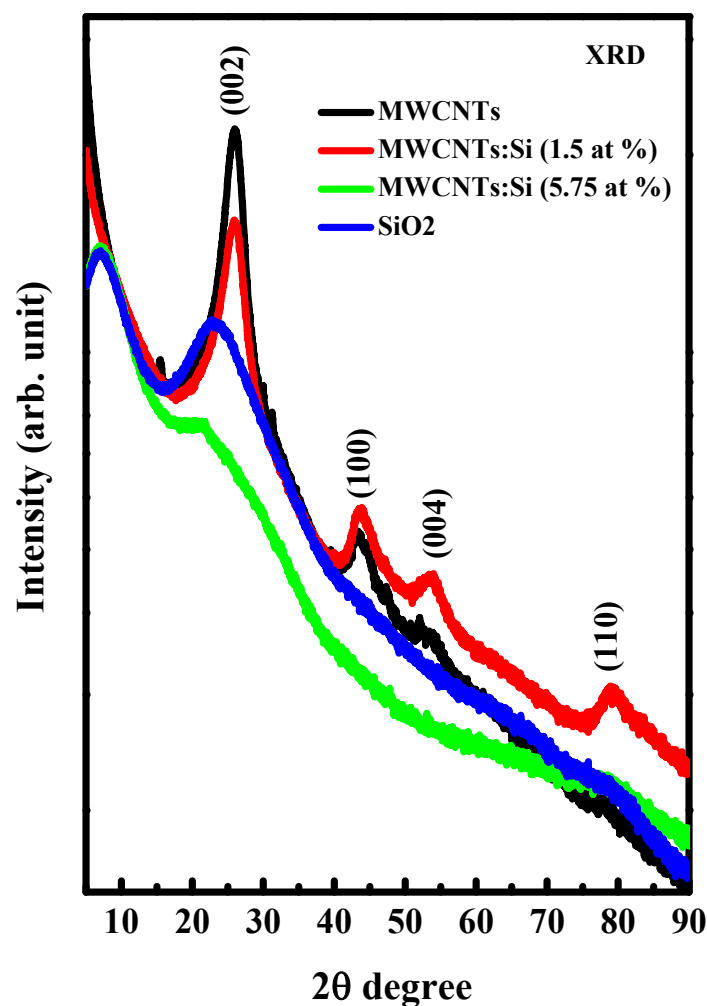


Figure 4.2. XRD pattern for  $\text{SiO}_2$ , MWCNTs, and MWCNTs:Si nanocomposites.

The Scherrer's equation ( $D = k\lambda/\beta\cos\theta$ ) [14] described in chapter three was used in calculating the crystallite sizes of the unfunctionalized and functionalized nanomaterials. The crystallite size of MWCNTs was calculated to be 2.84 nm. This value decreases to 2.58 nm for

MWCNTs:Si with 1.5 at % and increases to 5.15 nm for MWCNTs:Si with 5.75 at %. The variation in the crystallite size may be due to the formation of  $sp^3$  hybridization in MWCNTs [6].

### 4.3.3. Raman spectroscopy

Raman spectroscopy provides knowledge about the degree of hybridization, crystal disorder, and ordered structure. The Raman spectrum of  $SiO_2$ , MWCNTs, and MWCNTs functionalized with different concentrations ( $\sim 1.5$  at % and  $\sim 5.75$  at %) of  $SiO_2$  are shown in figure 4.3. (a) shows first and second-order silicon peaks ( $Si_1$  and  $Si_2$ ) at  $520\text{ cm}^{-1}$  and  $1036\text{ cm}^{-1}$  which indicates the absence of carbon material in the sample. (b) consist of four peaks comprises of the D mode, G mode, 2D mode, and D+G mode [15]. The D (disordered) and G (ordered) mode in the graphitic structure. The 2D and D+G mode occurred due to an implication of D mode from second-order vibration and combined vibrational process of the D and G mode, respectively. The D, G, 2D and D+G peaks are observed at  $1340\text{ cm}^{-1}$ ,  $1579\text{ cm}^{-1}$ ,  $2675\text{ cm}^{-1}$  and  $2929\text{ cm}^{-1}$  [15], respectively for MWCNTs. These peaks were also observed in (c) and (d), an additional second-order silicon peak ( $Si_2$ ) was observed in (d) at  $1063\text{ cm}^{-1}$ , which was due to a high concentration of  $SiO_2$  used in functionalizing MWCNTs. Whereas, (c) did not show any silicon peak due to the low content of silicon in the nano-composite. It was also observed that the D and G peaks for MWCNTs:Si with  $\sim 5.75$  at % of  $SiO_2$  shift towards lower wavenumber (see Table 4.1). A peak was also observed at  $1460\text{ cm}^{-1}$  corresponding to D' peak was due to phonon restrictions among the graphitic walls [16,17]. The observed change in the structure indicates that  $SiO_2$  has impacted the structure of MWCNTs.

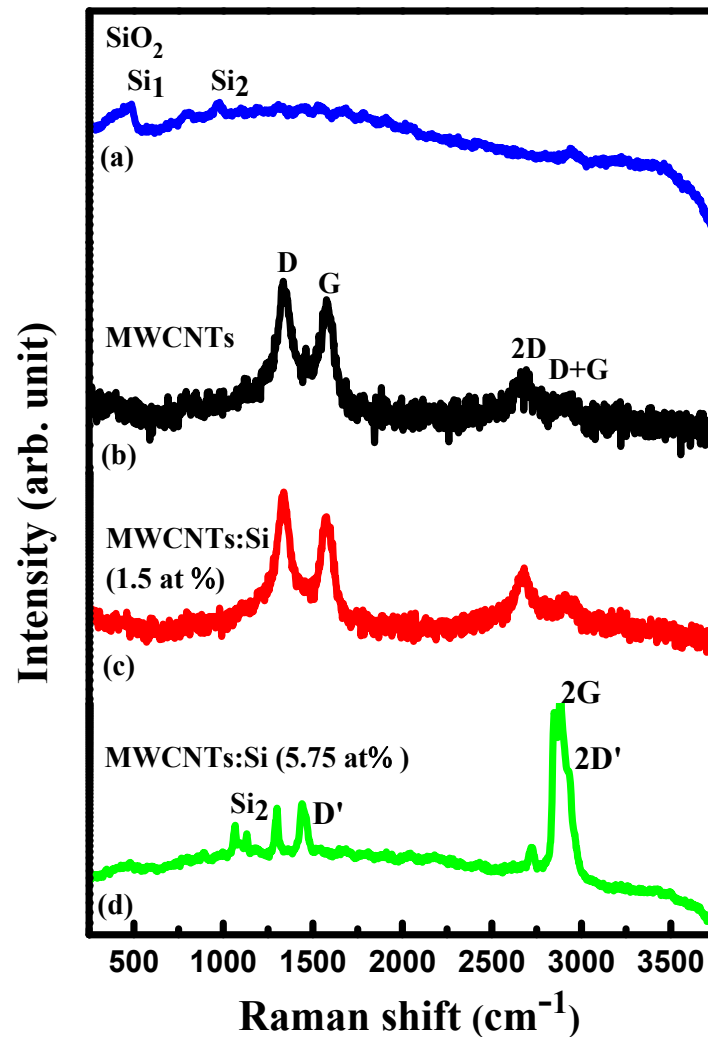


Figure 4.3. Raman spectra for  $\text{SiO}_2$ , MWCNTs, and MWCNTs:Si nanocomposites.

In order to identify the peaks height to determine the intensity ratios ( $I_D/I_G$ ) of MWCNTs and MWCNTs:Si nano-composites, we have de-convoluted their Raman spectra with multiple Gaussian fits and are presented in figure 4.4. Their peak positions (x), intensities (Int.) and width ( $\Delta\omega$ ) are also presented in Table 4.1.

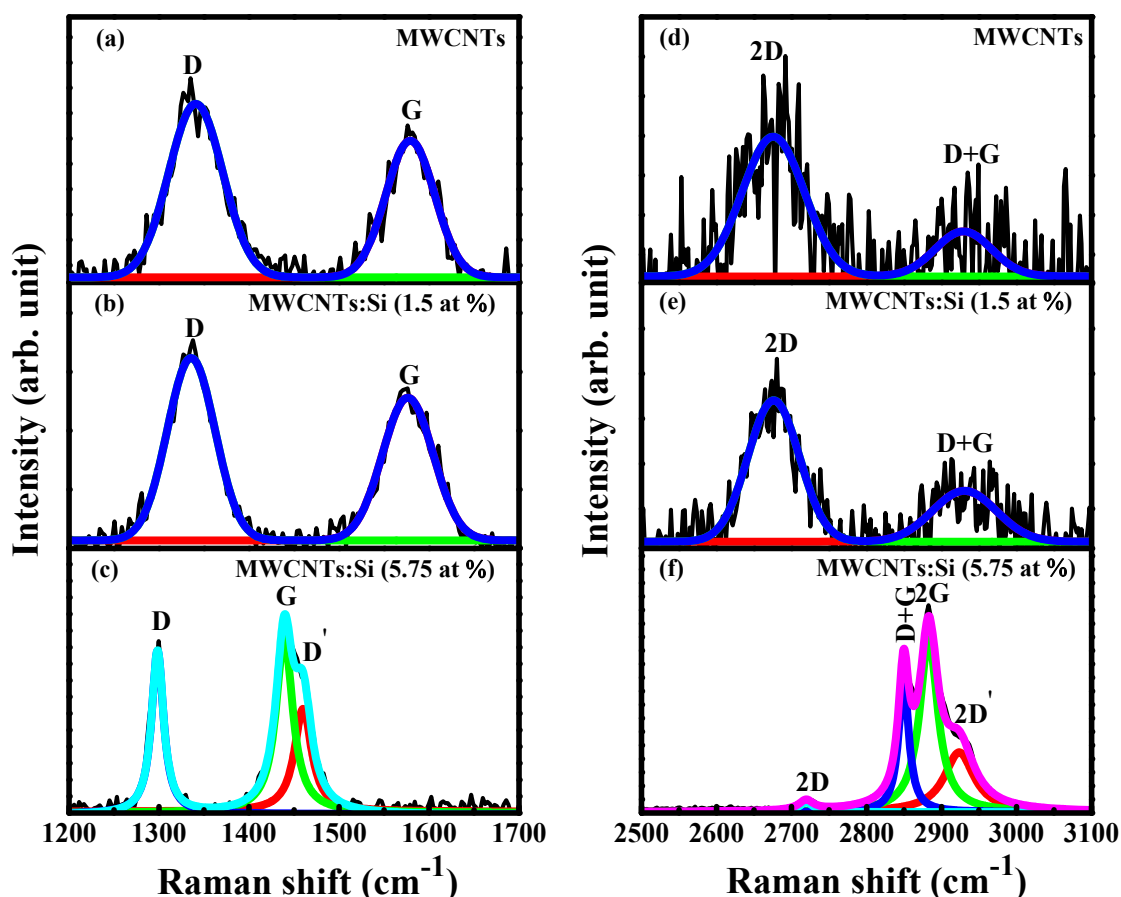


Figure 4.4. De-convolution Raman spectra for MWCNTs and MWCNTs:Si nanocomposites.

The  $I_D/I_G$  ratios were calculated from the intensity of D and G peaks and were used to evaluate the degree of  $sp^3$  and  $sp^2$  hybridizations. The values are presented in Table 1. The  $I_D/I_G$  ratio increase slightly from 1.24 for MWCNTs to 1.25 for MWCNTs:Si with ~1.5 at % and then decreases to 0.94 for MWCNTs:Si with ~5.75 at %. The values obtained from the  $I_D/I_G$  ratios 1.25 and 0.94 is an indication of increase and decrease in defect structure, which means that there is a conversion of carbon atoms leading to an increase in  $sp^3$  hybridization. The  $I_D/I_G$  ratios can also be confirmed from the width of D and G mode, the larger the width, the more increase in  $sp^2$  hybridization and vice versa.

Table 4.1: Different parameters obtained from the deconvolution of Raman spectra for MWCNTs and MWCNTs:Si nanocomposites.

1 <sup>st</sup> order vibration Raman spectra materials	D peaks			G peaks			D' peaks		
	Int. (a.u.)	x (cm <sup>-1</sup> )	$\Delta\omega$ (cm <sup>-1</sup> )	Int. (a.u.)	x (cm <sup>-1</sup> )	$\Delta\omega$ (cm <sup>-1</sup> )	Int. (a.u.)	x (cm <sup>-1</sup> )	$\Delta\omega$ (cm <sup>-1</sup> )
MWCNTs	2.1	1343	92	1.6	1574	82	--	--	--
MWCNTs:Si (1.5 at %)	3.9	1336	91	2.6	1573	77	--	--	--
MWCNTs:Si (5.75 at %)	2.8	1298	18	3.8	1439	23	2.4	1460	24
2 <sup>nd</sup> order vibration Raman spectra of materials	2D peaks			D+G peaks			2G peaks /2D' peaks		
MWCNTs	0.7	2679	118	0.5	2888	150	--	--	--
MWCNTs:Si (1.5 at %)	1.4	2673	116	0.7	2900	138	--	--	--
MWCNTs:Si (5.75 at %)	1.5	2727	38	14.2	2924	43	12.3 29.9	2850 2873	16 30

#### 4.3.4. X-ray photoelectron spectroscopy (XPS)

The electronic structure, chemical bonding, and quantification of SiO<sub>2</sub>, MWCNTs, and MWCNTs:Si nanocomposites were examined using XPS. Table 4.2 reveal each content of Si, C and O present in various material (SiO<sub>2</sub>, MWCNTs, and MWCNTs:Si nanocomposites).

Table 4.2: XPS quantificational analysis of silicon (Si), carbon (C) and oxygen (O)

Nanomaterials	XPS quantificational analysis		
	Si at %	C at %	O at %
SiO <sub>2</sub>	36.40	-	63.60
MWCNTs	-	98.37	01.63
MWCNTs:Si (1.5)	1.50	94.00	4.50
MWCNTs:Si (5.75)	5.75	85.00	9.25

The full XPS spectrum is presented in figure 3.5 with several peaks of index C 1s, O 1s, Si 2p, and Si 2s configurations. These peaks were extracted and de-convoluted with Gaussian fits in order to examine their peak positions which gives information about the bonding properties.

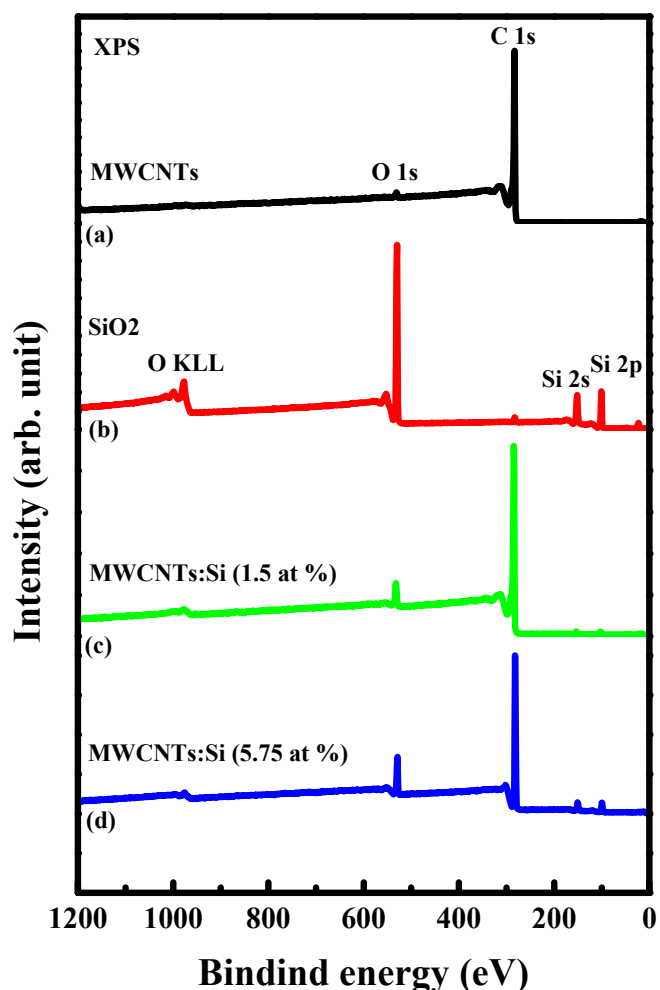
Figure 4.5. XPS spectra for SiO<sub>2</sub>, MWCNTs, and MWCNTs:Si nanocomposites.



Figure 4.6 (a and b), 4.7 (a and b) and 4.8 (a and b) shows the de-convolutions of C 1s and O 1s for MWCNTs, MWCNTs:Si with ~1.5 at % and MWCNTs:Si with ~5.75 at %, respectively and Si 2p and Si 2s for SiO<sub>2</sub>. Their peak positions (x) and intensities (Int.) are presented in Table 4.3. The C 1s configuration for MWCNTs was located at 283.4 eV/284.1 eV and 289.9 eV corresponding to C=C and C-O chemical bonding, respectively. The O 1s configuration was de-convoluted into two peaks at 530.4 eV and 532.1 eV, which are signatures of C=O and C-O [18], respectively. This bonding indicates that MWCNTs are more of carbon atoms. Figure 4.6 (c and d), 4.7 (c and d) and 4.8 (c and d) show the de-convolution of Si 2p and Si 2s for SiO<sub>2</sub>, MWCNTs:Si with ~1.5 at % and MWCNTs:Si with ~5.75 at %, respectively. Si 2p and Si 2s configurations for SiO<sub>2</sub> were de-convoluted into two and three peaks, respectively. These peaks were observed at 100.7 eV, 101.1 eV and 150.1 to 153.1 eV corresponding to Si 2p<sub>3/2</sub>, Si 2p<sub>1/2</sub> [19] and Si-Si bond [20], respectively.

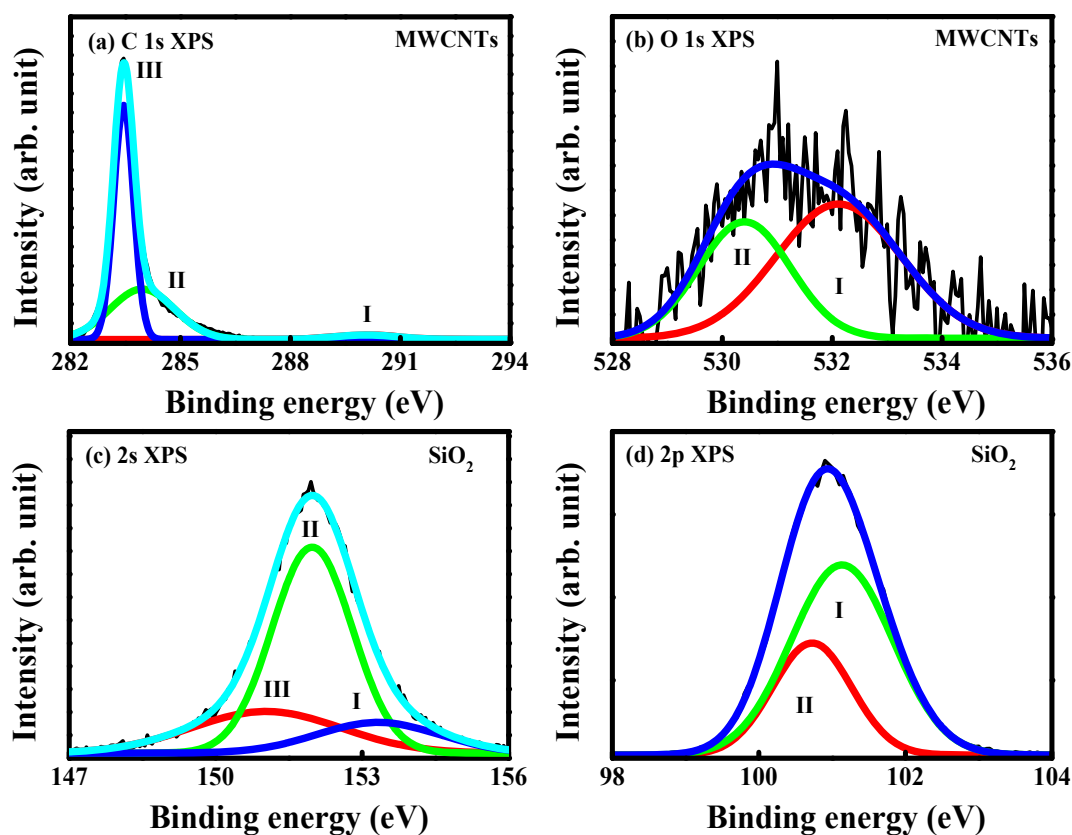


Figure 4.6. De-convolution of C1s and O1s XPS spectra for MWCNTs.

From figure 4.7 (a), the C 1s configuration is de-convoluted into three peaks located at 284.4 eV (C=C), 285.3 eV (Si-C-O) and 291.0 eV (-COOH). It was observed that these peaks shift towards high binding energy, thereby forming a defect peak (285.3 eV) [21]. This means that there is a structural change in the electronic behavior of MWCNTs:Si with ~1.5 at %. In figure 4.8 (a), the C 1s configuration was de-convoluted into two peaks at 281.7 eV and 282.1 eV corresponding to C-Si bond [22], which is an indication of the strong formation of MWCNTs:Si nanocomposites. The O 1s configuration of MWCNTs:Si nanocomposites were shown in figure 4.7 (b) and 4.8 (b) and were de-convoluted into two Gaussian peaks corresponding to O-C and O-Si bond [28].

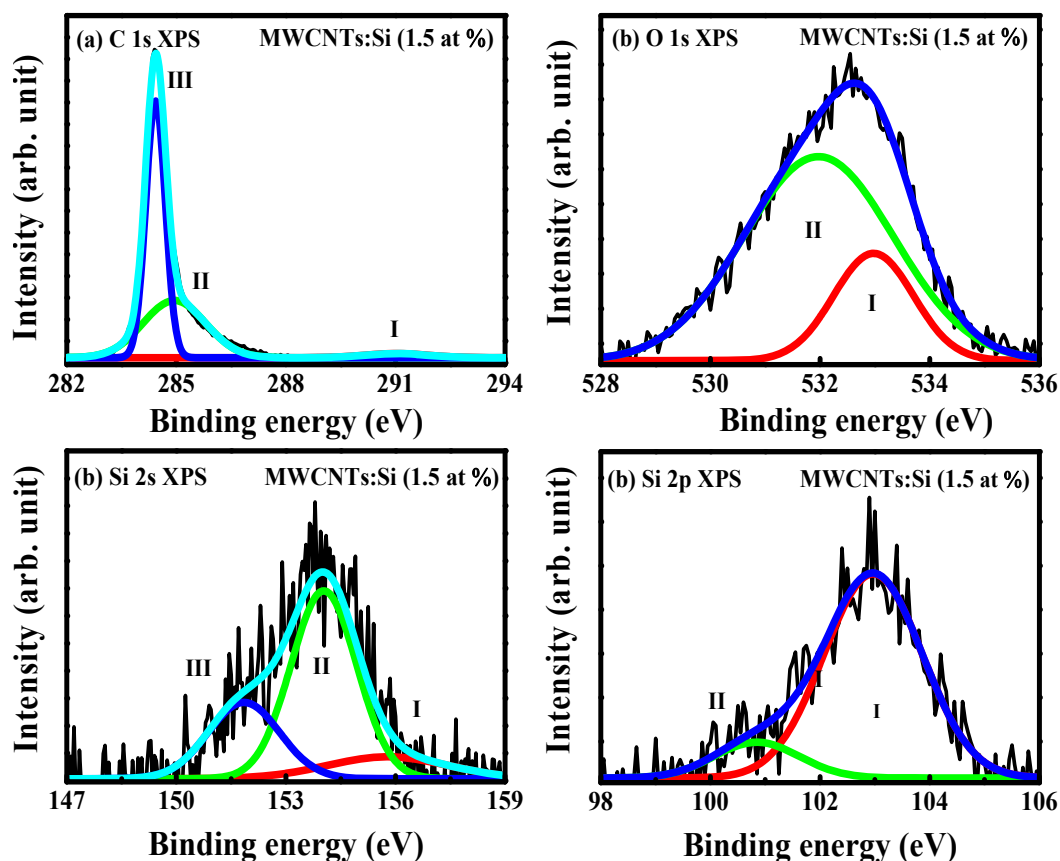


Figure 4.7. De-convolution of C1s, O1s, Si 2s and Si 2p XPS spectra for MWCNTs functionalized with 1.5 at % concentration of SiO<sub>2</sub>.

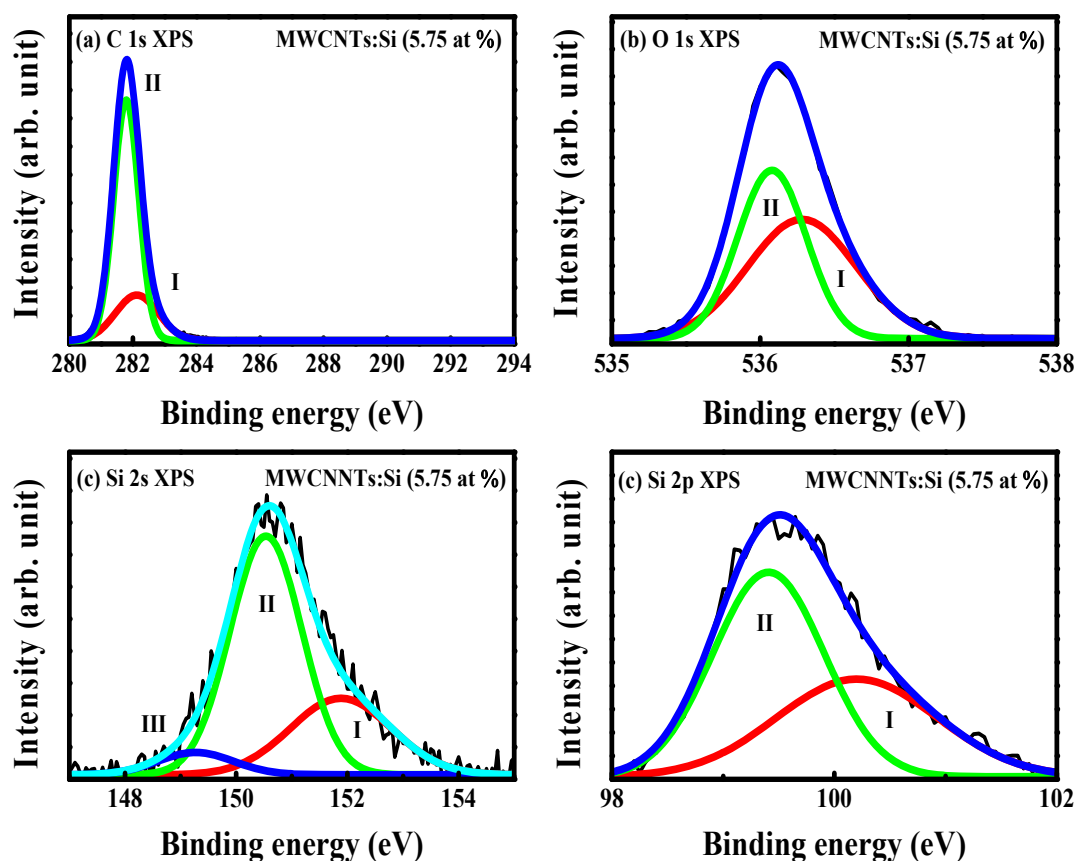


Figure 4.8. De-convolution of C1s, O1s, Si 2s and Si 2p XPS spectra for MWCNTs functionalized with 5.75 at % concentration of SiO<sub>2</sub>.

Figure 4.7 (c and d) and 4.8 (c and d) show the Si 2s and 2p spectra of MWCNTs:Si nanocomposites. These peaks were decomposed into two and three Gaussian peaks for Si 2p and Si 2s respectively as shown in the figures. However, these peaks are also observed in SiO<sub>2</sub> as discussed earlier. From figure 4.8 (c and d), the decomposed peaks are observed from 100.8 eV to 102.9 eV which are assigned to Si-C or Si-C-O and the peak at 103.0 corresponds to Si-O. In the case of figure 4.7 (c and d), the peaks ranging from 150.1 to 153.0 eV are Si-Si bond, and other peaks greater than 153.0 eV are Si-O bond [20]. From the results discussed earlier, it is obvious that there is a significant change in the bonding structures of MWCNTs:Si nanocomposites. Also, the de-convoluted XPS spectra of MWCNTs:Si nanocomposites

confirmed the decrease in  $sp^2$  to an increase in  $sp^3$  cluster as observed from Raman spectroscopy.

Table 4.3: C 1s, O 1s, Si 2p and Si 2s XPS parameters obtained from the de-convoluted of SiO<sub>2</sub>, MWCNTs, MWCNTs:Si nanocomposites

Nanomaterials	C 1s XPS						O 1s XPS			
	Peak I		Peak II		Peak III		Peak I		Peak II	
	Int. (eV)	x1 (a.u.)	Int. (eV)	x2 (a.u.)	Int. (eV)	x3 (a.u.)	Int. (eV)	x1 (a.u.)	Int. (eV)	x2 (a.u.)
MWCNTs	48.7	283.5	25.0	284.3	26.3	288.8	60.6	530.5	39.4	531.9
MWCNTs:Si (1.5 at %)	49.4	284.4	24.7	285.3	25.8	289.5	56.2	531.5	43.8	533.0
MWCNTs:Si (5.75 at %)	87.8	281.8	12.2	282.4	--	--	67.6	529.2	32.4	529.8
	Si 2s XPS						Si 2p XPS			
SiO <sub>2</sub>	375	150.7	389	151.9	259	153.1	7241	101.2	7689	100.8
MWCNTs:Si (1.5 at %)	270	151.6	588	154.1	142	156.3	28.0	100.4	72.0	103.0
MWCNTs:Si (5.75 at %)	231	148.6	1224	150.6	851	151.6	60.0	99.4	40.0	100.2

#### 4.3.5. X-ray absorption near edge structure (XANES) spectroscopy

Figure 4.9, 4.10, and 4.11 show XANES spectrums of normalized C *K*-edge, O *K*-edge, and Si *L*<sub>3,2</sub>-edge for MWCNTs, MWCNTs:Si nanocomposites and SiO<sub>2</sub>. From figure 4.9, the C *K*-edge spectra display two features  $\pi^*$  and  $\sigma^*$ . The  $\pi^*$  and  $\sigma^*$  features correspond to  $sp^2$  and  $sp^3$  configurations and were located at 286.2 and 293.5 eV, respectively [23,24]. Figure 4.9 also shows an inset which is a Gaussian subtraction of  $\pi^*$  region ranging from 283.5 to 289 eV. The inset reveals two features of  $\pi^*$  at 286.2 ( $sp^2$  C-C bond) and 287.6 eV (C-H / Si-C(:H) / Si-

C(:O) bond [25] for MWCNTs and MWCNTs with Si  $\sim 1.5$  at %, but shift slightly towards high photon energy for MWCNTs with Si  $\sim 5.75$  at %. It was observed that the intensity of  $\pi^*$  increases for MWCNTs with Si  $\sim 1.5$  at % and decreases for MWCNTs with Si  $\sim 5.75$  when compared to MWCNTs. The spectra difference between pristine MWCNTs and MWCNTs:Si nanocomposites gives a clear understanding of the effects of SiO<sub>2</sub> in MWCNTs. These indicate the effect of Si-C(:O) and/or Si-C(:H) bonding on the electronic structure of MWCNTs:Si nanocomposites. The spectra difference also indicates an increase and decrease in the number of unoccupied near-edge C 2*p* derived states in MWCNTs with Si  $\sim 1.5$  at % and MWCNTs with Si content  $\sim 5.75$  at %, respectively. Also, it can be said that the variation in their intensities as displayed by the inset corresponds to the variation in the I<sub>D</sub>/I<sub>G</sub> ratio as observed from the Raman spectra of the nanomaterials.

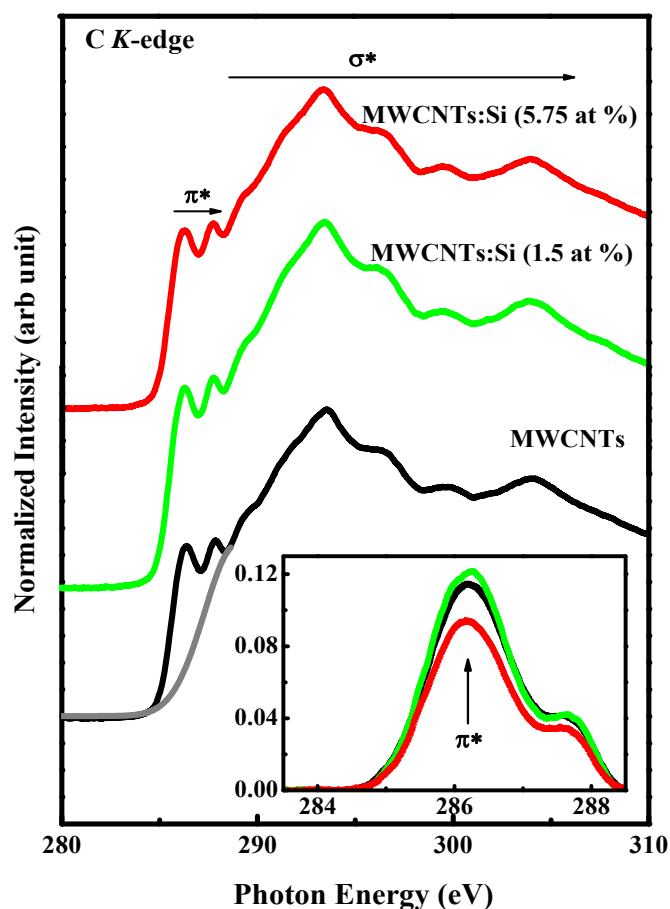


Figure 4.9. C K-edge XANES spectra of MWCNTs and MWCNTs:Si nanocomposites.

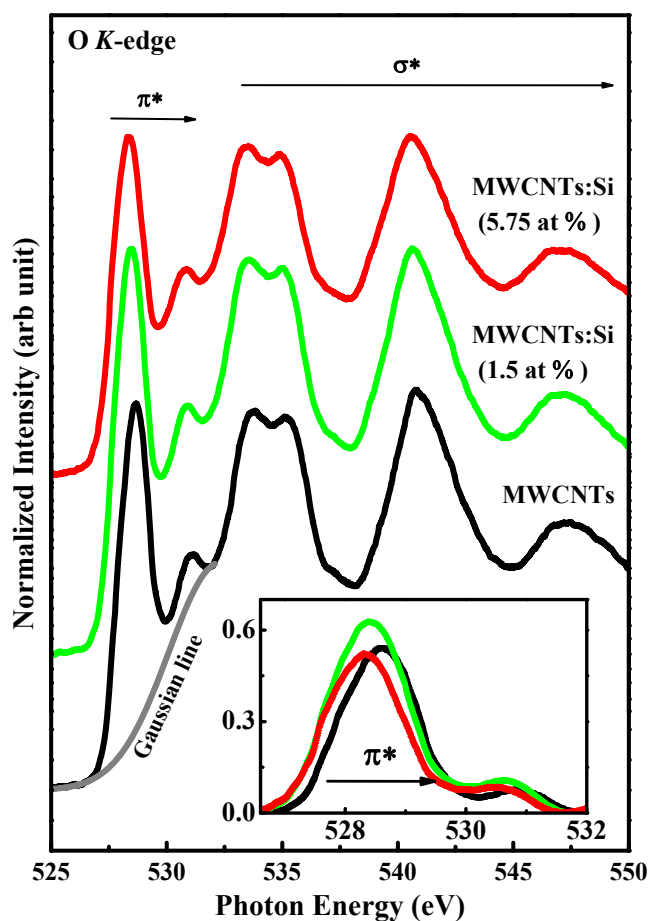


Figure 4.10. O *K*-edge XANES spectra of MWCNTs and MWCNTs:Si nanocomposites.

The XANES normalized O *K*-edge spectra of MWCNTs and MWCNTs:Si nanocomposites are presented in figure 4.10. The spectrum displays  $\pi^*$  and  $\sigma^*$  features as seen in C *K*-edge at 528.6/531.1 eV and 538-547 eV corresponding to transitions from C=O (carboxylic) and C-O/O-H (hydroxyl) groups [26]. Peaks (double structure) are also found at 533.8 and 535.1 eV corresponding to the physical absorption of O<sub>2</sub>, which may occur throughout preparation [27] as shown in each spectrum. The double structure was due to the use of chemicals during the synthesis of MWCNTs and MWCNTs:Si nanocomposites. The O *K*-edge of MWCNTs:Si nanocomposites shifted 0.4 eV towards low photon energy compared to MWCNTs. This shift implies the relationship between Si, C, and O in MWCNTs. The double peaks at 533.7 and 535.1 eV are denoted to  $t_{2g}$  and  $e_g$  Si d states [27]. Considering the inset in figure 4.10, an increase and decrease in intensity of  $\pi^*$  were observed which correspond to increase and

decrease in O vacancies for MWCNTs:Si nanocomposites with Si content of  $\sim 1.5$  at % and  $\sim 5.75$  at %, respectively when compared to that of MWCNTs. The coupling among O  $2p$  and Si  $3p$  states may result in the change in the intensity of MWCNTs:Si nanocomposites.

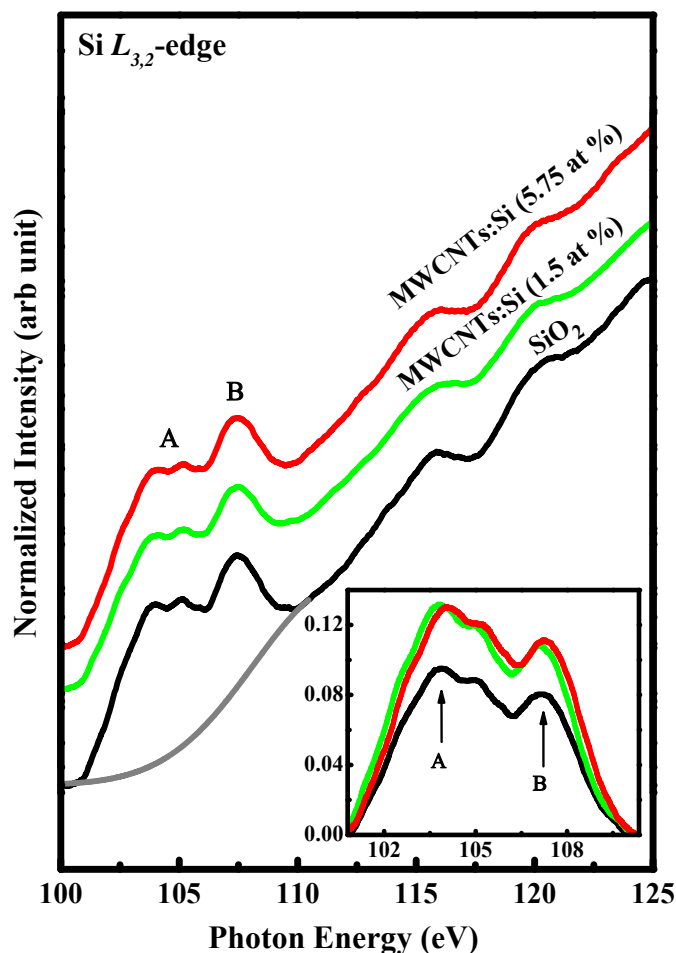


Figure 4.11. Si  $L_{3,2}$ -edge XANES spectra of SiO<sub>2</sub> and MWCNTs:Si nanocomposites.

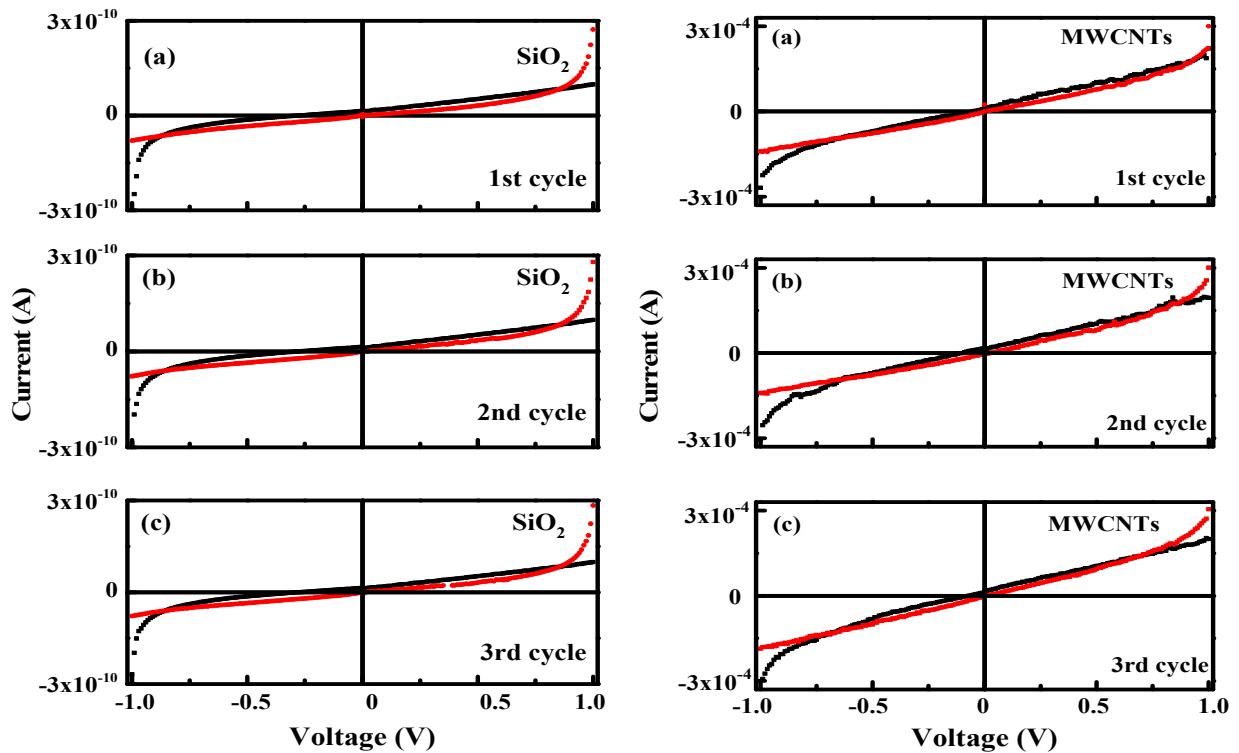
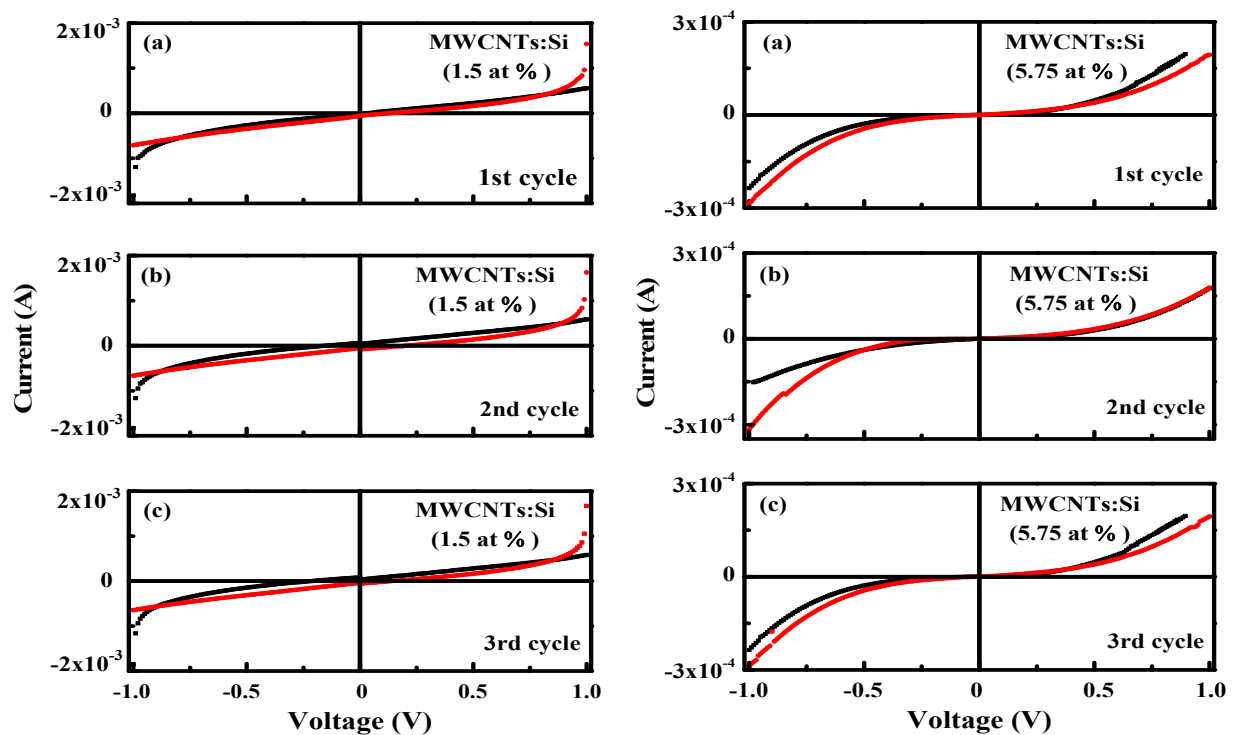
Figure 4.11 demonstrates the normalized XANES Si  $L_{3,2}$ -edge spectrums of SiO<sub>2</sub> and MWCNTs:Si nanocomposites. The spectra show two structures A and B for each of SiO<sub>2</sub> and MWCNTs:Si nanocomposites and are separated by 2.0 eV. Structure A exhibits two features that are also confirmed by the inset as seen in the figure. These features appear as a spin-orbit doublet and are observed at 104 and 105 eV corresponding to the alterations of Si  $2p_{3/2}$  and  $2p_{1/2}$  core states, respectively to Si  $3s$  derived states [27] with separation of 1.0 eV. Structure B allowed the alteration of  $2p$  to  $3p$  corresponding to Si  $3d$  or  $3s$  derived states [27-29]. The

inset in the figure shows a slight shift and variation in the intensities of MWCNTs:Si nanocomposites, indicate a change of electronic structure and formation of the amorphous phase is possible for SiO<sub>2</sub> in MWCNTs.

#### **4.3.6. Current-voltage (I-V) measurement**

Figures 4.12 to 4.13 shows the current-voltage (I-V) curves of SiO<sub>2</sub>, MWCNTs, and MWCNTs:Si nanocomposites. The I-V of these samples were measured at room temperature ranging from -1 to +1 V. From the figures, SiO<sub>2</sub>, MWCNTs, and MWCNTs with Si ~1.5 at % displayed an insulating and conducting behavior. The I-V curve of MWCNTs with Si ~5.75 at % nanocomposites shows that the materials are semiconducting in nature. It was also observed that the electrical conductivity of MWCNTs with Si ~1.5 at % is higher than that of MWCNTs and MWCNTs with Si ~5.75 at %. The electrical conductivity of MWCNTs with Si ~1.5 at % and MWCNTs with Si ~5.75 at % increases and decreases, respectively when compared with that of MWCNTs. The variation in the conductivity of the nanocomposites was as a result of the formation of a dangling bond in MWCNTs. The dangling bond builds up a separation between the energy levels in the band gap of the nanocomposites structure. The separation between the energy levels (hopping distances) may change constantly with a change in input voltage. Hence, the higher the hopping distances the lesser the charge carrier which is analogous to a minute flow of current. On the other hand, smaller hopping distance corresponds to the maximum current.



Figure 4.12. I-V curve for SiO<sub>2</sub> and MWCNTs.Figure 4.13. I-V curve for MWCNTs functionalized with 1.5 and 5.75 at % concentration of SiO<sub>2</sub>.

The I-V log plot of SiO<sub>2</sub>, MWCNTs, and MWCNTs:Si nanocomposites were depicted in figures 4.14 and 4.15. It was observed that the I-V log plot of MWCNTs with Si ~5.75 at % shows a considerable hysteresis loop when compared to that of SiO<sub>2</sub>, MWCNTs, and MWCNTs with Si ~1.5 at %. The observed loop indicates a charge storage capability and ferroelectric behavior of the nanocomposite compared to that of SiO<sub>2</sub>, MWCNTs, and MWCNTs with Si ~1.5 at % with no hysteresis loop. Considering figure 4.15, the hysteresis loop of MWCNTs with Si ~5.75 at % implies semiconducting material than MWCNTs with Si ~1.5 at %. Comparing the cycles of Si ~5.75 at %, it was also observed that there is a variation in one loop region to the other, indicating a Coulombic blockade/ recombination of holes and electrons, which is in agreement with a single electron silicon transistor. Based on this fact, MWCNTs:Si nanocomposites may be useful for ferroelectric devices.

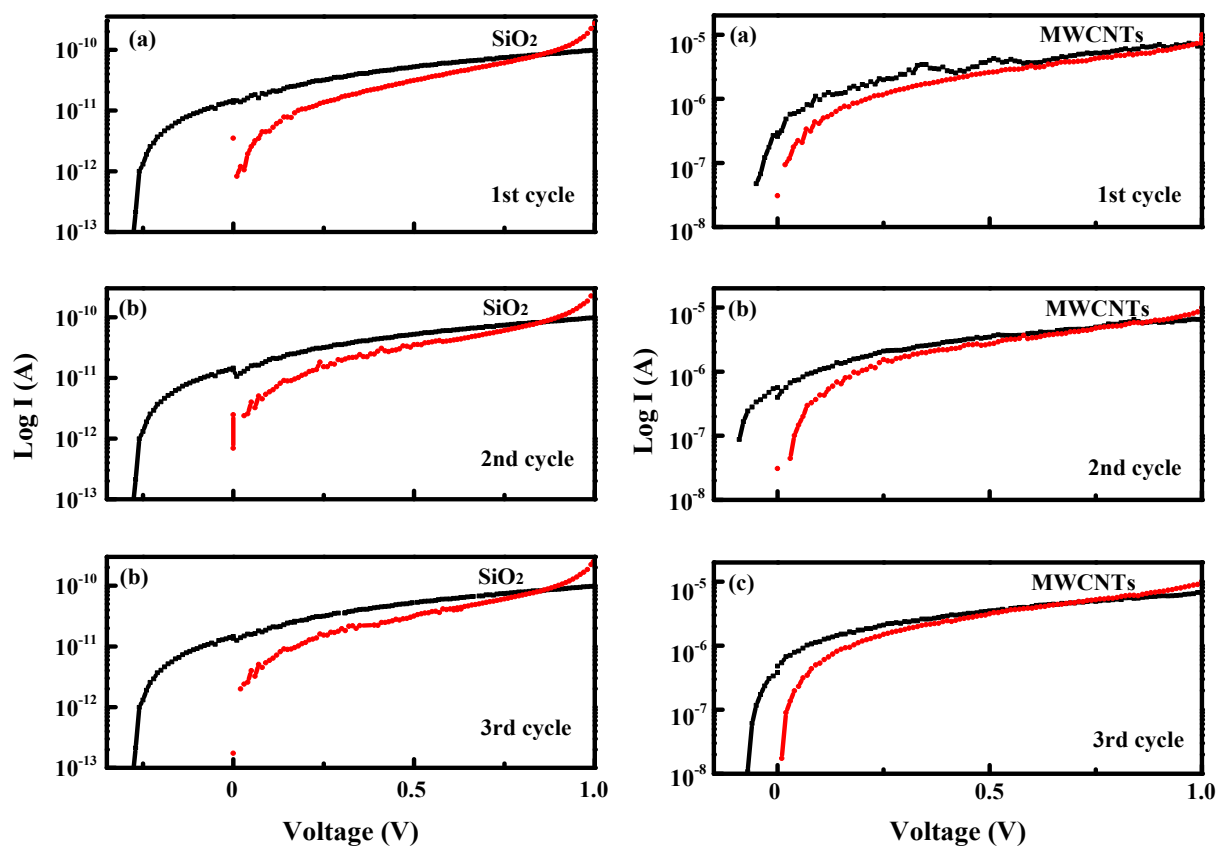


Figure 4.14. I-V log plot for SiO<sub>2</sub> and MWCNTs.

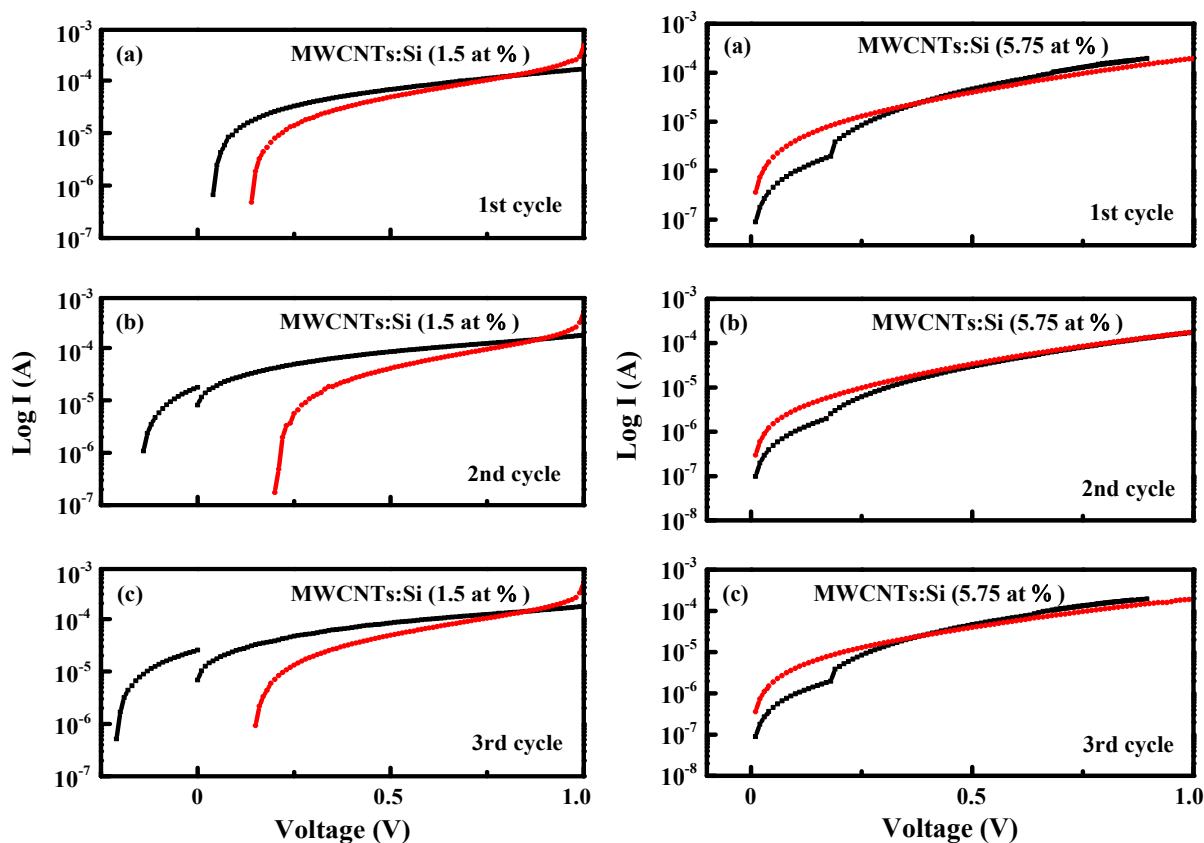


Figure 4.15. I-V log plot for MWCNTs functionalized with 1.5 and 5.75 at % concentration of  $\text{SiO}_2$ .

#### 4.3.7. M-H loop and temperature-dependent magnetization measurement

The magnetic properties of  $\text{SiO}_2$ , MWCNTs, and MWCNTs:Si nanocomposites were measured using a superconducting quantum interface device (SQUID) under room temperature of 300 K and temperature of 40 K, and the M-H curves are shown in figure 4.16 (a). The values obtained from this measurement were also presented in Table 4.4. From figure 4.16 (a (i and ii)),  $\text{SiO}_2$  and MWCNTs show a paramagnetic and ferromagnetic behavior, respectively. Considering figure 4.16 (a (iii and iv)), it is observed that the magnetization for MWCNTs with Si ~1.5 at % slightly increases, whereas decreases drastically for MWCNTs with Si ~5.75 at % when compared to that of MWCNTs in figure 4.16 (a (i)), thus Si ~5.75 at % loses its ferromagnetic behavior. The decrease in magnetization is attributed to tetrahedral Si-C bonding formation,

indicating a strong interaction between MWCNTs and SiO<sub>2</sub> [20]. This interaction led to an increase in sp<sup>3</sup> hybridization [20]. In reference to XPS spectra, the formation of Si-C-O (defect structure) and -COOH/C-O bonding was observed and can be attributed to the slight increase in the magnetization of MWCNTs with Si ~1.5 at %. The formation of these bonds was a result of an oxygen functional group, which produce a positive center to capture an electron in a restricted form [30,31]. The restricted electron retain magnetic moment which contributed to the enhanced magnetization in MWCNTs with Si ~1.5 percent. These results also correspond to the observations in C K-edge and O K-edge XANES spectroscopy.

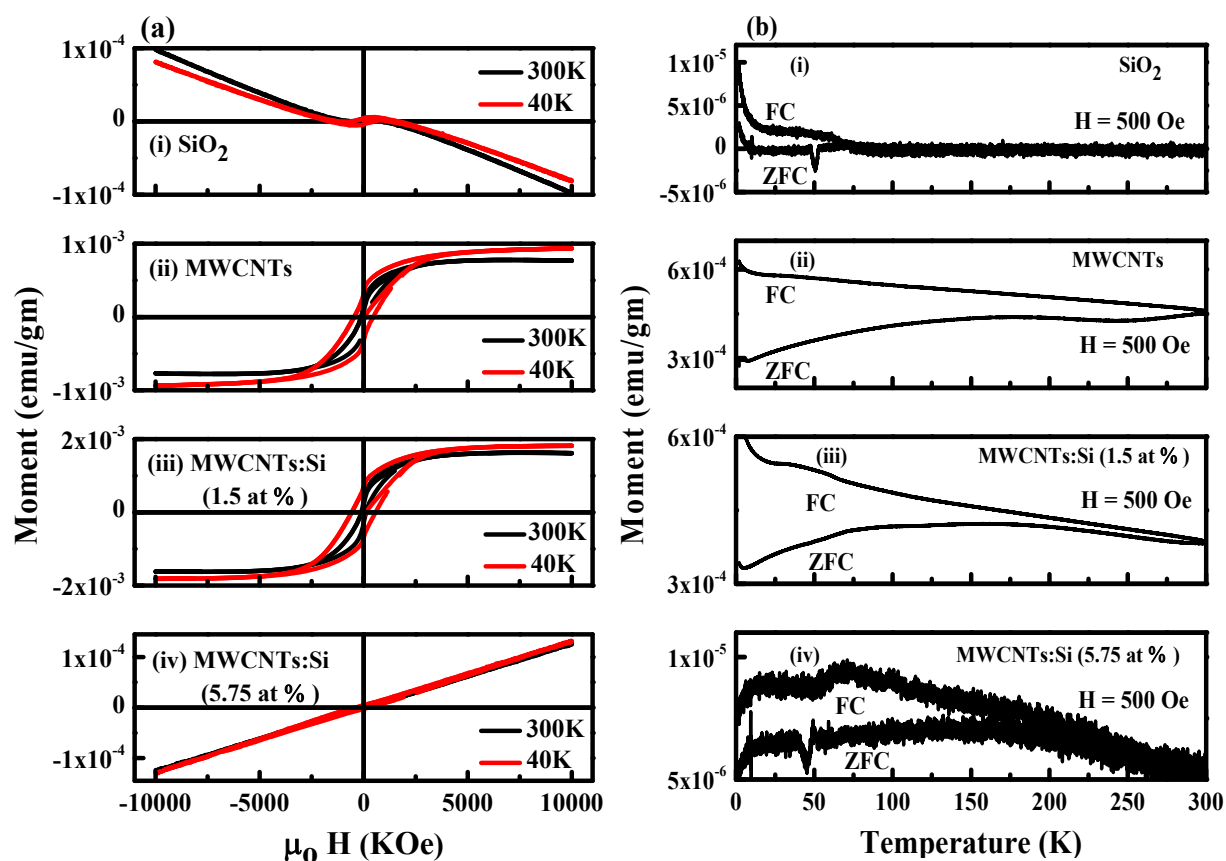


Figure 4.16. (a) Comparison of M-H loop for SiO<sub>2</sub>, MWCNTs, and MWCNTs:Si nanocomposites at different temperatures. (b) Field cooling (FC) and zero-field cooling (ZFC) for SiO<sub>2</sub>, MWCNTs, and MWCNTs:Si nanocomposites.

In order to have an in-depth understanding of magnetic properties, we have measured the field cooling (FC) and zero-field cooling (ZFC) magnetization of SiO<sub>2</sub>, MWCNTs, and MWCNTs:Si nanocomposites. Figure 4.16 (b) shows the temperature dependence FC and ZFC of each material with an applied field of 500 Oe. From figure 4.16 (b (ii and iii)), a ferromagnetic behavior is observed with an increase in the magnetic moment of MWCNTs with Si ~1.5 at % compare to MWCNTs. FC and ZFC have confirmed the ferromagnetic behavior of MWCNTs and MWCNTs with Si ~1.5 at %, which is analogous to the trend of the M-H loop.

Table 4.4: Parameters obtained from M-H loops [Retentivity (M<sub>R</sub>) Coercivity (H<sub>C</sub>), Magnetic and Saturation (M<sub>S</sub>),] measured at 40 K and 300 K for SiO<sub>2</sub>, MWCNTs, MWCNTs:Si nanocomposites

Materials	40 K			300 K		
	M <sub>R</sub>	H <sub>C</sub>	M <sub>S</sub>	M <sub>R</sub>	H <sub>C</sub>	M <sub>S</sub>
SiO <sub>2</sub>	43 x 10 <sup>-4</sup>	515	0.0057	36.0 x 10 <sup>-4</sup>	379	49 x 10 <sup>-4</sup>
MWCNTs	73 x 10 <sup>-4</sup>	813	0.019	25.0 x 10 <sup>-4</sup>	112	140 x 10 <sup>-4</sup>
MWCNT:Si (1.5 at %)	76 x 10 <sup>-4</sup>	689	0.022	23.0 x 10 <sup>-4</sup>	123	130 x 10 <sup>-4</sup>
MWCNT:Si (5.75 at %)	0.071 x 10 <sup>-4</sup>	357	--	0.2 x 10 <sup>-4</sup>	60	--

#### 4.3.8. Electron spin resonance (ESR)

Also, to understand the defect arising from ferromagnetism in SiO<sub>2</sub>, MWCNTs, and MWCNTs:Si nanocomposites, a room temperature electron spin resonance (ESR) has been put into consideration and are plotted in figure 4.17. A sharp microwave signal is observed for all spectral. The values estimated from ESR are tabulated in table 4.5. These signals are observed at high and low fields ranging from 3200 G to 1700 G, respectively. The ESR signal (line width ( $\Delta H$ )) changes from 203 to 367, 190 to 433, 117 to 711, and 148 to 1284 in the low and high

field for SiO<sub>2</sub>, MWCNTs, MWCNTs with Si ~1.5 and ~5.75 at % respectively. The Landé gfactor (g-value) and  $\Delta g/g$  values vary with the percentage of SiO<sub>2</sub> in MWCNTs:Si nanocomposites. We observed a  $\Delta H$  with active g value more than 4.0 and 2.0 at a low and high field in ESR of MWCNTs with Si ~1.5 and ~5.75 at %, respectively, which implies a magnetic stage in MWCNTs [32]. The increase in  $\Delta H$  with active g value above 2.0 may be due to a shift in the resonance field ( $H_r$ ) towards the lower field, indicating a broad  $\Delta H$  has overlapped the resonance line of an unpaired electron trapped within an oxygen vacancy. The related effect has been reported by Majchrzycki *et al.* [33].  $P_{asy} = (1 - h_u/h_l)$  [34] was used to calculate the asymmetric factor ( $P_{asy}$ ), where  $h_u$  and  $h_l$  are the peak height (upper and lower) from the zero lines. From the values calculated, we observed that an increase in SiO<sub>2</sub> content in MWCNTs:Si nanocomposite led to a gradual increase of  $P_{asy}$  and are presented in Table 4.5. The gradual increase of  $P_{asy}$  led to a very high magnetic anisotropy in MWCNTs:Si nanocomposites.

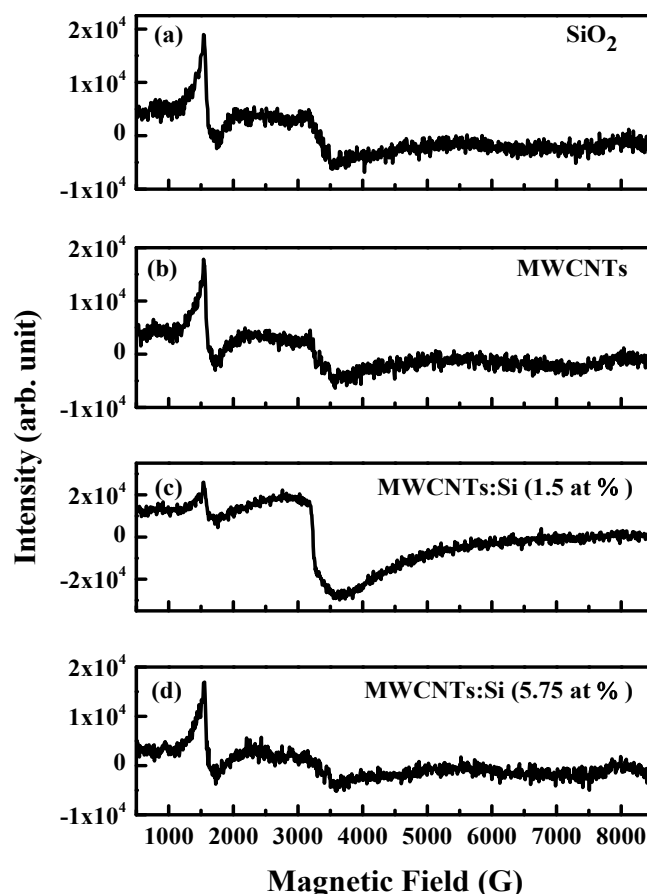


Figure 4.17. ESR spectra for  $\text{SiO}_2$ , MWCNTs, and MWCNTs:Si nanocomposites.

The whole quantity of spin was assessed using:  $N = 0.285 \times I_{p-p} \times (\Delta H)^2$  [35] to confirm the magnetization in MWCNTs:Si nanocomposites as observed in M-H loop, where  $N$  is the total spin,  $I_{p-p}$  is the peak-to-peak height of signal and  $\Delta H$  is the Gauss line width. Based on the assessment of  $N$ , a higher  $N$  value was observed in MWCNTs with Si ~1.5 at % compare to MWCNTs and MWCNTs with Si ~5.75 at % which led to the higher value of magnetization in MWCNTs with Si ~1.5 at %. In reference to ESR result, MWCNTs with Si ~1.5 at % can retain magnetism like pristine MWCNTs.

Table 4.5: Parameters obtained from ESR of SiO<sub>2</sub>, MWCNTs, MWCNTs:Si nanocomposites at 300 K

Nanomaterials	g- value		$\Delta H$		$H_r$		$\Delta g/g$	N	$P_{asy}$
	High field	Low field	High field	Low field	High field	Low field			
SiO <sub>2</sub>	2.08	4.03	367	203	3243	1673	0.0375	$3.67 \times 10^8$	0.32
MWCNTs	2.04	4.17	433	190	3298	1680	0.0182	$6.11 \times 10^8$	0.23
MWCNTs:Si (1.5 at %)	2.11	4.29	711	117	3198	1572	0.0511	$7.54 \times 10^9$	0.24
MWCNTs:Si (5.75 at %)	2.04	4.11	1284	148	3303	1616	0.0182	$3.65 \times 10^9$	0.56

The magnetic and electrical behavior are related due to the fact that their properties changes based on the mobility of free electrons among the atoms. The non-restricted electrons were able to move freely to the conduction band from the valence band, which contributed to the enhanced electrical conductivity [36]. The magnetism in a material can also be attributed to the non-restricted electrons not captured by the positive center [37]. Moreover, the exchange interactions between atoms can be enhanced by the non-restricted electrons, thereby improving the ferromagnetism in MWNCTs:Si nanocomposite [37,38].

#### 4.4. Conclusion

SiO<sub>2</sub>, MWCNTs, and MWCNTs:Si nanocomposites were synthesized and their electronic, electrical, and magnetic behavior were studied. It was observed that there is an increase/decrease in the hybridization of  $sp^3/sp^2$  with a decrease/increase in the electrical conductivity of the Si ~5.75/Si ~1.5 at % nanocomposites, respectively. An electrical hysteresis loop was observed for Si ~5.75 at % nanocomposite, indicating a ferroelectric behavior and a



change in the electrical structure of MWCNTs. Also, the magnetic behavior of nanocomposites showed a semiconducting structure compared to the semi-metallic structure of MWCNTs. In conclusion, the Si-incorporation is another way to tune the electrical/ electronic and magnetic properties of MWCNTs for electrical/ electronic, magnetic, and electro-magnetic device applications.

## References

- [1] S. Iijima, "Helical microtubules of graphitic carbon," *Nature*, vol. 354, no. 6348, pp. 56–58, 1991.
- [2] D. T. Karousis, Nikolaos, Nikos Tagmatarchis, "Current progress on the chemical modification of carbon nanotubes.," *Chem. Rev.*, vol. 110, no. 9, pp. 5366–5397, 2010.
- [3] P. J. F. Harris, E. Hernández, and B. I. Yakobson, "Carbon Nanotubes and Related Structures : New Materials for the Twenty-First Century Teaching Physics with the Physics Suite," vol. 415, pp. 415, 2004.
- [4] C. Gao, Z. Guo, J. H. Liu, and X. J. Huang, "The new age of carbon nanotubes: An updated review of functionalized carbon nanotubes in electrochemical sensors," *Nanoscale*, vol. 4, no. 6, pp. 1948–1963, 2012.
- [5] J. J. Adjizian *et al.*, "Boron- and nitrogen-doped multi-wall carbon nanotubes for gas detection," *Carbon N. Y.*, vol. 66, pp. 662–673, 2014.
- [6] R. J. Baierle, S. B. Fagan, R. Mota, A. J. R. da Silva, and A. Fazzio, "Electronic and structural properties of silicon-doped carbon nanotubes," *Phys. Rev. B - Condens. Matter Mater. Phys.*, vol. 64, no. 8, pp. 854131–854134, 2001.
- [7] C. Song *et al.*, "Functionalization of silicon-doped single walled carbon nanotubes at the doping site: An ab initio study," *Phys. Lett. Sect. A Gen. At. Solid State Phys.*, vol. 358, no. 2, pp. 166–170, 2006.
- [8] V. Vatanpour, S. S. Madaeni, R. Moradian, S. Zinadini, and B. Astinchap, "Fabrication and characterization of novel antifouling nanofiltration membrane prepared from

- oxidized multiwalled carbon nanotube/polyethersulfone nanocomposite,” *J. Memb. Sci.*, vol. 375, no. 1-2, pp.284-294, 2011.
- [9] P. Das, A. Saha, A. R. Maity, S. C. Ray, and N. R. Jana, “Silicon nanoparticle based fluorescent biological label via low temperature thermal degradation of chloroalkylsilane,” *Nanoscale*, vol. 5, no. 13, pp. 5732–5737, 2013.
- [10] Y. Chen, N. Du, H. Zhang, and D. Yang, “Facile synthesis of uniform MWCNT@Si nanocomposites as high-performance anode materials for lithium-ion batteries,” *J. Alloys Compd.*, vol. 622, pp. 966–972, 2015.
- [11] V. B. Koli, A. G. Dhodamani, A. V. Raut, N. D. Thorat, S. H. Pawar, and S. D. Delekar, “Visible light photo-induced antibacterial activity of TiO<sub>2</sub>-MWCNTs nanocomposites with varying the contents of MWCNTs,” *J. Photochem. Photobiol. A Chem.*, vol. 328, no. May, pp. 50–58, 2016.
- [12] Y. Luo *et al.*, “Electric field induced structural color changes of SiO<sub>2</sub>@TiO<sub>2</sub>core-shell colloidal suspensions,” *J. Mater. Chem. C*, vol. 2, no. 11, pp. 1990–1994, 2014.
- [13] R. Casati, M. H. Nasab, M. Coduri, V. Tirelli, and M. Vedani, “Effects of platform pre-heating and thermal-treatment strategies on properties of als10mg alloy processed by selective laser melting,” *Metals (Basel)*, vol. 8, no. 11, p. 954, 2018.
- [14] L. A. A. Rodriguez and Di. N. Travessa, “Core/Shell Structure of TiO<sub>2</sub>-Coated MWCNTs for Thermal Protection for High-Temperature Processing of Metal Matrix Composites,” *Adv. Mater. Sci. Eng.*, vol. 2018, 2018.
- [15] S. C. Ray, S. K. Bhunia, A. Saha, and N. R. Jana, “Electric and ferro-electric behaviour of polymer-coated graphene-oxide thin film,” *Phys. Procedia*, vol. 46, no. 19, pp. 62–

- 70, 2013.
- [16] W. Kiefer, A. P. Mazzolini, and P. R. Stoddart, “Monitoring oxidation of multiwalled carbon nanotubes by Raman spectroscopy,” *J. Raman Spectrosc.*, vol. 38, no. 6, pp. 1538–1553, 2007.
- [17] D. O. Idisi *et al.*, “Electronic, electrical and magnetic behaviours of reduced graphene-oxide functionalized with silica coated gold nanoparticles,” *Appl. Surf. Sci.*, vol. 483, no. 12, pp. 106–113, 2019.
- [18] T. I. T. Okpalugo, P. Papakonstantinou, H. Murphy, J. McLaughlin, and N. M. D. Brown, “High resolution XPS characterization of chemical functionalised MWCNTs and SWCNTs,” *Carbon N. Y.*, vol. 43, no. 1, pp. 153–161, 2005.
- [19] L. Zhang, N. Kuramoto, Y. Azuma, A. Kurokawa, and K. Fujii, “Thickness Measurement of Oxide and Carbonaceous Layers on a  $^{28}\text{Si}$  Sphere by XPS,” *IEEE Trans. Instrum. Meas.*, vol. 66, no. 6, pp. 1297–1303, 2017.
- [20] S. C. Ray, D. K. Mishra, A. M. Strydom, and P. Papakonstantinou, “Magnetic behavioural change of silane exposed graphene nanoflakes,” *J. Appl. Phys.*, vol. 118, no. 11, 2015.
- [21] N. G. Shang *et al.*, “Catalyst-free efficient growth, orientation and biosensing properties of multilayer graphene nanoflake films with sharp edge planes,” *Adv. Funct. Mater.*, vol. 18, no. 21, pp. 3506–3514, 2008.
- [22] M. Pedio, F. Borgatti, A. Giglia, N. Mahne, S. Nannarone, S. Giovannini, C. Cepek, E. Magnano, G. Bertoni, E. Spiller and M. Sancrotti, Annealing temperature dependence of C<sub>60</sub> on silicon surfaces: bond evolution and fragmentation as detected by

- NEXAFS. *Phys. Scr.*, vol. 2005, no. 115, p.695, 2005.
- [23] S. C. Ray *et al.*, “A comparative study of the electronic structures of oxygen- and chlorine-treated nitrogenated carbon nanotubes by x-ray absorption and scanning photoelectron microscopy,” *Appl. Phys. Lett.*, vol. 91, no. 20, 2007.
- [24] C. W. Pao, S. C. Ray, H. M. Tsai, Y. S. Chen, H. C. Chen, I. N. Lin, W. F. Pong, J. W. Chiou, M. H. Tsai, N. G. Shang and P. Papakonstantinou, “Change of structural behaviors of organo-silane exposed graphene nanoflakes,” *J. Phys. Chem. C*, vol. 114, no. 18, pp. 8161–8166, 2010.
- [25] V. A. Terekhov *et al.*, “A study of the local electronic and atomic structure in a-Si<sub>6</sub>C<sub>1-x</sub> amorphous alloys using ultrasoft X-ray emission spectroscopy,” *Semiconductors*, vol. 39, no. 7, pp. 830–834, 2005.
- [26] S. Banerjee, T. Hemraj-Benny, S. S. Wong, M. Balasubramanian, J. A. Misewich, and D. A. Fischer, “Ozonized single-walled carbon nanotubes investigated using NEXAFS spectroscopy,” *Chem. Commun.*, vol. 10, no. 7, pp. 772–773, 2004.
- [27] “Electronic structure analysis of  $\alpha$ -SiO<sub>2</sub> via x-ray absorption near-edge structure at the Si K, L<sub>2,3</sub> and O K edges,” *J. Phys. Condens. Matter*, vol. 10, no. 36, pp. 8083–8092, 1998.
- [28] S. Di Mo and W. Y. Ching, “X-ray absorption near-edge structure in alpha-quartz and stishovite: Ab initio calculation with core-hole interaction,” *Appl. Phys. Lett.*, vol. 78, no. 24, pp. 3809–3811, 2001.
- [29] M. W. Gaultois and A. P. Grosvenor, “XANES and XPS investigations of (TiO<sub>2</sub>)<sub>x</sub>(SiO<sub>2</sub>)<sub>1-x</sub>: The contribution of final-state relaxation to shifts in absorption and binding

- energies,” *J. Mater. Chem.*, vol. 21, no. 6, pp. 1829–1836, 2011.
- [30] S. C. Ray, S. Sarma, M. Pontsho, S. Pattanaik, and D. K. Mishra, “Tuning of the electronic structure and magnetic properties of xenon ion implanted zinc oxide,” *J. Phys. D. Appl. Phys.*, vol. 51, no. 9, pp.095304 2018.
- [31] T. Wu, H. Sun, X. Hou, L. Liu, H. Zhang, and J. Zhang, “Significant room-temperature ferromagnetism in porous TiO<sub>2</sub> thin films,” *Microporous Mesoporous Mater.*, vol. 190, pp.63-66, 2014.
- [32] R. G. Oxide, T. Carbon, D. Yerchuck, and A. Dovlatova, “ESR evidence for disordered magnetic phase from ultra-small carbon nanotubes embedded in zeolite nanochannels. *Europhys. Lett.*, vol. 90, no. 5, pp.57003. 2010.
- [33] Majchrzycki, M. A. Augustyniak-Jabłokow, R. Strzelczyk, and M. Maćkowiak, “Magnetic centres in functionalized graphene,” *Acta Phys. Pol. A*, vol. 127, no. 2, pp. 540–542, 2015.
- [34] J. Das, D. K. Mishra, and V. V. Srinivasu, “Spin canting and magnetism in nanocrystalline Zn<sub>1-x</sub>Al<sub>x</sub>O,” *J. Alloys Compd.*, vol. 704, pp.237-244, 2017.
- [35] B. Bleaney, and R. S. Rubins, “Explanation of some ‘forbidden’ transitions in paramagnetic resonance,” *Proc. Phys. Soc.*, vol. 77, no. 1, pp. 103–112, 1961.
- [36] Z. Shuai, L. Wang, and Q. Li, “Evaluation of charge mobility in organic materials: From localized to delocalized descriptions at a first-principles level,” *Adv. Mater.*, vol. 23, no. 9, pp. 1145–1153, 2011.
- [37] T. Wu, H. Sun, X. Hou, L. Liu, H. Zhang, and J. Zhang, “Significant room-temperature ferromagnetism in porous TiO<sub>2</sub> thin films,” *Microporous Mesoporous Mater.*, vol. 190,

pp. 63–66, 2014.

- [38] H. Ohno, “Making nonmagnetic semiconductors ferromagnetic,” *Science*, vol. 281, no. 5379, pp. 951–956, 1998.

## **Chapter Five**

### **Tuning the Electronic and Electrical Behaviour of MWCNTs- TiO<sub>2</sub> Nanocomposites.**



## 5.1. Introduction

Carbon nanotubes (CNTs) have attracted attention due to their unique electrical, thermal and mechanical properties [1,2]. This uniqueness of CNTs has generated great interest for different potential applications in various research areas such as solar cells, energy conversion devices, sensors, electromagnetic interference shielding, hydrogen storage media, and micro-electronics. [2–4]. In recent years, there have been demands from semiconductor industries for nanomaterials with a high storage density [5,6]. It would be of huge interest if CNTs were been used for ferroelectric and memristive devices. The main challenge is due to their low density [1] and conducting nature [7]. To meet these demands, the surface of CNTs needs to be modified. Modifying the surface of CNTs with nanoparticles is expected to offer excellent performances in nano/microelectronic devices and are also useful for nanoprobe, nano cable, coaxial, and sensor tips [8].

However, CNTs usually need sufficient binding sites to absorb precursors of nanoparticles which normally result in low efficiency and weak dispersion in solution [9]. Purification of CNTs through acid treatment are been used to attach additional binding sites such as hydroxyl, carbonyl, and carboxyl groups (functional groups) to CNTs [9]. These functional groups on CNTs do not only give room for the deposition of nanoparticles but also enhance their dispersion in a solution [8,9]. Moreover, changing the number of chemical functionalities attached to the surface of CNTs can control its electrical behavior. One promising approach is the use of lightweight metal as a reinforcing phase on CNTs matrix. Metal like titanium has excellent physical properties such as lightweight, corrosion resistance, and high strength which can be oxidized to produce titanium dioxide ( $\text{TiO}_2$ ) [10].  $\text{TiO}_2$ -anatase could be considered as a supporting nanomaterial due to its semiconducting properties [11].

Several studies have emphasized the benefits resulting in the combination of CNTs-anatase-TiO<sub>2</sub> nanocomposites of their potential properties [12–15] owing to thermodynamic stability and non-destructive of TiO<sub>2</sub> and therefore better their properties to meet exceptional demands in several applications (solar energy and optoelectronics). The anatase-TiO<sub>2</sub> phase has remarkable photocatalytic activity owing to its greater mobility electron carrier ( $80 \text{ cm}^2\text{V}^{-1}\text{s}^{-1}$ ) which are approximately 90 times rapid compare to the rutile phase [16]. Purifying CNTs through acid treatment and synthesizing CNTs-TiO<sub>2</sub> nano-composites using several techniques have been reported [9,11,17–19].

In view of the above, we have synthesized MWCNTs-TiO<sub>2</sub> nano-composites with different concentrations of TiO<sub>2</sub> (~15 and ~20 at %) by a simple hydrothermal technique to enhance the electronic and electrical structure of MWCNTs. The MWCNTs-TiO<sub>2</sub> electronic, structure, and electrical behaviors were examined using different research techniques.

## **5.2. Methodology**

### **5.2.1. Synthesis of MWCNTs**

Chemical vapor decomposition (CVD) [20] techniques were used to prepare MWCNTs. In the CVD process, C<sub>2</sub>H<sub>2</sub> (acetylene - carbon source) and C<sub>10</sub>H<sub>10</sub>Fe (ferrocene - catalyst) were used to prepare MWCNTs in a horizontal tube furnace. A quartz boat of ferrocene was fed in the center of a quartz tube. An Argon (Ar) gas was introduced to flow through the furnace at a heating temperature rate of  $10^\circ\text{C min}^{-1}$ . Acetylene was then introduced alongside with N<sub>2</sub> as the temperature increases to  $900^\circ\text{C}$ . The flow of acetylene was stopped after a reaction time of 60 min but the N<sub>2</sub> was left flowing through the furnace. The boat was taken out of the furnace after it was left to cool to room temperature and MWCNTs were obtained. The purification of MWCNTs was employed using the method described in the previous study. MWCNTs were

acid-treated in a 60mL of mixture 1:3 volume ratio (HNO: H<sub>2</sub>SO<sub>4</sub>) at 100 °C for 5 hours. The content (mixture) was cooled, filtered, and washed with distilled water. Moreover, the content was dried at 80 °C for 15 hours and a purified form was obtained.

### **5.2.2. Synthesis of MWCNTs-TiO<sub>2</sub> nanocomposites**

The hydrothermal process was employed to prepare MWCNTs:TiO<sub>2</sub>. 10 mg of MWCNTs was dispersed in water and the purchased TiO<sub>2</sub> (Sigma-Aldrich (Pty) Ltd) was added at different concentrations (Ti-15 at% and Ti-20 at %) to the suspension. The solution was sonicated for 15 min and thereafter, heated on a hot plate at 80°C for 5 hours. An Ar flow was introduced across the surface of the suspension while heating to speed up the vaporization of water. Afterward, the samples were kept in an oven to dry overnight at 100°C to prevent CNTs from being oxidized in the presence of oxygen at a higher temperature. Furthermore, the samples were deposited on a silicon substrate using a drop cast method and were air-dried overnight prior to analysis.

### **5.2.3. Characterization**

Characterization of TiO<sub>2</sub>, MWCNTs, and MWCNTs-TiO<sub>2</sub> nano-composites were carried out using Field emission scanning electron microscopy (FE-SEM) of model Jeol JEM 2100 coupled with Energy-dispersive X-ray spectroscopy (EDS) for the study of morphology and chemical impurities, X-ray diffraction (XRD) of model Rigaku Smartlab X-ray diffractometer and wavelength ( $\lambda$ ) of 0.154 nm with Cu  $K_{\alpha}$ -line radiation was used for the study of crystalline structure, Raman spectroscopy of model Horiba scientific XploRA with laser light excitation energy ( $E_{ex} = 2.41$  eV) at 532 nm to study the degree of hybridization, X-ray photoemission spectroscopy (XPS) of model KRATOS-SUPRA spectrometer with base pressure ( $1.2 \times 10^{-9}$  Torr) and monochromatic Al  $K_{\alpha}$  radiation possessing excitation energy ( $h\nu = 1486.6$  eV) and X-ray absorption near-edge spectroscopy (XANES) for the study of electronic and chemical

bonding properties. The current-voltage relationship was measured with silver paste as conducting electrodes using Keithley 6487 with voltage sweep ranging from -1 to 1 for the study of electrical conductivity, ferroelectric, and memristive behavior. All characterizations were done at room temperature.

## **5.3. Result and discussion**

### **5.3.1. Field emission-scanning electron microscopy (FE-SEM)**

The FE-SEM image of TiO<sub>2</sub>, MWCNTs, and MWCNTs-TiO<sub>2</sub> nano-composites are shown in Figure 5.1 (a), (b) and (c) respectively. Figure 5.1 (a) and (b) displayed a typical spherical and tube-like shape, respectively. Figure 5.1 (c) shows the homogenous distribution of TiO<sub>2</sub> agglomeration on the MWCNTs surface. The agglomeration is due to more TiO<sub>2</sub> on the MWCNTs surface [21]. The aggregation of TiO<sub>2</sub> over MWCNTs surface implies that MWCNTs support the deposition and growth of TiO<sub>2</sub> and also confirming a good contact between MWCNTs and TiO<sub>2</sub>. These good connections between MWCNTs and TiO<sub>2</sub> can be due to the advantage of electron transfer. Figure 5.1 (d) shows the EDS spectra of MWCNTs:TiO<sub>2</sub> nano-composites. The spectra show a high level of carbon, low level of oxygen, and titanium, indicating that there is no impurity contained in the nanocomposites material.

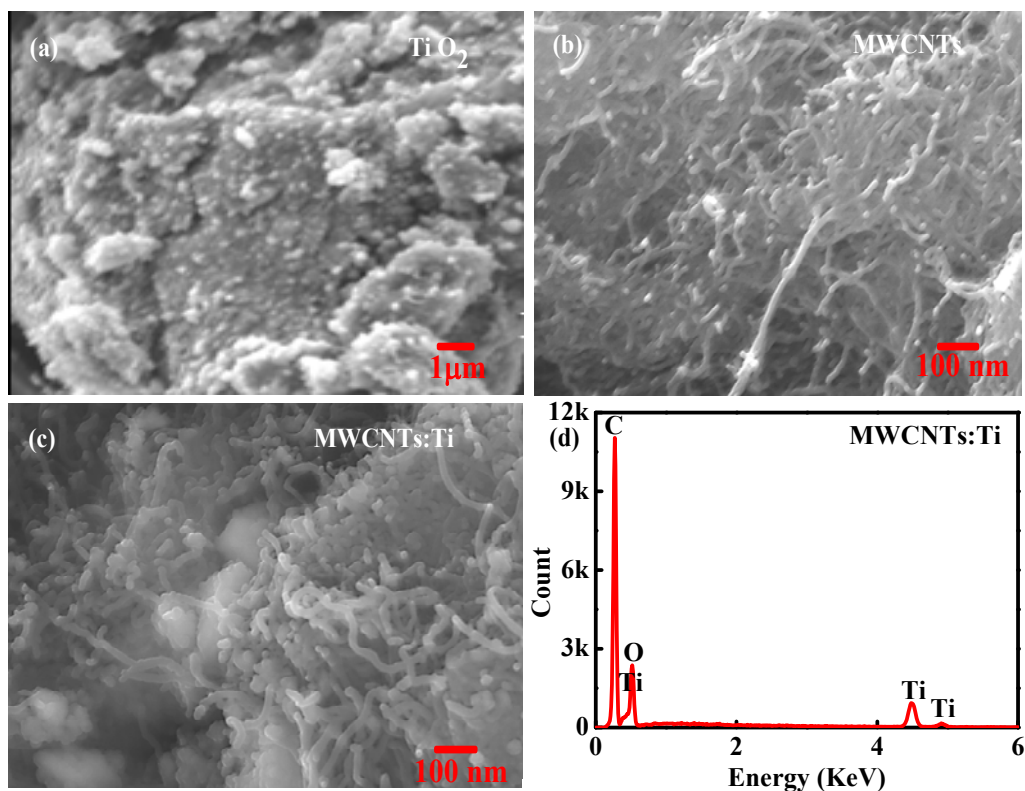


Figure 5.1. (a), (b), (c) SEM images of  $\text{TiO}_2$ , MWCNTs and MWCNTs- $\text{TiO}_2$  nanocomposite (d) EDS spectra for MWCNTs: $\text{TiO}_2$  nanocomposite.

### 5.3.2. X-Ray diffraction (XRD) patterns

Figure 5.2 shows the XRD patterns of  $\text{TiO}_2$ , MWCNTs, and MWCNTs- $\text{TiO}_2$  nano-composites. In the case of MWCNTs, a broad diffraction peak  $2\theta$  is observed at  $25.9^\circ$  corresponding to (002) plane of graphitic structure and a less intense peak at  $43.2^\circ$  corresponding to (100) plane. These peaks match with standard graphite carbon (JCPD 75-1621) [22]. The XRD pattern of  $\text{TiO}_2$  shows characteristic peaks  $2\theta$  at (101), (103), (004), (112), (200), (105), (211) (213) (204) (116) (220) and (215) corresponding to  $25.3^\circ$ ,  $37.1^\circ$ ,  $37.9^\circ$ ,  $38.7^\circ$ ,  $48.1^\circ$ ,  $54.2^\circ$ ,  $55.3^\circ$ ,  $62.6^\circ$ ,  $62.9^\circ$ ,  $68.9^\circ$ ,  $70.3^\circ$  and  $75.3^\circ$  anatase phase [11]. MWCNTs- $\text{TiO}_2$  (15 at %) XRD pattern shows the same peaks as  $\text{TiO}_2$ , while that of MWCNTs- $\text{TiO}_2$  (20 at %) shows the disappearance of (103), (112), (105), (213) and (116) peaks. It was also observed that the (002) plane was overlapped by (101) and there is a disappearance of (100) carbon peak. This may be due to

much percentage of TiO<sub>2</sub> in the nano-composites. Although, the presence of MWCNTs was later confirmed by Raman spectroscopy.

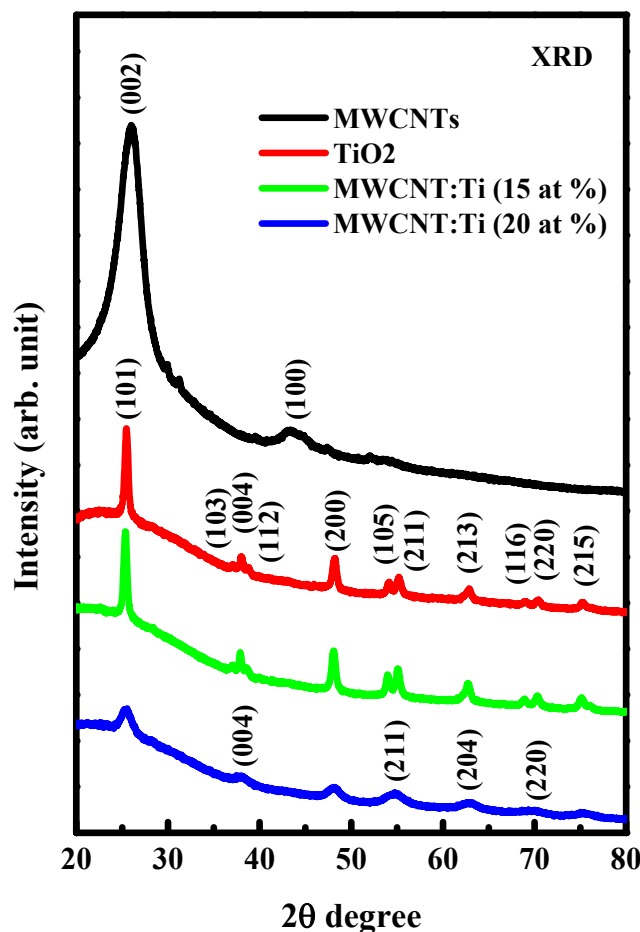


Figure 5.2. XRD spectra for MWCNTs, TiO<sub>2</sub>, and MWCNTs-TiO<sub>2</sub> nanocomposites.

The crystallite size ( $D$ ) was calculated by Scherrer's equation ( $D = k\lambda/\beta\cos\theta$ ) [20], which was described in chapter three. The crystallite size of TiO<sub>2</sub> is 18.10, MWCNTs-TiO<sub>2</sub> (~15 at %) is 18.26 nm and MWCNTs-TiO<sub>2</sub> (~20 at %) is 6.08 nm suggesting that MWCNTs allows the growth of TiO<sub>2</sub> in MWCNTs-TiO<sub>2</sub> which is in agreement with FE-SEM result.

### 5.3.3. Raman spectroscopy

Raman spectroscopy provides information on the degree of hybridization and crystal disorder. The Raman spectrum and its de-convolution are shown in Figures 5.3 and 4.4 respectively.

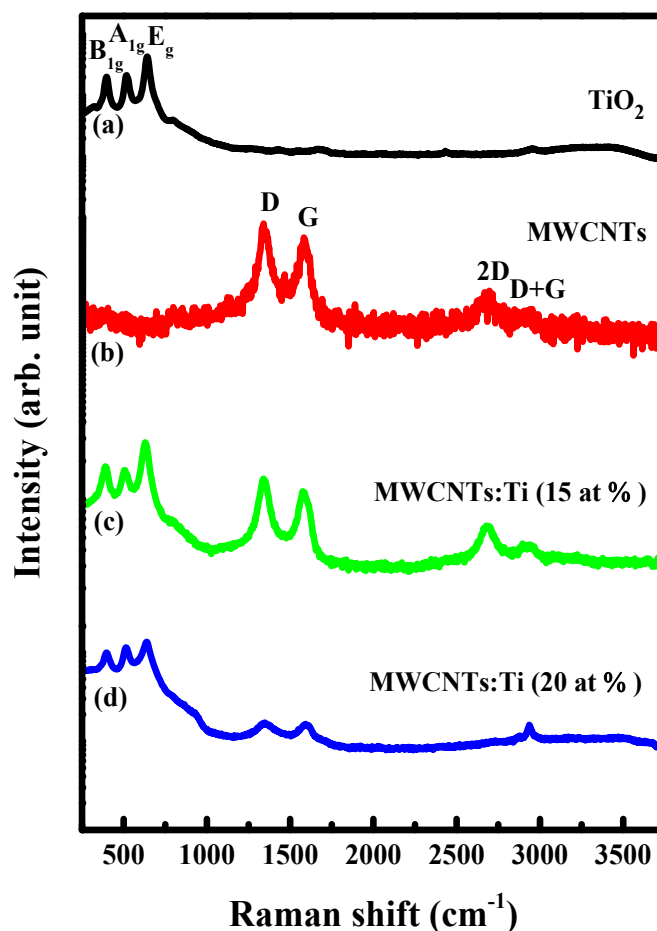


Figure 5.3. Raman spectra for MWCNTs, TiO<sub>2</sub> and MWCNTs-TiO<sub>2</sub> nanocomposites

From Figure 5.3, different peaks at 396, 516 and 636 cm<sup>-1</sup> correspond to B<sub>1g</sub>, A<sub>1g</sub>, and E<sub>g</sub> band of the TiO<sub>2</sub> anatase phase, respectively [23,24]. It can be seen that MWCNTs consist of four main peaks at 1345, 1585, 2664, and 2912 cm<sup>-1</sup> which are assigned to D, G, 2D, and D+G mode, respectively as expected for graphitic carbon [5]. The D and G mode is an indication of disordered and ordered structure, respectively. The 2D mode is an overtone of D mode which occurs due to the second-order vibration process and D+G mode occurs due to the vibration of the D and G mode. These peaks are also observed in MWCNTs-TiO<sub>2</sub> nano-composites with additional three peaks associated with anatase TiO<sub>2</sub> [23]. Moreover, these changes in MWCNTs Raman spectra are due to the deposition of TiO<sub>2</sub> on the surface of MWCNTs. Also, the reduction and slight shift of B<sub>1g</sub>, A<sub>1g</sub>, and E<sub>g</sub> mode in MWCNTs-TiO<sub>2</sub> (~15 at %) nano-

composites Raman shift can be due to increasing in crystallite size of anatase TiO<sub>2</sub> nanoparticles [18]. The MWCNTs-TiO<sub>2</sub> (20 at%) shows further reduction and slight broadening peaks indicating a reduction in the crystallite size [23]. These variations in crystalline size are in agreement with the XRD result.

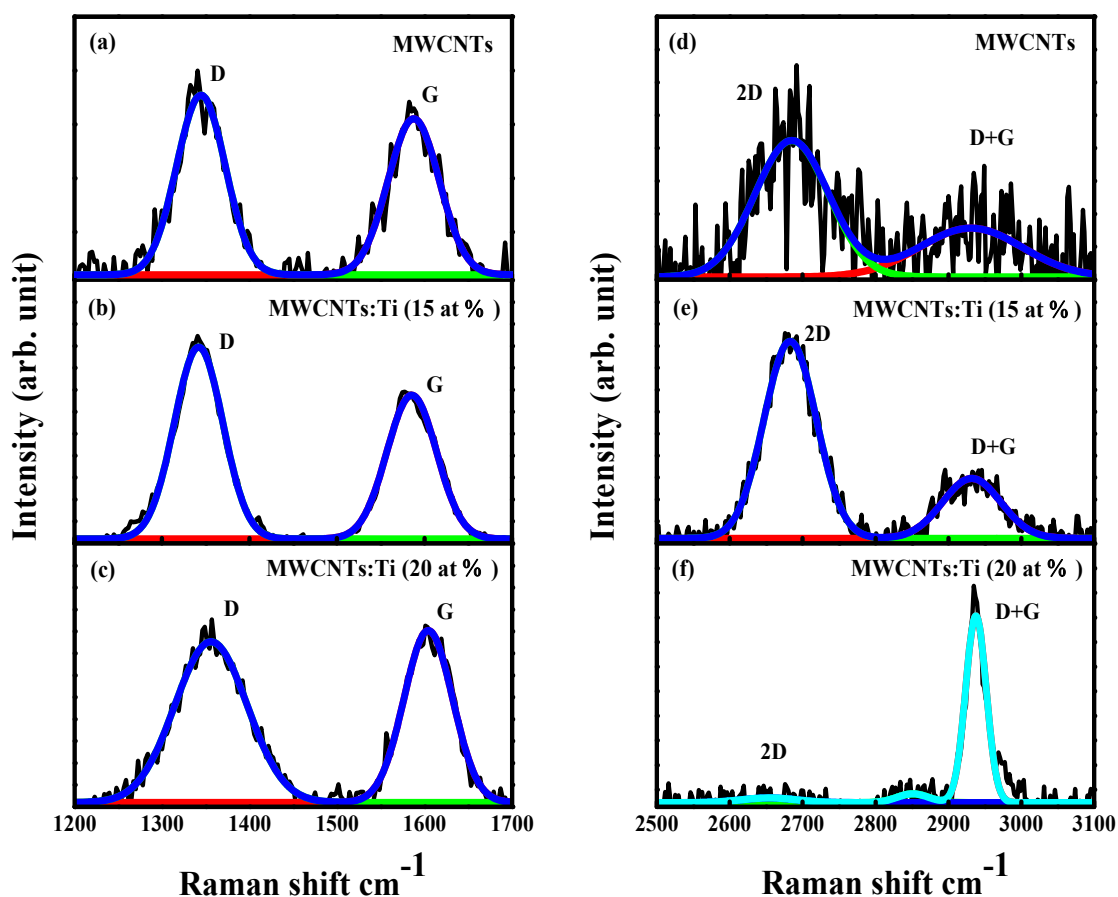


Figure 5.4. De-convolution of Raman spectra for MWCNTs, TiO<sub>2</sub> and MWCNTs-TiO<sub>2</sub> nanocomposites

The values obtained from the de-convolution of MWCNTs and MWCNTs-TiO<sub>2</sub> nanocomposite are displayed in Figure 5.4. Both MWCNTs and MWCNTs-TiO<sub>2</sub> nanocomposites are de-convoluted into four Gaussian peaks corresponding to D, G, 2D, and D+G band and their peak positions (x), intensities (y), widths ( $\omega$ ) and ratio ( $I_D/I_G$ ) of D and G band are tabulated in Table 5.1. It is observed that there is an increase in the  $\omega$  of D band and a slight



shift of D and G peaks for MWCNTs:TiO<sub>2</sub> (~20 at%), whereas G band remains unchanged. These observations indicate a more graphitic structure corresponding to an increase in sp<sup>2</sup> hybridization. This observation was denied in MWCNTs-TiO<sub>2</sub> (~15 at %) Raman spectra resulting in an enhancement of sp<sup>3</sup> hybridization. Also, this effect is seen in the calculated intensity ratios of the D and G band. The relative peak intensity ratio gives information about the degree of hybridization of MWCNTs and MWCNTs:Ti nanocomposites [25,26]. The I<sub>D</sub>/I<sub>G</sub> ratio decreases from 1.3 for MWCNTs to 0.9 for MWCNT-TiO<sub>2</sub> (~15 at %) and increases to 1.7 for MWCNT-TiO<sub>2</sub> (~20 at %). The decrease/increase in the I<sub>D</sub>/I<sub>G</sub> ratio indicates a decrease/increase in sp<sup>2</sup> hybridization.

The change observed generally in  $x$ ,  $y$ , and  $\omega$  for nanocomposites correspond to the improvement of surface electric charge of the oxides in them [14]. Therefore, there is an improvement in the surface charge of the oxides in MWCNTs-TiO<sub>2</sub> owing to the fact that the atoms of Ti substituted atoms of carbon in MWCNTs as seen later in XPS quantification results (Table 5.2). This improvement induces a potential electronic change of  $n$  to  $\pi^*$  and  $\pi$  to  $\pi^*$  of MWCNTs and among the  $n$ -orbit of the oxygen species of MWCNTs and TiO<sub>2</sub> [14].

Table 5.1: Parameters obtained from the deconvolution of Raman spectra for MWCNTs and MWCNTs-TiO<sub>2</sub> nanocomposites.

Nanomaterials	First-order Raman spectra						Second-order Raman spectra						Ratio
	D Peak			G Peak			2D Peak			D+G Peak			
	Int.	x1	$\Delta\omega$	Int.	x2	$\Delta\omega$	Int.	x3	$\Delta\omega$	Int.	x4	$\Delta\omega$	
MWCNTs	2.1	1345	83	1.6	1586	74	0.3	2664	79	0.1	2912	87	1.3
MWCNTs-TiO <sub>2</sub> (15 at %)	5.2	1342	51	5.7	1584	64	2.7	2682	85	1.0	2922	90	0.9
MWCNTs-TiO <sub>2</sub> (20 at %)	6.6	1355	111	3.7	1604	64	0.3	2732	70	1.9	2938	37	1.7

### 5.3.4. X-ray photoelectron spectroscopy (XPS)

The electronic structure and chemical properties of TiO<sub>2</sub>, MWCNTs, and MWCNTs:TiO<sub>2</sub> nano-composites are analyzed using XPS and are presented in figures 5.5, 5.6, 5.7, and 5.8. The composition and quantification of C, O, and Ti in MWCNT and MWCNTs-TiO<sub>2</sub> nanocomposites were also analyzed and are tabulated in Table 5.2. It is observed that the values in the Table show an increase in Ti and O content with a decrease in carbon content for MWCNTs-TiO<sub>2</sub> nanocomposites. This variation implies that the atoms of carbon have been substituted by the atoms of Ti and O.

Table 5.2: XPS compositional and quantificational analysis of silicon (Ti), carbon (C) and oxygen (O)

Nanomaterials	XPS compositional and quantificational of nanomaterials		
	Ti at %	C at %	O at %
TiO <sub>2</sub>	33	--	66
MWCNTs	--	98	02
MWCNTs-TiO <sub>2</sub> (15 at %)	15	45	40
MWCNTs-TiO <sub>2</sub> (20 at %)	20	26	54

Figure 5.5 displays the full XPS spectrum showing several peaks for TiO<sub>2</sub>, MWCNTs, and MWCNTs:TiO<sub>2</sub> nano-composites. C 1s, O 1s, and Ti 2p configurations were extracted from figure 5.5 and are presented in figure 5.6, 5.7, and 5.8. The extracted peaks were de-convoluted to know their peaks positions and the types of bonds formed in the nanomaterials.

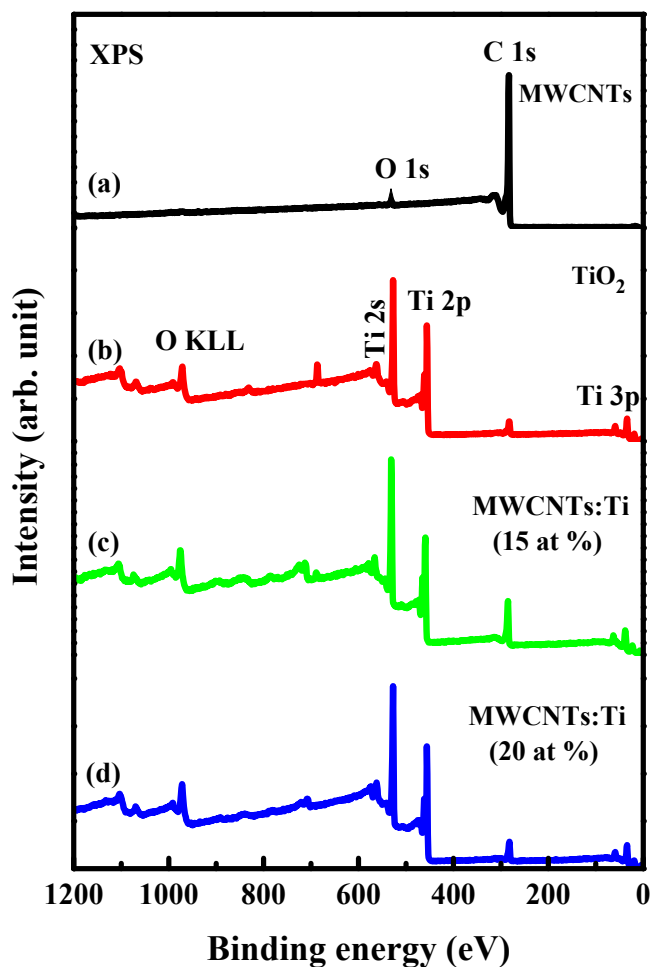


Figure 5.5. XPS spectra for MWCNTs, TiO<sub>2</sub>, and MWCNTs-TiO<sub>2</sub> nanocomposites.

In order to understand the bonding structures and electronic properties, we have de-convoluted the C 1s, O 1s and Ti 2p XPS spectra of MWCNT and MWCNTs-TiO<sub>2</sub> nano-composites with several Gaussian fits as seen in figures 5.6, 5.7 and 5.8 and their peak intensities (Int.), positions (x) and width ( $\Delta\omega$ ) are presented in Table 5.3. For analyzing the chemical nature of carbon, we study the high-resolution XPS spectrum of the C 1s, O 1s, and Ti 2p regions. In the case of C 1s XPS spectra for MWCNTs (figure 5.5), three major peaks were observed at 283.5 eV/ 284.3 eV and 288.8 eV corresponding to C=C and C=O bonds respectively [27]. In O 1s spectra of MWCNTs, the peaks at 530.5 and 531.9 eV is assigned to C=O/O=C-OH and C-OH bonding, respectively [19].

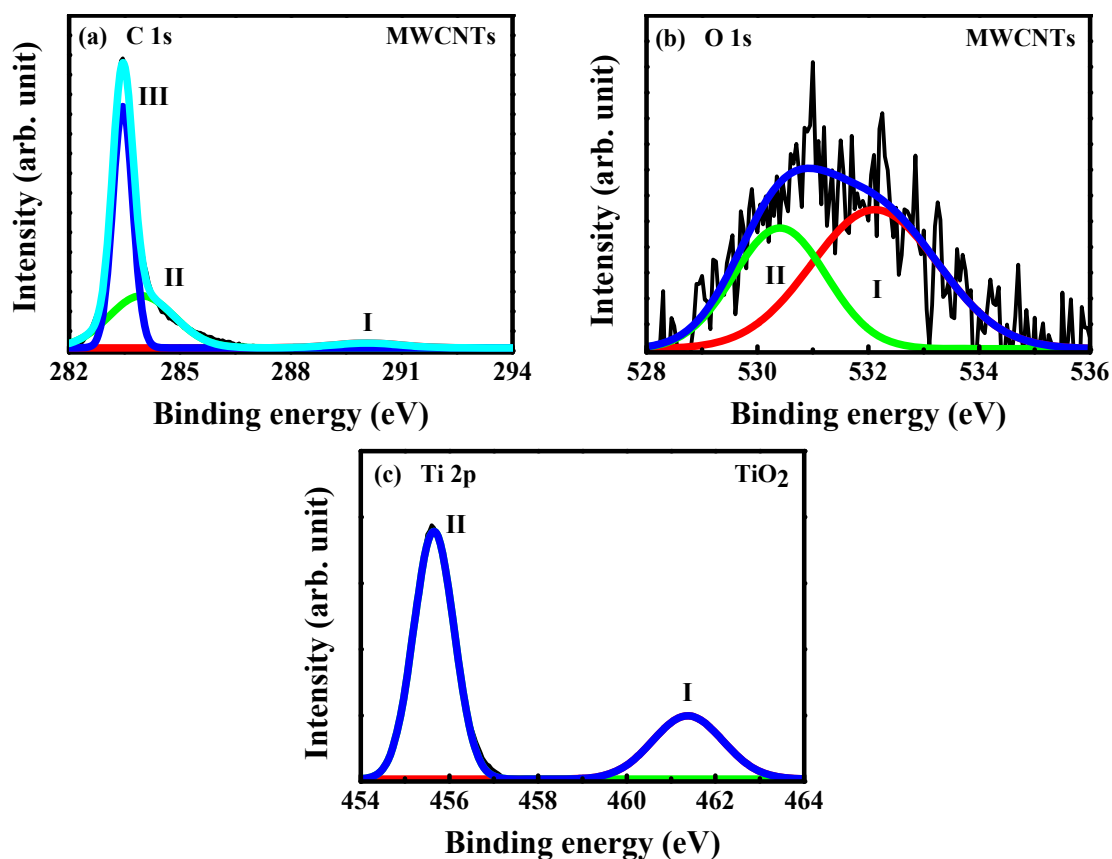


Figure 5.6. De-convolution of C1s and O1s XPS spectra for MWCNTs and Ti 2p spectra for TiO<sub>2</sub>.

The de-convolution of C 1s, O 1s, and Ti 2p for MWCNTs-TiO<sub>2</sub> nano-composites (Figure 5.7 and 5.8) pointed out different carbon, oxygen, and titanium species in the MWCNTs-TiO<sub>2</sub> nano-composites. The peaks located in C 1s spectra of MWCNTs shift to higher/lower binding energy at 284.6/281.9, 285.4/283.4, and to lower binding energy at 287.5/285.6 eV for MWCNTs with Ti content 15/20 at%, respectively. This shift implies that TiO<sub>2</sub> has impacted the electronic structure of MWCNTs. The peak at 285.4 is assigned to C-O. The O1s peaks also shift towards higher/lower binding energy (see Table 5.3) corresponding to Ti-O and Ti-O-H bond, respectively [28,29]. It is obvious that C-O, and Ti-O bonds (C 1s and O 1s) in C 1s and O 1s XPS spectra led to the good connection between MWCNTs and TiO<sub>2</sub> indicating

Ti–O–C bonds are present [19,28], which is due to esterification reaction with hydroxyl groups in MWCNTs:TiO<sub>2</sub> nano-composites [30].

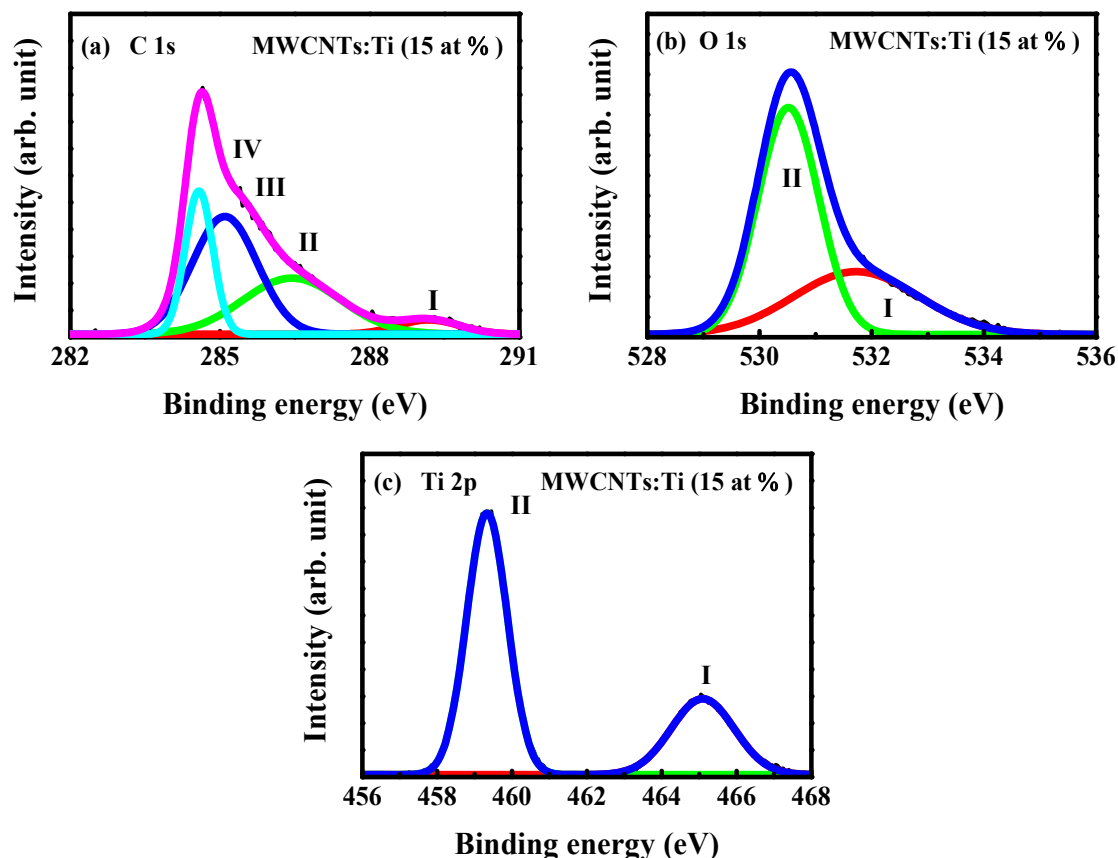


Figure 5.7. De-convolution of C1s, O1s and Ti 2p XPS spectra for MWCNTs functionalized with 15 at % of TiO<sub>2</sub>.

From figure 5.7 (c) and 5.8 (c), the de-convoluted Ti 2p configuration shows two peaks for MWCNTs-TiO<sub>2</sub> nano-composites. These peaks shift to the higher/lower binding energy for MWCNTs-TiO<sub>2</sub> (15 at %)/MWCNTs-TiO<sub>2</sub> (20 at %), respectively when compared to TiO<sub>2</sub>. These peaks are observed at 459.30/455.60 and 465.10/461.43 eV corresponding to Ti 2p<sub>3/2</sub> and Ti 2p<sub>1/2</sub> with constant core-shell spin-orbit splitting of 5.8 eV. This spin-orbit splitting indicates the presence of Ti<sup>4+</sup> oxidation state [22,27]. Furthermore, the observed change in the

binding energies of Ti 2p is due to the fact that electrons transferring through Ti–O–C bonds changed the electron density of  $Ti^{4+}$  state in  $TiO_2$  [19].

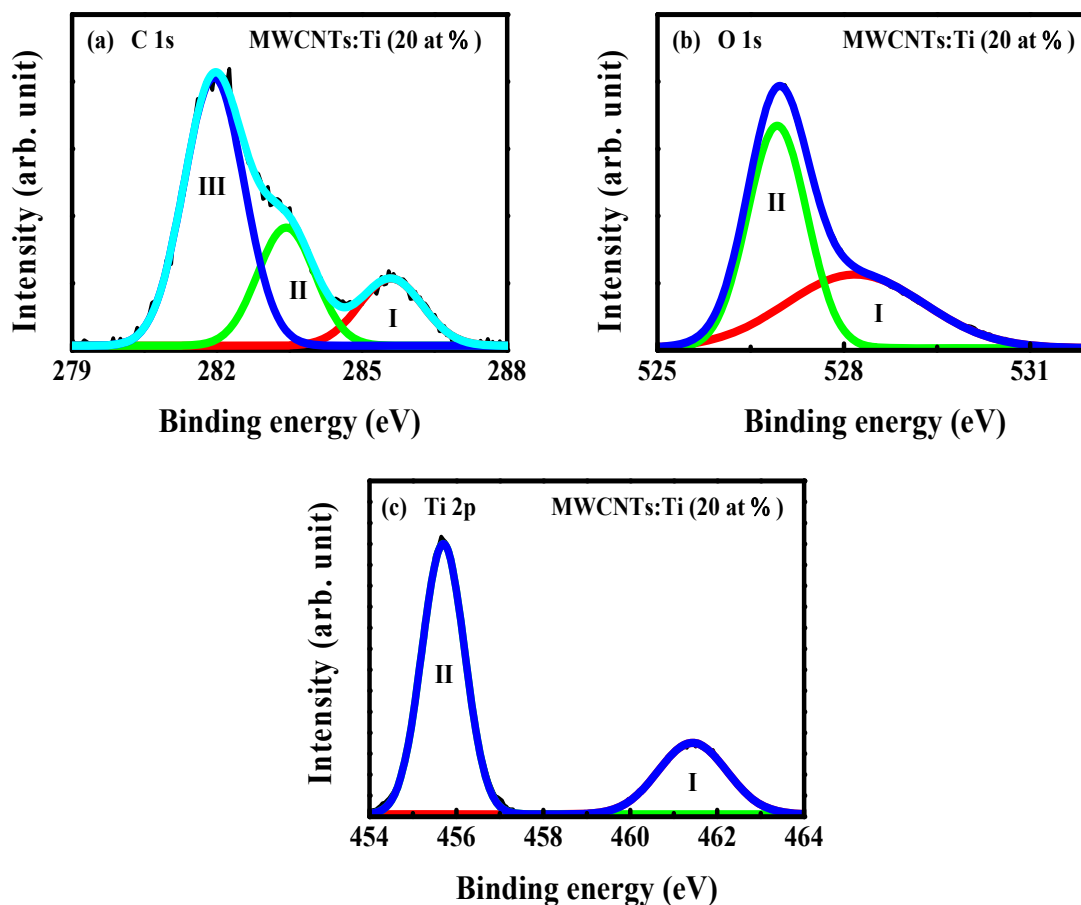


Figure 5.8. De-convolution of C1s, O1s and Ti 2p XPS spectra for MWCNTs functionalized with 20 at % of  $TiO_2$ .

Table 5.3: Parameters obtained from the de-convolution of C 1s, O 1s, and Ti 2p XPS spectra.

Nanomaterials	C 1s XPS								
	Peak I			Peak II			Peak III		
	Int.	x1	$\Delta\omega$	Int.	x2	$\Delta\omega$	Int.	x3	$\Delta\omega$
MWCNTs	3.1	288.8	6.5	1.3	284.3	2.3	2.1	283.5	0.7
MWCNTs-TiO <sub>2</sub> (15 at %)	0.4	287.5	3.3	0.9	285.4	1.7	0.5	284.6	0.6
MWCNTs-TiO <sub>2</sub> (20 at %)	0.2	285.6	1.3	0.3	283.4	1.2	0.6	281.9	1.2

Nanomaterials	O 1s XPS						Ti 2p XPS	
	Peak I			Peak II			Peak I	Peak II
	Int.	x1	$\Delta\omega$	Int.	x2	$\Delta\omega$	x1	x2
MWCNTs	0.7	531.9	2.2	2.6	530.5	2.7	--	--
MWCNTs-TiO <sub>2</sub> (15 at %)	2.6	531.7	2.5	3.8	530.4	1.1	465.1	459.3
MWCNTs-TiO <sub>2</sub> (20 at %)	3.8	528.2	2.5	3.9	526.9	0.9	461.4	455.6
TiO <sub>2</sub>	--	--	--	--	--	--	461.4	455.6

### 5.3.5. X-ray absorption near edge structure (XANES) spectroscopy

XANES is an effective tool that was used in examining the electronic, structural, and chemical information of TiO<sub>2</sub>, MWCNTs, and MWCNTs:TiO<sub>2</sub> nanocomposites. The C *K*-edge, O *K*-edge, and Ti *L*<sub>3,2</sub>-edge XANES spectra of TiO<sub>2</sub>, MWCNTs, and MWCNT:TiO<sub>2</sub> nanocomposites are shown in figures 5.9, 5.10 and 5.11. The C *K*-edge shows similar spectra for the nanomaterial as shown in the figure 5.9. From the same figure, the spectra display  $\pi^*$  (C-C  $sp^2$ ) and  $\sigma^*$  structures at 286 and 293.0 eV, respectively for MWCNTs [31] and the peak located at 287.5 eV is assigned to C-O/C-H bonding, which was as a result of the change in  $sp^3$  hybridization or metal bonding to MWCNTs lattice [32,33].

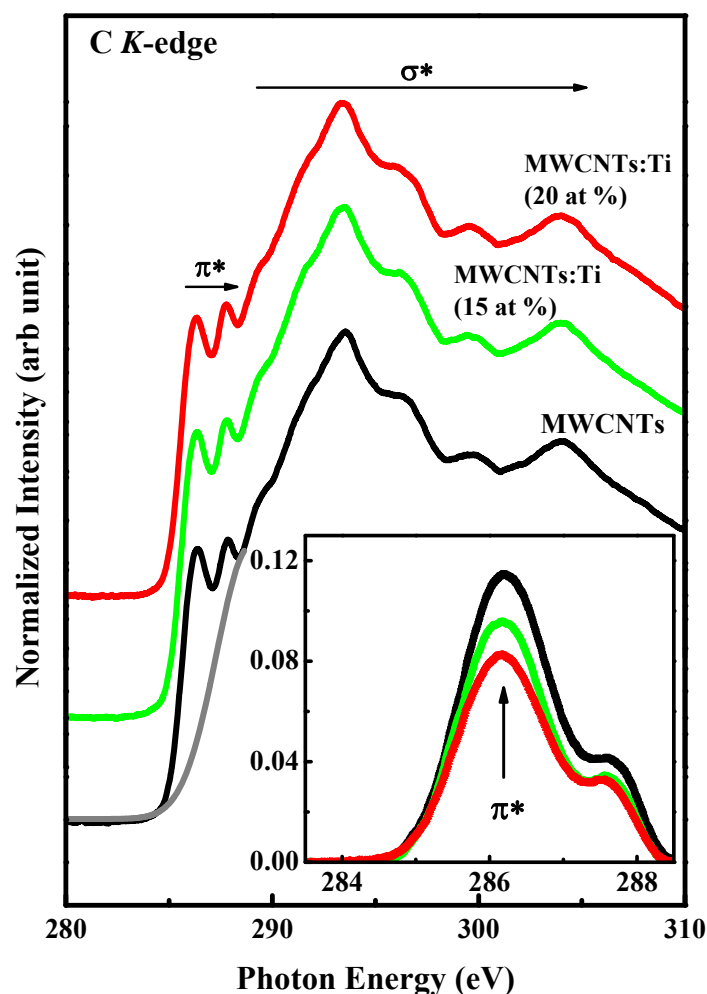


Figure 5.9. C K-edge XANES spectra for MWCNTs and MWCNTs functionalized with 15 and 20 at % concentration of TiO<sub>2</sub>.

Figure 5.10 shows the XANES spectrum of O K-edge for TiO<sub>2</sub>, MWCNTs, and MWCNTs:Ti nanocomposites. The O K-edge gives information on how TiO<sub>2</sub>, MWCNTs, and MWCNTs:Ti nanocomposites has been oxidized (degree of oxidation). The spectra display  $\pi^*$  and  $\sigma^*$  structures. From  $\pi^*$  structure, a double  $\pi^*$  structure is observed at 528.5 eV and 530.5 eV which are signature of C=O bond. The  $\sigma^*$  structure at 538-544 eV is assigned to C-O and O-H bonding [34]. The  $\pi^*$  and  $\sigma^*$  structures initiated from carboxylic and hydroxyl groups, respectively. Other peaks are observed at 533 eV to 535 eV are physical absorption of O<sub>2</sub> and can be assigned to the splitting of  $t_{2g}$  and  $e_g$  bands owing to effects of crystal field [35]. This



physical absorption is predicted to occur during the preparation of MWCNTs and MWCNTs:TiO<sub>2</sub> nanocomposites. Although, the range 532 to 536 eV in figure 4.10 indicates the presence of O 2*p* to Ti 3*d* states [35]. The *t*<sub>2*g*</sub> and *e*<sub>g</sub> splitting is very sensitive to the degree of hybridization and coordination number. Furthermore, the presence of O 2*p* hybridization states to Ti 4*sp* bands is due to 540 and 546 eV peaks observed, which are even more sensitive to long-range order [36].

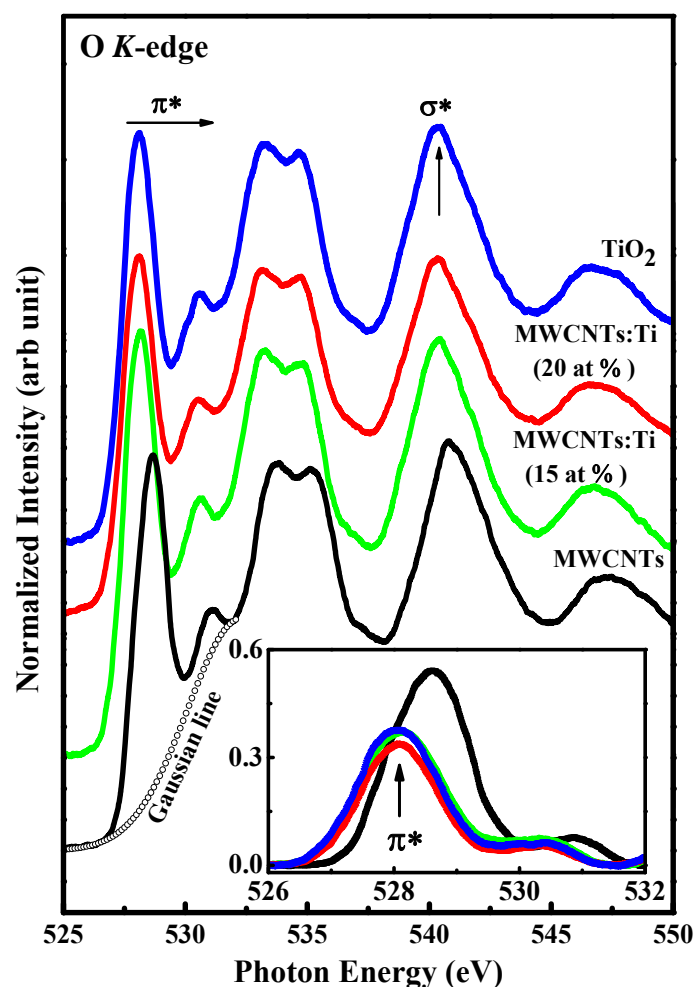


Figure 5.10. O K-edge XANES spectra for TiO<sub>2</sub>, MWCNTs, and MWCNTs functionalized with 15 and 20 at % concentration of TiO<sub>2</sub>.

Figure 5.11 displays the XANES spectrum of Ti *L*<sub>3,2</sub>-edge for TiO<sub>2</sub> and MWCNTs:Ti nanocomposites. The figure is considered to be a compound structure, owing to the merging

of the interaction of atoms and the effects of the crystal field [36]. The Ti  $L_{3,2}$ -edge shows typical  $L_3$ -edge and  $L_2$ -edge regions. These regions are located 456.4 and 458.6 eV and 461.6 and 470.1 eV and are assigned to O  $2p_{3/2}$  and O  $2p_{1/2}$  Ti  $3d$  bands respectively. The Ti  $3d$  band are been split into Ti  $t_{2g}$  and  $e_g$  bands by the effect of crystal field. Considering the inset in figure 5. 11, a decrease in intensity with an increase in the content of Ti is observed. This variation indicates that Ti atoms have substituted oxygen and/or carbon in the MWCNTs:TiO<sub>2</sub> nanocomposites.

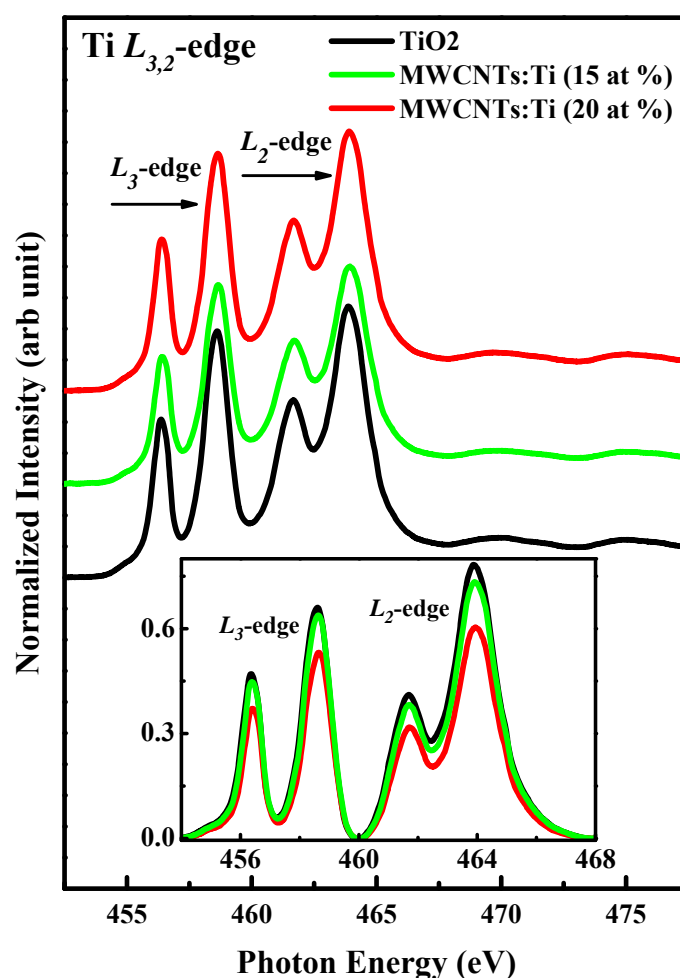
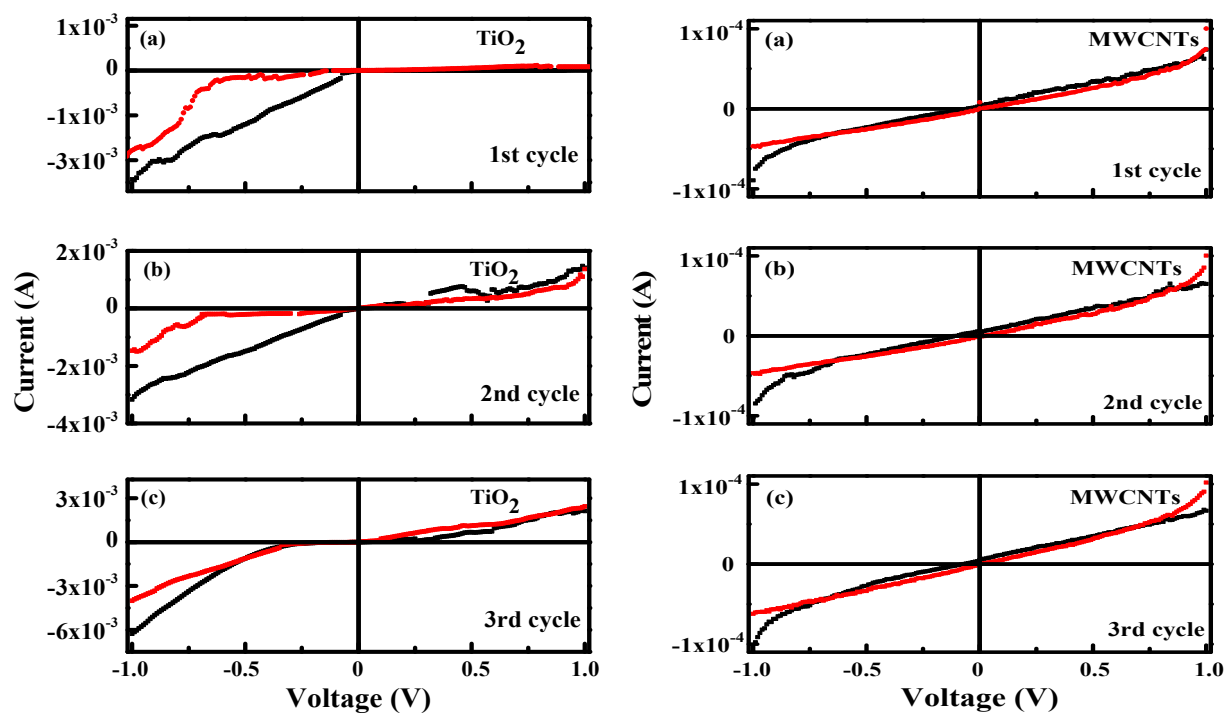
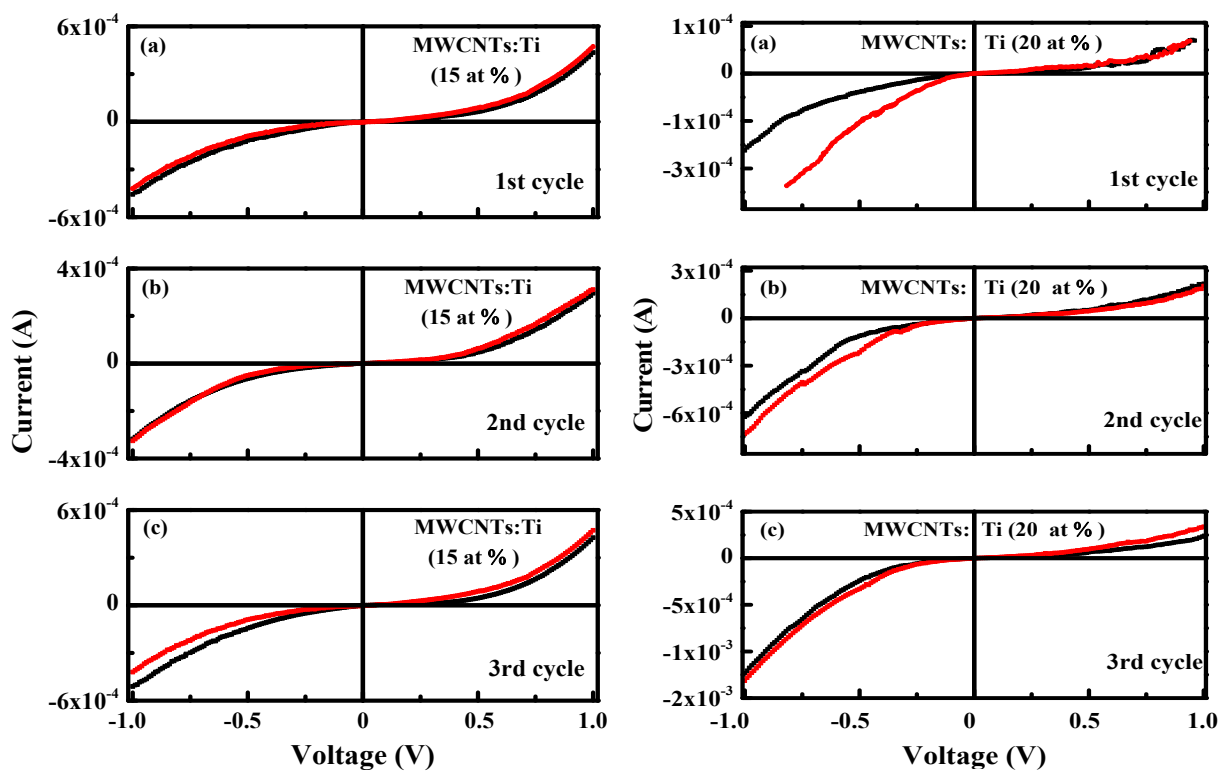
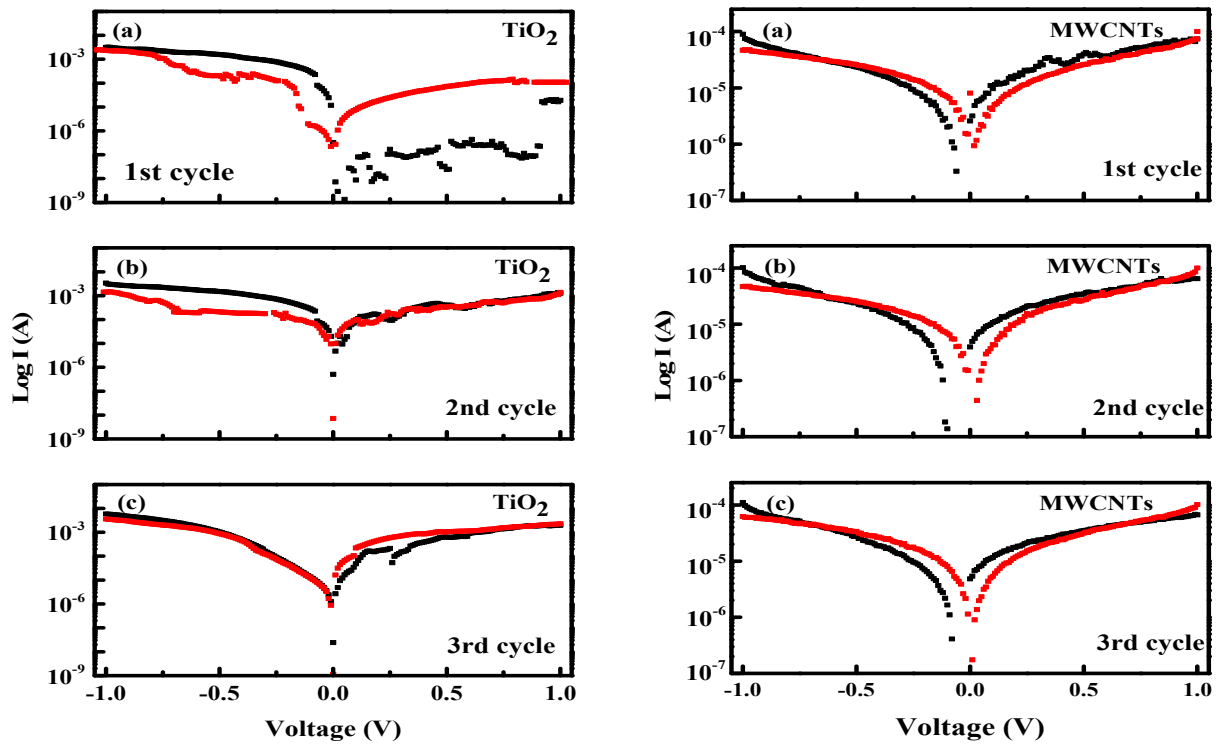
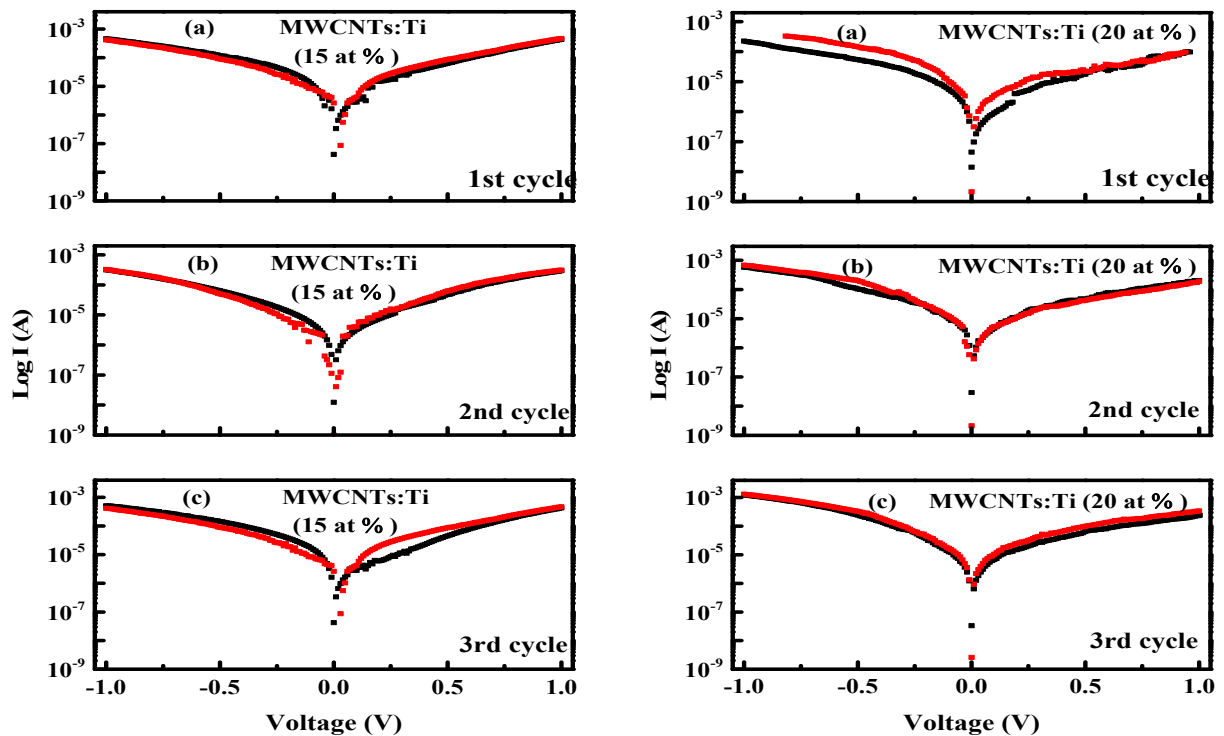


Figure 5.11. Ti  $L_{2,3}$ -edge XANES spectra for TiO<sub>2</sub> and MWCNTs functionalized with 15 and 20 at % concentration of TiO<sub>2</sub>.

### 5.3.6. Current-voltage (I-V) measurement

Figures 5.12, 5.13 and 5.14, 5.15 shows the I-V characteristic curves and I-V log plot. respectively of TiO<sub>2</sub>, MWCNTs, and MWCNTs-TiO<sub>2</sub> nano-composites. The I-V data was recorded from a voltage source ranging from -1 to +1 volt with an automatic voltage sweep option in three cycles for each as shown in the figures. In figures 5.12 and 5.13, a conducting structure is observed for MWCNTs whereas a semiconducting structure is observed for MWCNTs-TiO<sub>2</sub> nano-composites. Also, an increase in the conductivity of MWCNTs-TiO<sub>2</sub> nano-composites is observed compared to MWCNTs indicating that Ti has an impact on the electrical structure of MWCNTs. Although, enhancing the conductivity of MWCNTs was not our aim since the material is highly conducting but it is to improve its memristive capacity. From Figure 5.14 and 5.15, a significant hysteresis loop with an increased conductivity is observed in MWCNTs:TiO<sub>2</sub> nanocomposites. The hysteresis loop is indicative of ferroelectric behavior and the increase in conductivity is due to free electrons in the conduction band. This effect is lower in MWCNTs (see figure 5.14) due to the formation of a conducting structure. Comparing features in Figure 5.15, the hysteresis loop which was observed in MWCNTs with 15 at % content of TiO<sub>2</sub> is higher than that of MWCNTs with 20 at % content of TiO<sub>2</sub> indicating higher charge storage properties and memristive behavior. The electrical features observed in MWCNTs:TiO<sub>2</sub> nanocomposites could be useful for ferroelectric, charge storage, and memristive device applications. Also, It has been reported that conductive films are useful for capacitors and batteries [37].

Figure 5.12 I-V curve for TiO<sub>2</sub> and MWCNTs.Figure 5.13. I-V curve for MWCNTs functionalized with 15 and 20 at % concentration of TiO<sub>2</sub>.

Figure 5.14. I-V log plot for TiO<sub>2</sub> and MWCNTs.Figure 5.15. I-V log plot for MWCNTs functionalized with 15 and 20 at % concentration of TiO<sub>2</sub>.

## 5.4 Conclusion

We have synthesized MWCNTs and MWCNTs-TiO<sub>2</sub> nano-composites using CVD method and hydrothermal process, respectively. Their electronic and electrical structure have been examined with different characterization techniques. It was observed that the electrical structure of MWCNTs transforms from a conductor to a semiconductor due to the introduction of TiO<sub>2</sub> nanoparticles. The nano-composite materials also displayed a pronounced hysteresis loop indicating a ferroelectric, memristive, and charge storage behavior due to Ti<sup>+</sup> transfer in MWCNTs-TiO<sub>2</sub> nano-composites. We, therefore, conclude that these nano-composite materials can be useful for different nano/microelectronic devices, particularly for memristive and charge storage device applications.

## References

- [1] W. Shi *et al.*, “High pressure study of nitrogen doped carbon nanotubes using Raman spectroscopy and synchrotron X-ray diffraction,” *Arab. J. Chem.*, vol. 13, no. 1, pp. 3008-3016, 2018.
- [2] A. Kumar, K. Kumar, P. K. Ghosh, and K. L. Yadav, “MWCNT/TiO<sub>2</sub> hybrid nano filler toward high-performance epoxy composite,” *Ultrason. Sonochem.*, vol. 41, pp. 37–46, 2018.
- [3] R. H. Baughman, A. A. Zakhidov, and W. A. de Heer, “Carbon Nanotubes — the Route Toward,” *Sci. compass*, vol. 787, no. 2002, pp. 787–792, 2012.
- [4] W. Bauhofer and J. Z. Kovacs, “A review and analysis of electrical percolation in carbon nanotube polymer composites,” *Compos. Sci. Technol.*, vol. 69, no. 10, pp. 1486–1498, 2009.
- [5] S. C. Ray, S. K. Bhunia, A. Saha, and N. R. Jana, “Electric and ferro-electric behaviour of polymer-coated graphene-oxide thin film,” *Phys. Procedia*, vol. 46, no. 19, pp. 62–70, 2013.
- [6] G. I. Meijer *et al.*, “Who Wins the Nonvolatile Memory Race?,” *Science*, vol. 319, no. 5870, pp. 1625–1626, 2008.
- [7] M. S. . Shaffer, T. Prasse, A. . Windle, J. Sandler, K. Schulte, and W. Bauhofer, “Development of a dispersion process for carbon nanotubes in an epoxy matrix and the resulting electrical properties,” *Polymer (Guildf.)*, vol. 40, no. 21, pp. 5967–5971, 2002.
- [8] H. Dong and K. Lu, “Attaching titania nanoparticles onto shortened carbon nanotubes

- by electrostatic attraction,” *Int. J. Appl. Ceram. Technol.*, vol. 6, no. 2, pp. 216–222, 2009.
- [9] M. H. Haji Jumali, K. M. A. A. Firas, S. Radiman, and A. A. Umar, “Dressing of Mwents with TiO<sub>2</sub> Nanoparticles Using Modified Microwave Method,” *Adv. Mater. Res.*, vol. 364, pp. 228–231, 2011.
- [10] W. L. Johnson, A. Kahl, G. Duan, M. L. Lind, and A. Wiest, “Lightweight Ti-based bulk metallic glasses excluding late transition metals,” *Scr. Mater.*, vol. 58, no. 6, pp. 465–468, 2007.
- [11] S. Delpeux, A. Jitianu, S. Bonnamy, R. Benoit, T. Cacciaguerra, and F. Béguin, “Synthesis and characterization of carbon nanotubes–TiO<sub>2</sub> nanocomposites,” *Carbon N. Y.*, vol. 42, no. 5–6, pp. 1147–1151, 2004.
- [12] G. Li, S. Ciston, K. A. Gray, Y. Yao, and R. M. Lueptow, “Photoreactive TiO<sub>2</sub>/carbon nanotube composites: Synthesis and reactivity,” *Environ. Sci. Technol.*, vol. 42, no. 13, pp. 4952–4957, 2008.
- [13] W. Wang, P. Serp, P. Kalck, C. G. Silva, and J. L. Faria, “Preparation and characterization of nanostructured MWCNT-TiO<sub>2</sub> composite materials for photocatalytic water treatment applications,” *Mater. Res. Bull.*, vol. 43, no. 4, pp. 958–967, 2008.
- [14] Y. Ou, J. Lin, S. Fang, and D. Liao, “MWNT-TiO<sub>2</sub>:Ni composite catalyst: A new class of catalyst for photocatalytic H<sub>2</sub> evolution from water under visible light illumination,” *Chem. Phys. Lett.*, vol. 429, no. 1-3, pp. 199–203, 2006.
- [15] T. Y. Lee, P. S. Alegaonkar, and J. B. Yoo, “Fabrication of dye sensitized solar cell



- using TiO<sub>2</sub> coated carbon nanotubes,” *Thin Solid Films*, vol. 515, no. 12, pp.5131-5135, 2007.
- [16] D. C. Hurum, K. A. Gray, T. Rajh, and M. C. Thurnauer, “Recombination pathways in the degussa P25 formulation of TiO<sub>2</sub>: Surface versus lattice mechanisms,” *J. Phys. Chem. B*, vol. 109, no. 2, pp. 977–980, 2005.
- [17] B. S. Huang, F. Y. Chang, and M. Y. Wey, “An efficient composite growing N-doped TiO<sub>2</sub> on multi-walled carbon nanotubes through sol-gel process,” *J. Nanoparticle Res.*, vol. 12, no. 7, pp. 2503–2510, 2010.
- [18] S. D. Delekar *et al.*, “Structural and Optical Properties of Nanocrystalline TiO<sub>2</sub> with Multiwalled Carbon Nanotubes and Its Photovoltaic Studies Using Ru(II) Sensitizers,” *ACS Omega*, vol. 3, no. 3, pp. 2743–2756, 2018.
- [19] H. Liu, H. Zhang, and H. Yang, “Photocatalytic removal of nitric oxide by multi-walled carbon nanotubes-supported TiO<sub>2</sub>,” *Cuihua Xuebao/Chinese J. Catal.*, vol. 35, no. 1, pp. 66–77, 2014.
- [20] L. A. A. Rodriguez and Di. N. Travessa, “Core/Shell Structure of TiO<sub>2</sub>-Coated MWCNTs for Thermal Protection for High-Temperature Processing of Metal Matrix Composites,” *Adv. Mater. Sci. Eng.*, vol. 2018, 2018.
- [21] S. B. A. Hamid, T. L. Tan, C. W. Lai, and E. M. Samsudin, “Multiwalled carbon nanotube/TiO<sub>2</sub> nanocomposite as a highly active photocatalyst for photodegradation of Reactive Black 5 dye,” *Cuihua Xuebao/Chinese J. Catal.*, vol. 35, no. 12, pp. 2014–2019, 2014.
- [22] V. B. Koli, A. G. Dhodamani, A. V. Raut, N. D. Thorat, S. H. Pawar, and S. D. Delekar,

- “Visible light photo-induced antibacterial activity of TiO<sub>2</sub>-MWCNTs nanocomposites with varying the contents of MWCNTs,” *J. Photochem. Photobiol. A Chem.*, vol. 328, no. May, pp. 50–58, 2016.
- [23] J. Yu, T. Ma, and S. Liu, “Enhanced photocatalytic activity of mesoporous TiO<sub>2</sub> aggregates by embedding carbon nanotubes as electron-transfer channel,” *Phys. Chem. Chem. Phys.*, vol. 13, no. 8, pp. 3491–3501, 2011.
- [24] J. Yu, J. Fan, and B. Cheng, “Dye-sensitized solar cells based on anatase TiO<sub>2</sub> hollow spheres/carbon nanotube composite films,” *J. Power Sources*, vol. 196, no. 18, pp. 7891–7898, 2011.
- [25] A. Mathur *et al.*, “Enhancement of Field Emission Characteristics of Carbon Nanotubes on Oxidation,” *J. Nanosci. Nanotechnol.*, vol. 11, no. 8, pp. 7011–7014, 2011.
- [26] H. Murphy, P. Papakonstantinou, and T. I. T. Okpalugo, “Raman study of multiwalled carbon nanotubes functionalized with oxygen groups,” *J. Vac. Sci. Technol. B Microelectron. Nanom. Struct.*, vol. 24, no. 2, p. 715, 2006.
- [27] V. B. Koli, A. G. Dhodamani, S. D. Delekar, and S. H. Pawar, “In situ sol-gel synthesis of anatase TiO<sub>2</sub>-MWCNTs nanocomposites and their photocatalytic applications,” *J. Photochem. Photobiol. A Chem.*, vol. 333, pp. 40–48, 2017.
- [28] X. Lai *et al.*, “Carbon-doped TiO<sub>2</sub> coating on multiwalled carbon nanotubes with higher visible light photocatalytic activity,” *Appl. Catal. B Environ.*, vol. 107, no. 1–2, pp. 128–134, 2011.
- [29] H. Liu, G. Liu, and Q. Zhou, “Preparation and characterization of Zr doped TiO<sub>2</sub> nanotube arrays on the titanium sheet and their enhanced photocatalytic activity,” *J.*

- Solid State Chem.*, vol. 182, no. 12, pp. 3238–3242, 2009.
- [30] J. Yu, T. Ma, and S. Liu, “Enhanced photocatalytic activity of mesoporous TiO<sub>2</sub> aggregates by embedding carbon nanotubes as electron-transfer channel,” *Phys. Chem. Chem. Phys.*, vol. 13, no. 8, pp. 3491–3501, 2011.
- [31] V. B. Koli, A. G. Dhodamani, A. V. Raut, N. D. Thorat, S. H. Pawar, and S. D. Delekar, “Visible light photo-induced antibacterial activity of TiO<sub>2</sub>-MWCNTs nanocomposites with varying the contents of MWCNTs,” *J. Photochem. Photobiol. A Chem.*, vol. 328, pp.50-58, 2016.
- [32] S. Banerjee, T. Hemraj-Benny, M. Balasubramanian, D. A. Fischer, J. A. Misewich, and S. S. Wong, “Surface chemistry and structure of purified, ozonized, multiwalled carbon nanotubes probed by NEXAFS and vibrational spectroscopies,” *ChemPhysChem*, vol. 5, no. 9, pp. 1416–1422, 2004.
- [33] A. Kuznetsova *et al.*, “Oxygen-containing functional groups on single-wall carbon nanotubes: NEXAFS and vibrational spectroscopic studies,” *J. Am. Chem. Soc.*, vol. 123, no. 43, pp. 10699–10704, 2001.
- [34] S. Banerjee, T. Hemraj-Benny, S. S. Wong, M. Balasubramanian, J. A. Misewich, and D. A. Fischer, “Ozonized single-walled carbon nanotubes investigated using NEXAFS spectroscopy,” *Chem. Commun.*, vol. 10, no. 7, pp. 772–773, 2004.
- [35] M. Magnuson *et al.*, “Bonding mechanism in the nitrides Ti<sub>2</sub> AlN and TiN: An experimental and theoretical investigation,” *Phys. Rev. B - Condens. Matter Mater. Phys.*, vol. 76, no. 19, pp. 1–9, 2007.
- [36] F. M. F. de Groot, M. O. Figueiredo, M. J. Basto, M. Abbate, H. Petersen, and J. C.

Fuggle, “2 p X-ray absorption of titanium in minerals,” *Phys. Chem. Miner.*, vol. 19, no. 3, pp. 140–147, 1992.

- [37] E. Frackowiak and F. Béguin, “Electrochemical storage of energy in carbon nanotubes and nanostructured carbons,” *Carbon*, vol. 40, no. 10, pp.1775-1787, 2002.

## **Chapter Six**

### **Structural, Electronic and Electrical Behaviour of**

### **MWCNTs:(TiO<sub>2</sub>:SiO<sub>2</sub>) Nanocomposites**

## 6.1. Introduction

Carbon nanotubes (CNTs), graphene, and fullerene are graphitic carbon materials that are of great interest as a result of their excellent electrical conductivity, thermal properties, and mechanical strength [1]. The excellent properties of this graphitic carbon have been of significance to researchers and have a likelihood of utilizing them for several applications in areas such as hydrogen storage, electrochemical sensors, microelectronics and solar cells [1], [2]. Over a few years, CNTs have attracted attentiveness when compared to graphene and fullerene, as they entail the possibility of regulating their length, diameter, and morphology. These have a very large impact on modifying their behavior for different functions [3]. CNTs are cylindrical and hollow nanostructure with open or closed ends which are either in the form of single-walled (SW) or multi-walled (MW). SWCNT behaves as a metallic or semiconducting material with an energy gap ranging between 0 and 2 eV [4]. SWCNT having closed ends are recognized as fullerene, which has limitations as they cannot be produced in large quantities. These characteristics and behavior of MWCNTs made it an exceptional material then fullerene and graphene.

However, CNTs properties need to be modified for numerous applications. Several researchers have utilized metal oxide and heteroatoms like aluminum oxide ( $\text{Al}_2\text{O}_3$ ), tin oxide ( $\text{SnO}_2$ ), titanium dioxide ( $\text{TiO}_2$ ), zinc oxide ( $\text{ZnO}$ ) [5], and silicon (Si) [6], boron (Br), nitrogen (N) [7], respectively to modify the properties of MWCNTs for applications in various fields. Also, other studies have functionalized  $\text{TiO}_2$ - $\text{SiO}_2$  with different concentrations of MWCNTs for photocatalysis activity applications [8–10]. An alternative approach to be considered is functionalizing CNTs with bi-dopant. To the best of my knowledge, functionalizing CNTs with  $\text{SiO}_2$ - $\text{TiO}_2$  has not been given consideration elsewhere. Modifying the behavior of CNTs using this bi-dopant can lead to a potential material for varieties of applications. This is because  $\text{TiO}_2$  is a none toxic element, has an excellent photocatalytic activity, resistant to corrosion, and can

make electron transfer in CNTs possible, owing to its higher movement of free electrons [11]. On the other hand, the atoms or molecules of Si behave as a binding site for other atoms or molecules [12], which provides dangling bonds through chemisorption on the surface of CNTs, thereby, influencing the behavior of CNTs for various application in supplementary to the identified ones [13]. Also, it was found that the atoms or molecules of Si relax outward and make the formation of  $sp^3$  bonding possible, which transforms the electronic behavior of CNTs [6].

Our previous studies showed that MWCNTs-TiO<sub>2</sub> NPs [14] and MWCNTs:SiO<sub>2</sub> NPs [15] with percentage concentrations of Ti ~15 & ~20 at % and Si ~1.5 & ~5.75 at %, respectively transform the electrical structure, electronic and bonding properties of MWCNTs. Considering their electrical conductivity, the conductivity of MWCNTs-TiO<sub>2</sub> nanocomposites does not change but increases when compared with MWCNTs, whereas, the conductivity of MWCNTs:SiO<sub>2</sub> nanocomposites varies with 1.5 and 5.75 at % of Si on the surface of MWCNTs. In both cases, an electrical hysteresis loop was observed, which indicates a ferroelectric behavior. The results obtained from these previous studies serve as a motivation to further modify the behavior of MWCNTs with the combined effects of Si and TiO<sub>2</sub> on its surface for several applications in addition to the know ones.

In this study, the composite of SiO<sub>2</sub>:TiO<sub>2</sub> at different concentrations (Ti:Si ~6:6 at % and Ti:Si ~10:10 at %) on MWCNTs surface were prepared using hydrothermal technique. Afterward, their electrical, electronic, and structural behavior were studied using different research techniques. The novelty of this investigation is to enhance the properties of the material for multidisciplinary applications (opto/nano/microelectronics and catalytic activities applications), particularly for charge storage and memristive based devices and also for photocatalysis application.

## 6.2. Methodology

### 6.2.1. Synthesis of TiO<sub>2</sub>, SiO<sub>2</sub>, MWCNTs, and MWCNTs:Ti:Si

Ferrocene (C<sub>10</sub>H<sub>10</sub>Fe), acetylene (C<sub>2</sub>H<sub>2</sub>), toluene (C<sub>7</sub>H<sub>8</sub>), chloro(dimethyl) octadecylsilane, 1,3,5-trimethylbenzene, octadecylamine and TiO<sub>2</sub> were purchased from Sigma-Aldrich (Pty) Ltd.

MWCNTs were synthesized using a spray pyrolysis procedure [16]. The process involves the use of ferrocene (Fe(C<sub>5</sub>H<sub>5</sub>)<sub>2</sub>) as catalyst and toluene (C<sub>7</sub>H<sub>8</sub>) as a carbon source to form a solution. Afterward, the solution was positioned in a quartz tube and then inserted into a hot-wall reactor of temperature 850 °C - 900 °C. An argon flow was then introduced through the system until the growth of MWCNTs was completed (40 min). Moreover, acid treatment was used to purify the obtained MWCNTs. The solution of hydrochloric and nitric acid at ratio 1:1 was added to MWCNTs and stirred for 90 min. The mixture was then filtered to obtain pure MWCNTs.

The thermal decomposition technique [17] was utilized to prepare Si-NPs. In this process, the solution of 1,3,5-trimethylbenzene and chloro(dimethyl) octadecylsilane in presence of octadecylamine was placed in a quartz pipe in a vacuum condition and heated at a temperature of ~140 °C for 120 minutes. The mixture was left to air dry at room temperature to obtain Si-NPs. Silicon was oxidized upon exposure to air leading to the formation of SiO<sub>2</sub>.

Hydrothermal technique [18] was adopted to obtain MWCNTs:TiO<sub>2</sub>:SiO<sub>2</sub> nanocomposites. MWCNTs (10 mg) were dispersed in water. TiO<sub>2</sub> and SiO<sub>2</sub> were added to MWCNTs suspension at two stoichiometric ratios (Ti:Si ≈ 6: 6 at%) and (Ti:Si ≈ 10: 10 at%). The solutions were sonicated for 30 minutes and stirred at 80°C on a hot plate. Thereafter, we introduced an Ar flow through the suspension surface while the process of heating is still on to speed up the water vaporization. Afterward, MWCNTs:TiO<sub>2</sub>:SiO<sub>2</sub> nanocomposites (NCs)



were obtained in an oven at 100 °C after 15 hours. The samples were dropped cast on silicon wafers and air-dried for characterization purposes.

### **6.2.2. Characterization**

Characterization of TiO<sub>2</sub>, SiO<sub>2</sub>, MWCNTs, and MWCNTs:Ti:Si nanocomposites were carried using different techniques. The morphology of the nanomaterials was studied utilizing FE-SEM JSM-7800F supplied by JEOL Ltd. The crystallite structures were investigated using Smartlab X-ray diffractometer with 0.154 nm Cu K $\alpha$  radiation line supplied by Rigaku. Raman spectra of the nanomaterials were studied using scientific XploRA of LASER light excitation energy of ~2.41 eV at 532 nm from HORIBA. The core shells which provide information about the electronic structure were examined utilizing KRATOS-SUPRA spectrometer with monochromatic Al K $\alpha$  radiation of pressure and excitation energy of  $1.2 \times 10^{-9}$  Torr and 1486.6 eV, respectively. The XANES spectra measurements of Ti *L*<sub>3,2</sub>-edge, Si *L*<sub>3,2</sub>-edge, C *K*-edge, and O *K*-edge were achieved using Taiwan Light Source (TLS) at NSRRC (National Synchrotron Radiation Research Centre), Hsinchu, Taiwan. The electrical conductivity of the nanomaterials was performed using conducting silver paste as electrodes to study their electrical properties. The I-V measurements were carried out using Keithley 6487 with a voltage sweep from -1 to +1 V (-1 to 0 V, 0 to -1 V, +1 to 0 V, 0 to +1 V) in 3 cycles for each studied material. The voltage was saturated at 1 V with an applied current limit of 2.5 mA. All characterizations were performed at room temperature.

## **6.3. Result and discussion**

### **6.3.1. Field emission-scanning electron microscopy (FE-SEM)**

Figure 6.1 displays the FE-SEM images of TiO<sub>2</sub>, SiO<sub>2</sub>, MWCNTs, MWCNTs:Ti:Si nanocomposites, and EDS spectra of MWCNTs:Ti:Si nanocomposites. In Figure 6.1, (a-c)

shows typical images of  $\text{TiO}_2$ ,  $\text{SiO}_2$ , and MWCNTs, respectively. (d) exhibits a tube shape, like roots of a tree with no agglomeration, implying a good dispersion of  $\text{TiO}_2$  and  $\text{SiO}_2$  on the MWCNTs matrix. (e) also shows a tube-like shape along-side with agglomerations on the surface of MWCNTs which may be due to an increased percentage of  $\text{TiO}_2$  and  $\text{SiO}_2$ . This indicates a good contact and growth of  $\text{TiO}_2$  on the MWCNTs surface, which is later confirmed by XRD. The spectra in (f) display different peaks corresponding to carbon, oxygen, titanium, and silicon denoted by C, O, Ti, and Si respectively. The presence of O in the nanocomposite may be due to the hydroxyl functional group of MWCNTs or from  $\text{TiO}_2$  and  $\text{SiO}_2$  nanoparticles. It is also observed that the spectra do not exhibit any contamination.

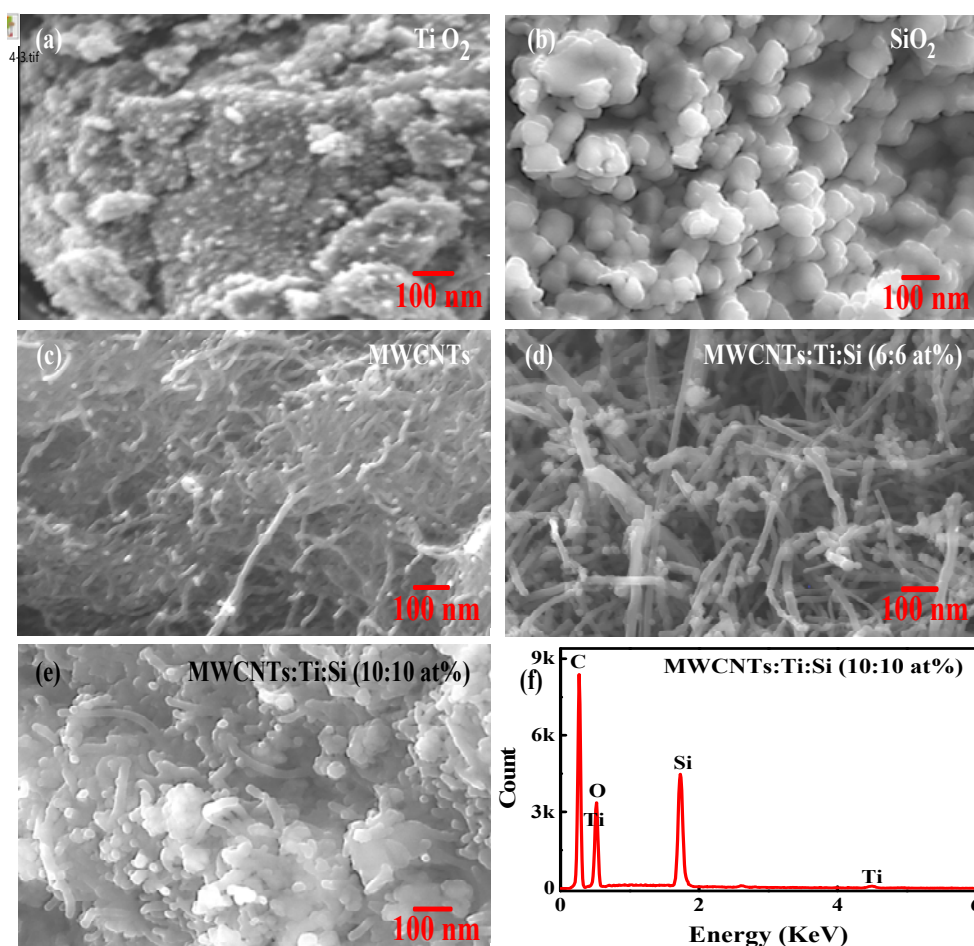


Figure 6.1. (a, b, c, d and e) FESEM images for  $\text{TiO}_2$ ,  $\text{SiO}_2$ , MWCNTs, and MWCNTs:Ti:Si nanocomposites. (f) EDS spectra for MWCNTs:Ti:Si nanocomposites.

### 6.3.2. X-Ray Diffraction (XRD) Patterns

XRD shows the crystal structure of  $\text{TiO}_2$ ,  $\text{SiO}_2$ , MWCNTs, MWCNTs:Ti:Si nanocomposites as presented in figure 6.2. The XRD spectrum of MWCNTs shows usual graphitic carbon peaks  $2\theta$  at  $25.9^\circ$ ,  $43.6^\circ$ , and  $53.6^\circ$  assigned to plane (002), (100), and (004) respectively [19]. A low intense  $2\theta$  peak at  $7^\circ$  [20] and  $22.7^\circ$  [21,22] corresponding to (111) and  $\text{SiO}_2$ , respectively are observed for the pattern of  $\text{SiO}_2$ . Typical peaks  $2\theta$  at  $25.3^\circ$ ,  $37.1^\circ$ ,  $37.9^\circ$ ,  $38.7^\circ$ ,  $48.1^\circ$ ,  $54.2^\circ$ ,  $55.3^\circ$  and  $62.9^\circ$  are assigned to (101), (103), (004), (112), (200), (105), (211) and (204) plane of  $\text{TiO}_2$  anatase phase [23]. In the XRD spectrum of MWCNTs:Ti:Si nanocomposites, the same peaks is observed as seen in the  $\text{TiO}_2$  pattern with additional rutile phase  $2\theta$  at  $27.3^\circ$  and  $41.4^\circ$  assigned to (110) and (111) plane, respectively [24,25]. This indicates that  $\text{TiO}_2$  and  $\text{SiO}_2$  have impacted the crystal structure of MWCNTs. Also, a minute carbon peak is observed in the pattern of MWCNTs:Ti:Si (~6:6 at %), which later disappeared as Ti:Si atoms increases on the surface of MWCNTs, which implies that Ti atoms were gradually replacing carbon atoms as the content of Ti:Si increases. The absence of Si peaks doesn't indicate the absence of Si content in the nanocomposites, which may be due to the fact that Ti peaks might have overlapped its peaks.

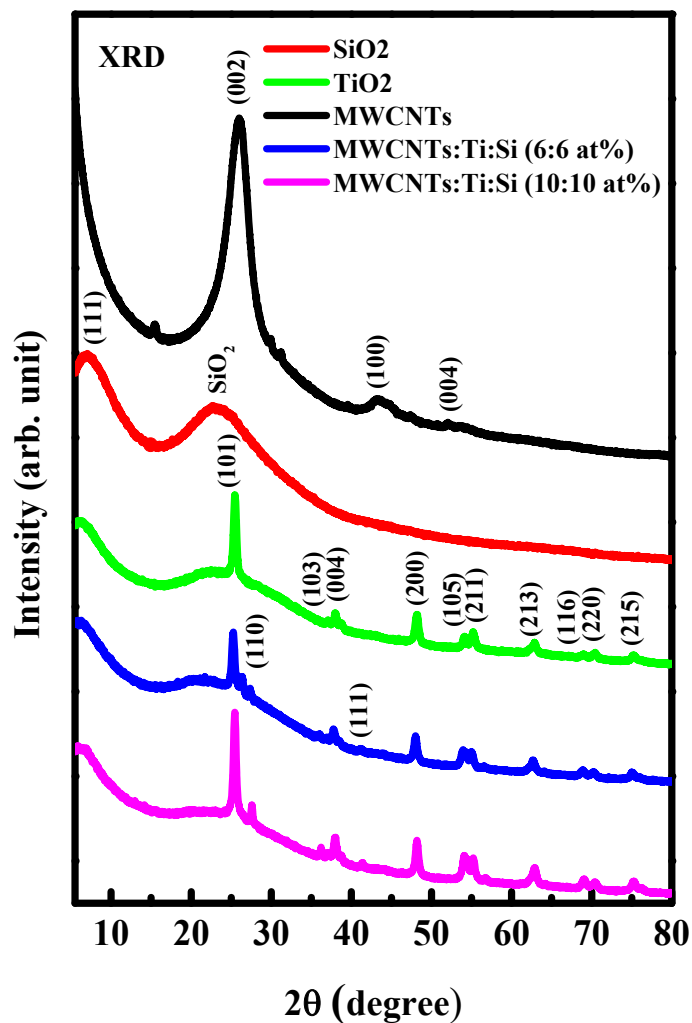


Figure 6.2. XRD spectra for TiO<sub>2</sub>, SiO<sub>2</sub>, MWCNTs, and MWCNTs:Ti:Si nanocomposites.

$D = k\lambda/\beta\cos\theta$  [26] Scherrer's equation was used to estimate the crystallite size of nanomaterials, the parameters in the equation has been described earlier in chapter three. The crystallite size was estimated from (101) plane of TiO<sub>2</sub>, MWCNTs:Ti:Si (~6:6 atom %) and MWCNTs:Ti:Si (~10:10 at %). The crystallite size of TiO<sub>2</sub> is 18.10, MWCNTs:Ti:Si (~6:6 at %) is 19.09 nm and MWCNTs:Ti:Si (~10:10 at %) is 19.27 nm suggesting the growth of TiO<sub>2</sub> in the nanocomposites.

### 6.3.3. Raman spectroscopy

Raman is an essential tool that gives information about the degree of hybridization of carbon materials. Figure 6.3 represents the Raman spectrum of TiO<sub>2</sub>, SiO<sub>2</sub>, MWCNTs,

MWCNTs:Ti:Si nanocomposites. The spectra of TiO<sub>2</sub> display several peaks and are located at 396 cm<sup>-1</sup> for B<sub>1g</sub>, 516 cm<sup>-1</sup> for A<sub>1g</sub>, and 636 cm<sup>-1</sup> for the E<sub>g</sub> band of anatase phases [27,28]. For SiO<sub>2</sub> spectra, Two peaks are observed at 520 and 1036 cm<sup>-1</sup> assigned to Si<sub>1</sub> and Si<sub>2</sub> (1st and 2nd silicon peaks). The peaks observed in both TiO<sub>2</sub> and SiO<sub>2</sub> indicate that carbon species was not present in the nanomaterials. As shown in the figure, MWCNTs exhibits four key peaks. These peaks are observed at 1345 cm<sup>-1</sup> for D peak, 1585 cm<sup>-1</sup> for G peak, 2664 cm<sup>-1</sup> for 2D peak, and 2912 for cm<sup>-1</sup> D+G peak [29]. From D (disordered peak) and G peaks (ordered peak), we can understand how graphitized is the structure and to what level is the degree of hybridization of carbon material. The occurrence of a 2D peak was owing to the 2nd-order vibrational effect of the D band. The appearance of the D+G peak was also due to the 2nd-order combined vibrational effect of the D and G band. The combined effect of TiO<sub>2</sub> and MWCNTs brings about the occurrence of anatase phase and usual graphitic features in MWCNTs:Ti:Si nanocomposites and no SiO<sub>2</sub> peak is observed. It can be said that the SiO<sub>2</sub> peaks might have been overlapped by anatase TiO<sub>2</sub> peaks. The change in the Raman spectrum of MWCNTs indicates that Ti:Si has changed the structure of MWCNTs. Also, the slight shift of anatase peaks in the nanocomposites may be due to an increase in the crystallite size of anatase TiO<sub>2</sub> nanoparticles [30] as observed from XRD. From the de-convolution of MWCNTs:Ti:Si (~10:10 at %) spectra in figure 6.4, a peak is observed at 1658 cm<sup>-1</sup> corresponding to D' peak which occur due to the broaden and a slight shift of G band and also due to phonon restrictions among the graphitic walls [31,32].

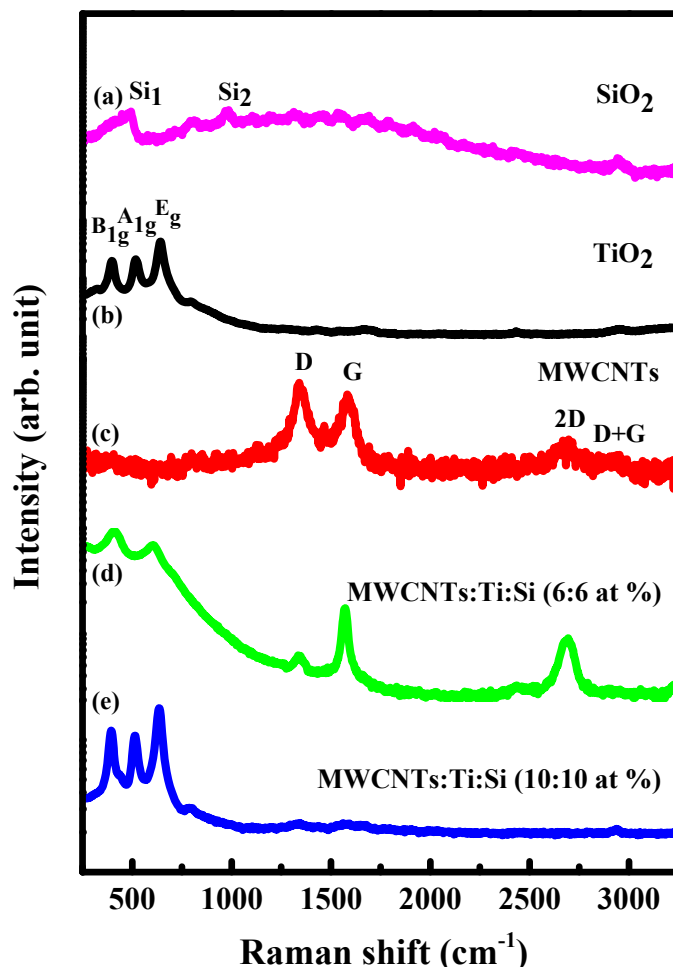


Figure 6.3. Raman spectra for TiO<sub>2</sub>, SiO<sub>2</sub>, MWCNT, and MWCNTs:Ti:Si nanocomposites.

The  $I_D/I_G$  ratios of Raman spectrum plays a vital role in understanding the degree of hybridization of carbon materials. To obtain the  $I_D/I_G$  ratios, the Raman spectra of the MWCNTs and MWCNTs:Ti:Si nanocomposites were de-convoluted into multiple Gaussian lines and are depicted in figure 6.4. The parameters obtained from the deconvolution of the Raman spectrum are also presented in Table 6.1. From figure 6.4 (b), it was observed that the width of D and G band got narrowed for Ti:Si (6:6 at%) deposition. Also, The intensity of D band decreases to an increase in the intensity of G band. These observations maybe be due to the longer isothermal exposure time rate of the nanocomposite. From figure 6.4 (c), a slight broadening of G band with occurrence of D' band for Ti:Si (10:10 at%) deposition was observed compared to MWCNTs, indicating a decrease in  $sp^2$  cluster. The  $I_D/I_G$  ratios were calculated to be  $\sim 1.18$  for MWCNTs,  $\sim 0.16$  for Ti:Si (6:6 at%), and  $\sim 0.97$  for Ti:Si (10:10 at%)

NCs. The observed variation in the  $I_D/I_G$  ratio indicates a reduction of defect density due to the replacement of a carbon by Ti:Si atoms on the surface of MWCNTs. However, it is noted that the  $I_D/I_G$  ratio for Ti:Si (10:10 at%) is higher than (6:6 at%) for Ti:Si decorated MWCNTs-NCs. This variation in the ratio with the concentration, indicates a structural change of the nanocomposite and it is consistent with those of XRD results discussed above.

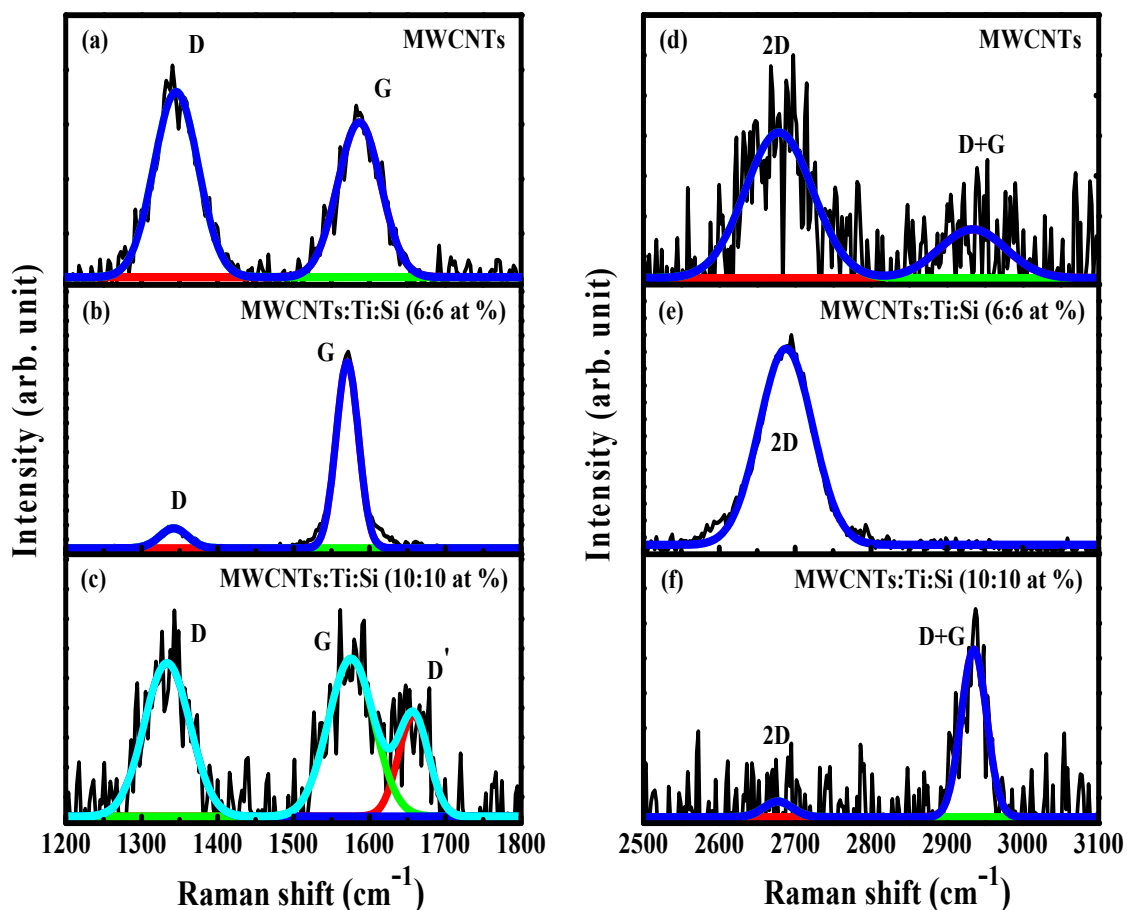


Figure 6.4. De-convolution of Raman spectra for MWCNTs and MWCNTs:Ti:Si nanocomposites.

Table 6.1: Parameters obtained from the deconvolution of Raman spectra for MWCNTs and MWCNTs:Ti:Si nanocomposites.

1 <sup>st</sup> order vibration Raman spectra materials	D peaks			G peaks			D' peaks		
	x (cm <sup>-1</sup> )	$\Delta\omega$ (cm <sup>-1</sup> )	Int. (a.u.)	x (cm <sup>-1</sup> )	$\Delta\omega$ (cm <sup>-1</sup> )	Int. (a.u.)	x (cm <sup>-1</sup> )	$\Delta\omega$ (cm <sup>-1</sup> )	Int. (a.u.)
MWCNTs	1343	92	2.1	1574	82	1.6	--	--	--
MWCNTs:Ti:Si (~6:6 at %)	1336	91	3.9	1573	77	2.6	--	--	--
MWCNTs:Ti:Si (~10:10 at %)	1298	18	2.8	1439	23	3.8	1460	24	2.4
2 <sup>nd</sup> order vibration Raman spectra of materials	2D peaks			D+G peaks			I <sub>D</sub> /I <sub>G</sub>		
MWCNTs	2679	118	0.7	2888	150	0.5	1.18		
MWCNTs:Ti:Si (~6:6 at %)	2673	116	1.4	2900	138	0.7	0.16		
MWCNTs:Ti:Si (~10:10 at %)	2727	38	1.5	2924	43	14.2	0.97		

#### 6.3.4. X-ray photoelectron spectroscopy (XPS)

The electronic structure, chemical bonding, and quantification of TiO<sub>2</sub>, SiO<sub>2</sub>, MWCNTs, and MWCNTs:Ti:Si nanocomposites was examined using XPS spectroscopy. Table 6.2 reveal the percentage of each content of Ti, Si, C, and O present in various material. The Table also shows that carbon content decreases as Ti and Si content increases on MWCNTs surface, translating to the gradual replacement of carbon atoms by Ti:Si atoms. The full XPS spectra are presented in figure 6.5 with several peaks of index C 1s, O 1s, Ti 2p, Ti 3p, Si 2p, and Si 2s configurations. These peaks were extracted and de-convoluted with Gaussian fits to examine their peak positions which gives information about the bonding properties.



Table 6.2: XPS quantificational analysis of titanium (Ti), silicon (Si), carbon (C) and oxygen (O)

Nanomaterials	Quantificational and compositional analysis from XPS			
	Ti at %	Si at %	C at %	O at %
TiO <sub>2</sub>	34	--	--	66
SiO <sub>2</sub>	--	36	--	64
MWCNTs	--	--	98	02
MWCNTs:Ti:Si (~6:6 at %)	6	6	59	29
MWCNTs:Ti:Si (~10:10 at %)	10	11	27	52

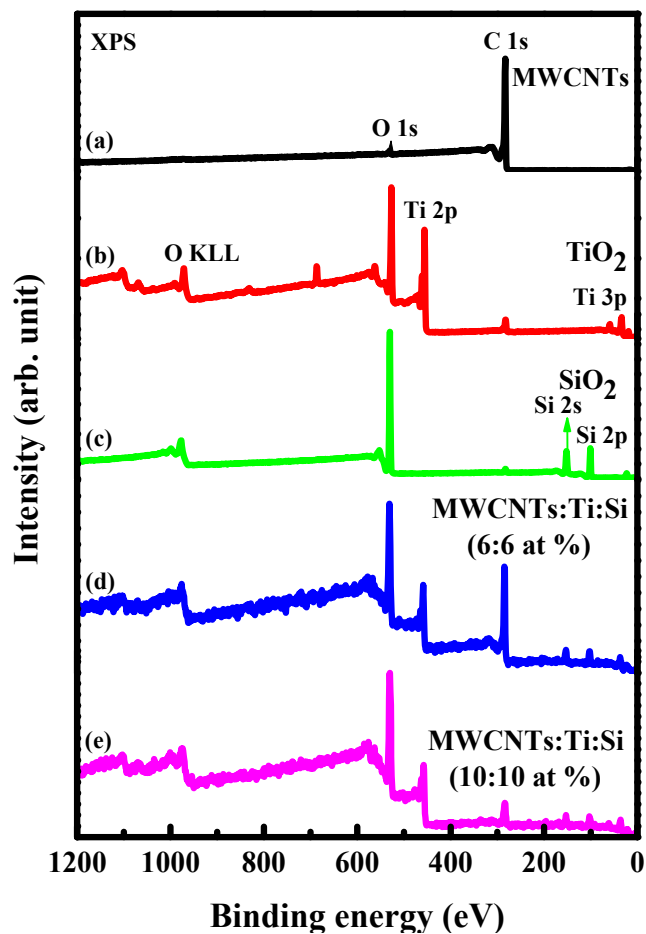


Figure 6.5. XPS spectra for TiO<sub>2</sub>, SiO<sub>2</sub>, MWCNTs, and MWCNTs:Ti:Si nanocomposites.

XPS is an essential tool that was used to examine the bonding and electronic structure of the nanomaterials. The spectra of these materials were de-convoluted with Gaussian line into several peaks as depicted in figures 6.6, 6.7, and 6.8, and their peak positions ( $x$ ), width ( $\Delta\omega$ ), and intensities (Int.) are shown in Table 6.2.

Table 6.3: Parameters obtained from the de-convolution of C 1s, O 1s, Ti 2p, and Si 2p XPS spectra

Nanomaterials	C 1s XPS								
	Peak I C=C			Peak II C=C/C-C/C-O			Peak III O=C-O		
	Int.	x	$\Delta\omega$	Int.	x	$\Delta\omega$	Int.	x	$\Delta\omega$
MWCNTs	31387	283.5	0.7	7554	284.3	2.3	1944	290.0	6.5
MWCNTs:Ti:Si (6:6 at %)	2658	284.6	1.2	890	285.7	2.2	--	--	--
MWCNTs:Ti:Si (10:10 at %)	776	284.6	1.7	264	286.3	1.9	--	--	--
	O 1s XPS								
	Ti-O-Ti/Ti-O-H			Peak – I C=O/C-O/Ti-O-Si			Peak – II C-O/Si-O-Si		
	Int.	x	$\Delta\omega$	Int.	x	$\Delta\omega$	Int.	x	$\Delta\omega$
MWCNTs	--	--	--	240	530.5	2.0	287	531.9	2.7
MWCNTs:Ti:Si (6:6 at %)	310	528.6	1.5	2373	530.6	1.7	2019	532.4	2.3
MWCNTs:Ti:Si (10:10 at %)	360	528.3	1.8	3355	530.2	1.7	2689	532.0	2.4
	Ti 2p XPS								
	$Ti^{3+} 2p_{3/2}$			Peak I $Ti^{4+} 2p_{3/2}$			Peak II $Ti^{4+} 2p_{1/2}$		
	Int.	x	$\Delta\omega$	Int.	x	$\Delta\omega$	Int.	x	$\Delta\omega$
TiO <sub>2</sub>	--	--	--	38748	455.6	1.0	10967	461.3	1.8
MWCNTs:Ti:Si (6, 6)	229	457.3	1.7	1558	459.2	1.5	477	464.8	2.0

MWCNTs:Ti:Si (10, 10)	414	457.1	2.4	2256	459.2	1.5	710	464.9	1.9
	Si 2p XPS								
	Peak – I Si-C/ Si-C-O			Peak – II Si-C/ Si-C-O/ Si-O			Peak – III Si-O		
SiO <sub>2</sub>	3044	100.6	1.2	101.1	1.6	6625	--	--	--
MWCNTs:Ti:Si (6:6 at %)	199	102.1	2.3	103.6	1.5	225	72	104.6	0.6
MWCNTs:Ti:Si (10:10 at %)	187	101.7	1.7	103.3	1.8	351	72	104.8	1.4

Figure 6.6 represents the deconvolution of C 1s and O 1s core-level spectra of MWCNTs, Ti 2p of TiO<sub>2</sub>, and Si 2p of SiO<sub>2</sub>. Considering the C 1s of MWCNTs, peaks are located at 283.5, 284.0, and 290.0 eV, which are signatures of C=C and O=C-O [33,34] bonding, respectively. In the case of the O 1s spectra, peaks are observed at 530.4 and 532.1 eV assigned to C=O and C-O [33], respectively. The peaks observed for the core level of Si 2p are found at 100.6 and 101.1 eV corresponding Si 2p<sub>3/2</sub> and 2p<sub>1/2</sub> [35]. The Ti 2p core level was de-convoluted into two peaks at 455.6 and 461.3 eV, which are signatures of Ti 2p<sub>3/2</sub> and Ti 2p<sub>1/2</sub> oxidation state, respectively. The spin energy splitting between them was calculated to be 5.7 eV, which indicates that the Ti<sup>4+</sup> state is present [4].

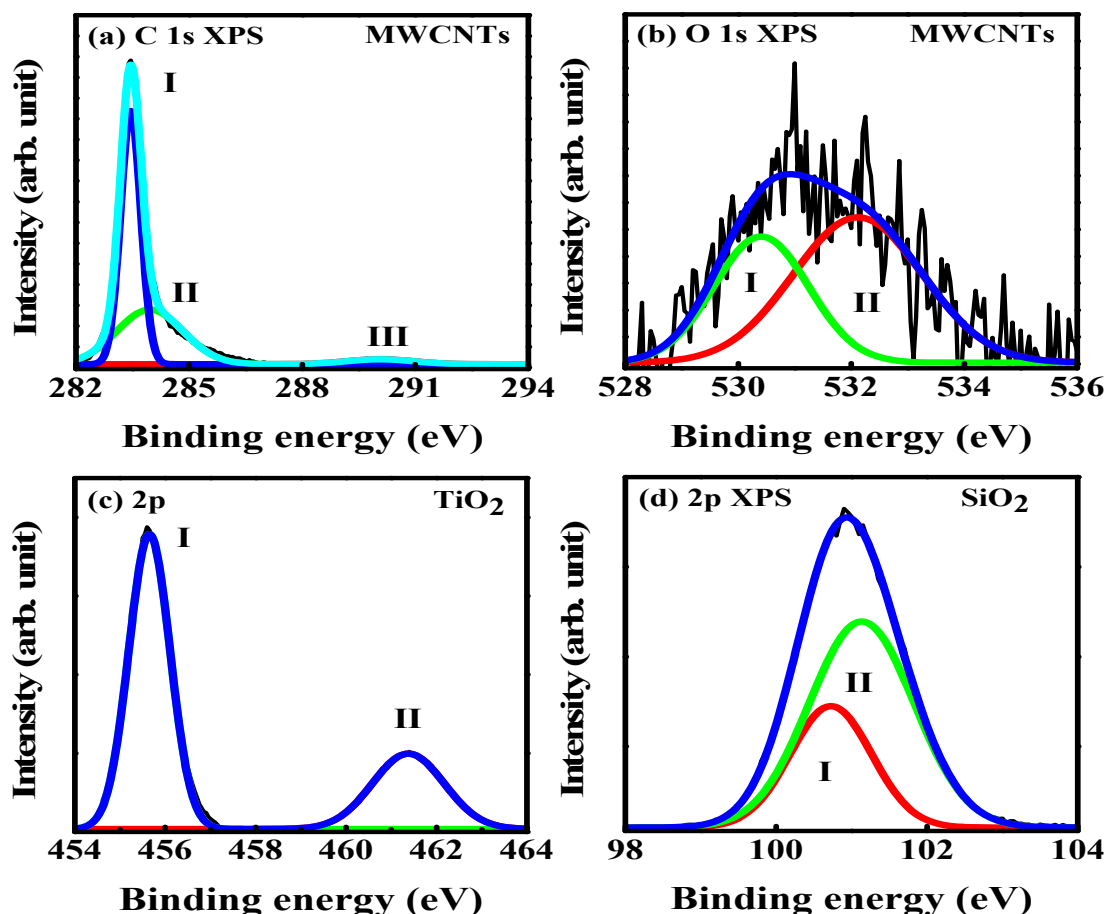


Figure 6.6. XPS de-convolution of (a and b) C1s and O1s spectra for MWCNTs. (c) Ti 2p spectra for TiO<sub>2</sub>. (d and e) Si 2s and 2p spectra for SiO<sub>2</sub>.

Figure 6.7 and 6.8 represent the de-convolutions of C 1s, O 1s, Ti 2p and Si 2p core levels of MWCNTs:Ti:Si (~6:6 at %) and MWCNTs:Ti:Si (~10:10 at %), respectively. For C 1s de-convoluted spectra, two peaks are observed at 284.6/284.7 and 285.7/286.3 eV for MWCNTs:Ti:Si (~6:6 at %)/MWCNTs:Ti:Si (~10:10 at %), respectively. In comparison with the C 1s of MWCNTs, it was observed that these peaks shift towards high binding energy resulting in a defect peak at 285.7 eV for MWCNTs:Ti:Si (~6:6 at %). The defect peak is an indication of weak attachment within MWCNTs:Ti:Si (~6:6 at %) nanocomposite. For O 1s of MWCNTs:Ti:Si (~6:6 at %) and MWCNTs:Ti:Si (~10:10 at %), a shift in peaks positions are observed compared to O 1s of MWCNTs. These peaks positions shift to 528.6/530.5, 532.4 eV

and 528.3/530.2, 532.0 eV corresponding to Ti-O-Ti/Ti-O-H/C=O/Ti-O-Si group [9,36], Si-O-Si chemical bonding [9,36] for MWCNTs:Ti:Si (~6:6 at %) and MWCNTs:Ti:Si (~10:10 at %), respectively. The chemical bonding Ti-O-Si is an indication of TiO<sub>2</sub> and SiO<sub>2</sub> connection.

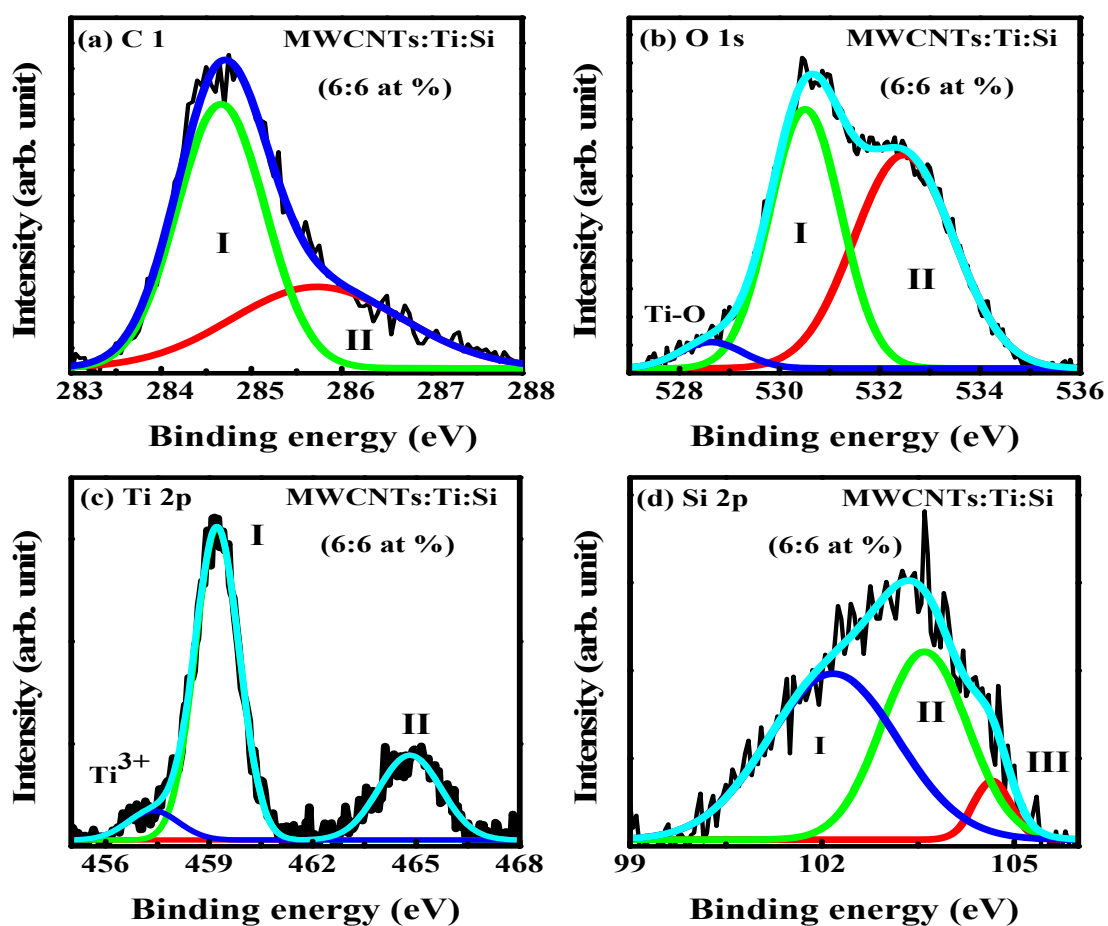


Figure 6.7. De-convolution of C1s, O1s, Ti 2p, and Si 2p XPS spectra for MWCNTs:Ti:Si nanocomposites.

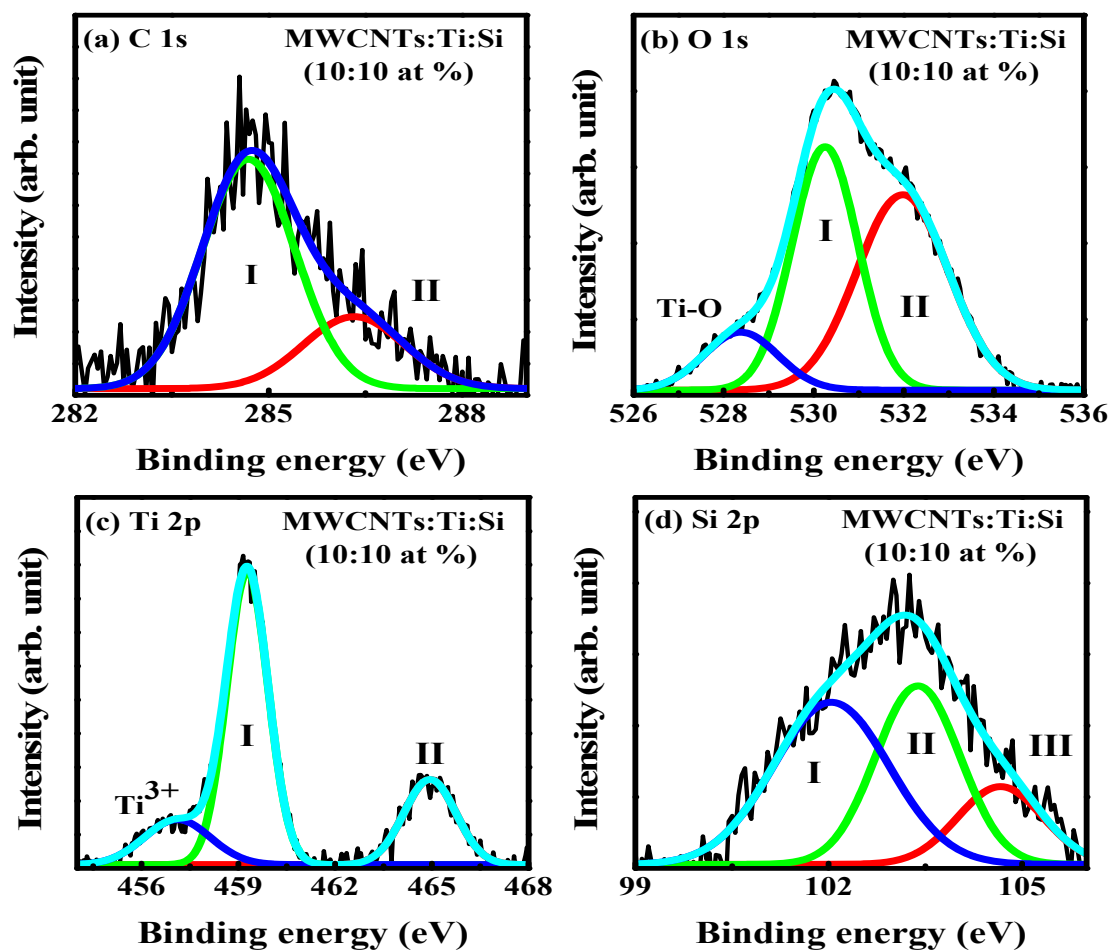


Figure 6.8. Deconvolution of C1s, O1s, Ti 2p, and Si 2p XPS spectra for MWCNTs:Ti:Si nanocomposites.

The core levels of Ti 2p of MWCNTs:Ti:Si (~6:6 at %) and MWCNTs:Ti:Si (~10:10 at %) also shift towards high binding energy compare to Ti 2p of TiO<sub>2</sub>, with additional peak at 457.3, eV for MWCNTs:Ti:Si (~6:6 at %) and 457.1 eV for MWCNTs:Ti:Si (~10:10 at %). The observed shift confirms the decoration of Ti on the MWCNTs surface [37,38]. The additional peak observed in the Ti 2p of the nanocomposites indicates the presence of Ti<sup>3+</sup> state [4,37]. It can be said that the deposition of Ti:Si on the surface of MWCNTs led to the occurrence of Ti<sup>3+</sup> state in MWCNTs:Ti:S nanocomposites. It has been reported elsewhere that Ti<sup>3+</sup> states can form radicals with O<sub>2</sub> [39]. From the previous report [40], the mechanism of photocatalysis of TiO<sub>2</sub> when exposing to light has been established, which reveals the generation of electron-

hole pair in the surface of the material. The generation of electron-hole pairs is associated with a short penetration depth from the formation of radical owing to oxidizing agents. The observed  $Ti^{3+}$  state and its ability to form oxidizing radicals with  $O_2$  can make the nanocomposites useful for photocatalytic activity application. The de-convoluted XPS Si 2p spectra for MWCNTs:Ti:Si (~6:6 at %) and MWCNTs:Ti:Si (~10:10 at %) shows peaks at 102.1 and 103.6 for MWCNTs:Ti:Si (~6:6 at %) and 101.7 and 103.3 eV for MWCNTs:Ti:Si (~10:10 at %). These peaks are assigned to Si-C/Si-C-O [41,42]. The third peaks at 104.6 and 104.8 are the signature of Si-O bonding [43]. This implies that the electronic and bonding system has been influenced due to the deposition of Si on the MWCNTs matrix.

### **6.3.5. X-ray absorption near edge structure (XANES) spectroscopy**

XANES is an essential tool in probing the local electronic structure of a material. XANES spectroscopy was used to investigate the local electronic structure as well as surface chemistry of  $TiO_2$ ,  $SiO_2$ , MWCNTs, and MWCNTs:Ti:Si nanocomposites. Their C *K*-edge, O *K*-edge, Si  $L_{3,2}$ -edge, and Ti  $L_{3,2}$ -edge spectra were depicted in figures 6.9, 6.10, 6.11 and 6.12. Figure 6.9 represents the C *K*-edge spectra of MWCNTs and MWCNTs:Ti:Si nanocomposites. Similar spectra are observed for the nanomaterial and peaks are located at 286.2 eV which is a signature of  $\pi^*$  ( $sp^2$ ) and 293.1 eV is assigned to  $\sigma^*$  ( $sp^3$ ) [19,44,45]. The inset in the figure was extracted using a Gaussian function from 283.5 to 288.5 eV. The inset shows that  $\pi^*$  is been split into two peaks at 286.2 and 287.6 eV, which was a formation of C-C and C-H bond [46]. Taking the spectra intensities displayed by the inset into consideration, there is a variation in the intensities indicating that the  $sp^2$  content of MWCNTs is decreasing gradually translating to a rise in  $sp^3$  content as observed from Raman.

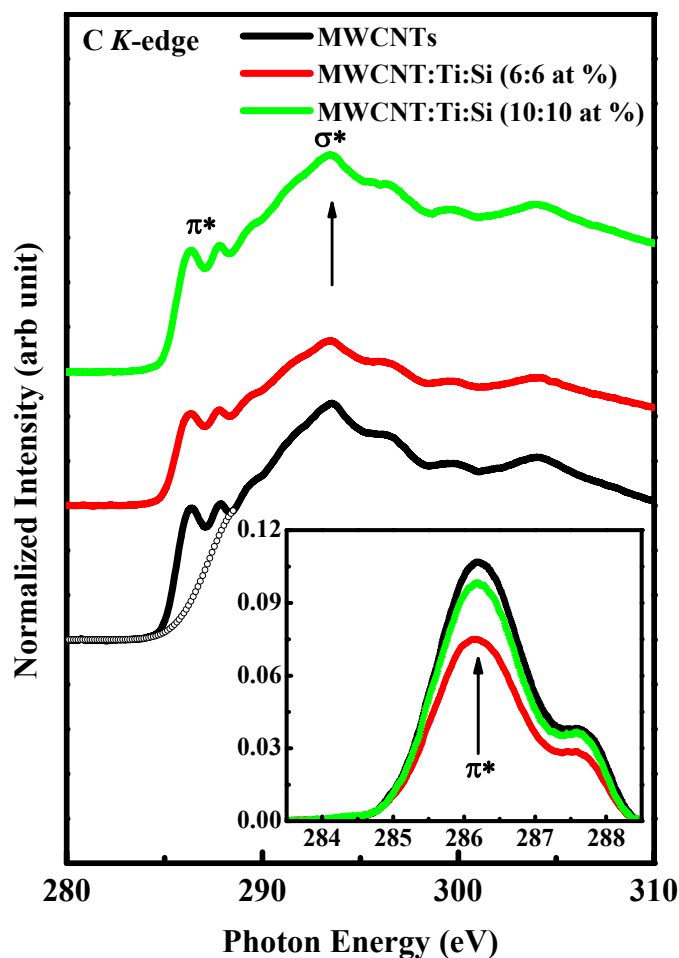


Figure 6.9. C *K*-edge XANES spectra of MWCNTs and MWCNTs:Ti:Si nanocomposites.

The O *K*-edge spectra give information concern the oxidation state and it is displayed in figure 6.10. From the figure, there are two major peaks for MWCNTs at 528.6 and 540 eV assigned to  $\pi^*$  and  $\sigma^*$  features, respectively. The bi-edge observed for  $\pi^*$  features at 528.6 and 530.1 eV as shown by the inset in the figure, initiated from the carboxylic group [47] and  $\sigma^*$  features was as a result of hydroxyl group [47]. Considering the spectra of the nanocomposites, a slight energy shift was observed implying the interaction of Ti:Si with O and C on the surface of MWNCTs. The appearance of peaks (533.7 and 535.1 eV) within the range 530 and 536 eV in the figure was a result of the physical absorption of O<sub>2</sub> during the preparation of the nanomaterials. These peaks were signatures of  $t_{2g}$  and  $e_g$ . The range between them is due to the orbit segregation of Ti 3d [48] and Si d states [49]. Also, the observed region from 530 - 536



eV appears due to the interaction of O 2p with the orbit of  $t_{2g}$  and  $e_g$  [48,49]. The above region of 536 eV occurs as a result of the interaction between O 2p and Si 3sp-Ti 4sp states [50]. From the inset presented in the figure, it was perceived that there is a decrease in the intensities of the nanocomposites compare to MWCNTs, implying de-oxidation as occur.

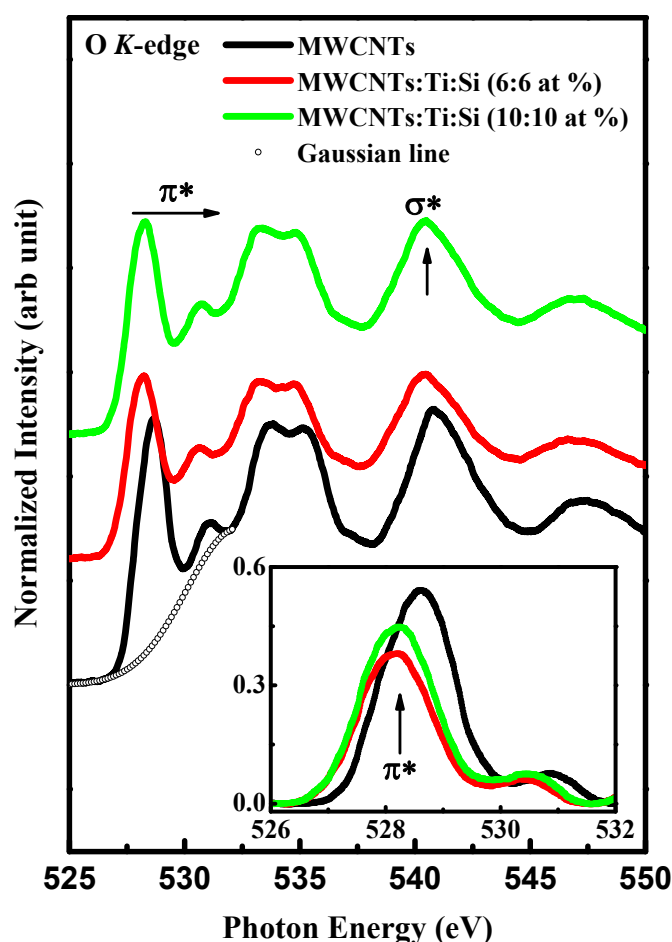


Figure 6.10. O K-edge XANES spectra of MWCNTs and MWCNTs:Ti:Si nanocomposites.

Figure 6.11 represents the Si  $L_{3,2}$ -edge XANES spectra of  $\text{SiO}_2$  and MWCNTs:Ti:Si nanocomposites. The spectra in the figure displayed binary features denoted by A and B and the separation between them is 3 eV from each other. Taking structure A into consideration, it was observed that the structure is split into two peaks at 103.8 and 105.0 eV as a result of a change in Si 2p to Si 3s derived states with separation 1.3 eV between them, translating to poor resolute peaks [49]. The appearance of structure B is owing to the transition from Si 2p to Si

3p in relation to Si 3s state from the hybridization of O 2p orbitals [49,51]. The above region of 105.0 eV are transition from Si 2p to Si 3d state [50]. The inset in the figure was extracted from the main spectra using the Gaussian function. Considering the inset, the intensities of the nanocomposites increases compare to that of SiO<sub>2</sub>. This suggests that there is a change in the electronic structure of MWCNTs by the inclusion of Si.

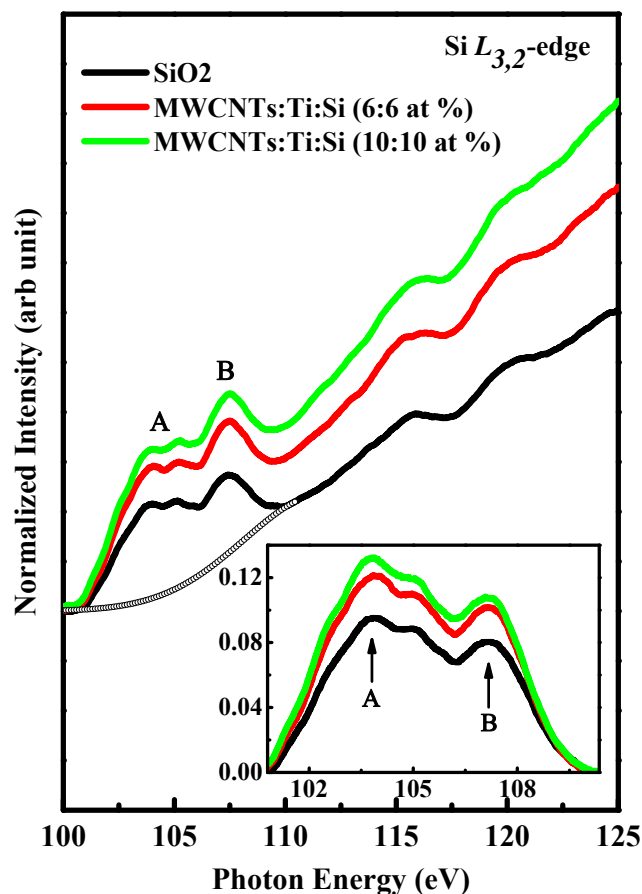


Figure 6.11. Si  $L_{3,2}$ -edge XANES spectra of SiO<sub>2</sub> and MWCNTs:Ti:Si nanocomposites.

Figure 6.12 represents the Ti  $L_{3,2}$ -edge XANES spectra of TiO<sub>2</sub> and MWCNTs:Ti:Si nanocomposites. The spectra in the figure depicted a complex feature of regions  $L_2$ -edge and  $L_3$ -edge signifying O 2p<sub>1/2</sub> and 2p<sub>3/2</sub> Ti 3d states, respectively. These regions appeared due to atomic contact and the effect of the crystal field [52]. The  $L_2$ -edge and  $L_3$ -edge region were divided into binary peaks each by the effect of the crystal field and are assigned to  $t_{2g}$  and  $e_g$  bands as viewed in the figure. These bands are positioned at 456.3 ( $t_{2g}$ ), 458.5 ( $e_g$ ) and 461.6

( $t_{2g}$ ), 463.9 eV ( $e_g$ ) [52] for  $L_3$ -edge and  $L_2$ -edge region, respectively. Concerning the inset in the figure, the difference in the intensities of  $\text{TiO}_2$  and MWCNTs:Ti:Si nanocomposites suggest the substituted of O or/and C by Ti in the nanocomposites.

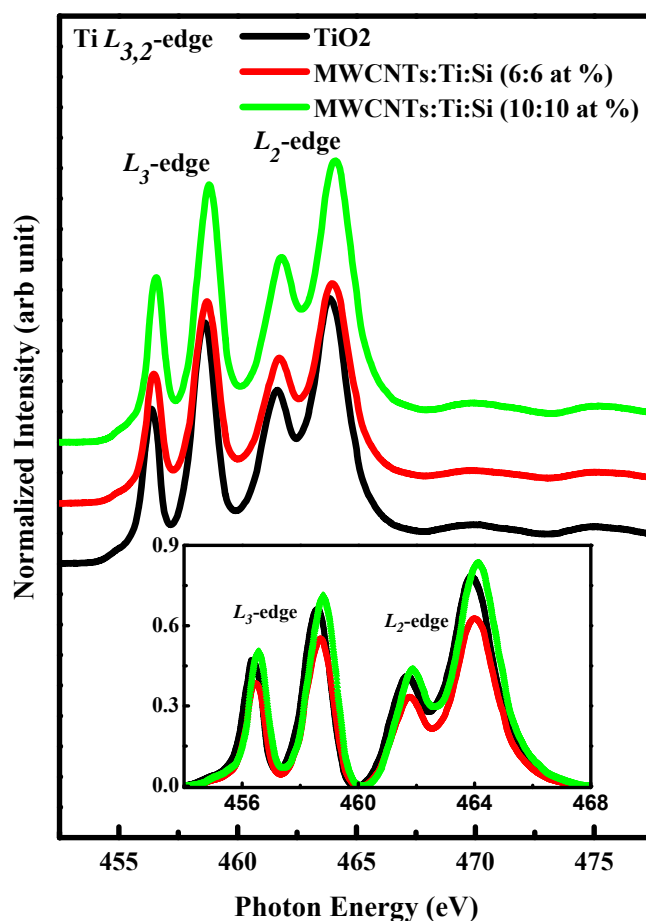


Figure 6.12. Ti  $L_{3,2}$ -edge XANES spectra of  $\text{TiO}_2$  and MWCNTs:Ti:Si nanocomposites.

### 6.3.6. Current-voltage (I-V) measurement

The electrical conductivity of  $\text{SiO}_2$ ,  $\text{TiO}_2$ , MWCNTs, and MWCNTs:Ti:Si nanocomposites were examined using the current-voltage (I-V) technique. The data obtained from their measurement were plotted and are depicted in figures 6.13, 6.14, and 6.15. The electrical conductivity was measured in three cycles as displayed in the figures. The electrical structure of MWCNTs and  $\text{SiO}_2$  indicates a conducting and insulating material, respectively, while  $\text{TiO}_2$  and MWCNTs:Ti:Si nanocomposites are semiconducting in nature. It is obvious that the

inclusion of  $\text{TiO}_2$  and  $\text{SiO}_2$  on the surface MWCNTs transform the electrical structure of the nanocomposites. Considering the electrical conductivity of MWCNTs:Ti:Si nanocomposites, an increased variation was observed compared to MWCNTs due to the inclusion of  $\text{TiO}_2$  and  $\text{SiO}_2$  nanoparticles. The electrical conductivity of MWCNTs:Ti:Si ( $\sim 10:10$  at%) is higher than that of MWCNTs:Ti:Si ( $\sim 6:6$  at%) nanocomposites. It was observed that the introduction of  $\text{SiO}_2$  is responsible for the variation in the electrical conductivity of the nanocomposites when compared to our previous work [14]. The increase in the conductivity is associated with the dangling bond formed by  $\text{SiO}_2$  in MWCNTs, which creates several levels in the energy gap and more mobility of free electrons from Ti:Si was able to jump freely to conduction band from valence band. Similarly, the higher conductivity in MWCNTs:Ti:Si ( $\sim 10:10$  at%) nanomaterial was due to higher numbers of free electrons, which were able to move freely to the conduction band from valence band, owing to an increased percentage of Ti:Si on MWCNTs matrix.

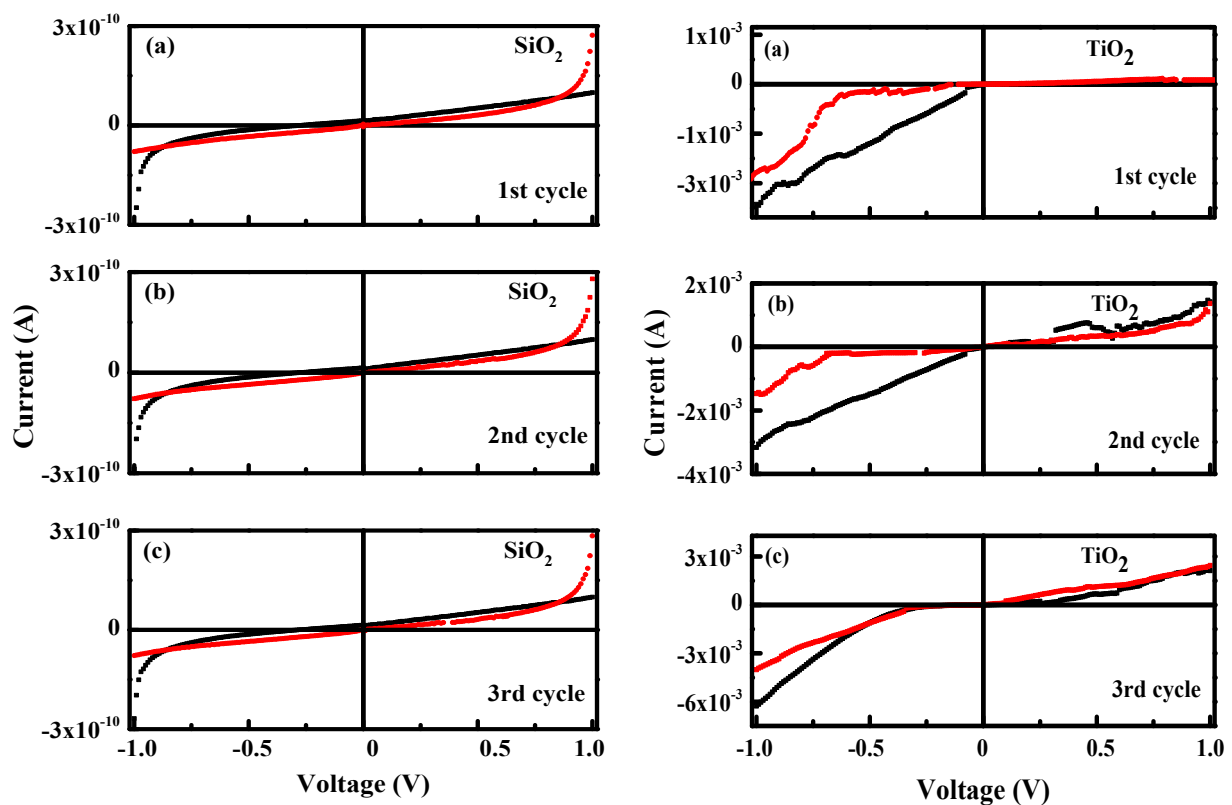


Figure 6.13. I-V curve for  $\text{SiO}_2$  and  $\text{TiO}_2$ .

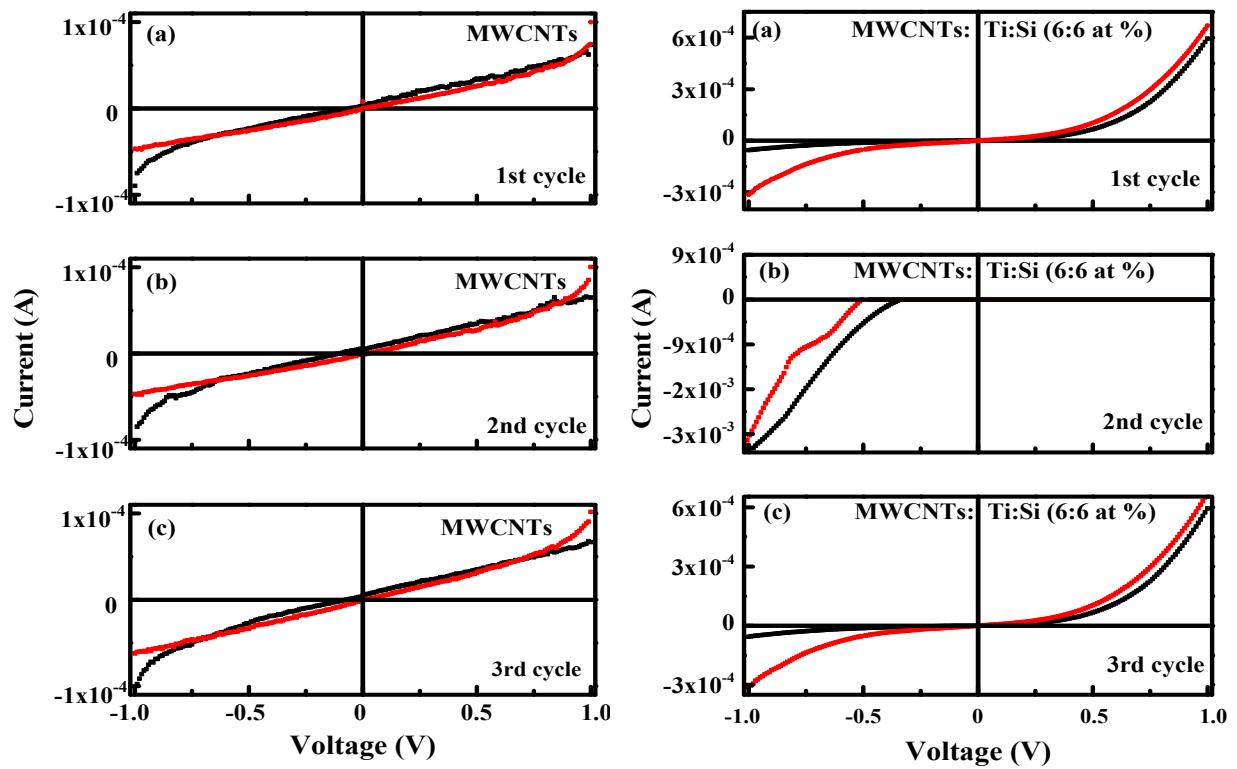


Figure 6.14. I-V curve for MWCNTs and MWCNTs:Ti:Si (6:6 at %) nanocomposite.

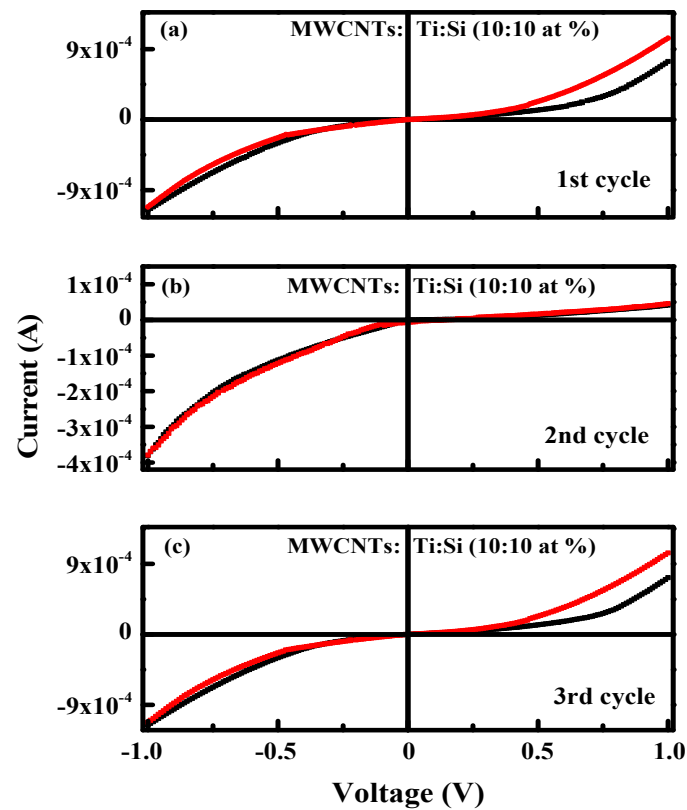


Figure 6.15. I-V curve for MWCNTs:Ti:Si (10:10 at %) nanocomposite.

The I-V log plot of the nanomaterials is shown in figures 6.16, 6.17, and 6.18. The log plot reveals the electrical hysteresis loop in each case as displayed in the figures. From these figures, it was observed that TiO<sub>2</sub> and the nanocomposites materials depicted a small hysteresis loop compared to SiO<sub>2</sub> and MWCNTs with none. The observed hysteresis loops imply charge storage capability, memristive, and ferroelectric behavior. The previous review on the memristive capability of TiO<sub>2</sub> [53] established its ionic bonding structure which is associated with Ti<sup>3+</sup> and O<sup>-</sup>. Apparently, oxygen vacancies can easily translate ionically thereby leading to an auto-doping phase behavior. The constituent oxygen ions can easily cause an anodic attachment. The ionic translation and anodic attachment are consistent with previously reported ReRAM properties [54]. Furthermore, SiO<sub>2</sub> has insulating properties that are useful for the fabrication of memory devices. The previous report of Yao et al [55] on SiO<sub>2</sub> showed encouraging resistive switching and memories. The main mechanism has been the switching property originating from switching sites that are embedded in SiO<sub>2</sub> and nanogap region that are associated with Si-Si bonds. The hysteresis loop region of MWCNTs:Ti:Si (~6:6 at %) is higher than that of MWCNTs:Ti:Si (~10:10 at %), suggesting higher charge storage and memristive capability.

Although, pristine MWCNT gives conducting electrical features, however, the inclusion Ti:Si leads to semiconducting behavior with an apparent hysteresis loop that is associated with charge storage behavior. Presumably, the formation of MWCNTs:Ti:Si leads to an attachment of ionic Ti<sup>3+</sup> and Si-Si bonds which could be a major factor in the observed memristive /charge storage behavior. Also, the increase in the conductivity of the nanocomposites can be attributed to the decrease in oxygen vacancy as observed in O *K*-edge XANES spectra.

The decoration of TiO<sub>2</sub> and SiO<sub>2</sub> on MWNCTs surface transform its electrical system as confirmed in the figures. The nanocomposites materials are said to be useful for ferroelectric device applications based on the obtained results.

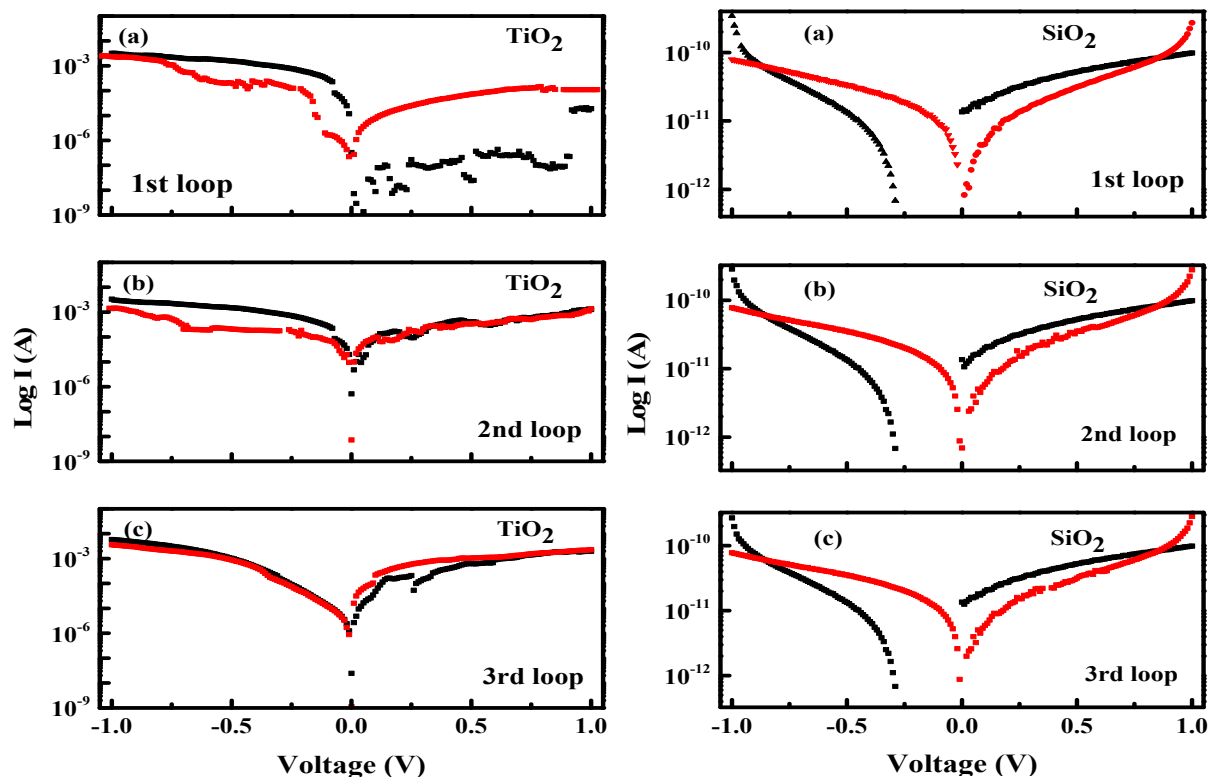
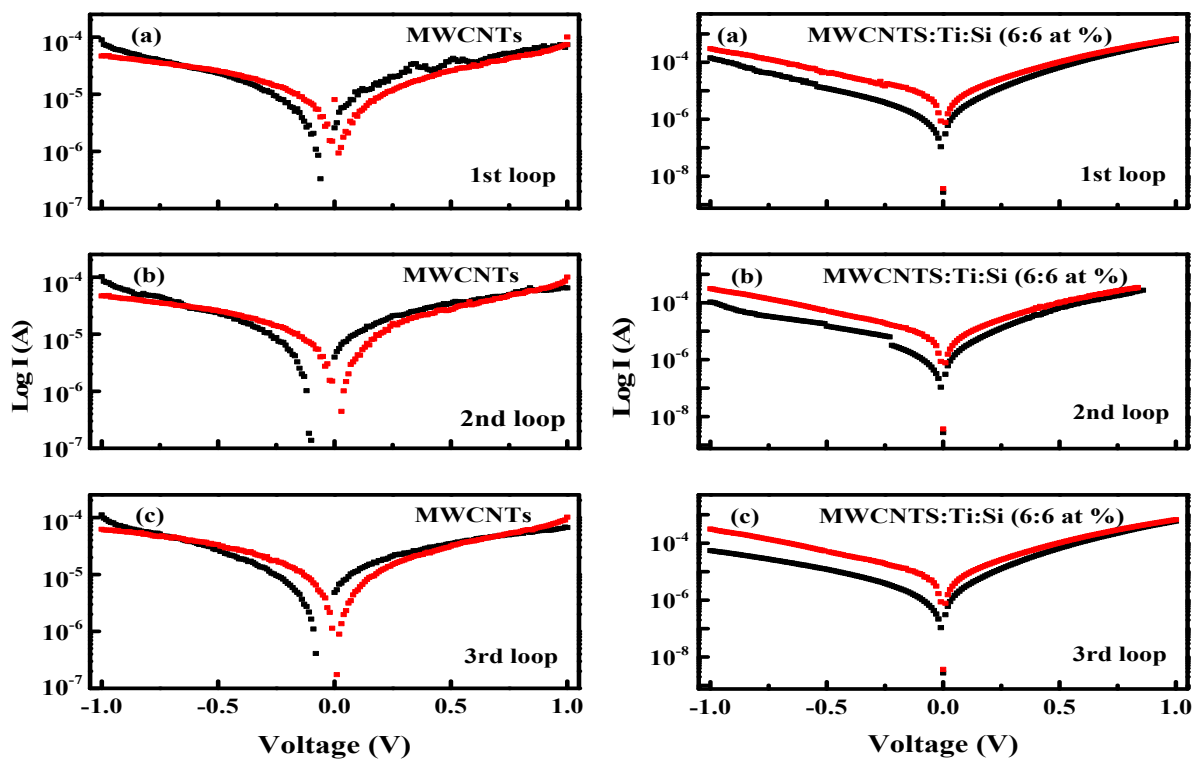
Figure 6.16. I-V log plot for TiO<sub>2</sub> and SiO<sub>2</sub>.

Figure 6.17. I-V log plot for MWCNTs and MWCNTs:Ti:Si (6:6 at %) nanocomposite.

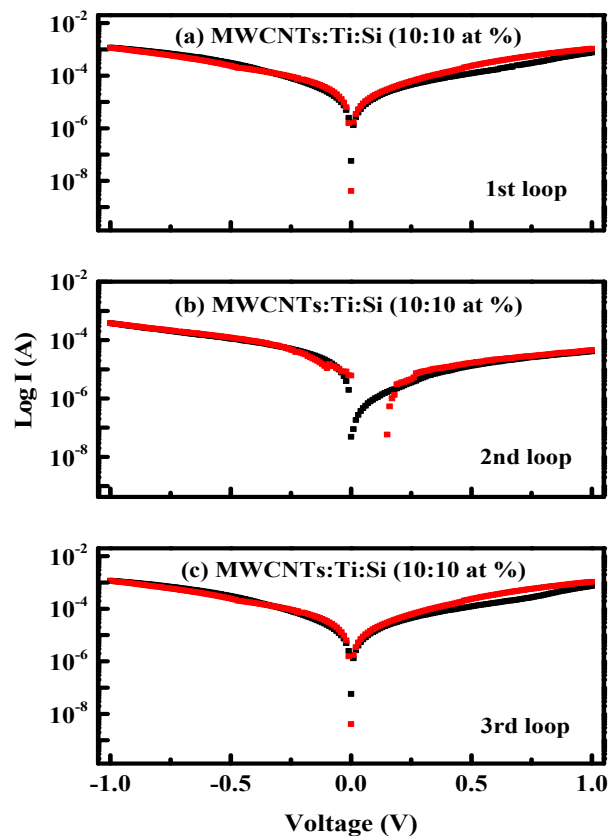


Figure 6.18. I-V log plot for MWCNTs:Ti:Si (10:10 at %) nanocomposite.

The agglomeration observed on the surface of MWCNTs:Ti:Si from FE-SEM image indicates a growth of Ti on MWCNTs surface and it is consistent with XRD and Raman results. The observed growth of Ti was confirmed by XRD due to the calculated increase in the crystallite sizes of Ti in the nanocomposites. This increase in crystallite size also corresponds to the decrease in the  $I_D/I_G$  ratios of the nanocomposites. The blue shift and the broadening of G band with occurrence of D' band observed from Raman spectra of the nanocomposite when compared to that of MWCNTs is in agreement with XANES and XPS data. The XPS C1s spectra for nanocomposites show a positive shift to that of pristine MWCNTs. The XANES C  $K$ -edge spectra show a steady decrease in the intensities of  $\pi^*$  ( $C-sp^2$ ) with the concentration of the bi-dopant in comparison with MWCNTs. This observation signifies a reduction in the  $sp^2$  clusters of MWCNTs with a corresponding increase in  $sp^3$  clusters. The electrical conductivity of the nanocomposites increases for Ti:Si  $\approx$  6:6 at% and further increase for Ti:Si



$\approx 10:10$  at% with a considerable hysteresis loop that is associated with charge storage behaviour. As observed from the XANES spectra, the intensities of O *K*-edge showed the same trend as C *K*-edge. This observation translates to a reduction in oxygen (O) vacancies as inversely reported in a previous study [56]. The reduction in O vacancy may be responsible for an increase in the concentration of the mobile electrons resulting in an increase in electrical conductivity of the nanocomposites [57].

## 6.4. Conclusion

The structural, electrical, and electronic transition of MWCNTs:Ti:Si nanocomposites have been examined using different research techniques. It was perceived that the  $sp^2$  content of MWCNTs decreased with increased Ti:Si content as observed from Raman spectroscopy. These observations correspond to the variation in the intensities of XANES C 1s spectra, indicating a transition in the electronic configuration of MWCNTs. XPS reveals the chemical bonding of the nanocomposites materials which shows that  $TiO_2$  and  $SiO_2$  were connected through Ti-O-Si bonding. The observed  $Ti^{3+}$  bond from XPS is capable of forming oxidizing radicals with  $O_2$  which could be useful for photocatalytic applications. The electrical conductivity of the nanocomposites increased but varies when compared to MWCNTs with a considerable electrical hysteresis loop. The results from this study reveal the possibilities of utilizing MWCNTs:TiO<sub>2</sub>:SiO<sub>2</sub> nanocomposites for several electrical, electronic, and photocatalytic activity applications.

## References

- [1] A. Kumar, K. Kumar, P. K. Ghosh, and K. L. Yadav, "MWCNT/TiO<sub>2</sub> hybrid nano filler toward high-performance epoxy composite," *Ultrason. Sonochem.*, vol. 41, no. 3, pp. 37–46, 2018.
- [2] R. H. Baughman, A. A. Zakhidov, and W. A. de Heer, "Carbon Nanotubes — the Route Toward," *Sci. compass*, vol. 787, no. 2002, pp. 787–792, 2012.
- [3] M. Daenen, R. D. de Fouw, B. Hamers, P. G. A. Janssen, K. Schouteden, and M. A. J. Veld, "The Wondrous World of Carbon Nanotubes," *Eindhoven Univ. Technol.*, no. 2 pp. 1–35, 2003.
- [4] M. Božič *et al.*, "Enhanced catalytic activity of the surface modified TiO<sub>2</sub>-MWCNT nanocomposites under visible light," *J. Colloid Interface Sci.*, vol. 465, no. 4 pp. 93–105, 2016.
- [5] V. V. Bolotov *et al.*, "Formation of the N-MWCNT/TiO<sub>x</sub> nanocomposite structure using magnetron method for gas sensing application," *AIP Conf. Proc.*, vol. 1876, no. 2017, 2017.
- [6] R. J. Baierle, S. B. Fagan, R. Mota, A. J. R. da Silva, and A. Fazzio, "Electronic and structural properties of silicon-doped carbon nanotubes," *Phys. Rev. B - Condens. Matter Mater. Phys.*, vol. 64, no. 8, pp. 854131–854134, 2001.
- [7] J. J. Adjizian *et al.*, "Boron- and nitrogen-doped multi-wall carbon nanotubes for gas detection," *Carbon*, vol. 66, pp. 662–673, 2014.
- [8] B. Czech, W. Buda, S. Pasiieczna-Patkowska, and P. Oleszczuk, "MWCNT-TiO<sub>2</sub>-SiO<sub>2</sub>

- nanocomposites possessing the photocatalytic activity in UVA and UVC,” *Appl. Catal. B Environ.*, vol. 162, pp. 564–572, 2015.
- [9] B. Czech and W. Buda, “Photocatalytic treatment of pharmaceutical wastewater using new multiwall-carbon nanotubes/TiO<sub>2</sub>/SiO<sub>2</sub> nanocomposites,” *Environ. Res.*, vol. 137, pp. 176–184, 2015.
- [10] B. Czech and K. Tyszczyk-Rotko, “Visible-light-driven photocatalytic removal of acetaminophen from water using a novel MWCNT-TiO<sub>2</sub>-SiO<sub>2</sub> photocatalysts,” *Sep. Purif. Technol.*, vol. 206, no. May, pp. 343–355, 2018.
- [11] D. C. Hurum, K. A. Gray, T. Rajh, and M. C. Thurnauer, “Recombination pathways in the degussa P25 formulation of TiO<sub>2</sub>: Surface versus lattice mechanisms,” *J. Phys. Chem. B*, vol. 109, no. 2, pp. 977–980, 2005.
- [12] C. Song *et al.*, “Functionalization of silicon-doped single walled carbon nanotubes at the doping site: An ab initio study,” *Phys. Lett. Sect. A Gen. At. Solid State Phys.*, vol. 358, no. 2, pp. 166–170, 2006.
- [13] C. Gao, Z. Guo, J. H. Liu, and X. J. Huang, “The new age of carbon nanotubes: An updated review of functionalized carbon nanotubes in electrochemical sensors,” *Nanoscale*, vol. 4, no. 6, pp. 1948–1963, 2012.
- [14] J. A. Oke, D. O. Idisi, S. Sarma, S. J. Moloi, S. C. Ray, and K. H. Chen, “Diamond & Related Materials Tuning of electronic and electrical behaviour of MWCNTs-TiO<sub>2</sub> nanocomposites,” *Diam. Relat. Mater.*, vol. 100, no. 6, pp. 107570, 2019.
- [15] J. A. Oke *et al.*, “Electronic , Electrical , and Magnetic Behavioral Change of SiO<sub>2</sub> - NP- Decorated MWCNTs,” *ACS Omega*, vol. 4, no 11, pp. 14589–14598, 2019.

- [16] V. Vatanpour, S. S. Madaeni, R. Moradian, S. Zinadini, and B. Astinchap, "Fabrication and characterization of novel antifouling nanofiltration membrane prepared from oxidized multiwalled carbon nanotube/polyethersulfone nanocomposite," *J. Memb. Sci.*, vol. 375, no. 1-2, 2011.
- [17] P. Das, A. Saha, A. R. Maity, S. C. Ray, and N. R. Jana, "Silicon nanoparticle based fluorescent biological label via low temperature thermal degradation of chloroalkylsilane," *Nanoscale*, vol. 5, no. 13, pp. 5732–5737, 2013.
- [18] D. Chaudhary, N. Khare, and V. D. Vankar, "Ag nanoparticles loaded TiO<sub>2</sub>/MWCNT ternary nanocomposite: A visible-light-driven photocatalyst with enhanced photocatalytic performance and stability," *Ceram. Int.*, vol. 42, no. 14, pp. 15861–15867, 2016.
- [19] V. B. Koli, A. G. Dhodamani, A. V. Raut, N. D. Thorat, S. H. Pawar, and S. D. Delekar, "Visible light photo-induced antibacterial activity of TiO<sub>2</sub>-MWCNTs nanocomposites with varying the contents of MWCNTs," *J. Photochem. Photobiol. A Chem.*, vol. 328, no. May, pp. 50–58, 2016.
- [20] R. Casati, M. H. Nasab, M. Coduri, V. Tirelli, and M. Vedani, "Effects of platform pre-heating and thermal-treatment strategies on properties of alsi10mg alloy processed by selective laser melting," *Metals (Basel)*, vol. 8, no. 11, p. 954, 2018.
- [21] Y. Chen, N. Du, H. Zhang, and D. Yang, "Facile synthesis of uniform MWCNT@Si nanocomposites as high-performance anode materials for lithium-ion batteries," *J. Alloys Compd.*, vol. 622, pp. 966–972, 2015.
- [22] Y. Luo *et al.*, "Electric field induced structural color changes of SiO<sub>2</sub>@TiO<sub>2</sub>core-shell colloidal suspensions," *J. Mater. Chem. C*, vol. 2, no. 11, pp. 1990–1994, 2014.

- [23] S. Delpeux, A. Jitianu, S. Bonnamy, R. Benoit, T. Cacciaguerra, and F. Béguin, “Synthesis and characterization of carbon nanotubes–TiO<sub>2</sub> nanocomposites,” *Carbon N. Y.*, vol. 42, no. 5–6, pp. 1147–1151, 2004.
- [24] N. D. Abazović, M. I. Čomor, M. D. Dramićanin, D. J. Jovanović, S. P. Ahrenkiel, and J. M. Nedeljković, “Photoluminescence of anatase and rutile TiO<sub>2</sub> particles,” *J. Phys. Chem. B*, vol. 110, no. 50, pp. 25366–25370, 2006.
- [25] Y. S. Hu, L. Kienle, Y. G. Guo, and J. Maier, “High lithium electroactivity of nanometer-sized rutile TiO<sub>2</sub>,” *Adv. Mater.*, vol. 18, no. 11, pp. 1421–1426, 2006.
- [26] L. A. A. Rodriguez and Di. N. Travessa, “Core/Shell Structure of TiO<sub>2</sub>-Coated MWCNTs for Thermal Protection for High-Temperature Processing of Metal Matrix Composites,” *Adv. Mater. Sci. Eng.*, vol. 2018, 2018.
- [27] J. Yu, T. Ma, and S. Liu, “Enhanced photocatalytic activity of mesoporous TiO<sub>2</sub> aggregates by embedding carbon nanotubes as electron-transfer channel,” *Phys. Chem. Chem. Phys.*, vol. 13, no. 8, pp. 3491–3501, 2011.
- [28] J. Yu, J. Fan, and B. Cheng, “Dye-sensitized solar cells based on anatase TiO<sub>2</sub> hollow spheres/carbon nanotube composite films,” *J. Power Sources*, vol. 196, no. 18, pp. 7891–7898, 2011.
- [29] S. C. Ray, S. K. Bhunia, A. Saha, and N. R. Jana, “Electric and ferro-electric behaviour of polymer-coated graphene-oxide thin film,” *Phys. Procedia*, vol. 46, no. 19, pp. 62–70, 2013.
- [30] S. D. Delekar *et al.*, “Structural and Optical Properties of Nanocrystalline TiO<sub>2</sub> with Multiwalled Carbon Nanotubes and Its Photovoltaic Studies Using Ru(II) Sensitizers,”

- ACS Omega*, vol. 3, no. 3, pp. 2743–2756, 2018.
- [31] W. Kiefer, A. P. Mazzolini, and P. R. Stoddart, “Monitoring oxidation of multiwalled carbon nanotubes by Raman spectroscopy,” *J. Raman Spectrosc.*, vol. 38, no. 4, pp. 1538–1553, 2007.
- [32] D. O. Idisi *et al.*, “Electronic, electrical and magnetic behaviours of reduced graphene-oxide functionalized with silica coated gold nanoparticles,” *Appl. Surf. Sci.*, vol. 483, no. 12, pp. 106–113, 2019.
- [33] T. I. T. Okpalugo, P. Papakonstantinou, H. Murphy, J. McLaughlin, and N. M. D. Brown, “High resolution XPS characterization of chemical functionalised MWCNTs and SWCNTs,” *Carbon N. Y.*, vol. 43, no. 1, pp. 153–161, 2005.
- [34] D. Su, C. L. Teoh, A. Samanta, N. Y. Kang, S. J. Park, and Y. T. Chang, The development of a highly photostable and chemically stable zwitterionic near-infrared dye for imaging applications. *Chem. Comm.*, vol. 51, no. 19, pp.3989-3992, 2015.
- [35] L. Zhang, N. Kuramoto, Y. Azuma, A. Kurokawa, and K. Fujii, “Thickness Measurement of Oxide and Carbonaceous Layers on a <sup>28</sup> Si Sphere by XPS,” *IEEE Trans. Instrum. Meas.*, vol. 66, no. 6, pp. 1297–1303, 2017.
- [36] H. Zhang, X. Luo, J. Xu, B. Xiang, and D. Yu, “Synthesis of TiO<sub>2</sub>/SiO<sub>2</sub> core/shell nanocable arrays,” *J. Phys. Chem. B*, vol. 108, no. 39, pp. 14866–14869, 2004.
- [37] B. S. Huang, H. H. Tseng, and M. Y. Wey, “Comparison of visible-light-driven routes of anion-doped TiO<sub>2</sub> and composite photocatalyst,” *J. Ceram. Soc. Japan*, vol. 117, no. 1366, pp. 753–758, 2009.
- [38] X. Zhou, X. Ge, R. Tang, T. Chen, and G. Wang, “Preparation and catalytic property of

- modified multi-walled carbon nanotube-supported TiO<sub>2</sub> for the transesterification of dimethyl carbonate with phenol,” *Cuihua Xuebao/Chinese J. Catal.*, vol. 35, no. 4, pp. 481–489, 2014.
- [39] L. Bin Xiong, J. L. Li, B. Yang, and Y. Yu, “Ti<sup>3+</sup> in the surface of titanium dioxide: Generation, properties and photocatalytic application,” *J. Nanomater.*, vol. 2012, no. 5, pp. 1–13, 2012.
- [40] K. Szot, W. Speier, G. Bihlmayer, and R. Waser, “Switching the electrical resistance of individual dislocations in single-crystalline SrTiO<sub>3</sub>,” *Nat. Mater.*, vol. 5, no. 4, pp. 312–320, 2006.
- [41] M. Pedio, F. Borgatti, A. Giglia, N. Mahne, S. Nannarone, S. Giovannini, C. Cepek, E. Magnano, G. Bertoni, E. Spiller and M. Sancrotti, Annealing temperature dependence of C<sub>60</sub> on silicon surfaces: bond evolution and fragmentation as detected by NEXAFS. *Phys. Scr.*, vol. 2005, no. 115, p.695, 2005.
- [42] H. X. Deng, S. H. Wei, S. S. Li, J. Li, and A. Walsh, “Electronic origin of the conductivity imbalance between covalent and ionic amorphous semiconductors,” *Phys. Rev. B - Condens. Matter Mater. Phys.*, vol. 87, no. 12, pp. 1–5, 2013.
- [43] S. C. Ray, D. K. Mishra, A. M. Strydom, and P. Papakonstantinou, “Magnetic behavioural change of silane exposed graphene nanoflakes,” *J. Appl. Phys.*, vol. 118, no. 11, 2015.
- [44] C. W. Pao, S. C. Ray, H. M. Tsai, Y. S. Chen, H. C. Chen, I. N. Lin, W. F. Pong, J. W. Chiou, M. H. Tsai, N. G. Shang and P. Papakonstantinou, “Change of structural behaviors of organo-silane exposed graphene nanoflakes,” *J. Phys. Chem. C*, vol. 114, no. 18, pp. 8161–8166, 2010.

- [45] S. C. Ray, C. W. Pao, H. M. Tsai, J. W. Chiou, W. F. Pong, C. W. Chen, M. H. Tsai, P. Papakonstantinou, L. C. Chen, and K. H. Chen, "A comparative study of the electronic structures of oxygen- and chlorine-treated nitrogenated carbon nanotubes by x-ray absorption and scanning photoelectron microscopy," *Appl. Phys. Lett.*, vol. 91, no. 20, pp. 202102, 2007.
- [46] A. Kuznetsova, I. Popova, J. T. Yates Jr, M. J. Bronikowski, C. B. Huffman, J. Liu, R. E. Smalley, H. H. Hwu and J. G. Chen, "Oxygen-containing functional groups on single-wall carbon nanotubes: NEXAFS and vibrational spectroscopic studies," *J. Am. Chem. Soc.*, vol. 123, no. 43, pp. 10699–10704, 2001.
- [47] S. Banerjee, T. Hemraj-Benny, S. S. Wong, M. Balasubramanian, J. A. Misewich, and D. A. Fischer, "Ozonized single-walled carbon nanotubes investigated using NEXAFS spectroscopy," *Chem. Commun.*, vol. 10, no. 7, pp. 772–773, 2004.
- [48] M. Magnuson, M. Mattesini, S. Li, C. Höglund, M. Beckers, L. Hultman and O. Eriksson, "Bonding mechanism in the nitrides Ti<sub>2</sub>AlN and TiN: An experimental and theoretical investigation," *Phys. Rev. B - Condens. Matter Mater. Phys.*, vol. 76, no. 19, pp. 1–9, 2007.
- [49] Z. Y. Wu, F. Jollet and F. Seifert, "Electronic structure analysis of  $\alpha$ -SiO<sub>2</sub> via x-ray absorption near-edge structure at the Si K, L<sub>2,3</sub> and O K edges," *J. Phys. Condens. Matter*, vol. 10, no. 36, pp. 8083–8092, 1998.
- [50] M. W. Gaultois and A. P. Grosvenor, "XANES and XPS investigations of (TiO<sub>2</sub>)<sub>x</sub>(SiO<sub>2</sub>)<sub>1-x</sub>: The contribution of final-state relaxation to shifts in absorption and binding energies," *J. Mater. Chem.*, vol. 21, no. 6, pp. 1829–1836, 2011.
- [51] S. Di Mo and W. Y. Ching, "X-ray absorption near-edge structure in alpha-quartz and



- stishovite: Ab initio calculation with core-hole interaction,” *Appl. Phys. Lett.*, vol. 78, no. 24, pp. 3809–3811, 2001.
- [52] F. M. F. de Groot, M. O. Figueiredo, M. J. Basto, M. Abbate, H. Petersen, and J. C. Fuggle, “2 p X-ray absorption of titanium in minerals,” *Phys. Chem. Miner.*, vol. 19, no. 3, pp. 140–147, 1992.
- [53] E. Gale, “TiO<sub>2</sub>-based memristors and ReRAM: Materials, mechanisms and models (a review),” *Semicond. Sci. Technol.*, vol. 29, no. 10, pp. 1–29, 2014.
- [54] J. Yao, Z. Sun, L. Zhong, D. Natelson, and J. Tour, “Supporting Information - Resistive Switches and Memories from Silicon Oxide,” *Nano Lett.*, vol. 10, no. 1, pp. 1–7, 2010.
- [55] J. Schneider, M. Matsuoka, M. Takeuchi, J. Zhang, Y. Horiuchi, M. Anpo and D.W. Bahnemann, Understanding TiO<sub>2</sub> photocatalysis: mechanisms and materials. *Chemical reviews*, vol. 114 no. 19, pp. 9919-9986, 2014.
- [56] Z. Shuai, L. Wang and Q. Li, Evaluation of charge mobility in organic materials: from localized to delocalized descriptions at a first-principles level. *Advan. Mater.*, vol. 23, no. 9, pp. 1145-1153, 2011.
- [57] B. Ghosh, S.C. Ray, M. Pontsho, S. Sarma, D.K. Mishra, Y.F. Wang, W.F. Pong, and A.M. Strydom, Defect induced room temperature ferromagnetism in single crystal, polycrystal, and nanorod ZnO: A comparative study. *J Appl. Phys.*, vol. 123, no. 16, pp. 161507, 2018.

## **Chapter Seven**

### **Summary, Conclusions, Recommendations and Future work**

## 7.1 Thesis summary

The electronic and magnetic behavior of a material depends on the interaction of electrons in the material when subjected to an electric and magnetic field. The theory of an electron excellently explains the electronic, magnetic, and electrical properties of the material. This theory is important since new technology depends on it. The efforts in developing new technology have led to the search of carbon nanotubes (CNTs), which was utilized for this study.

Carbon materials exist in amorphous, diamond, and graphite structures. The well-known allotropes of carbon are graphite and diamond. Research methods have expanded the existing knowledge about carbonaceous materials and more allotropes have been identified. These allotropes include graphene, fullerene, and carbon nanotubes. Most research in material science has been about the allotropes (graphitic carbon) as a result of their excellent electrical conductivity, thermal properties, and mechanical strength. Over a few years, CNTs have attracted attentiveness when compared to graphene and fullerene, due to their better properties.

After the discovery of CNTs by Iijima in 1991, different techniques (arc discharge, laser ablation, and chemical vapor deposition (CVD)) have been used to synthesize CNTs. Arc discharge and laser ablation are techniques used in synthesizing CNTs with high quality. However, they have a disadvantage of being costly and low scale production. CVD is the most used technique in synthesizing CNTs on a large scale in the presence of a catalyst, which has the degree of control over length, diameter, and morphology. Due to the catalyst used, CNTs can be purified using oxidation, ultrasonication, acid treatment, annealing, micro filtering, and functionalization techniques. CNTs consist of single-wall (SW) CNT, double-wall (DW)

CNTs, and multi-wall (MW) CNTs, which are hollow, cylindrical nanostructures (wrapped graphene sheet) with open or closed (fullerene) ends.

The structure of CNTs depends on how the graphene sheet is been wrapped, which gives armchair, zigzag and chiral structures. These structures also have an effect on their electrical properties. Most CNTs are conducting and diamagnetic in nature. The surface of CNTs needs to be modified to establish its semiconducting and magnetic behavior. The two main methods used in functionalizing CNTs are covalent and non-covalent modification. The attachment of semiconducting and magnetic nanomaterials onto its surface either by covalent or non-covalent modification makes them a potential material for different electronic and magnetic applications.

The current study involves MWCNTs (a type of CNTs) which are more cost-effective and promising materials for several applications. The material is one-dimensional with perfect spin-transport medium and is ballistic with a weak spin-orbit coupling which yields a long spin relaxation time. SWCNTs act as a metallic or semiconductor with 0 to 2.0 eV bandgap. MWCNTs are composed of several coaxial SWCNTs and mostly conducting in nature. SWCNT having closed ends are recognized as fullerene, which has limitations as they cannot be produced in large quantities. These characteristics and behavior of MWCNTs made it an exceptional material then fullerene and graphene.

Despite the unique properties of MWCNTs, there is a need to modify its properties for preferred and more device applications, which is due to the following reasons; MWCNTs lack a magnetic moment which made them diamagnetic materials. Also, MWCNTs are conducting in nature and are low-density materials. Based on this fact, MWCNTs needs to be functionalized with some nanoparticle materials to establish their magnetic moment, semiconducting behavior with high storage density, and to vary its magnetization for different electronic, electrical, and

magnetic applications. Silicon dioxide ( $\text{SiO}_2$ ), Titanium dioxide ( $\text{TiO}_2$ ), and a composite of  $\text{SiO}_2:\text{TiO}_2$  were used to functionalize MWCNTs, the reason being that they are cheaper and abundant in nature. Also, silicon is a semiconducting material that acts as an insulating as well as conducting material. On the other hand, titanium has excellent physical properties such as lightweight, corrosion resistance, and high strength which can be oxidized to produce  $\text{TiO}_2$ .  $\text{TiO}_2$  could be considered as a supporting nanomaterial due to its semiconducting properties, nontoxic, and possibility of charge transfer behavior.

$\text{SiO}_2$ ,  $\text{TiO}_2$ , and  $\text{SiO}_2:\text{TiO}_2$  were used to functionalize MWCNTs using the covalent method. The materials used in synthesizing these nanomaterials were purchased from Sigma-Aldrich (Pty) Ltd. The synthesis of  $\text{SiO}_2$ , MWCNTs, MWCNTs: $\text{SiO}_2$ , MWCNTs- $\text{TiO}_2$ , and MWCNTs: $\text{TiO}_2:\text{SiO}_2$  nanocomposites were performed using thermal decomposition, spray pyrolysis and CVD, toluene suspension and hydrothermal process, respectively. The sample characterizations were also performed using FE-SEM, XRD, Raman spectroscopy, XPS, XANES, I-V, SQUID, and ESR to establish their electrical, electronic, and magnetic properties.

$\text{SiO}_2$ , MWCNTs, and MWCNTs:Si nanocomposites were prepared and characterized using the above techniques. MWCNTs were decorated with  $\text{SiO}_2$  at two different concentrations of Si  $\sim 1.5$  at % and Si  $\sim 5.75$  at %. The FE-SEM images of  $\text{SiO}_2$  and MWCNTs displayed a typical spherical and tube-like profile, respectively. MWCNTs: $\text{SiO}_2$  nanocomposites depicted a root-like profile, indicating uniform deposition of  $\text{SiO}_2$  onto the surface of MWCNTs. The EDS spectra showed that there are no impurities in the nanocomposites. From the XRD patterns of  $\text{SiO}_2$  and MWCNTs, usual peaks were observed. The pattern of Si  $\sim 1.5$  at % showed that the structure of MWCNTs was not destroyed and that of Si  $\sim 5.75$  at % revealed that carbon atoms

were replaced by Si atoms. The  $I_D/I_G$  ratios observed from Raman were indications of an increase in  $sp^2$  and  $sp^3$  content for Si ~1.5 at % and Si ~5.75 at % nanocomposites, respectively.

The Raman result corresponds to the increase and decrease in the intensities of C K-edge spectra, making  $sp^3$  content richer for Si ~5.75 at %. The O K-edge spectra also displayed an increase and decrease the intensities of Si ~1.5 at % and Si ~5.75 at %, implying an increase and decrease in the number of O vacancies, respectively. The XPS spectra depicted a defect structure for Si ~1.5 at% and a strong bond for Si ~5.75 at % nanocomposites. From the M-H loop, it is observed that the magnetization slightly increases and decreases drastically for Si ~1.5 at% and Si ~5.75 at %, respectively. In reference to XPS spectra, the strong bond between MWCNTs and  $SiO_2$  (Si-C tetrahedral bonding) led to an increase of  $sp^3$  hybridization, thereby decreasing the magnetization of MWCNTs. On the other hand, the formation of Si-C-O (defect structure) and -COOH/C-O bonds led to a slight increase in the magnetization of MWCNTs. This increase was a result of the oxygen functional group, which produce a positive center to capture an electron in a restricted form. The restricted electron retained magnetic moment which contributed to the enhanced magnetization in Si ~1.5 at %. These results also correspond to the observations in C K-edge and O K-edge XANES spectroscopy.

The electrical conductivity of Si ~1.5 at % increases, which is due to different energy levels created by the dangling bond formed in MWCNTs and the non-restricted electrons were able to move freely from valence band to conduction band. The slight decrease in the electrical conductivity of Si ~5.75 was due to the transformation from the conducting nature of MWCNTs to a semiconducting structure of the nanocomposite.

The synthesis and characterizations of  $TiO_2$ , MWCNTs, and MWCNTs:Ti nanocomposites were achieved using the research methods mentioned earlier.  $TiO_2$  was deposited on the surface of MWCNTs at Ti ~15 at % and Ti ~20 at % concentrations.  $TiO_2$ , MWCNTs, and

MWCNTs:Ti nanocomposites displayed the spherical, tube-like, and homogenous distribution of TiO<sub>2</sub> agglomeration on MWCNTs surface, respectively. The EDS spectra confirmed that the nanocomposites contain carbon, oxygen, and titanium materials. From XRD, a usual pattern was observed for MWCNTs, while TiO<sub>2</sub> and MWCNTs:Ti nanocomposites depicted anatase-TiO<sub>2</sub> phase, indicating carbon atoms were replaced by Ti atoms. The calculated crystallite size showed an increase for Ti ~15 at % and decreases for Ti ~20 at % when compared to MWCNTs. Raman showed the I<sub>D</sub>/I<sub>G</sub> ratio of 1.3 for MWCNTs, the inclusion of Ti ~15 at % in MWCNTs decreases the ratio to 0.9 and on Ti ~20 at % inclusion, the ratio increases to 1.7. The variation in the I<sub>D</sub>/I<sub>G</sub> ratio indicates a decrease and increase in sp<sup>2</sup> hybridization. It was observed from XPS, that the increase in Ti content in MWCNTs decreases its carbon content.

XPS also shows that the C–O and Ti–O bonds from C 1s and O 1s, respectively led to the good connection between MWCNTs and TiO<sub>2</sub>, indicating Ti–O–C bonds are present. Ti<sup>4+</sup> oxidation state was also present as a result of electrons transferring through Ti–O–C bonds, which change the electron density in MWCNTs:Ti nanocomposites. From C 1s XANES spectra, the observed C–O/C–H bonding was as a result of a change in sp<sup>3</sup> hybridization or metal bonding to MWCNTs lattice. A decrease in the intensity of Ti L<sub>3,2</sub>-edge XANES spectra with an increase in the content of Ti also confirms that Ti atoms were replaced by oxygen and/or carbon in the MWCNTs. The observed changes in XPS and XANES indicate that TiO<sub>2</sub> has influenced the bonding and electronic structure of MWCNTs.

The electrical conductivity of MWCNTs:Ti nanocomposites increases compared to MWCNTs. Although, enhancing the conductivity of MWCNTs was not our aim since the material is highly conductive but it was to improve its memristive capacity. The hysteresis loop which was observed in MWCNTs with ~15 at % content of TiO<sub>2</sub> is higher than that of MWCNTs with 20 at % content of TiO<sub>2</sub> indicating higher charge storage properties and memristive behavior.

The previously mentioned characterization techniques were used to study the synthesized TiO<sub>2</sub>, SiO<sub>2</sub>, MWCNTs, and MWCNTs:Ti:Si nanocomposites to establish the novelty of the nanocomposites materials for various applications. TiO<sub>2</sub>:SiO<sub>2</sub> was included in the suspension of MWCNTs at different stoichiometric ratios of Ti:Si ~6:6 at % and Ti:Si ~10:10 at %. The images of TiO<sub>2</sub>, SiO<sub>2</sub>, MWCNTs, and MWCNTs:Ti:Si nanocomposites depicted a roughly spherical, ball cluster, tube-like, and root-like profiles, respectively. The Ti:Si ~6:6 at % nanocomposite showed a uniform dispersion of TiO<sub>2</sub>:SiO<sub>2</sub> on MWCNTs lattice, while that of Ti:Si ~10:10 at % nanocomposite displayed some agglomeration. The observed agglomeration indicates that MWCNTs allowed the growth of Ti on its surface as confirmed later by XRD. The EDS displayed a spectrum without contaminants in the nanocomposites. The XRD patterns presented normal peaks for anatase TiO<sub>2</sub>, SiO<sub>2</sub>, and MWCNTs, while the nanocomposites showed anatase and rutile phases of TiO<sub>2</sub>, indicating TiO<sub>2</sub> and SiO<sub>2</sub> changed the crystalline structure of MWCNTs. The Ti:Si ~6:6 at % nanocomposites also displayed a very less intense carbon peak, which later vanished as Ti:Si content increases on MWCNTs lattice, implying that carbon atoms were gradually replaced by Ti atoms. The calculated crystallite size showed an increase in the growth of Ti on MWCNTs lattice.

Raman spectra of the nanocomposites depicted three peaks (B<sub>1g</sub>, A<sub>1g</sub>, and E<sub>g</sub>) of anatase TiO<sub>2</sub> with four carbon peaks (D, G 2D and D+G) for MWCNTs. A slight shift was observed for the anatase peaks of the nanocomposites when compared to pristine anatase TiO<sub>2</sub>, which may be due to an increase in the crystallite size of anatase TiO<sub>2</sub> as observed from XRD. The I<sub>D</sub>/I<sub>G</sub> ratios of MWCNTs and the nanocomposites were calculated to ascertain the degree of their hybridization and graphitization. The I<sub>D</sub>/I<sub>G</sub> ratios were obtained from the peak intensity of D and G peaks. The ratios showed a decrease in the I<sub>D</sub>/I<sub>G</sub> ratios, which is an indication of an increase in sp<sup>3</sup> hybridization but a decrease in graphitization. This decrease implies that carbon atoms were replaced by Ti:Si atoms.



From C *K*-edge XANES spectrum, there is a variation in the intensities of MWCNTs and Ti:Si nanocomposites, indicating that the graphitization of MWCNTs is decreasing gradually translating to a rise in  $sp^3$  content as observed from Raman. The O *K*-edge spectra also depicted a decrease in the intensities of the nanocomposites compared to MWCNTs, implying deoxidation has occurred. XPS revealed the chemical bonding of the nanocomposites materials which shows that  $TiO_2$  and  $SiO_2$  were connected through Ti-O-Si bonding and other bonds like Ti-O-Ti/Ti-O-H/C=O/Ti-O-Si were responsible for the deoxidation observed in O *K*-edge XANES spectra. The observed  $Ti^{3+}$  state from XPS can form oxidizing radicals with  $O_2$  which can be useful for photocatalytic activity.

The electrical structure of MWCNTs and  $SiO_2$  displayed conducting and insulating structures, respectively, while  $TiO_2$  and MWCNTs:Ti:Si nanocomposites are semiconducting in nature. An increased variation was observed in the electrical conductivity of Ti:Si nanocomposites compared to MWCNTs. The increase in conductivity may be due to the numbers of non-restricted electrons that were able to jump from the valence band to the conduction band. The I-V log plot displayed a small hysteresis loop for the nanocomposites material, implying a ferroelectric behavior.

## 7.2 Conclusions

This study synthesized and characterized  $TiO_2$ ,  $SiO_2$ , MWCNTs, MWCNTs: $SiO_2$  MWCNTs- $TiO_2$ , and MWCNTs: $TiO_2$ : $SiO_2$  nanocomposites using different research technique and their electronic, electrical, and magnetic behavior were studied. The results obtained were discussed in chapters four, five, and six and the following conclusions were deduced accordingly:

The study of MWCNTs: $SiO_2$  showed that the electrical conductivity of the Si ~1.5 and Si ~.75 at % nanocomposites increases and decreases, respectively when compared with MWCNTs.

An electrical hysteresis loop was observed for Si ~5.75 at % nanocomposite, indicating a ferroelectric behavior. Also, the magnetic behavior of nanocomposites showed a semiconducting structure compared to the semi-metallic structure of MWCNTs with a variation in the magnetization of the nanocomposites.

The study of MWCNTs-TiO<sub>2</sub> nanocomposites showed that the electrical structure of MWCNTs transforms from a conductor to a semiconductor with an increase in electrical conductivity due to the introduction of TiO<sub>2</sub> nanoparticles. The nanocomposite materials also displayed a pronounced hysteresis loop indicating a ferroelectric, memristive, and charge storage behavior due to Ti<sup>+</sup> charge transfer in MWCNTs.

The investigated MWCNTs:TiO<sub>2</sub>:SiO<sub>2</sub> nanocomposites revealed that Ti<sup>3+</sup> state is present in the nanocomposites. The observed Ti<sup>3+</sup> bond is capable of forming oxidizing radicals with O<sub>2</sub> which could be useful for photocatalytic applications. The electrical conductivity of the nanocomposites increased but varies when compared to the metallic structure of MWCNTs. A semiconducting structure was also observed for the nanocomposites with a minute electrical hysteresis loop, indicating a change in the electrical structure of MWCNTs.

In general, these studies revealed different routes in tuning or modifying the electrical, electronic, and magnetic behavior of MWCNTs for different electrical, electronic, and magnetic device applications.

### **7.3 Recommendations**

This study has established the electrical, electronic, and magnetic behavior of MWCNTs:SiO<sub>2</sub>, MWCNTs-TiO<sub>2</sub>, and MWCNTs:TiO<sub>2</sub>:SiO<sub>2</sub> nanocomposites and has shown different ways in which they can be synthesized and characterized. It has also established the fact that TiO<sub>2</sub>, SiO<sub>2</sub>, and TiO<sub>2</sub>:SiO<sub>2</sub> can tune properties of MWCNTs for different applications. Hence, these

nanocomposites materials could be useful for different electrical, electronic, and magnetic applications where ferroelectric, ferromagnetic, memristive, charge storage, and photocatalytic behavior are preferred.

## **7.4 Future work**

Means to improve the properties of MWCNTs using covalent functionalization through different synthesis methods have been achieved. However, more methods should be explored in synthesizing and purifying MWCNTs in order to develop or produce more cheaply and good quality of MWCNTs. In addition, effort should be made in the covalent functionalization of MWCNTs using non-acid as an oxidizing agent to avoid large usage of acid. Moreover, further work needs to be done on the functionalization of MWCNTs using the non-covalent method to improve their properties for several novel applications.

## **Appendix**

### **Published Papers**

## Appendix 1

This is an open access article published under an ACS AuthorChoice License, which permits copying and redistribution of the article or any adaptations for non-commercial purposes.



Cite This: ACS Omega 2019, 4, 14589–14598

http://pubs.acs.org/journal/acsofd

Article

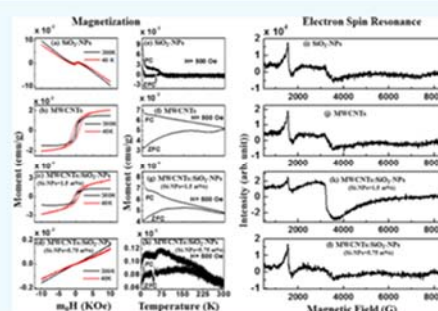
## Electronic, Electrical, and Magnetic Behavioral Change of SiO<sub>2</sub>-NP-Decorated MWCNTs

James A. Oke,<sup>†</sup> David O. Idisi,<sup>†</sup> Sweety Sarma,<sup>†</sup> Sabata J. Moloi,<sup>†</sup> Sekhar C. Ray,<sup>\*,†,‡</sup> Kuan Hung Chen,<sup>‡</sup> Anirudha Ghosh,<sup>‡</sup> Abhijeet Shelke,<sup>‡</sup> and Way Faung Pong<sup>\*,‡</sup>

<sup>†</sup>Department of Physics, CSET, University of South Africa, Private Bag X6, Florida, 1710, Science Campus, Christiaan de Wet and Pioneer Avenue, Florida Park, Johannesburg, South Africa

<sup>‡</sup>Department of Physics, Tamkang University, Tamsui 251, Taipei, Taiwan

**ABSTRACT:** Silicon-oxide-nanoparticle (SiO<sub>2</sub>-NP) heteroatoms were decorated/deposited onto multiwall carbon nanotube (MWCNT) surface to tune the properties of MWCNTs for electronic and magnetic applications. To achieve this objective, SiO<sub>2</sub>-NPs and MWCNTs were prepared and suspended together into toluene and heated at <100 °C for the formation of MWCNTs/SiO<sub>2</sub>-NP nanocomposites. A change in the microstructure, electronic, electrical, and magnetic behaviors of MWCNT nanocomposites decorated/deposited with silicon content was investigated using different techniques, viz., scanning electron microscopy, X-ray diffraction, Raman spectroscopy, and X-ray photoelectron spectroscopy for structural, compositional, and electronic structure, while current–voltage was used for electrical properties and field-dependent magnetization and electron spin resonance techniques were used for magnetic properties. The results indicated that SiO<sub>2</sub>-NPs adhered onto MWCNTs, resulting in variation in the material conductivity with the Si-NP content. The coercivity of MWCNT nanocomposites adhered with 1.5 atom % Si-NPs ( $H_C@40\text{ K} = 689\text{ Oe}$ ) is higher than that of those adhered with 5.75 atom % Si-NPs ( $H_C@40\text{ K} = 357\text{ Oe}$ ). In general, the results provide information about the possibilities of tuning the electronic, electrical, and magnetic properties of MWCNTs by adherence of SiO<sub>2</sub>-NPs onto them. This tuning of material properties could be useful for different electronic and magnetic device applications.



### 1. INTRODUCTION

Since their discovery in 1991,<sup>1</sup> single-walled and multiwalled carbon nanotubes (CNTs) have been materials of choice for a variety of applications due to their unique physical and electrical properties. The materials also possess properties that make them suitable for fabrication of electrochemical sensors.<sup>2</sup> Despite their potential for these applications, electronic, electrical, and magnetic properties of CNTs need to be tailored for more different device-based applications. Over few decades, significant progress has been made by various researchers in exploring graphitic carbon materials such as graphene, fullerene, and CNTs owing to their unique properties for different applications.<sup>3–5</sup> Zhang et al. explored the CNT semiconductor composites and their results showed a significant activity.<sup>5</sup> Other studies also showed the possibility of tuning the properties of multiwalled carbon nanotubes (MWCNTs) by introducing heteroatoms like nitrogen and boron.<sup>6</sup>

Theoretical studies have shown that in CNTs, Si atoms relax outward and form a sp<sup>3</sup> bonding to change the electronic and magnetic behaviors of the material.<sup>7</sup> Silicon (Si) atoms chemisorb on the surface of CNTs to provide dangling bonds that change the properties of the material for different applications in addition to the known ones.<sup>2,6</sup> Silicon atoms

can be binding centers for various atoms or molecules, making CNTs easier and more attractive for functionalization.<sup>8</sup> Silicon, therefore, could be a preferred element to functionalize CNTs due its large atomic size, which distorts the host lattice to generate/induce defects in the material.

In comparison to other dopants like nitrogen and boron, effects of silicon on properties of CNTs have not been fully explained nor understood. In comparison to theoretical studies, there is scarce experimental data presented on CNTs deposited with Si nanoparticles (NPs). In the present study, MWCNTs are a material of interest because they have better properties than graphene and fullerene. Although they have similar properties, graphene is a semiconductor with a zero forbidden gap,<sup>9</sup> while CNTs are metallic or semiconductor with the forbidden gap ranging from 0 to 2 eV.<sup>10,11</sup> The technique used in the production of CNTs has control over its length, diameter, and morphology,<sup>12</sup> which have a great influence in tailoring their properties for preferred applications. On the other hand, fullerene is a single-wall CNT (SWCNT) with closed ends and have similar properties to those of MWCNTs. The advantage of MWCNTs over SWCNT is that

Received: June 29, 2019

Accepted: August 9, 2019

Published: August 26, 2019

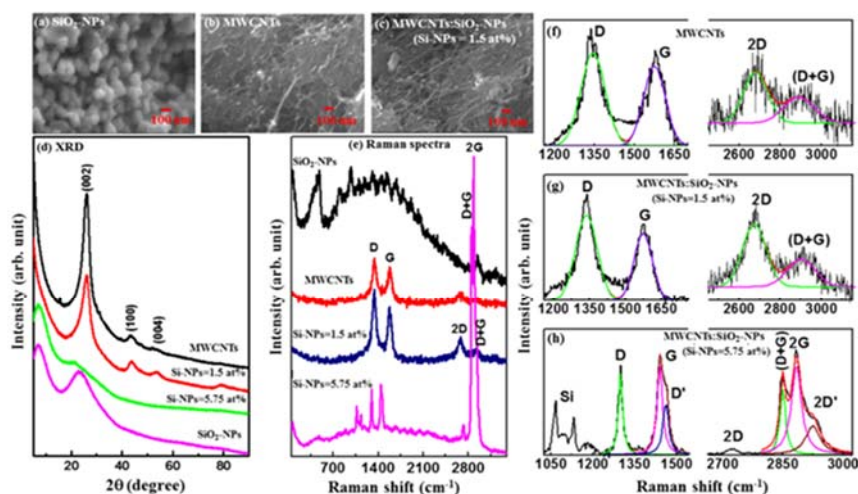


**Figure 1.** Scanning electron microscopy of (a) SiO<sub>2</sub>-NPs, (b) MWCNTs, and (c) MWCNTs/SiO<sub>2</sub>-NPs (Si-NPs = 1.5 atom %). (d) X-ray diffraction pattern, (e) Raman spectra for Si-NPs, MWCNTs, MWCNTs/SiO<sub>2</sub>-NP (Si-NPs = 1.5 atom %) nanocomposites, and MWCNTs/SiO<sub>2</sub>-NP (Si-NPs = 5.75 atom %) nanocomposites. First-order and second-order deconvoluted Raman spectra for (f) SiO<sub>2</sub>-NPs, (g) MWCNTs, (h) MWCNTs/SiO<sub>2</sub>-NP (Si-NPs = 1.5 atom %) nanocomposites, and (i) MWCNTs/SiO<sub>2</sub>-NP (Si-NPs = 5.75 atom %) nanocomposites.

there is a possibility to produce them in large quantity;<sup>12</sup> hence, we studied MWCNTs. We have synthesized MWCNT and deposited different concentrations of Si-NPs on MWCNTs and studied their structural, electronic, electrical, and magnetic properties using different spectroscopic techniques. The Si-NPs got oxidized during the synthesis process to form silicon-oxide-nanoparticles (SiO<sub>2</sub>-NPs) and adhered onto MWCNTs. Our motivation is that due to the adherence of Si-NPs, MWCNTs are a potential candidate for ferromagnetic and electromagnetic nanodevice applications. This motivation is based on the data acquired using different material research techniques.

## 2. RESULTS AND DISCUSSION

**2.1. Surface Morphology.** Surface morphologies of SiO<sub>2</sub>-NPs, MWCNTs, and MWCNTs/SiO<sub>2</sub>-NP (Si-NPs = 1.5 atom %) nanocomposites are shown in Figure 1a–c. Figure 1a shows small aggregates of SiO<sub>2</sub>-NPs, with size distribution varying from 50 to 100 nm. Figure 1b clearly indicates the formation of MWCNTs with a uniform diameter with little contamination, while Figure 1c confirms the decoration/deposition of SiO<sub>2</sub>-NPs on the surface of MWCNTs as indicated in the tree-buds-like structure on the anchored branches. It can also be seen from the figure that SiO<sub>2</sub>-NPs are well-dispersed and bounded to the surface of MWCNTs. This attachment and anchoring of SiO<sub>2</sub>-NPs to the surface of MWCNTs is important for the variation of the electrical conductivity of MWCNTs and for the prevention of an aggregation behavior of SiO<sub>2</sub>-NPs during the whole charging/discharging process among Si@C/CNTs (mixture of Si@C and CNTs) and oxygen. This variation of conductivity is shown later in the text. However, it is noted that as they were exposed to air, the Si-NPs were oxidized during the synthesis process to form SiO<sub>2</sub>-NPs on the surface of MWCNTs.

**2.2. X-Ray Diffraction.** Figure 1d shows the X-ray diffraction (XRD) spectra for all the synthesized nanocomposites. The spectrum for MWCNTs show a prominent peak at  $2\theta \approx 26^\circ$  corresponding to the (002) plane of the

graphitic structure<sup>13</sup> and less intense peaks at  $2\theta \approx 44$  and  $53^\circ$  corresponding to the (100) and (004) reflection,<sup>13</sup> respectively. This structure matches with that of pristine MWCNTs and/or standard graphite carbon, indicating a well-graphitized MWCNTs<sup>14</sup> without carbonaceous impurities and/or catalytic metal particles on the surface of the MWCNTs. The adherence of 1.5 atom % Si onto MWCNTs results in an additional peak at  $2\theta \approx 78^\circ$  corresponding to the (110) plane<sup>15</sup> along with the (002), (100), and (004) planes, indicating that the structure of MWCNT is still intact. However, when oxidized Si-NPs (5.75 atom %) is adhered onto MWCNTs, these peaks disappeared, resulting in two peaks at lower angles of  $2\theta \approx 22$  and  $7^\circ$ . We assume that these two peaks may arise from SiO<sub>2</sub>/Si–O–C and Si–Si structures respectively.<sup>16,17</sup> Casati et al. found a peak at  $2\theta \approx 6.5^\circ$  in AlSi<sub>10</sub>Mg alloy and claimed that the peak arises from silicon and is a reflection of Si (111),<sup>16</sup> whereas the peak at  $2\theta \approx 22^\circ$  is consistent with crystalline SiO<sub>2</sub> as previously reported by Svavarsson et al.<sup>17</sup>

**2.3. Raman Spectroscopy.** Figure 1e shows the Raman spectra of the synthesized SiO<sub>2</sub>-NPs, MWCNTs, and their nanocomposites. A wide peak at  $\sim 520$  cm<sup>-1</sup> observed for SiO<sub>2</sub>-NPs is attributed to the Si peak.<sup>18</sup> In the case of MWCNTs, four main peaks observed at approximately 1345, 1585, 2693, and 2937 cm<sup>-1</sup> correspond to the D-band (disordered graphitic), G-band, 2D-band, and (D + G)-band, respectively.<sup>19–23</sup> The D-peak is due to defected graphite.<sup>19–23</sup> The G-peak, on the other hand, has been found to be due to the doubly degenerate zone centered around the E<sub>2g</sub> mode resulting from the stretching modes of C–C bonds of typical graphite.<sup>19</sup> The 2D peak is an overtone of the D peak and occurs due to a second-order vibration process, and the D + G-peak occurs due to the combined vibration of D and G modes. These four peaks were also observed when different oxidized Si-NPs concentrations (1.5 and 5.75 atom %) were decorated/deposited on the MWCNTs surface and are found to be shifted slightly toward a lower wavelength for MWCNTs/SiO<sub>2</sub>-NPs (Si-NPs = 1.5 atom %). In the case of MWCNTs/SiO<sub>2</sub>-NPs (5.75 atom %), a peak representing SiO<sub>2</sub> is observed

in addition to four carbon peaks of MWCNTs. The existence of a SiO<sub>2</sub> peak in the Raman spectra indicates that Si-NPs were oxidized to form SiO<sub>2</sub>-NPs on the surface of MWCNTs (Table 1). The peak may also be due to the relatively high concentration of silicon atom onto MWCNTs. Thus, the measurements may also confirm that SiO<sub>2</sub>-NPs have been deposited on MWCNTs matrices. Presumably, the shift in the peak positions is consistent with the shift in the XRD spectra, implying the formation of the MWCNTs/SiO<sub>2</sub>-NP nanocomposites. Due to the large surface area of silicon,<sup>24</sup> the atom can easily create a bond length stretching, which leads to a significant softening effect of the MWCNT/SiO<sub>2</sub>-NP composites.<sup>25</sup> The adherence of silicon also induces a low-frequency shift of the MWCNTs spectrum. The first- and second-order Raman spectra deconvoluted into two Gaussian lines for MWCNTs and MWCNTs/SiO<sub>2</sub>-NPs (Si-NPs = 1.5 atom %) and three Gaussian lines for MWCNTs/SiO<sub>2</sub>-NP (Si-NPs = 5.75 atom %) nanocomposites are shown in Figure 1f–h. The evaluated peak intensities (int.), peak widths ( $\Delta\omega$ ), and peak positions ( $x$ ) of the deconvoluted spectra are presented in Table 2. It can be seen from the table that the peak widths of D- and G-bands are low (narrow) for MWCNTs/SiO<sub>2</sub>-NP composites. The narrowing of the peak width is due to reduction of defects as a result of substitutional SiO<sub>2</sub> atoms. To understand the degree of crystallization of the nanocomposites,  $I_D/I_G$  ratio was calculated from the deconvoluted Raman peaks. The  $I_D/I_G$  ratios are 1.3, 1.5, and 0.74 for MWCNTs, MWCNTs/SiO<sub>2</sub>-NPs (Si-NPs = 1.5 atom %), and MWCNTs/SiO<sub>2</sub>-NPs (Si-NPs = 5.75 atom %), respectively. The variation of the ratio indicates the degree of disordered carbon atoms in the nanocomposites.<sup>19–23,26</sup> The high ratio ( $I_D/I_G$ ) of the nanocomposites indicates a structural change of the composites. In MWCNTs, SiO<sub>2</sub>-NPs change the crystal structure of the composites. We have estimated the crystallite size using the Tuinstra–Koenig relation<sup>27</sup>

$$L_a \text{ (nm)} = \frac{4.4}{R} \left( \frac{2.41}{E_1} \right)^4$$

where the energy difference “R” is the integrated intensity ratio  $I_D/I_G$  and  $E_1$  is the excitation laser energy ( $\approx 2.33$  eV). The crystallite size of MWCNTs/SiO<sub>2</sub>-NP (Si-NPs = 5.75 atom %) nanocomposite is higher than that of pure MWCNTs as tabulated in Table 1. A change in  $L_a$  is due to oxidized silicon atoms relaxing outward and forming a sp<sup>3</sup> bond<sup>7</sup> in the MWCNTs/SiO<sub>2</sub>-NP nanocomposite. This conjecture is in good agreement with the XRD results as discussed above.

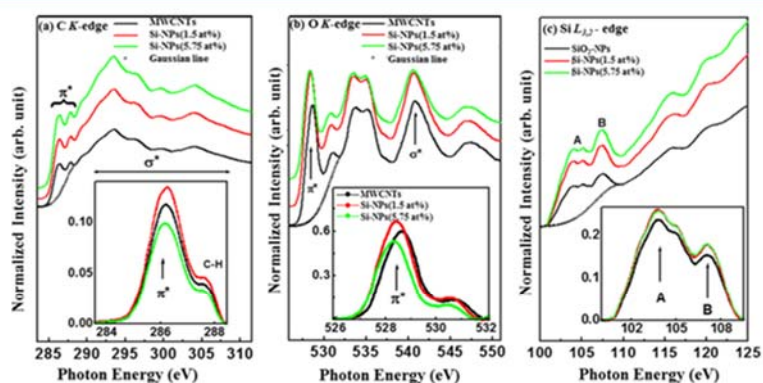
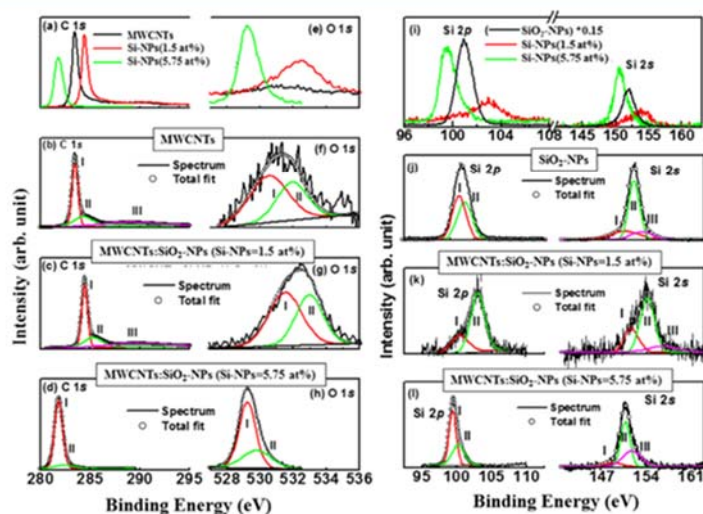
**2.4. X-Ray Adsorption Near Edge Spectroscopy.** The C K-edge X-ray adsorption near edge spectroscopy (XANES) spectrum in Figure 2a shows that there is a transition from C 1s core to p-like final states above the Fermi level ( $E_f$ ). The spectrum also shows the  $\pi^*$  features that are associated with sp<sup>2</sup>-bonding configurations at  $\sim 285.5$  ( $\pm 0.1$ ) eV<sup>28,29</sup> and  $\sigma^*$  features at  $\sim 292.8$  eV. The  $\pi^*$  region was subtracted within the range of 284–289 eV using a Gaussian line and is shown as an inset in Figure 2a. The inset shows double structural features centered at  $\sim 285.5$  ( $\pm 0.1$ ) and 287.1 eV for MWCNTs and MWCNTs/SiO<sub>2</sub>-NP nanocomposites, respectively. The intensity of pure MWCNT is found to be higher than that of MWCNT/SiO<sub>2</sub>-NP (Si-NPs = 5.75 atom %) and lower than the intensity of MWCNTs/SiO<sub>2</sub>-NPs (Si-NPs = 1.5 atom %). As suggested elsewhere,<sup>30</sup> these features in the  $\pi^*$  region may indicate that C–H or Si–C(H) or Si–C(O) and sp<sup>2</sup> C–C

**Table 1. Compositional/Quantificational Analysis from XPS, Crystallite Size from XRD, and ( $I_D/I_G$ ) Ratio from Raman Spectra of SiO<sub>2</sub>-NPs, MWCNTs, MWCNTs/SiO<sub>2</sub>-NPs (Si-NPs = 1.5 atom %), and MWCNTs/SiO<sub>2</sub>-NPs (Si-NPs = 5.75 atom %)**

	compositional and quantificational analysis from XPS			$I_D/I_G$ ratio	$L_a$ (nm) from XRD	$L_a$ (nm) from Raman
	C (atom %)	O (atom %)	Si (atom %)			
SiO <sub>2</sub> -NPs		63.60	36.40			
MWCNTs	98.37	01.63		1.3	2.8	3.8
MWCNTs/SiO <sub>2</sub> -NPs (Si-NPs = 1.5 atom %)	94.00	4.50	1.50	1.5	2.6	3.4
MWCNTs/SiO <sub>2</sub> -NPs (Si-NPs = 5.75 atom %)	85.0	9.25	5.75	0.74	5.1	6.8
				3.42		
				12.15		

**Table 2. Different Parameters Obtained after De-Convolution of Raman Spectra of SiO<sub>2</sub>-NPs, MWCNTs, MWCNTs/SiO<sub>2</sub>-NPs (Si-NPs = 1.5 atom %), and MWCNTs/SiO<sub>2</sub>-NPs (Si-NPs = 5.75 atom %)**

	$x$ (cm <sup>-1</sup> )	$\Delta\omega$ (cm <sup>-1</sup> )	int. (au)	$x$ (cm <sup>-1</sup> )	$\Delta\omega$ (cm <sup>-1</sup> )	int. (au)	$x$ (cm <sup>-1</sup> )	$\Delta\omega$ (cm <sup>-1</sup> )	int. (au)
First Order Raman Spectra	Peak-I (D-band)			Peak-II (G-band)			Peak-III D'-band		
MWCNTs	1343	92	2.1	1574	82	1.6			
MWCNTs/SiO <sub>2</sub> -NPs (Si-NPs = 1.5 atom %)	1336	91	3.9	1573	77	2.6			
MWCNTs/SiO <sub>2</sub> -NPs (Si-NPs = 5.75 atom %)	1298	18	2.8	1439	23	3.8	1460	24	2.4
Second Order Raman Spectra	(2D-band)			(D + G)-band			(2G-band/2D'-band)		
MWCNTs	2679	118	0.7	2888	150	0.5			
MWCNTs/SiO <sub>2</sub> -NPs (Si-NPs = 1.5 atom %)	2673	116	1.4	2900	138	0.7			
MWCNTs/SiO <sub>2</sub> -NPs (Si-NPs = 5.75 atom %)	2727	38	1.5	2924	43	14.2	2850	16	12.3
							2873	30	29.9

**Figure 2.** X-ray absorption near edge structure (XANES) spectroscopy for MWCNTs, MWCNTs/SiO<sub>2</sub>-NPs, and SiO<sub>2</sub>-NPs: (a) C K-edge, (b) O K-edge, and (c) Si-L<sub>3,2</sub>-edge.**Figure 3.** (a) C 1s and (e) O 1s XPS spectra for MWCNTs, MWCNTs/SiO<sub>2</sub>-NP (1.5 atom %) nanocomposites, and MWCNTs/SiO<sub>2</sub>-NP (5.75 atom %) nanocomposites. Deconvoluted C 1s (b–d) and O 1s (f–h) XPS spectra for MWCNTs, MWCNTs/SiO<sub>2</sub>-NP (Si-NPs = 1.5 atom %) nanocomposites, and MWCNTs/SiO<sub>2</sub>-NP (Si-NPs = 5.75 atom %) nanocomposites. (i) Si 2p XPS spectra and (j–l) deconvoluted Si 2p XPS of Si-NPs, MWCNTs/SiO<sub>2</sub>-NP (Si-NPs = 1.5 atom %) nanocomposites, and MWCNTs/SiO<sub>2</sub>-NP (Si-NPs = 5.75 atom %) nanocomposites.

bonds have been formed. Effects of Si–C(:H) and/or Si–C(:O) bonding on the electronic structure of MWCNTs is confirmed by the difference in the intensities of the nanocomposites. These results indicate that the MWCNTs changes the near-edge unoccupied C 2p states upon SiO<sub>2</sub>-NPs

decoration/deposition on the surface of MWCNTs, causing their structural/electronic properties to change. The normalized O K-edge XANES spectra of the nanocomposites in Figure 2b show several peaks at ~529 and ~531 eV and a double structure at ~533/~535 eV in the  $\pi^*$  region. The



origin of the peaks at  $\sim 529$  and  $\sim 531$  eV is attributed to bond resonance transitions from carboxylic groups and hydroxyl groups.<sup>31</sup> The observed double structure peaks at  $\sim 533$  and  $535$  eV in each O K-edge spectra were assigned to the physisorbed  $O_2$ <sup>32</sup> that may occur during the nanocomposite synthesis process. The peak at  $\sim 540.5$  eV for MWCNTs is assigned to  $\sigma^*$ <sup>30</sup> and is shifted to  $\approx 0.4$  eV toward the lower energy for MWCNTs/SiO<sub>2</sub>-NPs, indicating that the oxidized Si-NPs interacted with C and O in MWCNTs. The subtracted background shown as an inset of Figure 2b indicates that the intensity of MWCNTs is higher than that of MWCNTs/SiO<sub>2</sub>-NPs (Si-NPs = 5.75 atom %) and lower than that of MWCNTs/SiO<sub>2</sub>-NP (Si-NPs = 1.5 atom %) nanocomposites. This variation of intensities indicates that O 2p and Si 3p states are coupled in MWCNTs/SiO<sub>2</sub>-NPs. Figure 2c shows the normalized Si L<sub>3,2</sub>-edge XANES spectra of SiO<sub>2</sub>-NPs and MWCNTs/SiO<sub>2</sub>-NP composites. Spectral features, A and B, in Figure 2c for MWCNTs and MWCNTs/SiO<sub>2</sub>-NPs are separated by  $\sim 2.0$  eV. Feature A shows a splitting of 1.0 eV, indicating a poor resolved features at  $\sim 104$  and  $105$  eV.<sup>33</sup> The double split of A might be a spin-orbit doublet due to the transition of Si 2p<sub>3/2</sub> and 2p<sub>1/2</sub> core states to the antibonding Si 3s derived states.<sup>33</sup> The feature B, on the other hand, can be explained in terms of the Si 2p-to-3p transition and/or is associated with the resulted Si 3s or 3d derived states from hybridization with O 2p orbitals.<sup>33,34</sup> Both spectral features are shifted slightly toward the lower energy, indicating that the electronic structure of MWCNTs changed due to the incorporation of SiO<sub>2</sub>-NPs in the MWCNTs matrix.

**2.5. X-Ray Photoelectron Spectroscopy.** The chemical states of carbon/oxygen/silicon atoms in nanocomposites is shown by C 1s, O 1s, and Si 2sp X-ray photoelectron spectroscopy (XPS) spectra in Figure 3. Table 1 presents the elemental composition (C, O, and Si), quantification (atom %) and the weight percentage (wt %) obtained from XPS measurements. Quantificational analysis of C, O, and Si in MWCNT composites are explained in terms of the data presented in Table 1. It can be observed from the table that carbon/oxygen atoms are replaced/substituted by oxidized Si-NPs atoms. C 1s, O 1s, and Si 2sp XPS spectra were deconvoluted into different Gaussian lines (see Figure 3), and their different parameters are tabulated in Table 3. C 1s peak observed at  $\sim 283.5/284.4$  eV (peak I/peak II) for MWCNTs in Figure 3b is assigned to the C=C bond (carbon sp<sup>2</sup>-hybridization). This peak is shifted toward higher energy at  $\sim 285.3$  eV for the low concentration of oxidized Si-NPs (1.5 atom %) deposited MWCNTs and is shown in Figure 3c. This peak is known as a "defect peak"<sup>35</sup> or a Si-C-O bonding peak,<sup>36</sup> indicating a change in structural and electronic behavior of the composites due to SiO<sub>2</sub>-NPs deposition. The peaks at 288.8/289.5 eV for MWCNTs and MWCNTs/SiO<sub>2</sub>-NPs (Si-NPs = 1.5 atom %), arise from  $>C-O/-COOH$  bonds and/or along with Si bonds. The C 1s peak of oxidized Si-NPs decorated MWCNTs shifts towards a lower energy, significantly indicating the formation of sp<sup>3</sup>-rich material. The deconvoluted C 1s XPS peaks of MWCNTs/SiO<sub>2</sub>-NP (Si-NPs = 5.75 atom %) nanocomposites are observed at  $\sim 281.8$  and  $\sim 282.4$  eV which are strong indicators of the C-Si bonds,<sup>37</sup> and confirm the formation of MWCNTs/SiO<sub>2</sub>-NP nanocomposites.

MWCNTs spectrum shows two de-convoluted O 1s peaks at 530.5 and at 531.9 eV assigned to C=O and C-O, respectively. The two subpeaks at 533.3 and 532.7 eV for

**Table 3. Deconvoluted C 1s, O 1s, and Si 2p XPS Results of SiO<sub>2</sub>-NPs, MWCNTs, MWCNTs/SiO<sub>2</sub>-NPs (Si-NPs = 1.5 atom %) and MWCNTs/SiO<sub>2</sub>-NPs (Si-NPs = 5.75 atom %)**

	Peak-I (C=C/C-Si)			Peak-II (C=C)			Peak-III (C-O-Si/-COOH-Si)			Peak-I (C=O)			Peak-II (C-O)		
	x (eV)	$\Delta\omega$ (eV)	int. (au)	x (eV)	$\Delta\omega$ (eV)	int. (au)	x (eV)	$\Delta\omega$ (eV)	int. (au)	x (eV)	$\Delta\omega$ (eV)	int. (au)	x (eV)	$\Delta\omega$ (eV)	int. (au)
<b>C 1s and O 1s XPS</b>															
MWCNTs	283.5	0.7	48.7	284.3	2.3	25.0	288.8	6.5	26.3	530.5	2.7	60.6	531.9	2.2	39.4
MWCNTs/SiO <sub>2</sub> -NPs (Si-NPs = 1.5 atom %)	284.4	0.7	49.4	285.3	2.2	24.7	289.5	6.2	25.8	531.5	2.3	56.2	533.0	2.0	43.8
MWCNTs/SiO <sub>2</sub> -NPs (Si-NPs = 5.75 atom %)	281.8	0.9	87.8	282.4	2.4	12.2				529.2	1.2	67.6	529.8	2.1	32.4
<b>Si 2s and Si 2p XPS</b>															
SiO <sub>2</sub> -NPs	150.7	4.4	375	151.9	1.7	389	153.1	3.4	259	101.2	1.3	7241	100.8	1.2	7689
MWCNTs/SiO <sub>2</sub> -NPs (Si-NPs = 1.5 atom %)	151.6	2.3	270	154.1	2.2	588	156.3	4.9	142	100.4	3.1	28.0	103.0	2.4	72.0
MWCNTs/SiO <sub>2</sub> -NPs (Si-NPs = 5.75 atom %)	148.6	2.1	231	150.6	1.5	1224	151.6	2.9	851	99.4	1.2	60.0	100.2	2.1	40.0

MWCNTs/SiO<sub>2</sub>-NP nanocomposites are due to the O–C and O–Si groups, respectively.<sup>38</sup> The Si 2p and 2s XPS spectra of Figure 3i show the main peaks at ~100 and ~150 eV, respectively, for Si-NPs. These XPS spectra for Si 2p and 2s are also observed in Figure 3j–l for MWCNTs/SiO<sub>2</sub>-NP nanocomposites with different peak positions. Different decomposed peaks between ~99.0 and 102 eV for Si 2p are assigned to Si–C/Si–C–O and that at ~103.0 eV to Si–O.<sup>37–39</sup> The peaks at ~151.1–153.0 eV range for Si 2s XPS spectra are Si–Si peaks and those above 153.0 eV are assigned to Si–O.<sup>40</sup> These results clearly indicate that SiO<sub>2</sub>-NPs are responsible for the change in the electronic and bonding structure of the MWCNT/SiO<sub>2</sub>-NP composites. Based on the XPS decomposed peak intensity, it can be hypothesized that SiO<sub>2</sub>-NPs are responsible for the change in structural properties of MWCNTs and can make a material rich in sp<sup>3</sup>. This hypothesis is confirmed by the data acquired from the Raman spectra.

**2.6. Current–Voltage (*I–V*) Measurement.** Figure 4a shows that the ohmic *I–V* relationship is more pronounced for

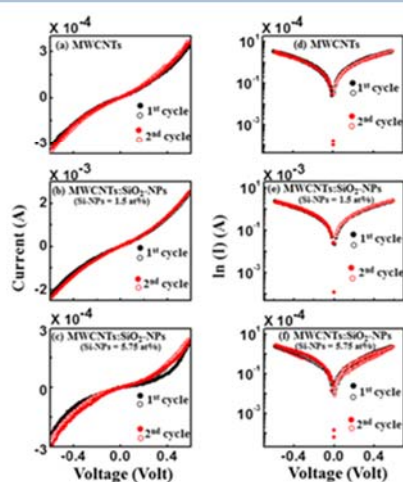


**Figure 4.** (a–c) Current (*I*)–voltage (*V*) linear and (d–f) (*ln I–V*) relationships of MWCNTs, MWCNTs/SiO<sub>2</sub>-NP (Si-NPs = 1.5 atom %) nanocomposites, and MWCNTs/SiO<sub>2</sub>-NP (Si-NPs = 5.75 atom %) nanocomposites, respectively [there are two cycles measurements of (*I–V*) and (*ln I–V*) for each case].

MWCNT. The results in Figure 4b,c also show that in MWCNTs, SiO<sub>2</sub>-NPs are responsible for the change in conductivity of the composites. As the concentration of the deposited SiO<sub>2</sub>-NPs increases, the *I–V* tends to deviate from ohmic to nonohmic behavior with a slight decrease in the electrical conductivity of the composites from conducting to semiconducting. The increase in conductivity of MWCNTs/SiO<sub>2</sub> (Si-NPs = 1.5 atom %) is due to a dangling bond formed in MWCNTs due to decreased silicon content.<sup>41</sup> The bond creates levels in the forbidden gap of the material that generate charge carriers to contribute to the measured current. On the other hand, a slight decrease in the electrical conductivity may be due to the change in the electrical structure of MWCNTs. The *I–V* hysteresis loops for MWCNTs and MWCNTs/SiO<sub>2</sub>-NP nanocomposites are shown in Figure 4d–f. Unlike in the case of MWCNTs and MWCNTs/SiO<sub>2</sub>-NPs (Si-NPs = 1.5 atom %), a small *I–V* hysteresis loop is observed for MWCNTs/SiO<sub>2</sub>-NPs (Si-NPs = 5.75 atom %), indicating a

charge storage property of these composites. The loop area of the first cycle is higher than that of the second cycle, signifying a Coulombic blockade and an electron–hole recombination, which is consistent with the silicon single-electron transistor.<sup>42</sup> Figure 4e,f shows that the loop for MWCNTs/SiO<sub>2</sub>-NPs (Si-NPs = 5.75 atom %) has an area larger than that for the MWCNTs/SiO<sub>2</sub>-NPs (Si-NPs = 1.5 atom %). The larger hysteresis loop indicates that the material has a high charge storage behavior. Based on the current (conductivity) variation of MWCNTs with the oxidized Si-NPs concentration, we can hypothesize that the material could be useful for ferroelectric device applications.

**2.7. *M–H* Hysteresis Loops.** The magnetic-field-dependent *M–H* hysteresis loops of the synthesized composites are presented in Figure 5a–d. In Figure 5a,b, a paramagnetic behavior is observed for SiO<sub>2</sub>-NPs, whereas pure MWCNTs show a ferromagnetic behavior. Considering Figure 5c,d, the magnetization of MWCNTs/SiO<sub>2</sub>-NPs (Si-NPs = 1.5 atom %) increases slightly but decreases for MWCNTs/SiO<sub>2</sub>-NP (Si-NPs = 5.75 atom %) nanocomposites. These results indicate that ferromagnetic behavior gets suppressed as the concentration of SiO<sub>2</sub>-NPs in MWCNTs increase. The hysteresis loops measured at 40 and 300 K are used to explain this variation of the magnetization, and different magnetization parameters are tabulated in Table 4. The structural change of magnetization (*M<sub>S</sub>*). The reduction of *M<sub>S</sub>* is due to the formation of Si–C bonding along with Si–O, making the material rich in sp<sup>3</sup>. The interaction of silicon atoms with other elements in MWCNTs has been explained elsewhere with possibilities of reducing sp<sup>2</sup> while increasing sp<sup>3</sup> hybridization.<sup>40,43</sup>

**2.8. Zero Field Cooling and Field Cooling.** The temperature dependence of zero field cooling (ZFC) and field cooling (FC) measurements of SiO<sub>2</sub>-NPs, MWCNTs, and MWCNTs/SiO<sub>2</sub>-NPs are presented in Figure 5e–g. The figure shows that MWCNTs and MWCNTs/SiO<sub>2</sub>-NPs have ferromagnetic features and thus are in agreement with the ferromagnetic behavior observed in the *M–H* hysteresis loops. This study reveals that the oxidized Si-NPs are responsible for the semiconducting magnetic behavior of MWCNTs. This ability to control the structural behavior of MWCNTs by manipulating their structure opens new vistas for more electronic and spintronic devices. As a low toxicity material, the ability to control the properties of MWCNTs also gives room for applications in biomedicine.

**2.9. Electron Spin Resonance.** Figure 5i–l shows the ferromagnetism behavior of the nanocomposites using electron spin resonance (ESR) technique at room temperature. A prominent resonant microwave absorption signal (*H<sub>r</sub>*) is observed at around 3200 G/1600 G for high/low field in the figure. The linewidth ( $\Delta H$ ) of ESR signals are 367/203, 433/190, 711/117, and 1284/148 for Si-NPs, MWCNTs, MWCNTs/SiO<sub>2</sub>-NPs (Si-NPs = 1.5 atom %), and MWCNTs/SiO<sub>2</sub>-NPs (Si-NPs = 5.75 atom %) in high/low field, respectively. Parameters calculated from the ESR spectra are presented in Table 5. The *g*-value (Landé *g* factor) or  $\Delta g/g$  value changes with the deposition of SiO<sub>2</sub>-NPs on MWCNTs surface. From Table 5, the linewidth with an effective *g* value for MWCNTs/SiO<sub>2</sub>-NP (Si-NPs = 1.5 atom %) nanocomposites is higher than that for pure SiO<sub>2</sub>-NPs, MWCNTs, and MWCNTs/SiO<sub>2</sub>-NPs (Si-NPs = 5.75 atom %), indicating that MWCNTs/SiO<sub>2</sub>-NPs (Si-NPs = 1.5 atom %) have a

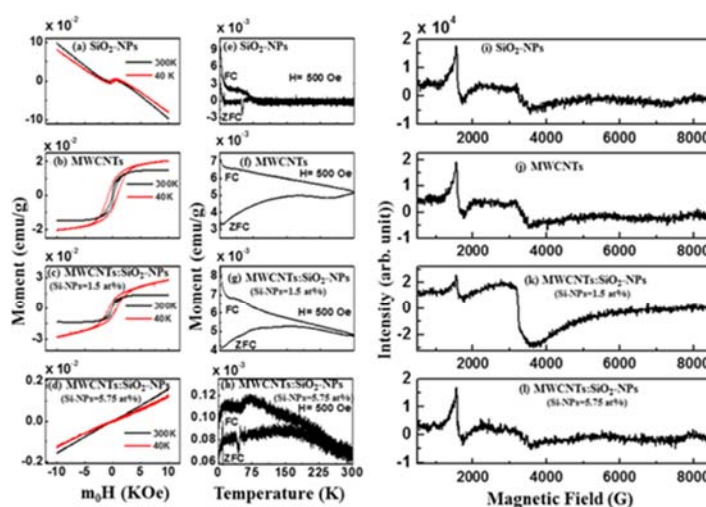


**Figure 5.** Magnetic hysteresis loops obtained for (a) SiO<sub>2</sub>-NPs, (b) MWCNTs, (c) MWCNTs/SiO<sub>2</sub>-NP (Si-NPs = 1.5 atom %) nanocomposites, and (d) MWCNTs/SiO<sub>2</sub>-NP (Si-NPs = 5.75 atom %) nanocomposites at 300 and 40 K. Temperature dependence of magnetization of (e) SiO<sub>2</sub>-NPs, (f) MWCNTs, (g) MWCNTs/SiO<sub>2</sub>-NPs (Si-NPs = 1.5 atom %), and (h) MWCNTs/SiO<sub>2</sub>-NPs (Si-NPs = 5.75 atom %) with applied magnetic field of 500 Oe after zero field cooling (ZFC) and field cooling (FC). Electron spin resonance spectra for (i) Si-NPs, (j) MWCNTs, (k) MWCNTs/SiO<sub>2</sub>-NP (Si-NPs = 1.5 atom %) nanocomposites, and (l) MWCNTs/SiO<sub>2</sub>-NP (Si-NPs = 5.75 atom %) nanocomposites at 300 K.

**Table 4. Magnetization Parameters [Magnetic Saturation ( $M_S$ ), Retentivity ( $M_R$ ), and Coercivity ( $H_C$ )] of Si-NPs, MWCNTs, MWCNTs/SiO<sub>2</sub>-NPs (Si-NPs = 1.5 atom %) and MWCNTs/SiO<sub>2</sub>-NPs (Si-NPs = 5.75 atom %) Obtained from the  $M-H$  Hysteresis Loops Measured at 300 and 40 K**

magnetization ( $M-H$ loops)	@300 K			@40 K		
	$M_S \times 10^{-4}$ (emu/g)	$M_R \times 10^{-4}$ (emu/g)	$H_C$ (Oe)	$M_S \times 10^{-4}$ (emu/g)	$M_R \times 10^{-4}$ (emu/g)	$H_C$ (Oe)
SiO <sub>2</sub> -NPs	49	36.0	379	57	43	515
MWCNTs	140	25.0	112	190	73	813
MWCNTs/SiO <sub>2</sub> -NPs (Si-NPs = 1.5 atom %)	130	23.0	123	220	76	689
MWCNTs/SiO <sub>2</sub> -NPs (Si-NPs = 5.75 atom %)		00.2	60		0.07	357

**Table 5. Electron Spin Resonance Parameters of Si-NPs, MWCNTs, MWCNTs/SiO<sub>2</sub>-NPs (Si-NPs = 1.5 atom %), and MWCNTs/SiO<sub>2</sub>-NPs (Si-NPs = 5.75 atom %) Measured at 300 K**

magnetization (ESR)	$\Delta H$ (Gauss)		$H_i$ (Gauss)		g-value		$N$ (no. of spin)	$P_{asy}$	$\Delta g/g$
	high field	low field	high field	low field	high field	low field			
SiO <sub>2</sub> -NPs	367	203	3243	1673	2.08	4.03	$3.67 \times 10^8$	0.32	0.0375
MWCNTs	433	190	3298	1680	2.04	4.17	$6.11 \times 10^8$	0.23	0.0182
MWCNTs/SiO <sub>2</sub> -NPs (Si-NPs = 1.5 atom %)	711	117	3198	1572	2.11	4.29	$7.54 \times 10^9$	0.24	0.0511
MWCNTs/SiO <sub>2</sub> -NPs (Si-NPs = 5.75 atom %)	1284	148	3303	1616	2.04	4.11	$3.65 \times 10^9$	0.56	0.0182

higher magnetic phase in MWCNTs.<sup>44</sup> Similar values have been reported elsewhere for other forms of carbon.<sup>45</sup> A possible overlap of the broad linewidth with resonance line of an unpaired electron that is trapped in an oxygen vacancy in MWCNTs makes  $H_i$  to shift toward the lower field for the g-value greater than 2. Majchrycki et al.<sup>46</sup> have reported similar results on functionalized graphene materials. The asymmetric factor ( $P_{asy}$ ) was estimated using the relation  $P_{asy} = (1 - h_u/h_l)$ ,<sup>47</sup> where  $h_u$  and  $h_l$  are the upper and lower peak heights, respectively, from zero line. It was observed that  $P_{asy}$  increases gradually with an increase of oxidized Si-NPs content in MWCNTs, as shown in Table 5. The highest magnetic anisotropy was obtained for MWCNTs/SiO<sub>2</sub>-NPs (Si-NPs = 1.5 atom %). The total number of spin ( $N$ ) regarding the ESR resonance was calculated using the following relation:  $N =$

$0.285 \times I_{p-p} \times (\Delta H)^2$ ,<sup>48</sup> where  $I_{p-p}$  is the peak-to-peak height of the ESR signal (in au) and  $\Delta H$  is the linewidth in Gauss. The  $\Delta g/g$  and  $N$  values are high in the case of MWCNTs/SiO<sub>2</sub>-NPs (Si-NPs = 1.5 atom %) nanocomposites leading to a high value of magnetization. These results confirm that the MWCNTs/SiO<sub>2</sub>-NP (Si-NPs = 1.5 atom %) nanocomposites can preserve the magnetism as MWCNTs that could be very useful for electromagnetic applications.

As observed from Raman spectra, the  $sp^2$  content is higher in MWCNTs/SiO<sub>2</sub>-NP (Si-NPs = 1.5 atom %) and lower in MWCNTs/SiO<sub>2</sub>-NP (Si-NPs = 5.75 atom %) composites than in pure MWCNTs, thereby giving rise to  $sp^3$  content for 5.75 atom % oxidized Si-NP-deposited MWCNTs. This observation is consistent with XPS and XANES data. The XPS spectra for pure MWCNTs show that the  $sp^2$  C=C peak at  $\sim 284.4$  eV

shifted toward a high binding energy, thereby forming a defect peak at 285.3 eV with a decrease in the intensity of the MWCNTs/SiO<sub>2</sub>-NPs. This defected peak is ~0.9 eV higher than that of pure MWCNTs. The weak attachment bond of MWCNTs/SiO<sub>2</sub>-NPs (Si-NPs = 1.5 atom %) on the surface of MWCNTs can be attributed to this defected peak. The increase/decrease in the intensity of C K-edge XANES spectra correspond to a increase/decrease in the  $I_D/I_G$  ratio, indicating a change in structural/electronic nature of MWCNTs/SiO<sub>2</sub>-NPs. The observed change in the structural/electronic properties of MWCNTs due to the deposition of SiO<sub>2</sub>-NPs (Si-NPs = 1.5 atom %) content leads to the formation of the Si-C-O and C-O/-COOH bonds due to oxygen (O) vacancy created, which may be responsible for the higher magnetization. The presence of oxygen functional group creates a positive center, which captures an electron in a localized form.<sup>49,50</sup> The local electrons possess magnetic moments that improve the magnetism in MWCNTs/SiO<sub>2</sub>-NP (Si-NPs = 1.5 atom %) nanocomposites. The strong interaction (tetrahedral bonding Si-C) between the atoms of Si and C may be responsible for the rapid decrease in the magnetization of MWCNTs due to an increase in the SiO<sub>2</sub>-NPs content.<sup>40</sup> The relationship between the electrical and magnetic properties of MWCNT:SiO<sub>2</sub>-NPs can be clarified by the transport properties of the MWCNTs/SiO<sub>2</sub>-NP nanocomposites. The ferromagnetism induced in MWCNT/SiO<sub>2</sub>-NPs was also based on the delocalized electrons not trapped by O vacancy.<sup>50</sup> The magnetic and electrical properties are mainly due to the mobility of electrons between the atoms. The delocalized electrons allow for easy transition between the valence and the conduction bands, leading to an enhancement in electrical conductivity.<sup>51</sup> In addition, the delocalized electrons also enhance the exchange interaction of atoms, which eventually improves the ferromagnetic behavior of MWCNT/SiO<sub>2</sub>-NP nanocomposites.<sup>50,52</sup>

### 3. CONCLUSIONS

The electrical, electronic, and magnetic behaviors of the synthesized MWCNTs and MWCNTs/SiO<sub>2</sub>-NP nanocomposites have been investigated. We observed that there is a change in the structure of MWCNTs from sp<sup>2</sup>- to sp<sup>3</sup>-rich hybridized carbon atoms with a change in the electrical conductivity of MWCNTs due to the deposition/decoration of SiO<sub>2</sub>-NPs on the surface of MWCNTs. The formation of Si-C, Si-Si, and Si-O-C/Si-O bonding features was observed, indicating that SiO<sub>2</sub>-NPs impacted the chemical bonding and electronic structure of MWCNTs. The magnetization of MWCNTs varies as a function of oxidized Si-NPs content adhered onto the surface of MWCNTs lattice. We therefore conclude that the deposition/decoration of oxidized Si-NPs on the surface of MWCNTs is an alternative method to tailor the structural, electrical, and magnetic properties of MWCNTs for future electronic and magnetic device applications.

### 4. EXPERIMENTAL DETAILS

**4.1. Synthesis Process.** Spray pyrolysis process was used to prepare MWCNTs using a solution of ferrocene (C<sub>10</sub>H<sub>10</sub>Fe as a catalyst) and toluene (C<sub>7</sub>H<sub>8</sub> as a carbon source),<sup>53</sup> whereas thermal decomposition process was used for the synthesis of silicon nanoparticles (SiO<sub>2</sub>-NPs) using chloro-(dimethyl) octadecylsilane in 1,3,5-trimethylbenzene in the presence of octadecylamine.<sup>54</sup> Since the synthesis process of

the nanocomposites was carried out in an atmospheric pressure, Si-NPs were oxidized to form SiO<sub>2</sub>-NP. For the preparation of MWCNT:SiO<sub>2</sub>-NPs composites, we used SiO<sub>2</sub>-NPs and MWCNTs at two different stoichiometric ratios (Si-NPs = 1.5 atom % and Si-NPs = 5.75 atom %), which were suspended in toluene and heated at above 100 °C to obtain MWCNTs/SiO<sub>2</sub>-NP nanocomposites. The deposited SiO<sub>2</sub>-NPs have been found to be possibly deposited on the MWCNTs matrices.

**4.2. Measurements.** SiO<sub>2</sub>-NPs, MWCNTs, and MWCNTs/SiO<sub>2</sub>-NP nanocomposites were characterized by the use of different techniques to establish and study the change in their surface morphology, microstructure, electronic, and magnetic properties due to the deposition of SiO<sub>2</sub>-NPs in the MWCNT lattice. The deposited SiO<sub>2</sub>-NPs on MWCNTs were denoted as MWCNTs/SiO<sub>2</sub>-NPs (Si-NPs = 1.5 atom %) and MWCNTs/SiO<sub>2</sub>-NPs (Si-NPs = 5.75 atom %) translating to 1.5% and 5.57 atom % of Si-NPs concentration in MWCNTs, respectively. The SiO<sub>2</sub>-NPs, MWCNTs, and MWCNTs/SiO<sub>2</sub>-NPs was drop-cast on a silicon substrate and air-dried overnight prior to measurements. All measurements were performed at room temperature except magnetic measurements. To obtain the surface morphology of SiO<sub>2</sub>-NPs, MWCNTs, and MWCNTs/SiO<sub>2</sub>-NP nanocomposites, field emission scanning electron microscopy (FESEM) images were recorded using a JSM-7800F FESEM from JEOL Ltd. coupled with an UltraDry EDS detector. The structural studies of the synthesized composites were performed using a Rigaku Smartlab X-ray diffractometer (0.154 nm Cu K $\alpha$  line). Raman spectra were recorded using a HORIBA scientific XploRA at 532 nm (~2.41 eV) LASER light excitation energy. The surface morphological structures were studied using JEOL JEM 2100. The C K-edge, O K-edge, and Si L<sub>3,2</sub>-edge XANES measurements were performed at the Taiwan Light Source (TLS), Hsinchu, Taiwan. The core shells C 1s, O 1s, and Si 2sp were performed using a KRATOS-SUPRA spectrometer with a monochromatic Al K $\alpha$  radiation possessing an excitation energy,  $h\nu = 1486.6$  eV, and a base pressure  $1.2 \times 10^{-9}$  Torr at UNISA (Florida Science Campus). The electrical conductivity was studied using Keithley 6487 with a voltage sweep ranging from -0.6 to +0.6 V. In this measurements, silver paste was used as the conducting electrodes to investigate the electrical behavior of the materials. The range voltage of 0-+0.6 V, +0.6-0 V, 0--0.6 V, and -0.6-0 V was used to obtain the  $I$ - $V$  data. The value of 0.6 V was the highest voltage applied for the current limit of 2.5 mA. A SQUID-type magnetometer with a sensitivity of  $<5 \times 10^{-8}$  emu was used for the  $M$ - $H$  loop and FC/ZFC measurements. All the measurements were performed at room temperature. Electron spin resonance (ESR) spectra were recorded using a Bruker EMX spectrometer at 9.45 GHz. Details of these measurement techniques are available elsewhere.<sup>55</sup>

### ■ AUTHOR INFORMATION

#### Corresponding Authors

\*E-mail: Raysc@unisa.ac.za.

\*E-mail: wfpong@mail.tku.edu.tw.

#### ORCID

Sekhar C. Ray: 0000-0003-3202-4739

#### Notes

The authors declare no competing financial interest.

## ACKNOWLEDGMENTS

The financial support received from the National Research Foundation (NRF), South Africa (Grant nos. 105292, PD-TWAS150813137166, and EQP13091742446) is gratefully acknowledged by J.A.O., D.O.I., S.J.M., S.S., and S.C.R.

## REFERENCES

- (1) Iijima, S. Helical microtubules of graphitic carbon. *Nature* **1991**, *354*, 356.
- (2) Gao, C.; Guo, Z.; Liu, J. H.; Huang, X. J. The new age of carbon nanotubes: an updated review of functionalized carbon nanotubes in electrochemical sensors. *Nanoscale* **2012**, *4*, 1948–1963.
- (3) Zhang, N.; Yang, M.-Q.; Liu, S.; Sun, Y.; Xu, Y.-J. Waltzing with the Versatile Platform of Graphene to Synthesize Composite Photocatalysts. *Chem. Rev.* **2015**, *115*, 10307–10377.
- (4) Chen, Y.; Xie, X.; Xin, X.; Tang, Z.-R.; Xu, Y.-J. Ti3C2T<sub>x</sub>-Based Three-Dimensional Hydrogel by a Graphene Oxide-Assisted Self-Convergence Process for Enhanced Photoredox Catalysis. *ACS Nano* **2019**, *13*, 295–304.
- (5) Zhang, N.; Zhang, Y.; Yang, M.-Q.; Tang, Z.-R.; Xu, Y.-J. A Critical and Benchmark Comparison on Graphene-, Carbon Nanotube-, and Fullerene-Semiconductor Nanocomposites as Visible Light Photocatalysts for Selective Oxidation. *J. Catal.* **2013**, *299*, 210–221.
- (6) Adjizian, J. J.; Leghrib, R.; Koos, A. A.; Suarez-Martinez, I.; Crossley, A.; Wagner, P.; Grobert, N.; Llobet, E.; Ewels, C. P. Boron- and nitrogen-doped multi-wall carbon nanotubes for gas detection. *Carbon* **2014**, *66*, 662–673.
- (7) Baierle, R. J.; Fagan, S. B.; Mota, R.; da Silva, A. J.; Fazzio, A. Electronic and structural properties of silicon-doped carbon nanotubes. *Phys. Rev. B* **2001**, *64*, No. 085413.
- (8) Song, C.; Xia, Y.; Zhao, M.; Liu, X.; Li, F.; Huang, B.; Zhang, H.; Zhang, B. Functionalization of silicon-doped single walled carbon nanotubes at the doping site: an ab initio study. *Phys. Lett. A* **2006**, *358*, 166–170.
- (9) Meric, I.; Han, M. Y.; Young, A. F.; Ozyilmaz, B.; Kim, P.; Shepard, K. L. Current saturation in zero-bandgap, top-gated graphene field-effect transistors. *Nat. Nanotechnol.* **2008**, *3*, 654.
- (10) Slepyan, G. Y.; Maksimenko, S. A.; Lakhtakia, A.; Yevtushenko, O.; Gusakov, A. V. Electrodynamics of carbon nanotubes: Dynamic conductivity, impedance boundary conditions, and surface wave propagation. *Phys. Rev. B* **1999**, *60*, No. 17136.
- (11) Pennington, G.; Goldsman, N. Semiclassical transport and phonon scattering of electrons in semiconducting carbon nanotubes. *Phys. Rev. B* **2003**, *68*, No. 045426.
- (12) Daenen, M.; De Fouw, R. D.; Hamers, B.; Janssen, P. G.; Schouteden, K.; Veld, M. A. *The Wondrous World of Carbon Nanotubes—A Review of Current Carbon Nanotube Technologies*; Eindhoven University of Technology, 2003; pp 1–96.
- (13) Atchudan, R.; Pandurangan, A.; Joo, J. Effects of nanofillers on the thermo-mechanical properties and chemical resistivity of epoxy nanocomposites. *J. Nanosci. Nanotechnol.* **2015**, *15*, 4255–4267.
- (14) Zhang, X.; Fu, J.; Zhang, Y.; Lei, L. A nitrogen functionalized carbon nanotube cathode for highly efficient electrocatalytic generation of H<sub>2</sub>O<sub>2</sub> in Electro-Fenton system. *Sep. Purif. Technol.* **2008**, *64*, 116–123.
- (15) Ciomaga, C. E.; Padurariu, L.; Curecheriu, L. P.; Lupu, N.; Lisiecki, I.; Deluca, M.; Tascu, S.; Galassi, C.; Mitoseriu, L. Using multi-walled carbon nanotubes in spark plasma sintered Pb (Zr<sub>0.4</sub>Ti<sub>0.55</sub>)O<sub>3</sub> ceramics for tailoring dielectric and tunability properties. *J. Appl. Phys.* **2014**, *116*, No. 164110.
- (16) Casati, R.; Hamidi Nasab, M.; Coduri, M.; Tirelli, V.; Vedani, M. Effects of Platform Pre-Heating and Thermal-Treatment Strategies on Properties of AlSi<sub>10</sub>Mg Alloy Processed by Selective Laser Melting. *Metals* **2018**, *8*, No. 954.
- (17) Svavarsson, H. G.; Arnardottir, H.; Einarsson, S.; Albertsson, A.; Brynjólfsson, A. In *Applications of Unmodified Geothermal Silica for Protein Extraction*, Proceedings of the World Geothermal Congress, Melbourne, Australia, 2015; pp 1–8.
- (18) Senez, V.; Armigliato, A.; De Wolf, I.; Carnevale, G. P.; Balboni, R.; Frabboni, S.; Benedetti, A. Strain Determination in Silicon Microstructures by Combined TEM/CBED, Process Simulation and micro-Raman Spectroscopy. *J. Appl. Phys.* **2003**, *94*, 5574–5583.
- (19) Ferrari, A. C.; Robertson, J. Interpretation of Raman spectra of disordered and amorphous carbon. *Phys. Rev. B* **2000**, *61*, No. 14095.
- (20) Ray, S. C.; Bhunia, S. K.; Saha, A.; Jana, N. R. Electric and Ferro-electric behaviour of polymer-coated graphene-oxide thin film. *Phys. Procedia* **2013**, *46*, 62–70.
- (21) Ferrari, A. C.; Basko, D. M. Raman spectroscopy as a versatile tool for studying the properties of graphene. *Nat. Nanotechnol.* **2013**, *8*, 235.
- (22) Soin, N.; Roy, S. S.; Ray, S. C.; McLaughlin, J. A. Excitation energy dependence of Raman bands in multiwalled carbon nanotubes. *J. Raman Spectrosc.* **2010**, *41*, 1227–1233.
- (23) Murphy, H.; Papakonstantinou, P.; Okpalugo, T. T. Raman study of multiwalled carbon nanotubes functionalized with oxygen groups. *J. Vac. Sci. Technol., B: Microelectron. Nanometer Struct. Process., Meas., Phenom.* **2006**, *24*, 715–720.
- (24) Moene, R.; Makkee, M.; Moulijn, J. A. High surface area silicon carbide as catalyst support characterization and stability. *Appl. Catal., A* **1998**, *167*, 321–330.
- (25) Tarui, T.; Takahashi, T.; Ohashi, S.; Uemori, R. In *Effect of Silicon on the Age Softening of High Carbon Steel Wire*, Proceedings of the 35th Mechanical Working and Steel Processing Conference; Iron & Steel Society of AIME, 1993; pp 231–239.
- (26) Jin, Y. Z.; Gao, C.; Hsu, W. K.; Zhu, Y.; Huczko, A.; Bystrzejewski, M.; Roe, M.; Lee, C. Y.; Acquah, S.; Krotto, H.; Walton, D. R. Large-scale synthesis and characterization of carbon spheres prepared by direct pyrolysis of hydrocarbons. *Carbon* **2005**, *43*, 1944–1953.
- (27) Tuinstra, F.; Koenig, J. L. Raman spectrum of graphite. *J. Chem. Phys.* **1970**, *53*, 1126–1130.
- (28) Pao, C. W.; Ray, S. C.; Tsai, H. M.; Chen, Y. S.; Chen, H. C.; Lin, I. N.; Pong, W. F.; Chiou, J. W.; Tsai, M. H.; Shang, N. G.; Papakonstantinou, P.; Guo, J.-H. Change of structural behaviors of organo-silane exposed graphene nanoflakes. *J. Phys. Chem. C* **2010**, *114*, 8161–8166.
- (29) Ray, S. C.; Pao, C. W.; Tsai, H. M.; Chiou, J. W.; Pong, W. F.; Chen, C. W.; Tsai, M. H.; Papakonstantinou, P.; Chen, L. C.; Chen, K. H. A comparative study of the electronic structures of oxygen- and chlorine-treated nitrogenated carbon nanotubes by x-ray absorption and scanning photoelectron microscopy. *Appl. Phys. Lett.* **2007**, *91*, No. 202102.
- (30) Terekhov, V. A.; Terukov, E. I.; Trapeznikova, I. N.; Kashkarov, M.; Kurilo, O. V.; Turishchev, S. Y.; Golodenko, A. B.; Domashevskaya, E. P. A study of the local electronic and atomic structure in a-Si<sub>x</sub>C<sub>1-x</sub> amorphous alloys using ultrasoft X-ray emission spectroscopy. *Semiconductors* **2005**, *39*, 830–834.
- (31) Banerjee, S.; Hemraj-Benny, T.; Balasubramanian, M.; Fischer, D. A.; Misewich, J. A.; Wong, S. S. Ozonized single-walled carbon nanotubes investigated using NEXAFS spectroscopy. *Chem. Commun.* **2004**, 772–773.
- (32) Stöhr, J. *NEXAFS Spectroscopy*; Springer Science+Business Media, 2013.
- (33) Wu, Z. Y.; Jollet, F.; Seifert, F. Electronic structure analysis of alpha-quartz and stishovite: Ab initio calculation with core–hole interaction. *Appl. Phys. Lett.* **2001**, *78*, 3809–3811.
- (34) Mo, S. D.; Ching, W. Y. X-ray absorption near-edge structure in alpha-quartz and stishovite: Ab initio calculation with core–hole interaction. *Appl. Phys. Lett.* **2001**, *78*, 3809–3811.
- (35) Shang, N. G.; Papakonstantinou, P.; McMullan, M.; Chu, M.; Stamboulis, A.; Potenza, A.; Dhesi, S. S.; Marchetto, H. Catalyst-free efficient growth, orientation and biosensing properties of multilayer graphene nanoflake films with sharp edge planes. *Adv. Funct. Mater.* **2008**, *18*, 3506–3514.
- (36) Maruyama, T.; Naritsuka, S. *Nanotechnology and Nanomaterials: Carbon Nanotubes—Synthesis, Characterization, Applications*, In Yellampalli, S., Ed.; Department of Material Science and Engineering,

Meijo University; Japan, 2011; <https://www.intechopen.com/books/carbon-nanotubes-synthesis-characterization-applications>.

(37) Pedio, M.; Borgatti, F.; Giglia, A.; Mahne, N.; Nannarone, S.; Giovannini, S.; Cepek, C.; Magnano, E.; Bertoni, G.; Spiller, E.; Sancrotti, M.; Giovanelli, L.; Floreano, L.; Gotter, R.; Morgante, A. Annealing temperature dependence of C60 on silicon surfaces: bond evolution and fragmentation as detected by NEXAFS. *Phys. Scr.* **2005**, *2005*, No. 695.

(38) Moulder, J. F.; Stickle, W. F.; Sobol, P. E. *KD Bomben Handbook of X-Ray Photoelectron Spectroscopy: A Reference Book of Standard Spectra for Identification and Interpretation of XPS Data*; Electro Inc.: USA, 1992; p 42.

(39) Deng, H. X.; Wei, S. H.; Li, S. S.; Li, J.; Walsh, A. Electronic origin of the conductivity imbalance between covalent and ionic amorphous semiconductors. *Phys. Rev. B* **2013**, *87*, No. 125203.

(40) Ray, S. C.; Mishra, D. K.; Strydom, A. M.; Papakonstantinou, P. Magnetic behavioural change of silane exposed graphene nanoflakes. *J. Appl. Phys.* **2015**, *118*, No. 115302.

(41) Račiukaitis, G.; Brikas, M.; Kazlauskienė, V.; Miškinis, J. Doping of silicon with carbon during laser ablation process. *Appl. Phys. A* **2006**, *85*, 445–450.

(42) Fujiwara, A.; Takahashi, Y.; Murase, K. Observation of single electron-hole recombination and photon-pumped current in an asymmetric Si single-electron transistor. *Phys. Rev. Lett.* **1997**, *78*, No. 1532.

(43) Mostafa, M.; Banerjee, S. Effect of functional group topology of carbon nanotubes on electrophoretic alignment and properties of deposited layer. *J. Phys. Chem. C* **2014**, *118*, 11417–11425.

(44) Rao, S. S.; Stesmans, A.; Noyen, J. V.; Jacobs, P.; Sels, B. ESR evidence for disordered magnetic phase from ultra-small carbon nanotubes embedded in zeolite nanochannels. *Europhys. Lett.* **2010**, *90*, No. 57003.

(45) Gerstner, E. G.; Lukins, P. B.; McKenzie, D. R.; McCulloch, D. G. Substrate bias effects on the structural and electronic properties of tetrahedral amorphous carbon. *Phys. Rev. B* **1996**, *54*, No. 14504.

(46) Majchrzycki, L.; Augustyniak-Jablokow, M. A.; Strzelczyk, R.; Maćkowiak, M. Magnetic Centres in Functionalized Graphene. *Acta Phys. Pol., A* **2015**, *127*, No. 540.

(47) Das, J.; Mishra, D. K.; Srinivasu, V. V. Spin canting and magnetism in nano-crystalline Zn<sub>1-x</sub>Al<sub>x</sub>O. *J. Alloys Compd.* **2017**, *704*, 237–244.

(48) Bleaney, B.; Rubins, R. S. Explanation of some Forbidden Transitions in Paramagnetic Resonance. *Proc. Phys. Soc.* **1961**, *77*, 103.

(49) Ghosh, B.; Ray, S. C.; Pattanaik, S.; Sarma, S.; Mishra, D. K.; Pontsho, M.; Pong, W. F. Tuning of the electronic structure and magnetic properties of xenon ion implanted zinc oxide. *J. Phys. D: Appl. Phys.* **2018**, *51*, No. 095304.

(50) Wu, T.; Sun, H.; Hou, X.; Liu, L.; Zhang, H.; Zhang, J. Significant room-temperature ferromagnetism in porous TiO<sub>2</sub> thin films. *Microporous Mesoporous Mater.* **2014**, *190*, 63–66.

(51) Shuai, Z.; Wang, L.; Li, Q. Evaluation of Charge Mobility in Organic Materials: From Localized to Delocalized Descriptions at a First-Principles Level. *Adv. Mater.* **2011**, *23*, 1145–1153.

(52) Ohno, H. Making nonmagnetic semiconductors ferromagnetic. *Science* **1998**, *281*, 951–956.

(53) Vatanpour, V.; Madaeni, S. S.; Moradian, R.; Zinadini, S.; Astinchap, B. Fabrication and characterization of novel antifouling nanofiltration membrane prepared from oxidized multiwalled carbon nanotube/polyethersulfone nanocomposite. *J. Membr. Sci.* **2011**, *375*, 284–294.

(54) Das, P.; Saha, A.; Maity, A. R.; Ray, S. C.; Jana, N. R. Silicon nanoparticle based fluorescent biological label via low temperature thermal degradation of chloroalkylsilane. *Nanoscale* **2013**, *5*, 5732–5737.

(55) Idisi, D. O.; Ali, H.; Oke, J. A.; Sarma, S.; Moloi, S. J.; Ray, S. C.; Wang, H. T.; Jana, N. R.; Pong, W. F.; Strydom, A. M. Electronic, electrical and magnetic behaviours of reduced graphene-oxide

functionalized with silica coated gold nanoparticles. *Appl. Surf. Sci.* **2019**, *483*, 106–113.

## Appendix 2

Diamond &amp; Related Materials 100 (2019) 107570



Contents lists available at ScienceDirect

## Diamond &amp; Related Materials

journal homepage: [www.elsevier.com/locate/diamond](http://www.elsevier.com/locate/diamond)

## Tuning of electronic and electrical behaviour of MWCNTs-TiO<sub>2</sub> nanocomposites



James A. Oke<sup>a</sup>, David O. Idisi<sup>a</sup>, Sweety Sarma<sup>a</sup>, S.J. Moloi<sup>a</sup>, Sekhar C. Ray<sup>a,\*</sup>, K.H. Chen<sup>b</sup>, A. Ghosh<sup>b</sup>, A. Shelke<sup>b</sup>, S.-H. Hsieh<sup>c</sup>, W.F. Pong<sup>b,\*</sup>

<sup>a</sup> Department of Physics, CSET, University of South Africa, Private Bag X6, Florida, 1710, Science Campus, Christiaan de Wet and Pioneer Avenue, Florida Park, Johannesburg, South Africa

<sup>b</sup> Department of Physics, Tamkang University, Tamsui 251, Taipei, Taiwan

<sup>c</sup> National Synchrotron Radiation Research Center (NSRRC), 101 Hsin-Ann Rd., Hsinchu Sci. Park, Hsinchu 30076, Taiwan

## ARTICLE INFO

## Keywords:

TiO<sub>2</sub>  
MWCNTs  
MWCNTs-TiO<sub>2</sub>  
Raman spectroscopy  
XPS  
I-V measurements

## ABSTRACT

The improvement of electronic structure and electrical behaviour of low-density materials have been of great concern. Multiwall carbon nanotube (MWCNT) has been identified as a low-density material, which needs attention to be used mostly as a strengthening phase in lightweight metal lattice composites (MLC). In this work, vaporization and drying process were used to produce TiO<sub>2</sub> incorporated MWCNTs nanocomposites. The incorporation of TiO<sub>2</sub> is to improve electronic system as well as electrical behaviour of MWCNTs in oxidized atmosphere, which is essential in most of MLC processing methods. We have used field-emission scanning electron microscopy Raman spectroscopy, X-ray diffraction and X-ray photoemission spectroscopy techniques for the study of structural and electronic properties; whereas current-voltage technique was used for the study of electrical behaviour of the nanocomposites. The observed change in electrical behaviour of the nanocomposites with improvement of electric/bonding structure indicates possibilities of the material properties be tailored for electronic/electrical devices as well as photo-catalytic activity applications.

## 1. Introduction

Multiwall carbon nanotubes (MWCNTs) have been considered as a potential material for varieties of applications owing to their remarkable photoelectrical, mechanical, chemical stability. With distinctive electronic properties, the material has several possible applications [1] in research areas such as hydrogen storage media, energy conversion devices, electromagnetic interference shielding, sensors, solar cells and microelectronics devices [2–4]. In trying to improve the performance to meet new demands of unconventional requests in different areas such as optoelectronics and solar energy utilization [5]. Some works have highlighted the synthesis of CNTs-anatase titanium dioxide (CNT-TiO<sub>2</sub>) double nanocomposites with synergetic mixture of their essential properties [6–9]. The introduction of TiO<sub>2</sub> was motivated by its non-toxicity and long-term thermodynamic stability. The anatase-phase of TiO<sub>2</sub> exhibits an impressive photocatalytic activity and is higher than the rutile phase owing to its high mobility of free electrons (80 cm<sup>2</sup> V<sup>-1</sup> s<sup>-1</sup>), ≈ 90 times faster than that of rutile phase [10]. The advantage of the mixture CNTs and TiO<sub>2</sub> semiconductor composites can be extended to the defined carbon structures with tailored electronic

properties for optoelectronics and/or microelectronics devices. Several researchers have synthesized CNTs-TiO<sub>2</sub> using sol-gel [11–14], hydrothermal treatment [15–17], electro-spinning [18,19], hydrolysis [20–22], laser pyrolysis [23] and electrode-position [24] techniques. Huang et al. [14] and Tettey [25] et al. studied the electrical conductivity of CNTs-TiO<sub>2</sub> composites materials and found that the conductivity of the CNTs increases due to the incorporation of TiO<sub>2</sub>. Most of these works [11–13,15–25], TiO<sub>2</sub> is the parent material doped with different concentrations of CNTs and their focus was to tailor conductivity, electronic, photo catalysis, electro catalysis and optical properties of the materials for solar cells. Both TiO<sub>2</sub> and MWCNTs exhibit antifouling properties that potentially complementary each-other. The novelty of the work presented here is the investigation and to establishment of possibilities of the material having improved complementary properties for applications such as the catalytic activities, optoelectronics, and microelectronics devices. In additions, the stability of the materials as a nano-filler for non-photo-coupled applications will be reported for the first time in this work. In this present study, we have synthesized multi-walled carbon nanotubes (MWCNTs) by chemical vapour decomposition (CVD) process. TiO<sub>2</sub> with different

\* Corresponding authors.

E-mail addresses: [Raysc@unisa.ac.za](mailto:Raysc@unisa.ac.za) (S.C. Ray), [wfpong@mail.tku.edu.tw](mailto:wfpong@mail.tku.edu.tw) (W.F. Pong).

<https://doi.org/10.1016/j.diamond.2019.107570>

Received 27 June 2019; Received in revised form 1 October 2019; Accepted 4 October 2019  
0925-9635/© 2019 Elsevier B.V. All rights reserved.

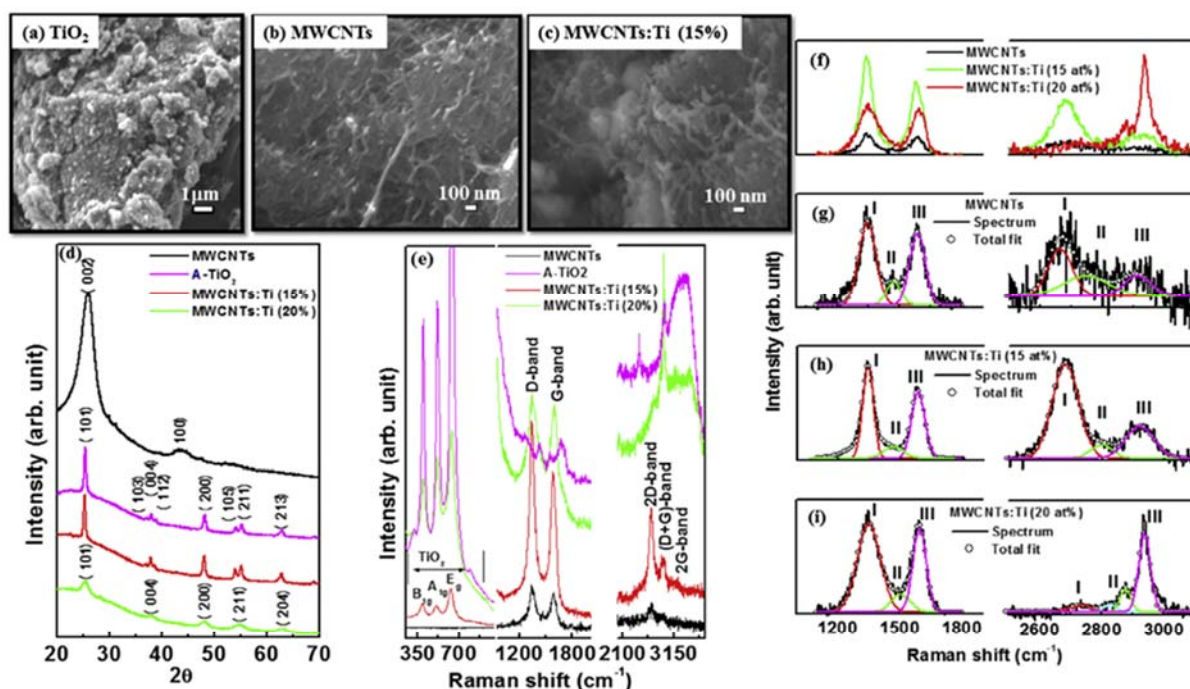


**Fig. 1.** FE-SEM images of (a) anatase  $\text{TiO}_2$ -powder ( $< 25$  nm), (b) synthesized MWCNTs and (c) MWCNTs- $\text{TiO}_2$  (Ti-15 at.%) nanocomposites. (d) X-ray diffraction spectra and (e) Raman spectra of anatase- $\text{TiO}_2$ , MWCNTs and MWCNTs- $\text{TiO}_2$  nanocomposites (Ti-15 at.% and Ti-20 at.%), respectively; (f) first/second order Raman spectra of MWCNTs, MWCNTs- $\text{TiO}_2$  (Ti-15 at.%) and MWCNTs- $\text{TiO}_2$  (Ti-20 at.%), (g) first/second order deconvoluted Raman spectrum of MWCNTs, (h) first/second order deconvoluted Raman spectrum of MWCNTs- $\text{TiO}_2$  (Ti-15 at.%) and (i) first/second order deconvoluted Raman spectrum of MWCNTs- $\text{TiO}_2$  (Ti-20 at.%).

concentrations (15 and 20 at.%) were incorporated in MWCNTs using hydrothermal method with the aim to tailor its properties for micro and nano-electronic devices applications, especially for memristive devices through increasing the current (I) – voltage (V) characteristics loops. The purpose of this research was to investigate the novel and complementary effects of  $\text{TiO}_2$  NPs and MWCNTs nanocomposites on three important properties: microstructural, electronic and bonding properties and enhancing the current (I) – voltage (V) characteristics loops area through several cycles electrical measurements. In trying to achieve this material properties, different characterization techniques have been used for the study of microelectronic structure and electrical behaviour of the synthesized nanocomposites.

## 2. Experimental details

Acetylene ( $\text{C}_2\text{H}_2$ ), ferrocene [ $\text{Fe}(\text{C}_5\text{H}_5)_2$ ] and  $\text{TiO}_2$  were purchased from Sigma-Aldrich (Pty) Ltd. CVD techniques was adopted to synthesize MWCNTs in a horizontal tube furnace using acetylene ( $\text{C}_2\text{H}_2$ ) and ferrocene [ $\text{Fe}(\text{C}_5\text{H}_5)_2$ ] as carbon source and catalyst precursor, respectively. The ferrocene (0.2 g) was spread over a quartz boat and placed in the centre of the quartz tube. The furnace was then heated at  $10^\circ\text{Cmin}^{-1}$  under the flow of Argon (Ar) gas.  $\text{C}_2\text{H}_2$  was introduced along with  $\text{N}_2$  when the temperature reaches  $900^\circ\text{C}$ . After 60 min of reaction time, the flow of  $\text{C}_2\text{H}_2$  was stopped and the furnace was cooled to room temperature. The boat was taken out from the furnace and the synthesized MWCNTs were collected. The synthesized MWCNT were washed with nitric and hydrochloric acid and filtered in order to remove impurities [17]. For the synthesis of anatase- $\text{TiO}_2$  and MWCNTs composite structures with different Ti at.%, we have used hydrothermal method following vaporization and drying technique [17].

Initially 10 mg of synthesized MWCNTs was dispersed in water and sonicated for 10 min. Afterwards,  $\text{TiO}_2$ -powder (particle size  $< 25$  nm)

was added to the suspension while stirring in different stoichiometric ratios. The mixture was stirred on a hot plate at  $80^\circ\text{C}$  with the flow of Ar through the surface of the mixture to speed up the vaporization of water. Thereafter, the mixture was kept in an oven at  $100^\circ\text{C}$  to dry for 15 h for formation of the MWCNTs- $\text{TiO}_2$  nanocomposites.

Different characterization techniques used to characterize the prepared nanocomposites were X-ray diffraction (XRD), field emission scanning electron microscopy (FE-SEM), Raman spectroscopy, X-ray absorption near edge structure spectroscopy (XANES), X-ray photo-emission spectroscopy (XPS) and current-voltage (I-V) [26]. All measurements were performed at room temperature. To obtain the surface morphology of  $\text{TiO}_2$ , MWCNTs, and MWCNTs- $\text{TiO}_2$  nanocomposites, field emission scanning electron microscopy (FE-SEM) images were recorded using a JSM-7800F FESEM from JEOL Ltd. coupled with an UltraDry EDS detector. The structural studies of the synthesized composites were performed using a Rigaku Smartlab X-ray diffractometer (0.154 nm Cu K $\alpha$  line). Raman spectra were recorded using a HORIBA scientific XploRA at 532 nm ( $\sim 2.41$  eV) LASER light excitation energy. The surface morphological structures were studied using JEOL JEM 2100. The C K-edge, O K-edge, and Ti  $L_{3,2}$ -edge XANES measurements were performed at the Taiwan Light Source (TLS), Hsinchu, Taiwan. The core shells C 1s, O 1s, and Ti 2p were performed using a KRATOS-SUPRA spectrometer with a monochromatic Al K $\alpha$  radiation possessing an excitation energy,  $h\nu = 1486.6$  eV, and a base pressure  $1.2 \times 10^{-9}$  Torr at UNISA (Florida Science Campus). The electrical conductivity was studied using Keithley 6487 with a voltage sweep ranging from  $-1.0$  to  $+1.0$  V. In this measurement, silver paste was used as the conducting electrodes to investigate the electrical behaviour of the materials. The range voltage of  $0 \rightarrow +1.0$  V,  $+1.0 \rightarrow 0$  V,  $0 \rightarrow -1.0$  V, and  $-1.0 \rightarrow 0$  V was used to obtain the I-V data. The value of 1.0 V was the highest voltage applied for the current limit of 2.5 mA.



**Table 1**  
Compositional/quantificational analysis from XPS, crystallite size from XRD and ( $I_D/I_G$ ) ratio from Raman Spectra.

	Compositional and quantificational analysis from XPS			Crystallite size (nm) from XRD	$(I_D/I_G)$ ratio from Raman spectra
	C at.%	O at.%	Ti at.%		
TiO <sub>2</sub>	–	66	33	18.10	–
MWCNTs	98	02	–	–	1.6
MWCNTs-TiO <sub>2</sub> (Ti-15 at.%)	45	40	15	18.26	1.2
MWCNTs-TiO <sub>2</sub> (Ti-20 at.%)	26	54	20	06.08	2.1

**Table 2**  
Different parameters obtained after de-convolution of Raman spectra.

	First order Raman spectra									Second order Raman spectra								
	Peak – I (D-band)			Peak – II (Auxiliary D-band)			Peak – III (G-Band)			Peak – I (2D-Band)			Peak – II (D + Aux.D)-Band			Peak – III (D + G)-Band		
	x (cm <sup>-1</sup> )	$\Delta\omega$ (cm <sup>-1</sup> )	Int. (a.u.)	x (cm <sup>-1</sup> )	$\Delta\omega$ (cm <sup>-1</sup> )	Int. (a.u.)	x (cm <sup>-1</sup> )	$\Delta\omega$ (cm <sup>-1</sup> )	Int. (a.u.)	x (cm <sup>-1</sup> )	$\Delta\omega$ (cm <sup>-1</sup> )	Int. (a.u.)	x (cm <sup>-1</sup> )	$\Delta\omega$ (cm <sup>-1</sup> )	Int. (a.u.)	x (cm <sup>-1</sup> )	$\Delta\omega$ (cm <sup>-1</sup> )	Int. (a.u.)
MWCNTs	1345	83	2.1	1471	72	0.5	1586	74	1.6	2664	79	0.3	2746	148	0.2	2912	87	0.1
MWCNTs-TiO <sub>2</sub> (Ti-15 at.%)	1342	51	5.2	1456	195	1.5	1584	64	5.7	2682	85	2.7	2799	70	0.3	2922	90	1.0
MWCNTs-TiO <sub>2</sub> (Ti-15 at.%)	1348	111	6.6	1504	94	1.1	1595	64	3.7	2732	70	0.3	2827	43	0.2	2938	37	1.9
	–	–	–	–	–	–	–	–	–	–	–	–	2876	33	0.5	–	–	–

### 3. Results and discussion

#### 3.1. Surface morphology

FE-SEM images of TiO<sub>2</sub>, MWCNTs and MWCNTs-TiO<sub>2</sub> nanocomposites are shown in Fig. 1(a–c), respectively. The images show a usual spherical shape and tubular-like shape structure of TiO<sub>2</sub> nanoparticles and MWCNTs. The images also indicate that TiO<sub>2</sub> is closely and homogeneously bounded to the surface of MWCNTs yet displayed minute agglomeration along the surface of MWCNTs, [27]. The aggregation observed in the figure indicates that TiO<sub>2</sub> is well deposited/grown on the MWCNTs surface. This type of connection might result in free electrons transfer among TiO<sub>2</sub> and MWCNTs nanomaterials hence improving electronic and electrical properties of the nanocomposites.

#### 3.2. X-ray diffraction

Fig. 1(d) displays the XRD patterns of TiO<sub>2</sub>, MWCNTs and MWCNTs-TiO<sub>2</sub> nanocomposites. The XRD pattern of TiO<sub>2</sub> shows characteristic peaks at  $2\theta \sim 25.3^\circ, \sim 37.1^\circ, \sim 37.9^\circ, \sim 38.7^\circ, \sim 48.1^\circ, \sim 54.2^\circ, \sim 55.3^\circ$  and  $\sim 62.9^\circ$  corresponding to anatase-phase of (101), (103), (004), (112), (200), (105), (211) and (204), respectively [28]. In the case of MWCNTs, a broad diffraction peak  $2\theta \sim 25.9^\circ$  corresponding to (002) of graphitic features and a less intense peak at  $\approx 43.2^\circ$  corresponding to (100) reflection match well with standard graphite carbon [29]. The patterns of MWCNTs-TiO<sub>2</sub> (Ti-15 at.%) and MWCNTs-TiO<sub>2</sub> (Ti-20 at.%) show similar peaks as TiO<sub>2</sub> with (103), (112) and (105) peaks not observed for MWCNTs-TiO<sub>2</sub> (Ti-20 at.%) pattern. It can be seen that the (002) plane for MWCNTs overlaps with that of (101) and the carbon plane (100) disappeared for MWCNTs-TiO<sub>2</sub> nanocomposites pattern. This pattern may be due to the presence of TiO<sub>2</sub> in the MWCNTs. We have obtained the crystallite size, D (nm) of TiO<sub>2</sub> in (101) plane of MWCNTs-TiO<sub>2</sub> (Ti-15 at.%) and MWCNTs-TiO<sub>2</sub> (Ti-20 at.%) using Scherrer's equation ( $D = k\lambda/\beta\cos\theta$ ), where k is  $\sim 0.9$ ,  $\lambda = 1.54 \text{ \AA}$  (wavelength of X-ray),  $\beta$  is full width at half maximum and  $\theta$  is the Bragg's angle. The crystallite sizes were found to be 18.10 nm, 18.26 nm and 6.08 nm for TiO<sub>2</sub>, MWCNTs-TiO<sub>2</sub> (Ti-15 at.%) and MWCNTs-TiO<sub>2</sub> (Ti-20 at.%), respectively (see Table 1), suggesting the growth of TiO<sub>2</sub> on the MWCNTs surface.

#### 3.3. Raman spectroscopy

Fig. 1(e) shows that TiO<sub>2</sub> has three prominent peaks at  $\sim 398, \sim 519$  and  $\sim 642 \text{ cm}^{-1}$  which are allocated to TiO<sub>2</sub>-anatase phase of B<sub>1g</sub>, A<sub>1g</sub> and E<sub>g</sub> mode, respectively [30,31]. In the case of MWCNTs, four main peaks at  $\sim 1345, \sim 1585, \sim 2664$  and  $\sim 2912 \text{ cm}^{-1}$  correspond to D-band, G-band, 2D-band and (D + G)-band, respectively [32–37]. The G band owes to the binary degenerate zone centre E<sub>2g</sub> mode while the D-band owes to the defected graphite [32–37]. The 2D band is an overtone of D band and it occurs due to the second order vibration process, and D + G band occurs due to the combine vibration of D- and G-bands. MWCNTs-TiO<sub>2</sub> nanocomposites, on the other hand, show the combine effect i.e. the Raman peaks that arise from anatase-phase of TiO<sub>2</sub> and MWCNTs. These combined effects are due to introduction of TiO<sub>2</sub>-anatase phase on MWCNTs surface. It is also observed that the intensity of all three anatase-phase-TiO<sub>2</sub> peaks (B<sub>1g</sub>, A<sub>1g</sub> and E<sub>g</sub> mode) are reduced drastically with their peak positions shifting towards lower energy from  $398 \rightarrow 395 \rightarrow 388$  (B<sub>1g</sub>),  $519 \rightarrow 511 \rightarrow 508$  (A<sub>1g</sub>) and  $642 \rightarrow 636 \rightarrow 629$  (E<sub>1g</sub>) for TiO<sub>2</sub>  $\rightarrow$  MWCNTs-TiO<sub>2</sub> (Ti-15 at.%)  $\rightarrow$  MWCNTs-TiO<sub>2</sub> (20 at.%), respectively. These peak shifts imply a reduction in crystal matrix vibrational energy [38] hence crystallinity consistency with the crystallite size obtained from XRD. For a detailed microstructural study, we have de-convoluted first order and second order Raman spectra into three Gaussian lines for each and these are shown in Fig. 1 and the results are tabulated in Table 2. For de-convolution of the first order Raman spectra, we consider one auxiliary D-lines along with D and G-bands. The comparative intensity proportion of the D and G-bands is the index of graphitization to examine the MWCNTs/MWCNTs-TiO<sub>2</sub> nanocomposites microstructure [39]. We have obtained the proportion ( $I_D/I_G$ ) of MWCNTs-TiO<sub>2</sub> as 1.2 (Ti: 15 at.%) and 2.1 (Ti:20 at.%), compared to MWCNTs (1.6) as given in Table 1, showing the graphitic system of MWCNTs-TiO<sub>2</sub> nanomaterials varies, according to the TiO<sub>2</sub>-content bonded on the MWCNTs surface after formation of MWCNTs-TiO<sub>2</sub> nanocomposites. It is observed that the G-band peak-width ( $\Delta\omega$ ) does not change, while that of D-band  $\Delta\omega$  increases significantly for the MWCNTs-TiO<sub>2</sub> (20 at.%) nanocomposites. The increase of D-band width with the shifts of D- and G-bands signifies the formation of more graphitic nature of the MWCNTs-TiO<sub>2</sub> nanocomposites. The 2nd order Raman spectra was also de-convoluted into three Gaussian lines assigned as 2D-peak, which is the overtone of D-peak,

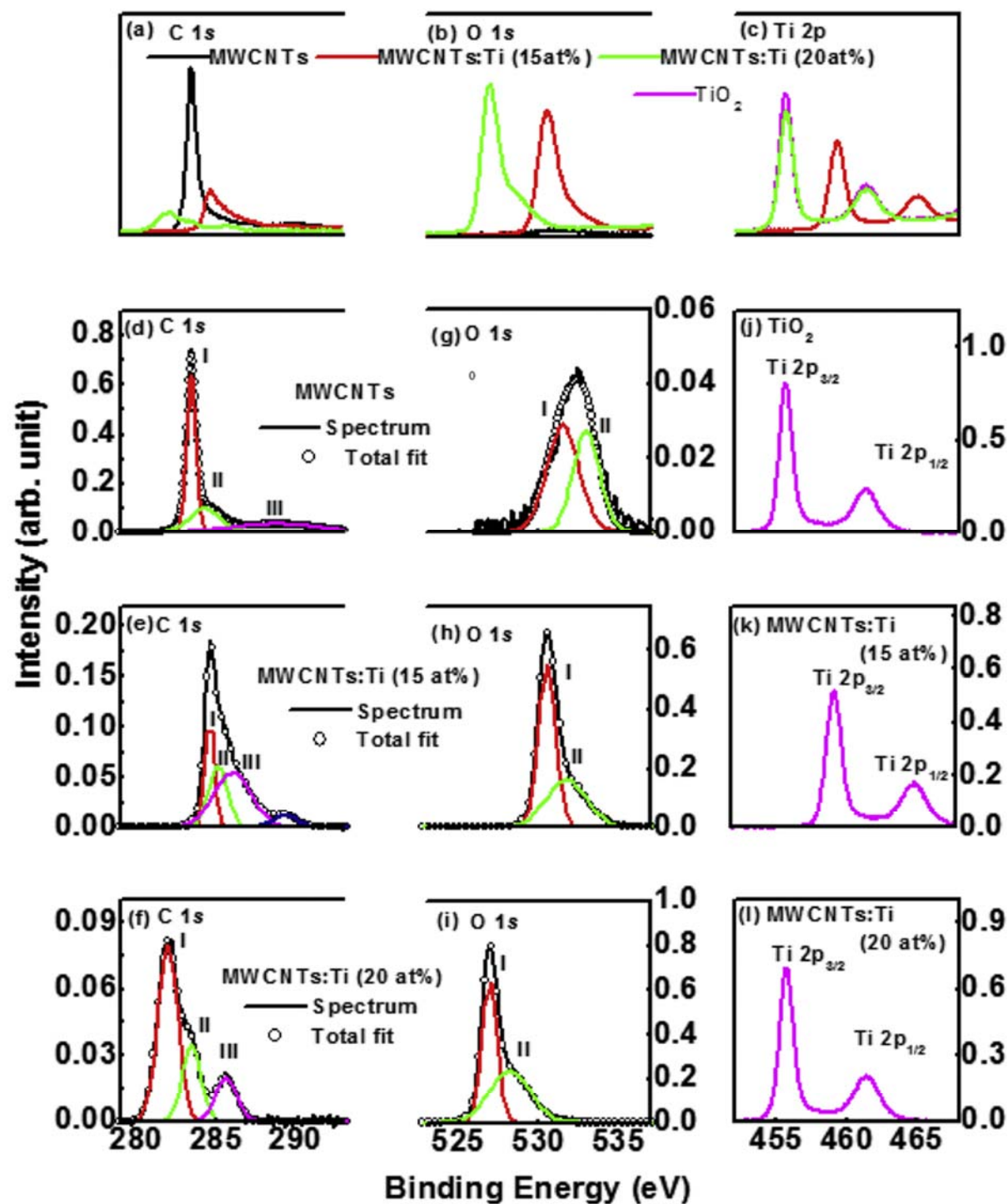


Fig. 2. XPS of (a) C 1s, (b) O 1s, (c) Ti 2p for MWCNTs, MWCNTs-TiO<sub>2</sub> (Ti-15 at%) and MWCNTs-TiO<sub>2</sub> (Ti-20 at%); (d-f) deconvoluted C 1s (g-i) deconvoluted O 1s XPS spectra of MWCNTs, MWCNTs-TiO<sub>2</sub> (Ti-15 at%) and MWCNTs-TiO<sub>2</sub> (Ti-20 at%); (j-l) Ti 2p spectrum of TiO<sub>2</sub>, MWCNTs-TiO<sub>2</sub> (Ti-15 at%) and MWCNTs-TiO<sub>2</sub> (Ti-20 at%).

**Table 3**  
Different parameters obtained after de-convolution of C 1s, O 1s and Ti 2p XPS spectra.

	C 1s XPS									O 1s XPS						Ti 2p XPS	
	Peak - I			Peak - II			Peak - III			Peak - I			Peak - II			Ti 2p <sub>3/2</sub>	Ti 2p <sub>1/2</sub>
	x	$\Delta\omega$	Int.	x	$\Delta\omega$	Int.	x	$\Delta\omega$	Int.	x	$\Delta\omega$	Int.	x	$\Delta\omega$	Int.	x	x
(eV)	(eV)	(a.u.)	(eV)	(eV)	(a.u.)	(eV)	(eV)	(a.u.)	(eV)	(eV)	(a.u.)	(eV)	(eV)	(a.u.)	(eV)	(eV)	
MWCNTs	283.5	0.7	2.1	284.3	2.3	1.3	288.8	6.5	3.1	530.5	2.7	2.6	531.9	2.2	0.7	-	-
MWCNTs-TiO <sub>2</sub> (Ti-15 at.%)	284.6	0.6	0.5	285.4	1.7	0.9	287.5	3.3	0.4	530.4	1.1	3.8	531.7	2.5	2.6	459.3	465.1
MWCNTs-TiO <sub>2</sub> (Ti-20 at.%)	281.9	1.2	0.6	283.4	1.2	0.3	285.6	1.3	0.2	526.9	0.9	3.9	528.2	2.5	3.8	455.6	461.4
TiO <sub>2</sub>	-	-	-	-	-	-	-	-	-	-	-	-	-	-	-	455.6	461.4

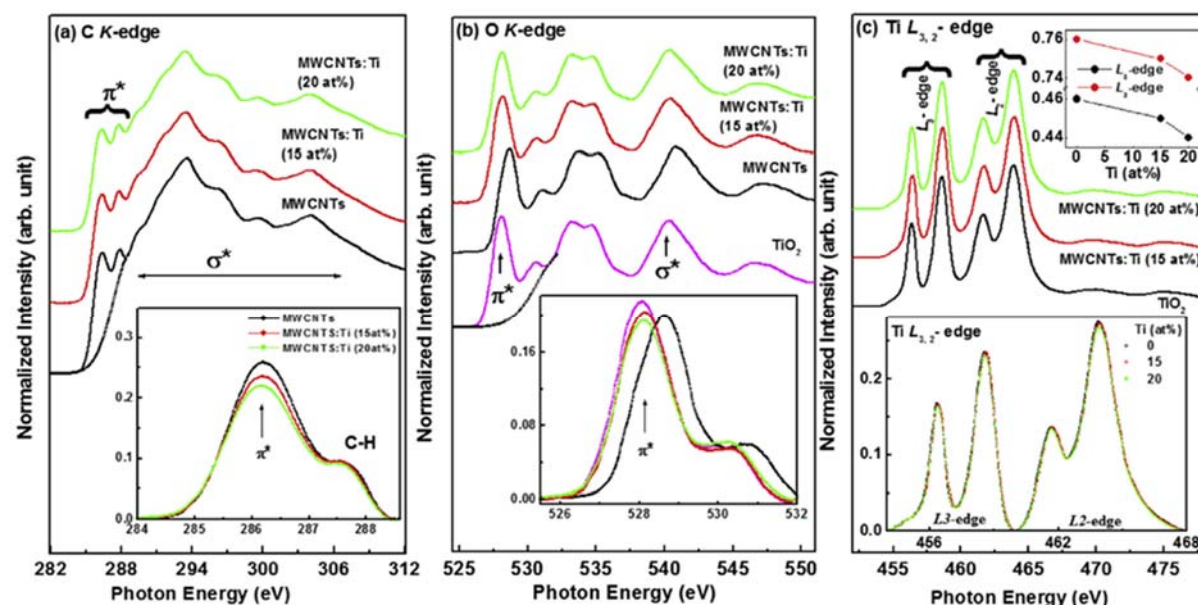


Fig. 3. XANES spectra of MWCNTs, MWCNTs-TiO<sub>2</sub> (Ti: 15 at.%) and MWCNTs-TiO<sub>2</sub> (Ti: 20 at.%) nanocomposites (a) C K-edge, (b) O K-edge and (c) Ti-L<sub>3,2</sub>-edge.

D + G peak the combine vibration of D- and G-modes and the combined vibration of auxiliary-D with D-bands. The overall change of different peak positions, peak widths and their intensities in the nanocomposites attributes to the improvement of surface electric charge of the oxides in the nanocomposite owing to the decoration of TiO<sub>2</sub>, inducing a promising electronic change of  $\pi \rightarrow \pi^*$  of MWCNTs and  $n \rightarrow \pi^*$  among the *n*-orbital of the oxygen species of TiO<sub>2</sub> and MWCNTs [40].

### 3.4. X-ray photoelectron spectroscopy

XPS was used to obtain the composition and quantification of C, O and Ti for MWCNTs and MWCNTs-TiO<sub>2</sub> (15 and 20 at.%) nanocomposites and these are shown in Table 1. From the table, we observed that carbon content decrease with an increase Ti at.% in the MWCNTs-TiO<sub>2</sub> nanocomposites indicating carbon atoms is replaced by Ti-atom and TiO<sub>2</sub> is bonded on the MWCNTs surface to enhance the surface electric charge of the oxides in the nanocomposites. For details bonding and electronic behaviour study of the MWCNTs-TiO<sub>2</sub> nanocomposites, we have used XPS spectra of C 1s and O 1s and Ti 2p presented in Fig. 2(a-c) respectively. It is found that the peaks of C 1s, O 1s and Ti 2p XPS spectrum of lower Ti-content (15 at.%) nanocomposites are shifted at higher binding energy side while that of higher Ti-content (20 at.%) shifted at lower binding energy side compared to pure MWCNTs. At the same time, the intensity of carbon content decreases and that of oxygen content increases with Ti-content in the MWCNTs-TiO<sub>2</sub> nanocomposites

indicating the formation of different electronic structured MWCNTs-TiO<sub>2</sub> nanocomposites. For details study, the spectra of C 1s and O 1s for MWCNTs/MWCNTs-TiO<sub>2</sub> nanocomposites were de-convoluted into three and two Gaussian lines respectively as shown Fig. 2(d-f) & (g-i), and their peak positions (x), peak width ( $\Delta\omega$ ) intensities are presented in Table 3. In the case of XPS spectra of C 1s, three main peaks at  $\sim 283.5/\sim 284.3$  eV and  $\sim 288.8$  eV assigned to  $sp^2$  C=C and C=O bonding, [28] respectively are observed in MWCNTs as shown in Fig. 2(d). These peaks are shifted to 284.6/281.9 eV, 285.4/283.4 eV and 287.5/285.6 eV respectively for the MWCNTs-TiO<sub>2</sub> (15 at.%) /MWCNTs-TiO<sub>2</sub> (20 at.%) nanocomposites, respectively after TiO<sub>2</sub> bonded with MWCNTs implying that the TiO<sub>2</sub> imparted the structural change in MWCNTs-TiO<sub>2</sub> nanocomposites. Considering the XPS spectra of O 1s, two peaks located at  $\approx 530.5$  and  $\approx 531.9$  eV for the MWCNTs correspond to C=O/O=C-OH and C-OH group, respectively [41]. These peaks are shifted at lower binding energy at  $\sim 530.4/526.9$  (I) and  $531.7/528.2$  eV (II), respectively for the MWCNTs-TiO<sub>2</sub> (15 at.%) /MWCNTs-TiO<sub>2</sub> (20 at.%) nanocomposites. This shift may be due to a formation of different bonding like Ti-C/Ti-O-H/Ti-OH and C=O in anatase TiO<sub>2</sub> [42,43] whereas the 531.7 eV peak is associate to Ti-O-H or C=O [44]. However, these functional groups in MWCNTs-TiO<sub>2</sub> nanocomposites experience an esterification reaction and C-O-Ti or O=C-O-Ti bonding [30]. This is due to reaction with Ti precursor -OH groups [30]. The Ti 2p core level binding energy regions of TiO<sub>2</sub> and MWCNTs-TiO<sub>2</sub> (15 at.%) /MWCNTs-TiO<sub>2</sub> (20 at.%) nanocomposites are

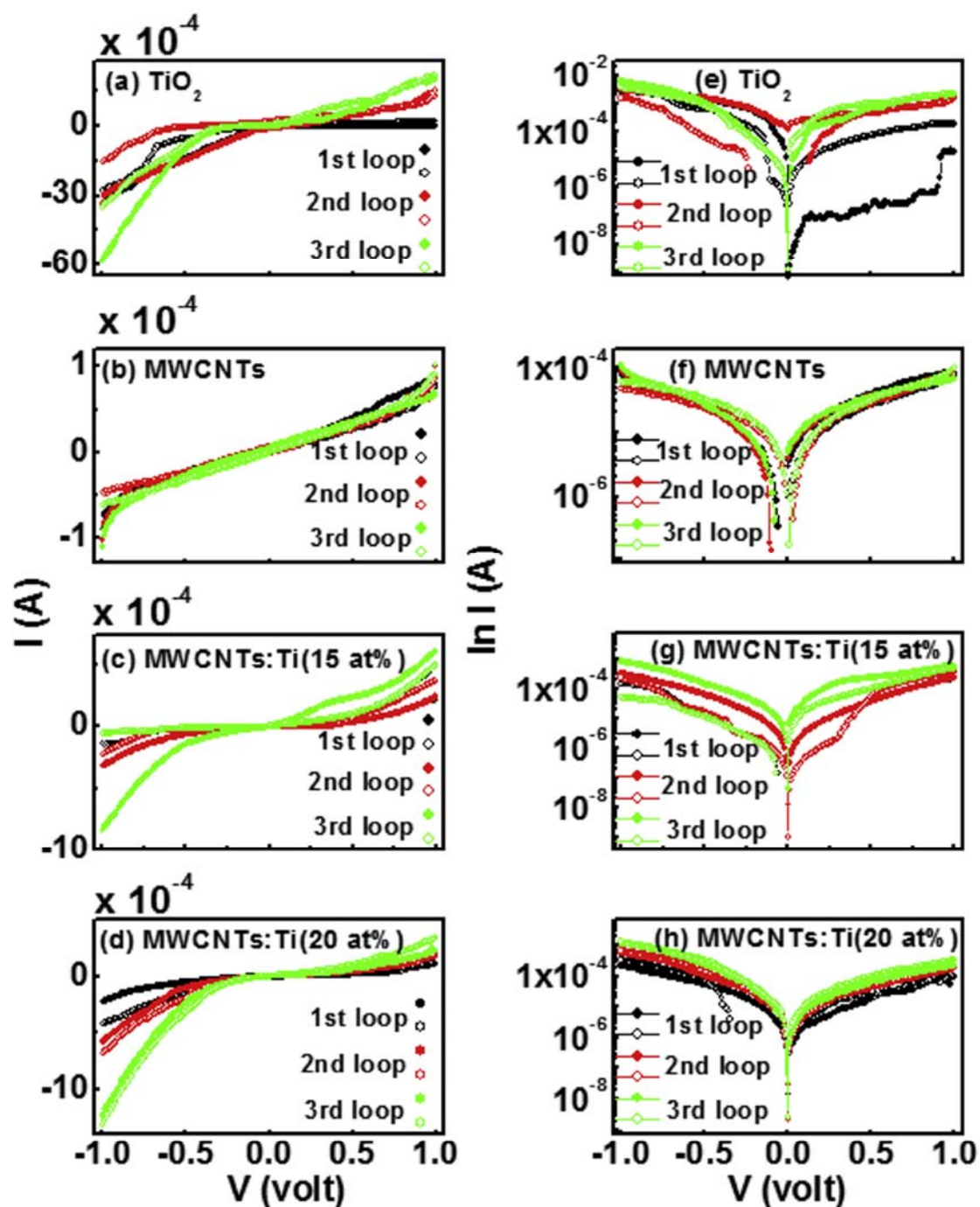


Fig. 4. (a-d) Current (I)-Voltage (V) linear and (e-h) ( $\ln I$ -V) relationships of  $\text{TiO}_2$ , MWCNTs, MWCNTs- $\text{TiO}_2$  (Ti-15 at%) and MWCNTs- $\text{TiO}_2$  (Ti-20 at%) respectively [Each case three cycles measurements of (I-V) and ( $\ln I$ -V)].

shown in Fig. 2(j-l). The two peaks of Ti 2p located at  $\sim 459.3$  and at  $\sim 465.1$  eV are assigned to Ti  $2p_{3/2}$  and  $2p_{1/2}$ , respectively with core-shell spin-orbit splitting of 5.8 eV. These two peaks are shifted to  $\sim 455.6$  eV and  $\sim 461.4$  eV respectively keeping spin-orbit splitting the same for both MWCNTs- $\text{TiO}_2$  nanocomposites implying the presence of

$\text{Ti}^{4+}$  oxidation state [28,44]. The observed change in their binding energies of Ti 2p is due to the electrons moving through Ti-O-C bonds with change of electron density of  $\text{Ti}^{4+}$  in  $\text{TiO}_2$  [43] (Table 3).

### 3.5. X-ray absorption near edge spectroscopy

XANES is an effective technique to examine the local and electronic structures and surface chemistry of MWCNTs. The XANES spectra of C K-edge, O K-edge and Ti  $L_{2,3}$ -edge for TiO<sub>2</sub>, MWCNTs and MWCNTs-TiO<sub>2</sub> nanocomposites are presented in Fig. 3. The figure shows that the C K-edge spectra of MWCNTs and MWCNTs-TiO<sub>2</sub> nanocomposites are similar. The double structures at ~286 and ~293.0 eV are transitions of  $\pi^*$  (C-C) and  $\sigma^*$  for MWCNTs, respectively [29,44]. The peak at ~287.5 eV is identified as change in hybridization to  $sp^3$  states owing to C-H and/or C-O bonding or change in metal bonding with the lattice of MWCNT [44,45]. Fig. 3(b) displays edge jump XANES spectra of O K-edge which give more vital evidence concerning the degree of oxidation of MWCNTs and MWCNTs-TiO<sub>2</sub> nanocomposites. The spectra exhibit typical structures at 528.5 and 530.5 eV corresponding to transitions of  $\pi^*$  (C=O) and 538–544 eV peaks corresponding to  $\sigma^*$  (C-O and O-H) integrating from carboxylic and hydroxyl groups, respectively [46]. Apart from these peaks, a double structure peak at ~533 eV and 535 eV shown within the range of 530–536 eV in the spectra of O K-edge assigned to the physisorbed O<sub>2</sub> [47], is expected to arise from the chemicals as well as TiO<sub>2</sub> used during the synthesis of the nanocomposites. However, the spectra regions of 530–536 eV in MWCNTs-TiO<sub>2</sub> nanocomposites are recognized as the hybridization of O 2p to Ti 3d states [48]. The degenerate Ti 3d band splits into two peaks, 533 eV and 535 eV corresponding to  $t_{2g}$  and  $e_g$  splitting owing to the effect of crystal field [48]. This splitting is very sensitive to the degree of hybridization and coordination number. The peaks at ~540 eV and at ~546 eV, on the other hand, are recognized as the hybridization of O 2p to Ti 4sp state [49,50] that are sensitive to long-range order. The complex system of Ti  $L_{2,3}$ -edge XANES spectra occurs due to connection of atomic contact and crystal field effect [51,52]. Fig. 3(c) displays the Ti  $L_{2,3}$ -edge XANES spectra of MWCNTs/MWCNTs-TiO<sub>2</sub> nanocomposites and the characteristic XANES spectrum of TiO<sub>2</sub> nanoparticles. The  $L_3$  and  $L_2$  regions are assigned to O 2p<sub>3/2</sub>-Ti 3d and O 2p<sub>1/2</sub>-Ti 3d alterations, respectively. The regions at ~456.4, 458.6 and 461.6, 470.1 eV correspond to crystal field splitting of 3d band into  $t_{2g}$  and  $e_g$  bands. Since the Ti  $e_g$  orbitals pointed straight to the direction of 2p orbitals of the neighbouring O atoms, the  $e_g$  band is more delicate to the local atmosphere. The intensity for both  $L_3$  and  $L_2$  decreases with increase of Ti-content (at.%) as shown in an inset of (c). This variation of regions with Ti-content indicates carbon and/or oxygen is replaced by Ti-atom in the MWCNTs-TiO<sub>2</sub> nanocomposites.

### 3.6. Current-voltage (I-V) measurement

Electrical conductivity study were performed using current (I) – voltage (V) relationships of TiO<sub>2</sub>, MWCNTs, MWCNTs-TiO<sub>2</sub> (Ti-15 at.%) and MWCNTs-TiO<sub>2</sub> (Ti-20 at.%). The results are shown in Fig. 4. Working electrodes for solar cells depends on electrical property of a material owing to the constant flow of electrons leading to an effective gathering of photoelectrons generated by TiO<sub>2</sub> nanomaterial as well as MWCNTs [15]. Batteries and capacitors can be produced from these conductive films [53]. The current-voltage (I-V) characteristics data was recorded for sweeping voltage from 0 to +1 V, +1 to 0 V, 0 to -1 and -1 to 0 and are presented in different ways to properly understand the conduction mechanism. Fig. 4(a-d) linear I-V curve; whereas Fig. 4(e-h) shows log (I) versus V for TiO<sub>2</sub>, MWCNTs, MWCNTs-TiO<sub>2</sub> (Ti-15 at.%) and MWCNTs-TiO<sub>2</sub> (Ti-20 at.%) nanocomposites device respectively. The focus of the current-voltage measurements study of MWCNTs-TiO<sub>2</sub> (Ti-20 at.%) nanocomposites is geared to improve the memristive behaviour by changing the electrical conductivity of MWCNT. Since MWCNT is conductive as shown in Fig. 4(b) and then composite with TiO<sub>2</sub> enhance the memristive capability. In each case, we presented three cycles I-V curve to ascertain ferroelectric behaviour of these materials. The range of the voltage source was -1 to +1 V with an automatic voltage sweep option in three cycles for each are

shown in the Fig. 4(e-h). The linear (I-V) behaviour clearly shows that the MWCNTs is a conducting material in nature while non-linear behaviour of TiO<sub>2</sub> and MWCNTs-TiO<sub>2</sub> nanocomposites are semi-conducting materials. Log (I) vs V characteristics curve exhibit extended memristive properties by enhancing the I-V loops area in TiO<sub>2</sub>-MWCNTs nanocomposites materials. It is observed during second and third cycle I-V measurements that the composites may have charge storage mechanism that could be comparable with the electrical conductivity measurements of bristle-like TiO<sub>2</sub>-MWCNT nanocomposites [14,25]. This conjecture is confirmed in Fig. 4(e-h), where the trends for MWCNTs-TiO<sub>2</sub> (Ti-15 at.%) have higher memristive as well as charge storage behaviour. Particularly, the MWCNTs-TiO<sub>2</sub> (Ti-15 at.%) shows a considerable electric I-V hysteresis loop indicating a ferroelectric behavior, which could be useful for ferroelectric applications. Higher conductive I-V hysteresis loops is found to be more considerable for MWCNTs-TiO<sub>2</sub> (Ti-15 at.%) due to deposition of TiO<sub>2</sub> impurity in Ti-sites on the MWCNTs surface and availability of higher number of free electrons to contribute to the measured current.

## 4. Conclusion

MWCNTs and MWCNTs-TiO<sub>2</sub> nanocomposites have been synthesized using chemical vapour deposition and hydrothermal process, respectively. The electronic and electrical behaviour of the synthesized MWCNTs/MWCNTs-TiO<sub>2</sub> nanocomposites were studied using FESEM, XRD, Raman, XPS and I-V techniques. We observed for the first time that MWCNTs change from a conducting to a semiconducting material when incorporated with TiO<sub>2</sub> nanoparticles. The TiO<sub>2</sub> incorporated MWCNTs nanocomposites showed the tailored microstructural, electronic and electrical properties for their application towards micro and nano electronic devices, especially for memristive devices, charge storage and ferroelectric devices due to transfer Ti-charge into MWCNTs as well as photo-catalytic activity applications. Therefore, these possibilities of tailoring MWCNTs can make the material suitable for different electrical/electronic device applications.

## Acknowledgements

The authors appreciate the financial support received from the National Research Foundation (NRF), South Africa (Grant Nos. 105292, PD-TWAS150813137166 and EQP13091742446).

## Declaration of competing interest

The authors declare no conflict of interest.

## References

- [1] B. Wei, R. Vajtai, Y.J. Jung, J.W. Ward, R. Zhang, G. Ramanath, P.M. Ajayan, Assembly of highly organized carbon nanotube architectures by chemical vapor deposition, *Chem. Mater.* 15 (2003) 1598–1606.
- [2] A. Kumar, K. Kumar, P. Kumar Ghosh, K.L. Yadav, MWCNT/TiO<sub>2</sub> hybrid nano filler toward high performance epoxy composite, *Ultrason. Sonochem.* 41 (2018) 37–46.
- [3] R.H. Baughman, A.A. Zakhidov, W.A. de Heer, Carbon nanotubes—the route toward, *Sci. Compass* 787 (2002) (2012) 787–792.
- [4] Wolfgang Bauhofer, Josef Z. Kovacs, A review and analysis of electrical percolation in carbon nanotube polymer composites, *Compos. Sci. Technol.* 69 (10) (2009) 1486–1498.
- [5] S. Jain, R. Yamgar, R. Jayram, Photolytic and photocatalytic degradation of atrazine in the presence of activated carbon, *Chem. Eng. J.* 148 (2009) 342–347.
- [6] Y. Yao, G. Li, S. Ciston, R.M. Lueptow, K.A. Gray, Photoreactive TiO<sub>2</sub>/carbon nanotube composites: synthesis and reactivity, *Environ. Sci. Technol.* 42 (2008) 4952–4957.
- [7] W. Wang, P. Serp, P. Kaleck, C.G. Silva, J.L. Faria, Preparation and characterization of nanostructured MWCNT-TiO<sub>2</sub> composite materials for photocatalytic water treatment applications, *Mater. Res. Bull.* 43 (2008) 958–967.
- [8] Tae Young Lee, Prashant S. Alegaonkar, Ji-Beom Yoo, Fabrication of dye sensitized solar cell using TiO<sub>2</sub> coated carbon nanotubes, *Thin Solid Films* 515 (2007) 5131–5135.
- [9] Y. Ou, J. Lin, S. Fang, D. Liao, MWNT-TiO<sub>2</sub>:Ni composite catalyst: a new class of catalyst for photocatalytic H<sub>2</sub> evolution from water under visible light illumination,

J.A. Oke, et al.

Diamond &amp; Related Materials 100 (2019) 107570

- Chem. Phys. Lett. 429 (2006) 199–203.
- [10] D.C. Hurum, K.A. Gray, T. Rajh, M.C. Thurnauer, Recombination pathways in the Degussa P25 formulation of TiO<sub>2</sub>: surface versus lattice mechanisms, *J. Phys. Chem. B* 109 (2005) 977–980.
- [11] Yongsong Luo, Jiping Liu, Xiaohong Xia, Xiaoqin. Li, Tao. Fang, Suqin Li, Qinfeng Ren, Jialin Li, Zhijie Jia, Fabrication and characterization of TiO<sub>2</sub>/short MWNTs with enhanced photocatalytic activity, *Mater. Lett.* 61 (2007) 2467–2472.
- [12] W. Yu Cheng, L. Xiao Liu, M. Ye, X. Ting, X.M. Huang, Preparation and properties of carbon nanotube-TiO<sub>2</sub> nanocomposites, *Acta Phys. -Chim. Sin.* 24 (2008) 97–102.
- [13] Mohammad Bagher Askari, Zoha Tayakoli Banizi, Majid Seifi, Sedigheh Bagheri Dehaghi, Payam Veisi, Synthesis of TiO<sub>2</sub> nanoparticles and decorated multi-wall carbon nanotube (MWCNT) with anatase TiO<sub>2</sub> nanoparticles and study of optical properties and structural characterization of TiO<sub>2</sub>/MWCNT nanocomposite, *Optik* 149 (2017) 447–454.
- [14] X. Huang, M. Feng, X. Liu, Design of bristle-like TiO<sub>2</sub>-MWCNT nanotubes to improve the dielectric and interfacial properties of polymer-based composite films, *RSC Adv.* 4 (2014) 4985–4992.
- [15] S. Muduli, W. Lee, V. Dhas, S. Mujawar, M. Dubey, K.P. Vijayamohan, S.-H. Han, S. Ogale, Enhanced conversion efficiency in dye-sensitized solar cells based on hydrothermally synthesized TiO<sub>2</sub>-MWCNT nanocomposites, *ACS Appl. Mater. Interfaces* 1 (2009) 2030–2035.
- [16] K. Byrappa, A.S. Dayananda, S. Ponnappa, B. Basavalingu, M.B. Shayan, K. Soga, M. Yoshimura, Hydrothermal preparation of ZnO:CNT and TiO<sub>2</sub>:CNT composites and their photocatalytic applications, *J. Mater. Sci.* 43 (2008) 2348–2355.
- [17] D. Chaudhary, N. Khare, V.D. Vankar, Ag nanoparticles loaded TiO<sub>2</sub>/MWCNT ternary nanocomposite: a visible-light-driven photocatalyst with enhanced photocatalytic performance and stability, *Ceram. Int.* 42 (2016) 15861–15867.
- [18] Santosh Aryal, Chul Ki Kim, Kwan-Woo Kim, Myung Seob Khil, Hak Yong Kim, Multi-walled carbon nanotubes/TiO<sub>2</sub> composite nanofiber by electrospinning, *Mater. Sci. Eng., C* 28 (2008) 75–79.
- [19] Z. Peining, A.S. Nair, Y. Shengyuan, P. Shengjie, N.K. Elumalai, S. Ramakrishna, Rice grain-shaped TiO<sub>2</sub>-CNT composite—a functional material with a novel morphology for dye-sensitized solar cells, *J. Photochem. Photobiol. A* 231 (2012) 9–18.
- [20] L. Chen, B.-L. Zhang, M.-Z. Qu, Z.-L. Yu, Preparation and characterization of CNTs-TiO<sub>2</sub> composites, *Powder Technol.* 154 (2005) 70–72.
- [21] M. Božić, V. Vivod, R. Vogrinčić, I. Ban, G. Jakša, S. Hribernik, D. Fakin, V. Kokol, Enhanced catalytic activity of the surface modified TiO<sub>2</sub>-MWCNT nanocomposites under visible light, *J. Colloid Interface Sci.* 465 (2016) 93–105.
- [22] S. Sadhu, P. Poddar, Template-free fabrication of highly oriented single-crystalline 1D-rutile TiO<sub>2</sub>-MWCNT composite for enhanced photo electrochemical activity, *J. Phys. Chem. C* 118 (2014) 19363–19373.
- [23] J. Wang, Y. Lin, M. Pinault, A. Floramo, M. Fabert, B. Ratier, J. Bouclé, N. Herlin-Boime, Single-step preparation of TiO<sub>2</sub>/MWCNT nano-hybrid materials by laser pyrolysis and application to efficient photovoltaic energy conversion, *ACS Appl. Mater. Interfaces* 7 (2015) 51–56.
- [24] L.-C. Jiang, W.-D. Zhang, Electrodeposition of TiO<sub>2</sub> nanoparticles on multiwalled carbon nanotube arrays for hydrogen peroxide sensing, *Electroanalysis* 21 (2009) 988–993.
- [25] K.E. Tetey, M.Q. Yee, D. Lee, Photocatalytic and conductive MWCNT/TiO<sub>2</sub> nanocomposite thin films, *ACS Appl. Mater. Interfaces* 2 (2010) 2646–2652.
- [26] D.O. Idisi, H. Ali, J.A. Oke, S. Sarma, S.J. Moloi, S.C. Ray, H. Wang, N.R. Jana, W.F. Pong, A.M. Strydom, Electronic, electrical and magnetic behaviours of reduced graphene-oxide functionalized with silica coated gold nanoparticles, *Journal of Applied Surface Science* 483 (2019) 108–113.
- [27] Sharifah Bee Abd Hamid, Tong Ling Tan, Chin Wei Lai, Emy Marlina Samsudin, Multiwalled carbon nanotube/TiO<sub>2</sub> nanocomposite as a highly active photocatalyst for photodegradation of Reactive Black 5 dye, *Chinese J. Catal.* 35 (12) (2014) 2014–2019.
- [28] Andrei Jitianu, Thomas Cacciaguerra, Roland Benoit, Sandrine Delpoux, Francandois Béguin, Sylvie Bonnamy, Synthesis and characterization of carbon nanotubes-TiO<sub>2</sub> nanocomposites, *Carbon* 42/5–6 (2004) 1147–1151.
- [29] Valmiki Koli, Ananta Dhodamani, Abhinav Raut, Nanasahab Thorat, Shivaji Pawar, Sagar Delekar, Visible light photo-induced antibacterial activity of TiO<sub>2</sub>-MWCNTs nanocomposites with varying the contents of MWCNTs, *J. Photochem. Photobiol. A Chem.* 328 (2016) 50–58.
- [30] Jiaguo Yu, Tingting Ma, Shengwei Liu, Enhanced photocatalytic activity of mesoporous TiO<sub>2</sub> aggregates by embedding carbon nanotubes as electron-transfer channel, *Phys. Chem. Chem. Phys.* 13 (8) (2011) 3491–3501.
- [31] Jiaguo Yu, Jiajie Fan, Bei Cheng, Dye-sensitized solar cells based on anatase TiO<sub>2</sub> hollow spheres/carbon nanotube composite films, *J. Power Sources* 196 (18) (2011) 7891–7898.
- [32] Sekhar Chandra Ray, Susanta Kumar Bhunia, Arindam Saha, Nikhil Ranjan Jana, Electric and ferro-electric behaviour of polymer-coated graphene-oxide thin film, *Phys. Procedia* 46 (2013) 62–70.
- [33] Andrea C. Ferrari, Denis M. Basko, Raman spectroscopy as a versatile tool for studying the properties of graphene, *Nat. Nanotechnol.* 8 (2013) 235–246.
- [34] Navneet Soin, Susant Sinha Roy, Sekhar Chandra Ray, James A. McLaughlin, Excitation energy dependence of Raman bands in multiwalled carbon nanotubes, *J. Raman Spectroscopy* 41 (2010) 1227–1233.
- [35] S.D. Delekar, A.G. Dhodamani, K.V. More, T.D. Dongale, R.K. Kamat, S.F.A. Acquah, N.S. Dalal, D.K. Panda, Structural and optical properties of nanocrystalline TiO<sub>2</sub> with multiwalled carbon nanotubes and its photovoltaic studies using Ru(II) sensitizers, *ACS Omega* 3 (3) (2018) 2743–2756.
- [36] A. Mathur, S.S. Roy, S.C. Ray, K.S. Hazra, J. Hamilton, C. Dickinson, J. McLaughlin, D.S. Mishra, Enhancement of field emission characteristics of carbon nanotubes on oxidation, *J. Nanosci. Nanotechnol.* 11 (8) (2011) 7011–7014.
- [37] H.M. Pagona Papakonstantinou, T.I.T. Okpalugo, Raman study of multiwalled carbon nanotubes functionalized with oxygen groups, *J. Vac. Sci. Technol. B Microelectron. Nanom. Struct.* 24 (2) (2006) 715–720.
- [38] L. Grigorian, K.A. Williams, S. Fang, G. Sumanasekera, A.L. Loper, E.C. Dickey, S.J. Pennycook, P.C. Eklund, Reversible intercalation of charged iodine chains into carbon nanotube ropes, *Phys. Rev. Lett.* 80 (1998) 5560–5563.
- [39] C.M. Chen, Y.M. Dai, J.G. Huang, J.G. Huang, J.-M. Jehng, Intermetallic catalyst for carbon nanotubes (CNTs) growth by thermal chemical vapor deposition method, *Carbon* 44 (2006) 1808–1820.
- [40] Y. Ou, J. Lin, S. Fang, D. Liao, MWNT-TiO<sub>2</sub>:Ni composite catalyst: a new class of catalyst for photocatalytic H<sub>2</sub> evolution from water under visible light illumination, *Chem. Phys. Lett.* 429 (2006) 199–203.
- [41] Hao Liu, Hairu Zhang, Hongmin Yang, Photocatalytic removal of nitric oxide by multi-walled carbon nanotubes-supported TiO<sub>2</sub>, *Chinese J. Catal.* 35 (1) (2014) 66–77.
- [42] Ye Cong, Xuanke Li, Yun Qin, Zhijun Donga, Guanming Yuan, Zhengwei Cui, Xiaojun Lai, Carbon-doped TiO<sub>2</sub> coating on multiwalled carbon nanotubes with higher visible light photocatalytic activity, *Appl. Catal. B Environ.* 107/1–2 (2011) 128–134.
- [43] Haijin Liu, Guoguang Liu, Qingxiang Zhou, Preparation and characterization of Zr doped TiO<sub>2</sub> nanotube arrays on the titanium sheet and their enhanced photocatalytic activity, *J. Solid State Chem.* 182 (12) (2009) 3238–3242.
- [44] Sarbaji Banerjee, Tiradai Hemraj-Benny, Mahalingam Balasubramanian, Daniel A. Fischer, James A. Misewich, Stanislaus S. Wong, Surface chemistry and structure of purified, ozonized, multiwalled carbon nanotubes probed by NEXAFS and vibrational spectroscopies, *Chemphyschem* 5 (2004) 1416–1422.
- [45] A. Kuznetsova, I. Popova, J.T. Yates, M.J. Bronikowski, C.B. Huffman, J. Liu, R.E. Smalley, H.H. Hwu, J.G. Chen, Oxygen-containing functional groups on single-wall carbon nanotubes: NEXAFS and vibrational spectroscopic studies, *J. Am. Chem. Soc.* 123 (2001) 10699–10704.
- [46] S. Banerjee, T. Hemraj-Benny, M. Balasubramanian, D.A. Fischer, J.A. Misewich, S.S. Wong, Ozonized single-walled carbon nanotubes investigated using NEXAFS spectroscopy, *Chem. Commun.* 7 (2004) 772–773.
- [47] J. Stöhr, NEXAFS Spectroscopy, Springer-Verlag, New York, 1991.
- [48] M. Magnuson, M. Mattesini, S. Li, C. Höglund, M. Beckers, L. Hultman, O. Eriksson, Bonding mechanism in the nitrides Ti<sub>2</sub>AlN and TiN: an experimental and theoretical investigation, *Phys. Rev. B* 76 (195127) (2007) 1–9.
- [49] R.R.M.D. Brydson, H. Sauer, W. Engel, J.M. Thomas, E.H. Zeitler, N. Kosugi, H. Kuroda, Electron energy loss and X-ray absorption spectroscopy of rutile and anatase: a test of structural sensitivity, *J. Phys. Condens. Matter* 1 (1989) 797–812.
- [50] F.M.F. de Groot, M.O. Figueiredo, M.J. Basto, M. Abbate, O.H. Petersen, J.C. Fuggle, 2p X-ray absorption of titanium in minerals, *Phys. Chem. Miner.* 19 (1992) 140–147.
- [51] F.M.F. de Groot, J.C. Fuggle, B.T. Thole, G.A. Sawatzky, L<sub>2,3</sub> X-ray-absorption edges of d<sup>n</sup> compounds: K<sup>+</sup>, Ca<sup>2+</sup>, Sc<sup>3+</sup>, and Ti<sup>4+</sup> in O<sub>h</sub> (octahedral) symmetry, *Phys. Rev. B* 41 (1990) 928–937.
- [52] F.M.F. de Groot, J.C. Fuggle, B.T. Thole, G.A. Sawatzky, 2p X-ray absorption of 3d transition-metal compounds: an atomic multiplet description including the crystal field, *Phys. Rev. B* 42 (1990) 5459–5468.
- [53] Elzbieta Frackowiak, François Béguin, Electrochemical storage of energy in carbon nanotubes and nanostructured carbons, *Carbon* 40 (2002) 1775–1787.

## Appendix 3

Applied Surface Science 483 (2019) 106–113



Contents lists available at ScienceDirect

Applied Surface Science

journal homepage: [www.elsevier.com/locate/apsusc](http://www.elsevier.com/locate/apsusc)

Full length article

## Electronic, electrical and magnetic behaviours of reduced graphene-oxide functionalized with silica coated gold nanoparticles



David O. Idisi<sup>a</sup>, Haydar Ali<sup>b</sup>, J.A. Oke<sup>a</sup>, Sweety Sarma<sup>a</sup>, S.J. Moli<sup>a</sup>, Sekhar C. Ray<sup>a,\*</sup>, H.T. Wang<sup>c</sup>, Nikhil R. Jana<sup>b</sup>, W.F. Pong<sup>d</sup>, André M. Strydom<sup>e</sup>

<sup>a</sup> Department of Physics, CSET, University of South Africa, Private Bag X6, Florida, 1710, Science Campus, Christiaan de Wet and Pioneer Avenue, Florida Park, Johannesburg, South Africa

<sup>b</sup> Centre for Advanced Materials, IACS, Kolkata 700032, India

<sup>c</sup> Department of Physics, National Tsing-Hua University, Hsinchu 30013, Taiwan

<sup>d</sup> Department of Physics, Tamkang University, Tamsui, 251 Taipei, Taiwan

<sup>e</sup> Highly Correlated Matter Research Group, Physics Department, University of Johannesburg, P.O. Box 524, Auckland Park 2006, South Africa

## ARTICLE INFO

**Keywords:**  
R-GO  
R-GO: Au-NPs  
XANES  
XPS  
M-H  
I-V

## ABSTRACT

We have synthesized graphene-oxide (GO) by the modified hummer's process and subsequently reduced it with gold-nanoparticles (Au-NPs) using silica coated colloidal Au-NPs and hydrazine monohydrate solutions to form r-GO: Au-NPs nanocomposites. We have studied the microstructure, electronic, electrical and magnetic properties of r-GO and r-GO: Au-NPs nanocomposites. We have observed from the Raman spectroscopy that the intensity of D-peak (disorder) gets reduced with respect to G (graphite-cluster) in r-GO: Au-NPs composites. The reduction of  $I_D/I_G$  ratio obtained from Raman spectra [r-GO: 1.22  $\rightarrow$  r-GO:(Au-NPs)<sub>4.88</sub>: 0.98] clearly indicates that the  $sp^2$ -cluster is reduced in r-GO: Au-NPs nanocomposites. The reduction of  $sp^2$ -cluster and/or enhancement of  $sp^3$ -cluster is due to replacement of  $sp^2$ -cluster by the Au-NPs. This observation also observed from the X-ray absorption near edge structure (XANES) spectroscopy, X-ray photoelectron spectroscopy (XPS) measurements that are consistent with reduction of conductivity as we observe from the current (I) - voltage (V) characteristics of the nanocomposites. Magnetic M-H hysteresis loops show the magnetization is enhanced in r-GO: Au-NPs nanocomposites. We believe that the reduction of conductivity and enhancement of magnetization of r-GO: Au nanocomposites would be most suitable for ferro-electro-magnetic materials for the memory storage device applications.

## 1. Introduction

Carbon-based nanomaterials such as carbon nanotubes, graphene and mesoporous carbon are important supports for the metal nanoparticles in heterogeneous materials [1–3]. Among them, graphene, a novel one-atom-thick two-dimensional graphitic carbon system, has attracted particular research interest due to its high surface area, excellent mechanical, thermal and electrical properties [4–6]. However, the decoration of metal nanoparticles on the pristine graphene is very difficult, but the reduced graphene oxide (r-GO) which contains different oxygen groups can directly bind to the carbon skeleton of a two-dimensional graphene-derived backbone as an ideal support for decoration of the metal nanoparticles. The surface oxygen functionalities in r-GO serve as reactive sites for the direct nucleation and growth of metal nanoparticles on the r-GO surface. This GO/r-GO is a two-

dimensional (2D) nanomaterial, has attracted tremendous attention recently because of its extraordinary properties like graphene. Due to unevenly distribution of oxygen functionalities at the graphene-surface, the metal nanoparticles are also not even at the graphene surface [7]. To achieve a better distribution of metal nanoparticles like Ag, Au and other noble metal nanoparticles, both non-covalent and covalent methods have been applied in the modification of r-GO surface [8]. Due to the less stability of GO/r-GO, the chemical modification becomes essential to improve its stability and introduce special functionalities. The unique metal-decorated r-GO nanostructure holds great promise for the potential applications in extensive technological territories, such as nano-electronics [9], super-capacitors [10], batteries [11], and sensors [12]. Many nanomaterials such as Au-NPs are used to fabricate GO/r-GO: Au-NPs nanocomposites [13,14]. Zhang and co-workers constructed a sensor based on reduced graphene oxide (r-GO) hollow microspheres;

\* Corresponding author.

E-mail address: [Raysc@unisa.ac.za](mailto:Raysc@unisa.ac.za) (S.C. Ray).

<https://doi.org/10.1016/j.apsusc.2019.03.271>

Received 3 December 2018; Received in revised form 17 March 2019; Accepted 24 March 2019

Available online 25 March 2019

0169-4332/ © 2019 Published by Elsevier B.V.

which was encapsulated with gold nanoparticles (Au-NPs) by spray drying for the sensor applications [14]. In this present study, we have used gold nanoparticles (Au-NPs) for the reduction of GO and hence formation of r-GO:Au-NPs nanocomposite. In this r-GO:Au-NPs nanocomposite materials, the Au-NPs act as an ad-atoms on the surface of r-GO:Au-NPs nanocomposite and enhances the magnetic properties at nanoscale range.

In this study, r-GO:Au-NPs nanocomposite was prepared and its structural, electronic, electrical and magnetic behaviours for future electronic and magnetic devices applications were studied. X-ray diffraction (XRD) and transmission electron microscopy (TEM) techniques were used to study crystal structure and surface morphology of r-GO and r-GO: AuNPs nanocomposites. Raman spectroscopy, X-ray absorption near edge structure (XANES) and X-ray photoemission spectroscopy (XPS) techniques were used for the study of electronic structure and bonding properties of the composites. Ultraviolet photoemission spectroscopy (UPS) technique was used for the study of electronic structure at the valence band states and density of states (DOS) of r-GO and r-GO: Au-NPs nanocomposites. Furthermore, electrical properties and magnetic behaviour were studied using current (I)-Voltage (V) characteristics and high sensitivity M-H hysteresis loops techniques, respectively.

## 2. Experimental details

### 2.1. Preparation of graphene oxide

Colloidal graphene oxide was prepared by modified Hummer's method as demonstrated by our past report [15]. 300 mg graphite powder and 150 mg sodium nitrate were mixed with 8 mL concentrated sulphuric acid in a beaker. The solution was cooled to 0 °C with 900 mg of  $\text{KMnO}_4$  added stepwise under constant stirring. Following thirty minutes 20 mL water was added in two phases and appropriately bring the mixture to room temperature. 300  $\mu\text{L}$  of 3%  $\text{H}_2\text{O}_2$  was added to permanganate to form homogeneous mixture. The solid was washed with boiling water and air dried before dispersed in distilled water by sonication. The solution was then centrifuged at 3000 rpm to expel larger particles and the supernatant was used as colloidal GO solution with the concentration of one mg/mL.

### 2.2. Preparation of reduced graphene oxide (r-GO)

Reduced graphene oxide (r-GO) was prepared by chemical reduction method as per our previous report. At first, 6 mL GO solution (concentration one mg/mL) was taken in a beaker and 60  $\mu\text{L}$  of hydrazine monohydrate solution was added stepwise with constant stirring. Then the mixture was heated at  $\sim 70\text{--}80$  °C for 40 min, where the brown coloured solution turned into a black precipitate. The precipitate was washed with water to remove excess reagents. The precipitate was then dried using air-dryer and collected as r-GO.

### 2.3. Preparation of silica coated colloidal Au-nanoparticle solution

For the preparation of silica coated colloidal Au-nanoparticle solution; 40  $\mu\text{L}$  toluene solution of (3-mercaptopropyl) trimethoxysilane (0.1 M) was added to 2 mL of toluene solution of  $\text{AuCl}_3$  (0.1 M, prepared in the presence of one equivalent of didodecyltrimethylammonium bromide) with stirring condition, followed by 200  $\mu\text{L}$  of toluene solution of tetrabutylammonium borohydride (0.02 M, prepared in the presence of one equivalent of didodecyltrimethylammonium bromide). After that, 400  $\mu\text{L}$  of toluene solution of 3-(2-aminoethylamino) propyldimethoxymethylsilane (0.1 M) was added and heated at  $65\text{--}70$  °C for 1 h. Next, a pink precipitate was appeared and washed with toluene and chloroform repeatedly. Finally, the precipitate was dissolved in 2 mL of distilled water.

### 2.4. Preparation of reduced graphene oxide-gold nanoparticles nanocomposites (r-GO:AuNPs)

In order to prepare the r-GO:AuNPs nanocomposite, 5 mL GO solution (concentration 1 mg/mL) was taken in a beaker and 5 mL of silica coated colloidal Au nanoparticle solution was added dropwise with constant stirring. Next, 50  $\mu\text{L}$  hydrazine monohydrate solution was added to the mixture and heated at  $\sim 70\text{--}80$  °C for 40 min. As time progressed, the brown coloured solution turned black with the appearance of precipitate. The black precipitate was collected, completely washed with refined water, dried and collected as r-GO:AuNPs nanocomposites.

Characterization of the r-GO and r-GO:Au-NPs composites were carried out by X-ray diffractometer (XRD) and transmission electron microscopy (TEM) techniques using a Rigaku Smart-lab with  $\text{Cu K}\alpha$  radiation (Ni-filter) at 1.54 Å and FEI Tecnai G2 F20 microscope respectively. The C and O K-edge XANES measurements were performed at the National Synchrotron Radiation Research Centre (NSRRC), Hsinchu, Taiwan. The core-level XPS spectra were recorded on a KRATOS-SUPRA spectrometer at UNISA (Florida Science Campus), South Africa using monochromatic Al  $\text{K}\alpha$  radiation with excitation energy  $h\nu = 1486.6$  eV having base pressure  $1.2 \times 10^{-8}$  Torr. The UPS spectra were also recorded using KRATOS-SUPRA spectrometer using He-II ( $h\nu = 40.81$  eV) excitation and the base pressure was  $\sim 1.2 \times 10^{-9}$  Torr. Raman spectra were measured using HORIBA Scientific XploRA at 532 nm ( $\sim 2.41$  eV) LASER light excitation energy. Magnetic properties were measured using a superconducting quantum interference device (SQUID)-type magnetometer. The current (I) - voltage (V) relationship was measured with silver (Ag) conductive paste as the contacting electrodes using the commercial software, controlled by Keithley pico-voltage source meter to study the electrical properties of these composites.

## 3. Results and discussion

The transmission electron spectroscopy (TEM) images of typical r-GO and r-GO: Au-NPs composites materials are shown in Fig. 1(a) and (b) respectively. The TEM image of r-GO:Au-NPs composites shows that the distribution of Au-NPs on the surface of r-GO is not homogeneous. This non-uniform distribution is may be due to aggregation of some particles and/or Au-NPs preferentially attached to the edge of r-GO. Details of the distribution/attachment-mechanism could be available elsewhere [15]; where it is stated that the Au-NPs attachments to r-GO is due to electrostatic interactions between r-GO and Au-NPs, and covalent-bond formation through reaction of different oxygen functional groups present on the r-GO surface on the gold nanoparticle surfaces. Atomic force microscopy (AFM) images of r-GO and r-GO:Au-NPs nanocomposite with their corresponding height profiles are shown in Fig. 1(c, e) and (d, f), respectively. Images and height profiles indicate that r-GO and r-GO:Au-NPs nanocomposites are few layer GO. Fig. 1(g) shows the XRD patterns of r-GO and r-GO: AuNPs nanocomposites; where a wide diffraction peak is observed at  $2\theta = 26.2^\circ$  corresponding to (002) plane of graphite-structure. In addition, XRD pattern exhibit peaks at  $2\theta$  values of  $28.50^\circ$ ,  $33.50^\circ$ ,  $35.27^\circ$ ,  $44.31^\circ$ ,  $45.85^\circ$ , and  $54.06^\circ$  that correspond to Au-lattice planes of (220), (311), (222), (331), (420), and (511), respectively. These diffraction peaks suggest that Au-NPs are attached on the surface and they exists in r-GO matrix. The intensity and the shape of the peaks are the consequences of the face centered cubic (fcc) phase of Au-NPs-crystals. All peaks in the XRD pattern matches with JCPDS data (JCPDS-PDF No. 01-1172). From full-width at half-maximum (FWHM) of diffraction peaks, the average size of Au-NPs is estimated using Debye-Scherrer eq.  $2R = 0.9\lambda/\beta \cos\theta$  [16], where  $2R$  is the size (diameter) of NPs,  $\beta$  is the full width half maxima (FWHM) of XRD peak in radians,  $\theta$  is diffraction angle and  $\lambda$  is wavelength of X-ray (1.54 Å). The average size of Au-NPs is about = 10–15 nm. Raman spectroscopy has played an important role for



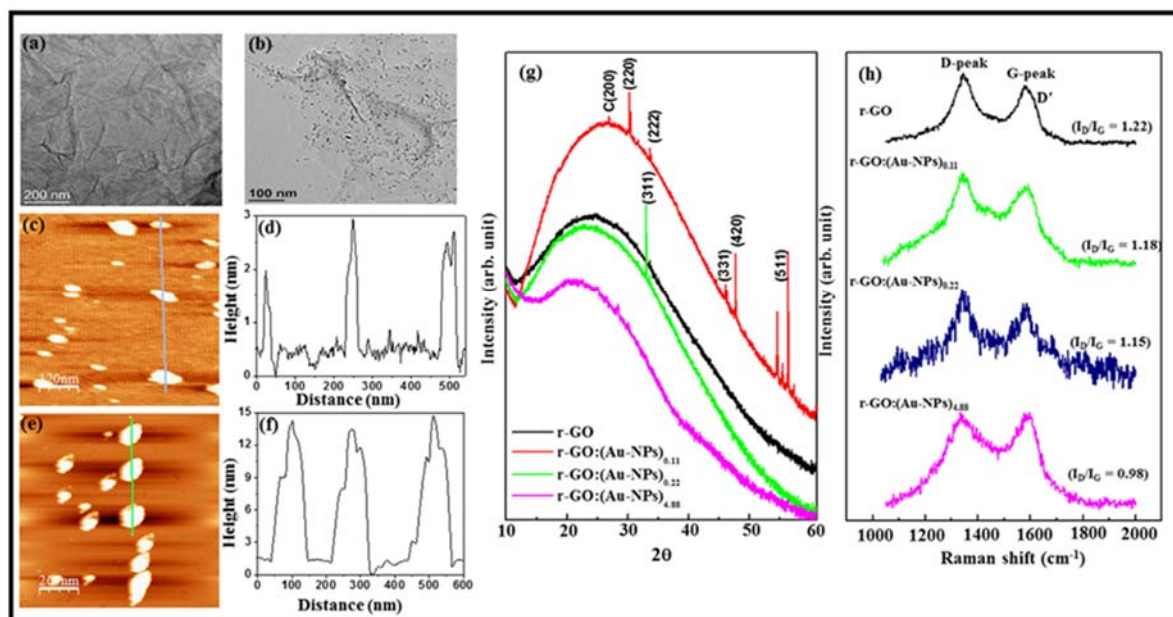


Fig. 1. A typical transmission electron microscopy (TEM) image of (a) r-GO and (b) r-GO: Au-NPs nanocomposites; Atomic force microscopy (AFM) images of (c) r-GO and (e) r-GO: Au-NPs nanocomposite and their corresponds height profiles, (d) r-GO and (f) r-GO: Au-NPs nanocomposites, respectively [With height profile showing the thickness of r-GO and r-GO: Au-NPs composites]; (g) XRD patterns of r-GO and r-GO: Au-NPs nano-composites, (h) Raman spectroscopy of r-GO and r-GO: Au-NPs nanocomposites.

characterizing graphitic materials because it is able to provide information on crystalline size, the degree of hybridization, crystal disorder, the extent of chemical modification, and distinguish single layer graphene or nanotubes from multilayer ones. The micro-Raman spectra of r-GO and r-GO: Au composites are shown in Fig. 1(h). They exhibit two main characteristic peaks: the G mode, a doubly degenerate (TO and LO) phonon mode ( $E_{2g}$  symmetry) at the Brillouin zone center observed at  $\sim 1578 \text{ cm}^{-1}$ , originating from in-plane vibration of  $sp^2$  carbon atoms; the D mode arising from the doubly resonant disorder-induced mode ( $\sim 1343 \text{ cm}^{-1}$ ) [17–19]. In addition a very weak peak, the symmetry-allowed 2D overtone mode ( $\sim 2700 \text{ cm}^{-1}$ ) [17–19] is also observed in our r-GO and r-GO: Au-NPs (not shown in this figure). The r-GO shows a prominent D peak with intensity comparable to G peak, in sharp contrast to the smaller D peak of r-GO: Au-NPs, indicative of significant structural order due to the removal of oxygen from the surface of r-GO. The D band, attributed to in-plane  $A_{1g}$  (LA) zone-edge mode, is innately Raman-active at the graphitic edges [17–19]. The decrease in  $I_D/I_G$  ratio from  $\sim 1.22$  for r-GO to 0.98 for r-GO: (Au-NPs)<sub>0.88</sub> indicates a decrease of defect-structure of r-GO: Au-NPs composites. The G peak of r-GO: (Au-NPs)<sub>0.88</sub> is shifted to higher wavenumbers ( $\sim 13 \text{ cm}^{-1}$ ) and broadens with respect to that of r-GO. It was related to the emergence of a new Raman active band (D' mode,  $\sim 1620 \text{ cm}^{-1}$ ) overlapped with the G band [17]. The D' band, usually inactive, becomes Raman-active due to phonon confinement caused by defects [20]. Besides the influence of D' band, Kudin et al. [21] have considered the contributions from the isolated double bonds as being responsible for yielding Raman bands at little higher frequencies, for oxidized r-GO and r-GO: Au-NPs.

The high-resolution C K-edge and O K-edge XANES spectra of r-GO and r-GO: Au-NPs nano-composites are shown in Fig. 2 (a, b), respectively. These C K-edge spectra provides a clear presence of both unoccupied  $\pi^*$  ( $1s \rightarrow \pi^*$ ) and  $\sigma^*$  ( $1s \rightarrow \sigma^*$ ) states around 284.8 eV and 292.5 eV respectively [22]. In O K-edge these peaks are observed at 533.8 eV and 541.3 eV respectively. In C K-edge the  $\pi^*$  feature at

$\sim 284.8 \text{ eV}$  is typical of the C=C bond ( $sp^2$ ), while the  $\sigma^*$  feature at  $\sim 292.5 \text{ eV}$  is typical of the tetrahedral C-C bond ( $sp^3$ ). In O K-edge the  $\pi^*$  feature at  $\sim 533.8 \text{ eV}$  is the  $\pi^*_{C-O}$  bands and the  $\sigma^*$  features at 541.3 eV is the  $\sigma^*_{C-O}$  bands. These  $\pi^*$  ( $1s \rightarrow \pi^*$ ) and  $\sigma^*$  ( $1s \rightarrow \sigma^*$ ) states in C K-edge and O K-edge XANES spectra reveal that r-GO and r-GO: Au-NPs composites maintain the aromaticity of the original pristine material r-GO. Although GO/r-GO/r-GO: Au-NPs produces a plethora of O-related resonances, unfortunately, XANES database in literature is not rich enough to de-convolute and assign all the peaks. Upon judicious review of the available literature, we have assigned the peak-positions [22,23] as shown in Fig. 2(a) & (b). Both C K-edge and O K-edge are slightly shifted at higher energy indicating the structural change/modification. Among the three resonance 286.7 eV ( $I_1$ ), 288.6 eV ( $I_2$ ) and 290.0 eV ( $I_3$ ) in between  $\pi^*$  and  $\sigma^*$  of C K-edge, the  $I_1$  and  $I_3$  are assigned to  $\pi^*$  (C=O/COOH) and  $\pi^*$  (COOH) respectively. Whereas the peak 288.6 eV ( $I_2$ ) is assigned to few layer graphene [23] and was attributed to the free electron like set of bands corresponding to electron excitations lying between graphite layers (interlayers states). Some researchers have provided the evidence that this feature ( $\sim 289 \text{ eV}$ ) originates from -COOH moieties present in GO/r-GO [24]. In the above of  $\sigma^*$  region the peaks are observed at 295.4 eV ( $I_4$ ), 298.8 eV ( $I_5$ ) and 303.4 eV ( $I_6$ ) and are assigned as C=O moieties [25]. We have estimated the  $\pi^*$  intensity of C K-edge/O K-edge by integrating the  $\pi^*$ -area after subtracting a Gaussian lines as shown in Fig. 2(a, b) and found a small change (see Table 1) that confirms the formation of different structure moiety. Moreover, the reduction of  $\pi^*$  intensity in C K-edge XANES spectra implies the decrease of  $sp^2$  content that is consistent with the value of  $I_D/I_G$  obtained from Raman spectra indicating a steady increase in the  $sp^3$  content induced by Au-NP in the r-GO: Au-NPs nanocomposites.

Fig. 3 (a, b) shows the C 1s and O 1s XPS spectra respectively of the r-GO and r-GO: Au-NPs composites. It is observed that the peak positions of both C 1s and O 1s for r-GO: (Au-NPs)<sub>0.22</sub> is shifted at lower energy side and for r-GO: (Au-NPs)<sub>0.88</sub>, the peak is shifted at higher

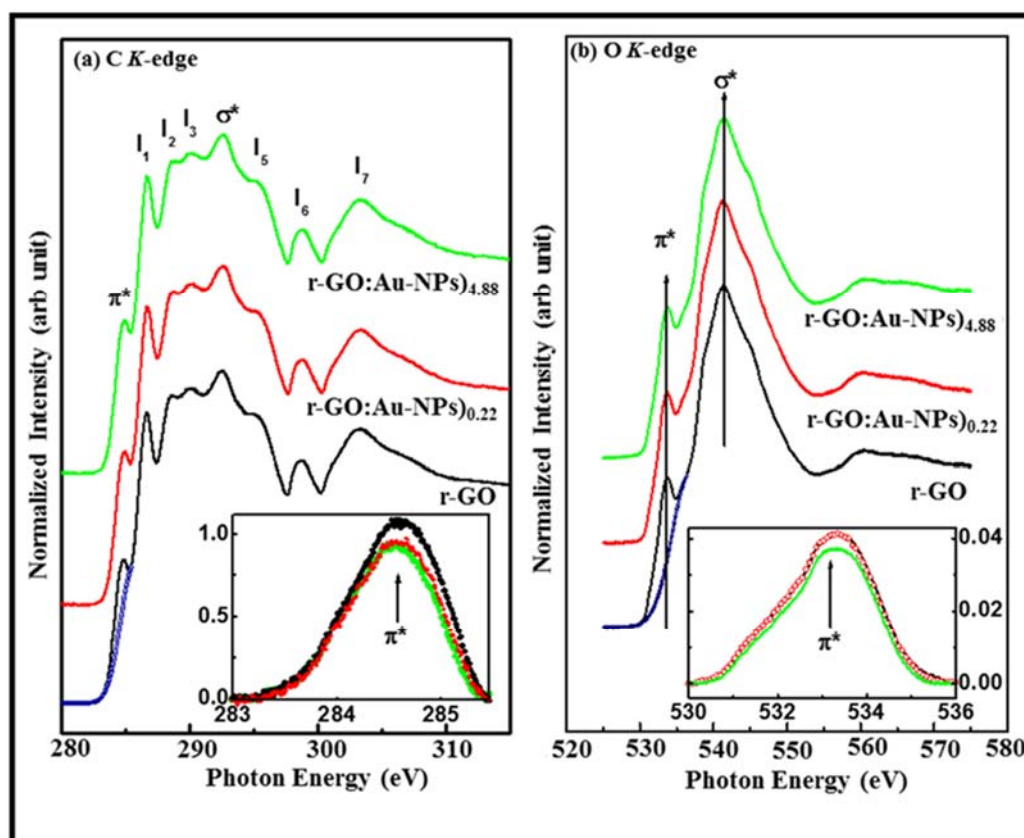


Fig. 2. X-ray absorption near edge structure (XANES) spectroscopy of r-GO and r-GO: Au-NPs nano-composites (a) C K-edge and (b) O K-edge.

energy side suggesting that the Au-NPs composites significantly influences the structural property of r-GO. It is found that the C/O ratio decreases with Au-NPs (see Table 1) and that further confirms the change of r-GO and r-GO: Au-NPs structural matrix. Both C 1s and O 1s are de-convoluted into different components and their peak positions, intensity and full-width-half maximum are tabulated in Table 2. The C 1s spectrum consists of peaks that correspond to  $sp^2$  carbon around 284.8 eV, O–H/O–C–O around 286.2 eV and C=O around 288.4 eV [26]. All the films show a dominant peak around 284.8 eV. However, r-GO and r-GO: Au-NPs composites show usual XPS spectral pattern of GO. It is rather interesting to note that the higher concentration of Au-NPs composites r-GO: (Au-NPs)<sub>4.88</sub>, there is a significant reduction of carbon signals ( $sp^2$ -C) and increase of oxygenated carbon signals (O–H / O–C–O and C=O). Szwarckopf et al. [27] reported that the Au-atoms could directly substitute vacancies in  $sp^2$  sites. In our present study,  $sp^2$  C–C peak is observed around 284.6 eV in r-GO, but the peak intensity of r-GO: Au-NPs is decreased and showing defected  $sp^2$  peak at

285.0 eV which is 0.4 eV higher than r-GO. Presumably, gold is weakly attaching to  $sp^2$  carbon since the C 1s XPS signal at 285.0 eV related to defected  $sp^2$  is observed. This “defect peak” slightly shifts to higher binding energy, which is probably due to carbon atoms out of  $sp^2$  configuration. XPS observations are shown in Table 1. This “defect peak” (285.0 eV) is due to carbon atoms involved in real structural defects. It also shows that the metal intercalation in graphite results in a defect peak with a slightly shift at high binding energy [27]. It was reported that carbon atoms bound to carbon atoms out of strictly  $sp^2$  configuration give rise to a C 1s peak around 285.0 eV. Such a high-energy shifted peak is also reported in carbons in partially  $sp^2/sp^3$  hybridized state [28]. Also a peak in 283.9 eV is observed in r-GO: (Au-NPs)<sub>4.88</sub> and is assigned to C–Au and is observed in graphene gold hybrids [29]. The barrier for Au-atoms to migrate between two C–C bond is of approximately 0.1 eV and therefore, at room temperature, it is possible that Au-atoms can migrate quite easily along the C–C bond [30]. Thus, adsorption and weak bonding of graphene on Au is possible.

Table 1  
Elemental composition and quantification analysis from XPS, XANES and Raman spectra analysis.

	C 1s (at.%)	O 1s (at.%)	Au 4f (at.%)	C/O ratio from XPS	$\pi^*$ -Intensity from XANES		$(I_D/I_G)$ ratio from Raman
					C K-edge	O K-edge	
r-GO	53.37	46.63	–	1.14	1.14	0.75	1.22
rGO: (Au-NPs) <sub>0.11</sub>	54.52	45.48	0.11	1.20	–	–	1.18
rGO: (Au-NPs) <sub>0.22</sub>	61.65	38.34	0.22	1.61	0.95	0.78	1.15
rGO: (Au-NPs) <sub>4.88</sub>	71.14	23.99	4.88	2.96	0.98	0.62	0.98

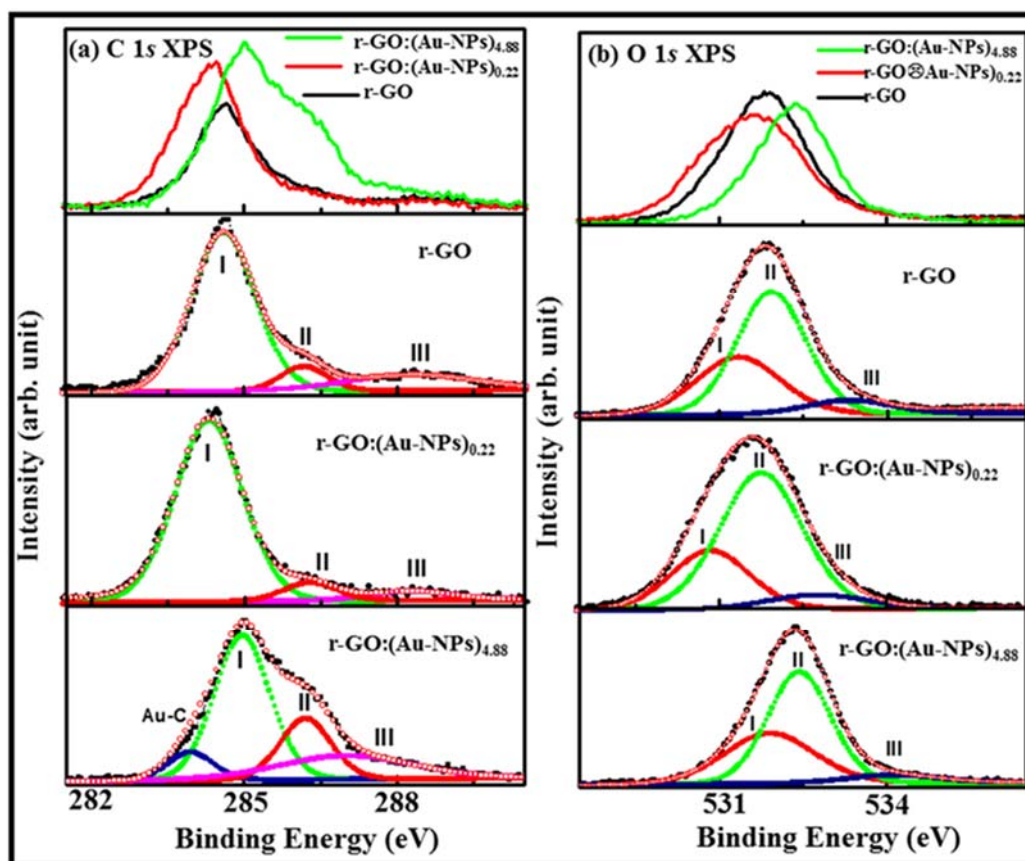


Fig. 3. X-ray photoemission spectroscopy (XPS) of r-GO and r-GO: Au-NPs nanocomposites (a) C 1s and (b) O 1s.

Table 2

De-convoluted different parameters from C 1s and O 1s X-ray photoemission spectroscopy.

	C 1s X-ray photoemission spectroscopy									O 1s X-ray photoemission spectroscopy											
	Peak (C–Au)			Peak I (sp <sup>2</sup> -C)			Peak II (O–H/O–C–O)			Peak III (C=O)			Peak I (O–H)			Peak II (C–O)			Peak III (C=O)		
	x	Δω	a	x1	Δω1	a1	x2	Δω2	a2	x3	Δω3	a3	x1	Δω1	a1	x2	Δω2	a2	x3	Δω3	a3
r-GO	–	–	–	284.6	1.5	75.5	286.2	1.1	8.7	288.3	3.1	15.7	531.3	1.8	31.9	531.9	1.5	56.0	532.3	1.8	7.7
r-GO: Au (0.22 at.%)	–	–	–	284.3	1.5	80.6	286.3	1.2	6.6	288.3	1.9	5.2	531.0	1.6	26.7	531.7	1.7	65.0	532.7	2.1	8.2
r-GO: Au (4.88 at.%)	283.9	1.0	8.3	285.0	1.3	51.4	286.2	1.2	19.9	287.0	3.3	20.4	531.9	1.9	36.9	532.4	1.3	57.0	534.1	1.9	6.0

Based on these studies and from our XPS analysis we assume that gold is attaching to  $sp^2$  carbon sites. This weak attachment of Au to  $sp^2$  carbon sites results in a defected  $sp^2$ , which is consistent with XPS results. In O 1s XPS spectra, different de-convoluted peaks are identified and are summarized in Table 2. The peaks of r-GO are at ~531.3 eV, 531.9 eV and 532.3 eV that are assigned to C=O (oxygen doubly bonded to aromatic carbon), C–O (oxygen singly bonded to aliphatic carbon), and phenolic (oxygen singly bonded to aromatic carbon) groups respectively [31]. These peaks are shifted at higher binding energy and their intensities change slightly for the r-GO:(Au-NPs)<sub>4.88</sub> indicating Au-NPs influence the structural change in r-GO: Au-NPs.

In order to quantify the density of states (DOS) of valence electrons

corresponding to various bonding and mixed states, the ultraviolet photoemission spectra (UPS), He-II ( $h\nu = 40.8$  eV) of r-GO and r-GO: Au-NPs along with Au-NPs as a reference within the range of 0 to 16 eV are shown in Fig. 4. All spectra are de-convoluted into different component peaks after background subtraction as shown in Fig. 4. The spectrum of Au-NPs reveals that there are about four component peaks in the valence band structure in the range 0 to 16 eV. These four peaks are  $2p-\pi$  (~3.5 eV),  $2\pi-\sigma$  (~7.6 eV),  $2s-2p$  mixed states (~10.6 eV) and  $2s$  (~15.4 eV). Using Au-NPs as the reference, ultraviolet photoemission spectra (UPS) of r-GO and r-GO: Au-NPs were processed for de-convolution into different Gaussian component peaks. These peaks are  $2p-\pi$  (~4.9 eV),  $2p-(\pi-\sigma)$  overlap (~6.5 eV – 7.8 eV),  $2p-\sigma$  (8.0 eV –

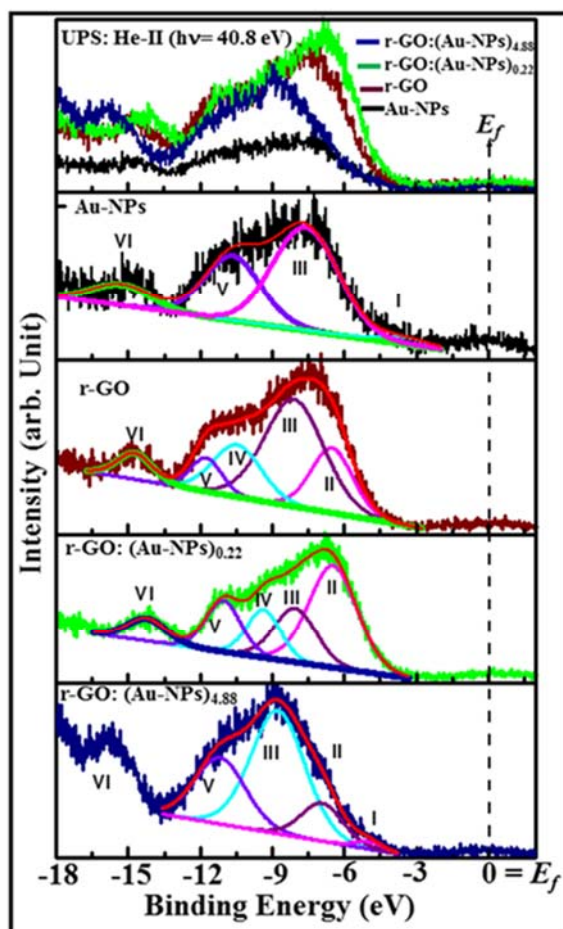


Fig. 4. Ultraviolet photoemission spectroscopy (UPS), He-II ( $h\nu=40.8$  eV) of Au-NPs, r-GO and r-GO:Au-NPs nanocomposites.

10.2 eV),  $2s-2p$  mixed states (9.4 eV–11.9 eV), and  $2s$  ( $-14.5$  eV– $15.0$  eV) [32]. The convoluted peak positions ( $x$ ) and their intensity ( $a$ ) as well as full-width-half-maximum ( $\Delta\omega$ ) of Au-NPs and r-GO:Au-NPs are tabulated in Table 3. The features at  $-11.7$  ( $\pm 0.2$ ) eV and  $14.6$  eV ( $\pm 0.2$ ) are attributed to the  $\sigma$  and  $\pi$  bonding of C=O, and the O lone pair [33–35]. In case of r-GO:(Au-NPs) $_{0.22}$  the spectrum is shifted towards fermi-edge, whereas for r-GO:(Au-NPs) $_{4.88}$  the spectrum is shifted away from the fermi-edge with respect to r-GO indicating the density of states increases and then decreases with

decrease/increase of Au-NPs ad-atoms on the r-GO:Au-NPs nanocomposites surface. It is noticeable that in case of r-GO:(Au-NPs) $_{4.88}$ , the  $2p-\sigma$  peak ( $\sim 7.8$  eV) is strong compared to r-GO/r-GO:(Au-NPs) $_{0.22}$  due to decrease of oxygen species as observed in O 1s XPS spectrum. Since, r-GO contains plenty of C and O bonding, the valence band structure is superimposed of partial DOS of C and O ( $2p$  and  $2s$  electrons) [36]. On functionalization of Au-NPs with r-GO, the peak position of  $2p-\pi$  band ( $\sim 4.9$  eV) shifted away from fermi-edge and decreased considerably in intensity accompanied by appearance of  $2p-(\pi-\sigma)$  overlap band  $\sim 7.8$  eV. The  $\sigma$  band and  $s-p$  mixed band and  $2s$  band were found to shift to higher binding energy in r-GO:(Au-NPs) $_{4.88}$ . The increase in DOS of  $\pi$ -electrons centered at  $\sim 3.9$  eV with concomitant appearance of  $\pi-\sigma$  overlap band and blue shift of  $2p-\sigma$  band are attributed to increase in graphitic carbon network. This explicates the effect of oxygen in controlling the valence band structure of r-GO and hence tunability of r-GO.

The M-H curves for the pristine r-GO and r-GO:Au-NPs were evaluated from  $-10$  kOe  $< H < 10$  kOe at room temperature 300 K and at 40 K. Fig. 5(a) shows the measured M-H loops for the r-GO and r-GO:(Au-NPs) $_{4.88}$ ; with high concentration Au-functionalized r-GO:Au-NPs displaying the higher magnetization. Suda et al. [37] studied the magnetization of two different sized Au-NPs (1.7 nm and 5.0 nm in diameter) and found that the smaller particles were ferromagnetic and the larger ones were diamagnetic. In our present study, Au-NPs show completely diamagnetic in nature, which may be due to comparatively larger size; whereas the r-GO is ferromagnetic as also found in our earlier studies [38,39]. However, the magnetization of r-GO:Au-NPs is ferromagnetic and is higher than r-GO confirming that the ferromagnetism is enhanced on Au-functionalized r-GO. The origin of magnetisation in Au-functionalized r-GO/graphene is still controversial and not known. However, in our present case we have found that the r-GO:(Au-NPs) $_{4.88}$  have higher graphitic in nature and even presence of higher number of oxygen functionalized groups that could be responsible for the higher magnetization. Besides the Au-NPs-content, C–Au bond is also formed as we observed in XPS study that it induces more defects in the GO: (Au-NPs) $_{4.88}$  structure and enhanced magnetization. Fig. 5(b) shows a linear in two cycles, within the range  $+1$  V to  $-1$  V. From this characteristic it is clear that the conductivity decreases when Au-NPs is incorporated with r-GO. High current for r-GO can be attributed to presence of high number of  $sp^2$ -cluster. This current is reduced in r-GO: (Au-NPs) $_{0.22}$ /r-GO: (Au-NPs) $_{4.88}$  composites due to reduction of  $sp^2$ -clustered by the atomic/structural re-arrangement as we observed in Raman, XANES and XPS results. In our present study, it is observed that the magnetization is enhanced with reduction of electrical conductivity because the concentration of Au-NPs is higher due to formation of C–Au bonds and Au–O in the r-GO:Au-NPs nanocomposite structures. The weak attachment of Au-NPs and reduction of C–C  $sp^2$  atoms are responsible for low mobility that leads to drop in conductivity. As a result the magnetization of r-GO:Au-NP nanocomposite is enhanced.

Table 3

De-convoluted different parameters from valence band photoemission spectroscopy from He - II ( $h\nu = 40.8$  eV) excitation.

	Peak I 2p- $\pi$ state			Peak II 2p-( $\pi-\sigma$ ) overlap state			Peak III 2p- $\sigma$ state			Peak IV 2s-2p mixed states			Peak V 2s-2p mixed states			Peak VI 2s state		
	x1 (eV)	$\Delta\omega 1$ (eV)	a1 (a.u.)	x2 (eV)	$\Delta\omega 2$ (eV)	a2 (a.u.)	x3 (eV)	$\Delta\omega 3$ (eV)	a3 (a.u.)	x4 (eV)	$\Delta\omega 4$ (eV)	a4 (a.u.)	x4 (eV)	$\Delta\omega 4$ (eV)	a4 (a.u.)	x5 (eV)	$\Delta\omega 5$ (eV)	a5 (a.u.)
Au-NPs	3.5	2.6	2.7	–	–	–	7.6	3.2	56.0	–	–	–	10.6	2.8	30.9	15.4	2.9	10.3
r-GO	–	–	–	6.5	2.0	20.0	8.1	2.9	47.0	10.5	2.4	18.5	11.7	1.5	7.7	14.5	1.7	6.8
r-GO:Au (0.32 at.%)	–	–	–	6.5	2.4	43.1	8.0	2.1	19.6	9.4	1.6	14.1	11.0	1.7	15.6	14.6	1.9	7.6
r-GO:Au (4.88 at.%)	4.9	1.0	3.5	7.8	2.9	57.0	10.2	2.7	31.6	–	–	–	11.9	1.8	7.9	15.0	–	–

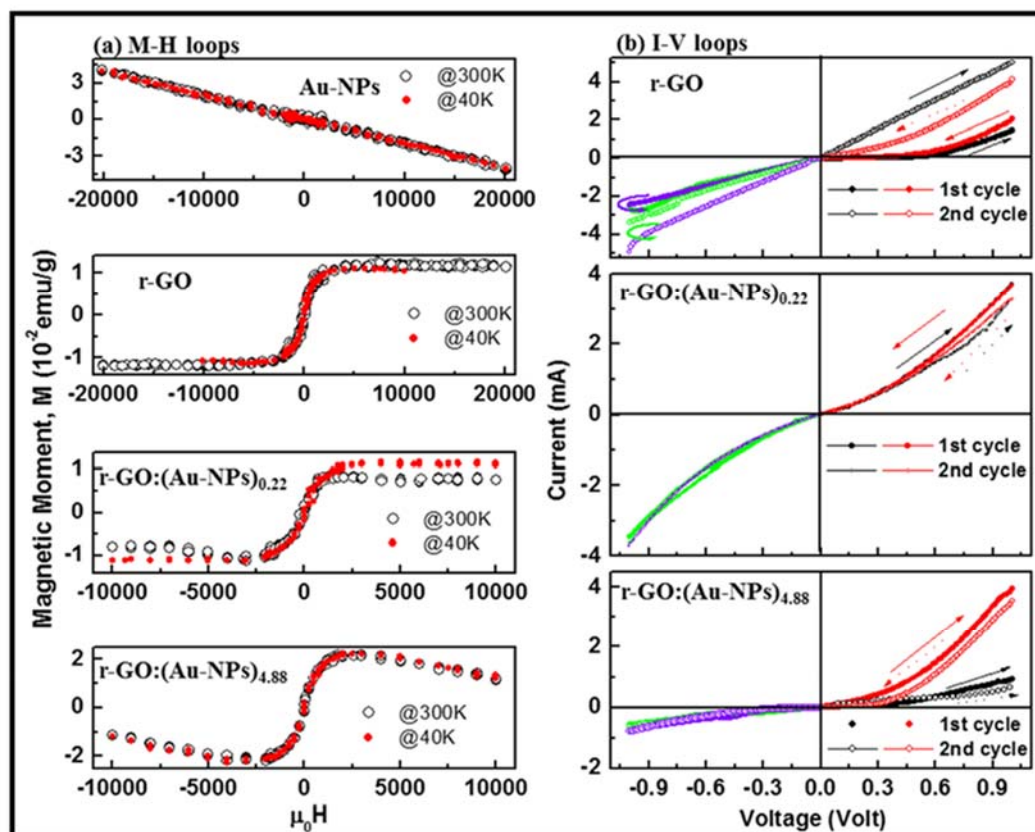


Fig. 5. (a) Magnetic moment ( $M$ ) versus magnetic field ( $H$ ) curves of r-GO and r-GO:Au-NPs nanocomposites and (b) Current ( $I$ ) – Voltage ( $V$ ) characteristics of r-GO and r-GO:Au-NPs nanocomposites.

#### 4. Conclusion

We have synthesized graphene-oxide (GO) and subsequently reduced it with gold-nanoparticles (Au-NPs) using silica coated colloidal Au-NPs and hydrazine monohydrate solutions to form r-GO:Au-NPs nanocomposites. We studied their electronic, electrical and magnetic properties. TEM image shows that the distribution of Au-NPs on the surface of r-GO:Au-NPs is not homogeneous and may be due to aggregation of some particles and/or Au-NPs preferentially attach to the edge of r-GO. The reduction of  $\pi^*$  intensity in C K-edge XANES spectra implies the decrease of  $sp^2$  content that consistent with the value of  $I_D/I_G$  ratios obtained from Raman spectra that indicates an increase in the  $sp^3$  content induced by Au-NP in the r-GO:Au-NPs nanocomposites. The density of states changes with Au-NPs ad-atoms on the r-GO:Au-NPs nanocomposites surface. With this ad-atoms (Au-NPs) on the r-GO:Au-NPs nanocomposites surface the magnetization and electrical conductivity changes due to formation of C–Au bonds and Au–O in the r-GO:Au-NPs nanocomposite structures. Based on these results it can be concluded that r-GO:Au-NPs nanocomposites could be useful for magnetic and electronic device applications.

#### Acknowledgements

D. I., J. A., S. J., S.S. and S.C.R. gratefully acknowledge the financial support received from the National Research Foundation (NRF), South Africa (Grant Nos. 105292, PD-TWAS150813137166 and EQP13091742446). AMS acknowledges financial assistance from FRC

and URC of UJ.

The authors declare no conflict of interest.

#### References





- [1] X. Huang, Z. Yin, S. Wu, X. Qi, Q. He, Q. Zhang, Q. Yan, F. Boey, H. Zhang, Graphene-based materials: synthesis, characterization, properties, and applications, *Small* 7 (2011) 1876–1902.
- [2] S. Wang, Q. Zhao, H. Wei, J.Q. Wang, M. Cho, H.S. Cho, O. Terasaki, Y. Wan, Aggregation-free gold nanoparticles in ordered mesoporous carbons: toward highly active and stable heterogeneous catalysts, *J. Am. Chem. Soc.* 135 (2013) 11849–11860.
- [3] S. Pang, Y. Hernandez, X. Feng, K. Müllen, Graphene as transparent electrode material for organic electronics, *Adv. Mater.* 23 (2011) 2779–2795.
- [4] D.A. Dikin, S. Stankovich, E.J. Zimney, Preparation and characterization of graphene oxide paper, *Nature* 448 (2007) 457–460.
- [5] C.G. Navarro, R.T. Weitz, A.M. Bittner, Electronic transport properties of individual chemically reduced graphene oxide sheets, *Nano Lett.* 7 (2007) 3499–3503.
- [6] Y.B. Zhang, Y.W. Tan, H.L. Stormer, Experimental observation of the quantum hall effect and Berry's phase in graphene, *Nature* 438 (2005) 201–204.
- [7] G. Goncalves, P.A.A.P. Marques, C.M. Granadeiro, H.I.S. Nogueira, M.K. Singh, J. Gracio, Surface modification of graphene nanosheets with gold nanoparticles: the role of oxygen moieties at graphene surface on gold nucleation and growth, *Chem. Mater.* 21 (2009) 4796–4802.
- [8] Y. Fang, S. Guo, C. Zhu, Y. Zhai, E. Wang, Self-assembly of cationic polyelectrolyte-functionalized graphene nanosheets and gold nanoparticles: a two-dimensional heterostructure for hydrogen peroxide sensing, *Langmuir* 26 (2010) 11277–11282.
- [9] K.I. Ho, C.H. Huang, J.H. Liao, W.J. Zhang, L.J. Li, C.S. Lai, C.Y. Su, Fluorinated graphene as high performance dielectric materials and the applications for graphene nanoelectronics, *Sci. Rep.* 4 5893 (2014) 1–7.
- [10] U.N. Maiti, J. Lim, K.E. Lee, W.J. Lee, S.O. Kim, Three-dimensional shape engineered, interfacial gelation of reduced graphene oxide for high rate, large capacity supercapacitors, *Adv. Mater.* 26 (2014) 615–619.
- [11] Y. Quan, X.B. Wei, L. Xiao, T. Wu, H.Y. Pang, T.F. Liu, W. Huang, S.H. Wu, S.B. Li,

- Z. Chen, Highly sensitive and stable flexible pressure sensors with micro-structured electrodes, *J. Alloys Compd.* 699 (2017) 824–831.
- [12] Y. Ahmad, M. Dubois, K. Guerin, A. Hamwi, E. Flahaut, High energy density of primary lithium batteries working with sub-fluorinated few walled carbon nanotubes cathode, *J. Alloys Compd.* 726 (2017) 852–859.
- [13] J. Wang, S.A. Kondrat, Y. Wang, G.L. Brett, C. Giles, J.K. Bartley, G.J. Hutchings, Au-Pd nanoparticles dispersed on composite titania/graphene oxide-supports as a highly active oxidation catalyst, *ACS Catal.* 5 (2015) 3575–3587.
- [14] J. Xu, Y. Yang, S. Hu, Nanocomposites of graphene and graphene oxides: synthesis, molecular functionalization and application in electrochemical sensors and biosensors. A review, *Microchim. Acta* 184 (2017) 1–44.
- [15] A. Mondal, A. Saha, A. Sinha, Nikhil R. Jana, Tunable catalytic performance and selectivity of a nanoparticle-graphene composite through finely controlled nanoparticle loading, *Chem. Asian J.* 7 (2012) 2931–2936.
- [16] A.L. Sunatkari, S.S. Talwatkar, Y.S. Tamgadge, G.G. Muley, Synthesis, characterization and optical properties of  $\alpha$ -arginine stabilized gold nanocolloids, *Nanosci. Nanotechnol.* 5 (2015) 30–35.
- [17] Y. Hamanaka, K. Fukuta, A. Nakamura, L.M. Liz-Marzan, P. Mulvaney, Enhancement of third-order nonlinear optical susceptibilities in silica-capped Au nanoparticle films with very high concentrations, *Appl. Phys. Lett.* 84 (2004) 4938–4930.
- [18] R. Tuinstra, J.L.J. Koenig, Raman spectrum of graphite, *Chem. Phys.* 53 (1970) 1126.
- [19] A. C. Ferrari, J. C. Meyer, V. Scardaci, C. Casiraghi, M. Lazzeri, F. Mauri, S. Piscanec, D. Jiang, K. S. Novoselov, S. Roth, A. K. Geim, Raman spectrum of graphene and graphene layers, *Phys. Rev. Lett.* 97 (2006) 187401:1–4.
- [20] M.S. Dresselhaus, A. Jorio, M. Hofmann, G. Dresselhaus, R. Saito, Perspectives on carbon nanotubes and graphene Raman spectroscopy, *Nano Lett.* 10 (2010) 751.
- [21] K.N. Kudin, B. Ozbas, H.C. Schniepp, R.K. Prud'homme, I.A. Aksay, R. Car, Raman spectra of graphite oxide and functionalized graphene sheets, *Nano Lett.* 8 (2008) 36–41.
- [22] G.S. Zhang, S. Sun, D. Yang, J.P. Dodelet, E. Sacher, The surface analytical characterization of carbon fibers functionalized by  $H_2SO_4/HNO_3$  treatment, *Carbon* 46 (2008) 196–205.
- [23] D. Pacilé, M. Papagno, A. F. Rodríguez, M. Gironi, L. Papagno, C. Girit, G. C. Meyer, G. E. Begtrup, A. Zettl, Near-edge X-ray absorption fine-structure investigation of graphene, *Phys. Rev. Lett.* 101 (2008) 66806:1–4.
- [24] V. Lee, L. Whittaker, C. Jaye, K.M. Baroudi, D.A. Fischer, S. Banerjee, Large-area chemically modified graphene films: electrophoretic deposition and characterization by soft X-ray absorption spectroscopy, *Chem. Mater.* 21 (2009) 3905–3916.
- [25] A. Kuznetsova, I. Popova, J.T. Yates, M.J. Bronikowski, C.B. Huffman, J. Liu, R.E. Smalley, H.H. Hwu, J.G. Chen, Oxygen-containing functional groups on single-wall carbon nanotubes: NEXAFS and vibrational spectroscopic studies, *J. Am. Chem. Soc.* 123 (2001) 10699–10704.
- [26] C. Kozłowski, P.M.A. Sherwood, X-Ray photoelectron-spectroscopic studies of carbon-fibre surfaces, *J. Chem. Soc. Faraday Trans. 1* (80) (1985) 2745–2756.
- [27] H.E. Szwarckopf, B. Rousseau, Photoelectron core level spectroscopy study of Cs-graphite intercalation compounds-I. Clean surfaces study, *J. Phys. Chem. Solids* 53 (1992) 419–436.
- [28] R. Haerle, E. Riedo, A. Pasquarello, A. Baldereschi,  $sp^2/sp^3$  hybridization ratio in amorphous carbon from C 1s core-level shifts: X-ray photoelectron spectroscopy and first-principles calculation, *Phys. Rev. B.* 35 45101 (2001) 1–9.
- [29] J.F. Moulder, W.F. Stickle, P.E. Sobol, K.D. Bomben, Handbook of X-ray photoelectron spectroscopy : a reference book of standard spectra for identification and interpretation of XPS data, Physical Electronics (1995) (Eden Prairie, MN).
- [30] A.J.R. Silva, J.C. Faria, E.Z. Silva, A. Fazio, Technical Proceedings of the Nanotechnology Conference and Trade Show, 3 (2003), pp. 165–168.
- [31] A. Ganguly, S. Sharma, P. Papakonstantinou, J. Hamilton, Probing the thermal deoxygenation of graphene oxide using high-resolution in situ X-ray-based spectroscopies, *J. Phys. Chem. C* 115 (2011) 17009–17019.
- [32] A. Bianconi, S.B.M. Hagström, R.Z. Bachrach, Photoemission studies of graphite high-energy conduction-band and valence-band states using soft-X-ray synchrotron radiation excitation, *Phys. Rev. B* 16 (1977) 5543–5548.
- [33] H.A. Becerril, J. Mao, Z. Liu, R.M. Stoltenberg, Z. Bao, Y. Chen, Evaluation of solution-processed reduced graphene oxide films as transparent conductors, *ACS Nano* 2 (2008) 463–470.
- [34] Z. Luo, S. Lim, Z. Tian, J. Shang, L. Lai, B. MacDonald, C. Fu, Z. Shen, T. Yu, J. Lin, Pyridinic N doped graphene: synthesis, electronic structure, and electrocatalytic property, *J. Mater. Chem.* 21 (2011) 8038–8044.
- [35] S.C. Ray, C.W. Pao, J.W. Chiou, H.M. Tsai, J.C. Jan, W.F. Pong, R. McCann, S.S. Roy, P. Papakonstantinou, J.A. McLaughlin, Electronic properties of a-CN<sub>x</sub> thin films: an X-ray-absorption and photoemission spectroscopy study, *J. App. Phys.* 98 033708 (2005) 1–4.
- [36] K.A. Mkhoyan, A.W. Contryman, J. Silcox, D.A. Stewart, G. Eda, C. Mattevi, S. Miller, M. Chhowalla, Atomic and electronic structure of graphene-oxide, *Nano Lett.* 9 (2009) 1058–1063.
- [37] M. Suda, N. Kameyama, A. Ikegami, M. Suzuki, N. Kawamura, Y. Einaga, Size-reduction induced ferromagnetism and photo-magnetic effects in azobenzene-thiol-passivated gold nanoparticles, *Polyhedron* 28 (2009) 1868–1874.
- [38] S. Sarma, Sekhar C. Ray, André M. Strydom, Electronic and magnetic properties of nitrogen functionalized graphene-oxide, *Dia. Rel. Mater.* 79 (2017) 1–6.
- [39] B. Ghosh, S. Sarma, M. Pontsho, Sekhar C. Ray, Tuning of magnetic behaviour in nitrogenated graphene oxide functionalized with iron oxide, *Dia. Rel. Mater.* 89 (2018) 35–42.

## Appendix 4

# Tuning of electronic and magnetic properties of multifunctional r-GO-ATA-Fe<sub>2</sub>O<sub>3</sub>-composites for magnetic resonance imaging (MRI) contrast agent

Cite as: J. Appl. Phys. 126, 035301 (2019); <https://doi.org/10.1063/1.5099892>  
Submitted: 12 April 2019 . Accepted: 03 June 2019 . Published Online: 16 July 2019

David O. Idisi , J. A. Oke , Sweety Sarma, S. J. Moloi , Sekhar C. Ray , W. F. Pong, and André M. Strydom

## COLLECTIONS

Note: This paper is part of the Special Topic on Magnetic and Plasmonic Nanoparticles for Biomedical Devices.

 This paper was selected as Featured



View Online



Export Citation



CrossMark

## ARTICLES YOU MAY BE INTERESTED IN

[Electron scattering mechanisms in polycrystalline sputtered zinc tin oxynitride thin films](#)  
Journal of Applied Physics 126, 035701 (2019); <https://doi.org/10.1063/1.5087408>

[Graphene nanocomposite material has potential MRI applications](#)  
Scilight 2019, 290004 (2019); <https://doi.org/10.1063/1.5116572>

[Tunability of localization length in naphthalene sulfonic acid doped polyaniline/nickel ferrite composite nanorods system](#)  
Journal of Applied Physics 126, 035102 (2019); <https://doi.org/10.1063/1.5085161>



# Tuning of electronic and magnetic properties of multifunctional r-GO-ATA-Fe<sub>2</sub>O<sub>3</sub>-composites for magnetic resonance imaging (MRI) contrast agent



Cite as: J. Appl. Phys. 126, 035301 (2019); doi: 10.1063/1.5099892

Submitted: 12 April 2019 · Accepted: 3 June 2019 ·

Published Online: 16 July 2019



David O. Idisi,<sup>1</sup> J. A. Oke,<sup>1</sup> Sweetey Sarma,<sup>1</sup> S. J. Moloi,<sup>1</sup> Sekhar C. Ray,<sup>1,a1</sup> W. F. Pong,<sup>2</sup> and André M. Strydom<sup>3</sup>

## AFFILIATIONS

<sup>1</sup>Department of Physics, CSET, University of South Africa, Private Bag X6, Florida, 1710, Science Campus, Christiaan de Wet and Pioneer Avenue, Florida Park, Johannesburg, South Africa

<sup>2</sup>Department of Physics, Tamkang University, Tamsui 251, Taipei, Taiwan

<sup>3</sup>Highly Correlated Matter Research Group, Physics Department, University of Johannesburg, P.O. Box 524, Auckland Park 2006, South Africa

**Note:** This paper is part of the Special Topic on Magnetic and Plasmonic Nanoparticles for Biomedical Devices.

**a1**Author to whom correspondence should be addressed: [Raysc@unisa.ac.za](mailto:Raysc@unisa.ac.za)

## ABSTRACT

We have synthesized r-GO-ATA-Fe<sub>2</sub>O<sub>3</sub> nanocomposites and studied their microstructural and electromagnetic properties for future possible magnetic resonance imaging for biomedical application. X-ray diffraction, transmission electron microscopy, Raman spectroscopy, X-ray photoelectron spectroscopy, and X-ray absorption near edge spectroscopy were used to study the structural and electronic properties, while a superconducting quantum interface device magnetometer was used for investigating the magnetic behavior of the nanocomposites. The nanocomposites have been found to reduce the graphitic structure of GO due to the substitution of carbon/oxygen and/or iron nanoparticles. Conversely, the electrical conductivity of nanocomposites is found to be high due to the formation of Fe—C/Fe—O bonds in the structure of the nanocomposites. The composites also exhibit superparamagnetic features as observed from the M-H hysteresis loop with saturation magnetization of  $\approx 0.1$  emu/g at 1.8 K temperature. The results, in general, suggest possible applicability of r-GO/Fe<sub>2</sub>O<sub>3</sub> nanocomposites as an effective multifunctional platform for magnetic resonance imaging in biomedical applications.

Published under license by AIP Publishing. <https://doi.org/10.1063/1.5099892>

## I. INTRODUCTION

Magnetic resonance imaging (MRI) is a versatile medical imaging technology that has attracted enormous attention from researchers because of the noninvasive technique that is involved. Graphene oxide (GO) and/or reduced graphene oxide (r-GO) is a material that has been used as a contrast agent in imaging modalities due to its excellent biocompatibility, cellular uptake, bioconjugation possibilities, and broad-wavelength absorbance characteristic.<sup>1</sup> Due to its diamagnetic nature, the material has, however, not been investigated for possibilities of it being used as an MRI contrast agent.<sup>2,3</sup> It is therefore important that studies are carried out on GO/r-GO in order to manipulate it to have properties that are suitable for this application. In addition to the excellent properties of GO/r-GO,

there is strong evidence that the defects can be created in the material. The created defects break the symmetry between graphene sublattices resulting in an induction of magnetic moment. As a result, the magnetic behavior of GO/r-GO can be altered possibly as a novel contrast agent for MRI applications.<sup>3,4</sup>

In MRI systems, high magnetic fields (ranging from 1.5 to 7 T) are used to achieve sufficient signal for short imaging time (less than few minutes) with a high spatial resolution (less than a millimeter). The GO/r-GO contrast agent, on the other hand, is used in clinical MRI to enhance the image contrast by either increasing (positive contrast)<sup>5</sup> or decreasing (negative contrast)<sup>6–8</sup> the local magnetic resonance signal. In achieving this, longitudinal ( $T_1$ ) and spin relaxation times ( $T_2$ ) need to be reduced for positive and



negative contrast, respectively.  $T_1$  comes from the fluctuating electron spin moment of the contrast agent coupling, while  $T_2$  comes from the long-range magnetic dipolar fields of the magnetic particles, leading to a short  $T_2$  and a reduced magnetic resonance signal.<sup>9</sup>

For MRI applications,  $\text{Fe}_3\text{O}_4$  nanoparticles have been widely explored and have received significant attention as sources of the superparamagnetic magnetic field that is essential for the application. The advantage of  $\text{Fe}_3\text{O}_4$  nanoparticles gives rise to an induced localized inhomogeneity of the magnetic field.<sup>10,11</sup> Jeong *et al.*<sup>12</sup> synthesized  $\gamma\text{-Fe}_2\text{O}_3$  and established the superparamagnetic properties where magnetic relaxation of the material was investigated. However, reduction in magnetic signal intensity was observed due to a steady drop of  $T_2$ . Ai *et al.*<sup>13</sup> and Liu *et al.*<sup>14</sup> modified  $\text{Fe}_3\text{O}_4$  with polymeric micelles to alleviate the relaxation problem. However,  $\text{Fe}_3\text{O}_4$  nanoparticles were found to aggregate when applied *in vivo*, thereby leading to a decrease in blood circulation.<sup>15</sup> The effect of superparamagnetic iron oxides nanoparticles (SPIONs)  $\text{Fe}_2\text{O}_3$  comprises of polydisperse inorganic cores with hydrodynamic diameter. The SPIONs can inhibit renal clearance after treatment leading to accumulation of iron in the body. The accumulated iron may cause negative MRI contrast in the long run.<sup>16,17</sup> To overcome this aggregation of  $\text{Fe}_3\text{O}_4$  nanoparticles and iron accumulation in the body, the composition of GO/r-GO and  $\text{Fe}_3\text{O}_4$  is a possible material to be used due to its hydrophilic, nontoxic, and biocompatible properties. The GO/r-GO- $\text{Fe}_3\text{O}_4$  composition was explored for MRI applications,<sup>18–20</sup> and the results showed an enhancement of cellular MRI contrast. GO- $\text{Fe}_2\text{O}_3$  nanocomposites, on the other hand, have not been widely explored as a contrast agent for MRI applications.

In our earlier study<sup>21</sup> about the magnetic behavior of nitrogenated graphene oxide functionalized with different types of iron oxides, we have not used any capping and/or stabilizing agent during functionalization of GO/r-GO. But, in the present study, we synthesized r-GO-ATA- $\text{Fe}_2\text{O}_3$  nanocomposites using coprecipitation. 2-Aminoterephthalic acid (ATA) was used as a capping/stabilizing agent due to its proven surface coating potential and shorter chain length which can enhance the magnetic properties of  $\text{Fe}_2\text{O}_3$ .<sup>22</sup> Electronic and magnetic properties of the composites for a contrast agent in magnetic resonance bioimaging applications were studied. In this case, challenges related to  $T_2$  and aggregation can be controlled with an introduction of GO/r-GO in r-GO-ATA- $\text{Fe}_2\text{O}_3$  nanocomposites.<sup>12</sup>

In this study, transmission electron microscopy (TEM) was used for the study of surface morphology, while for electronic and microstructural properties of the nanocomposites, X-ray diffraction (XRD), Raman spectroscopy, Fourier transform infrared spectroscopy (FTIR), and X-ray photoelectron spectroscopy (XPS) were used. X-ray absorption near edge structure (XANES) spectroscopy was used to ascertain the bonding structure of GO/r-GO and r-GO-ATA/ $\text{Fe}_2\text{O}_3$  nanocomposites. The electrical conductivity and superparamagnetic properties of the composites were explored using the current-voltage (I-V) technique and high sensitivity M-H hysteresis loops, respectively, in this work.

## II. EXPERIMENTAL DETAILS

GO, r-GO, and r-GO-ATA- $\text{Fe}_2\text{O}_3$  were synthesized using ferrous chloride [ $\text{Fe}(\text{Cl})_2 \cdot 4\text{H}_2\text{O}$ ], ferric chloride [ $\text{Fe}(\text{Cl})_3 \cdot 6\text{H}_2\text{O}$ ],

2-aminoterephthalic acid (ATA), ammonium hydroxide ( $\text{NH}_4\text{OH}$ ), and potassium hydroxide (KOH). All chemical reagents were acquired from Fisher Scientific and Sigma Aldrich. Initially, GO sheet, which is the anchor material, was prepared by the modified Hummers method and subsequently reduced using 3 ml of ammonium hydroxide ( $\text{NH}_4\text{OH}$ ). During the synthesis process, an aqueous solution of the prepared GO (20 ml) was magnetically stirred at the rate of 500 rpm for 6 h at a constant temperature of 70 °C. GO- $\text{NH}_4\text{OH}$  was left to stir overnight for the formation of black pigments. To reduce the effect of agglomeration and dispersion, the mixture was centrifuged at a rate of 5000 rpm.

The r-GO mixture was then washed several times using deionized water to reduce impurities and ammonia residues. The final r-GO powder was collected by drying the aqueous solution in an oven heated up to 60 °C. The  $\text{Fe}_2\text{O}_3$  nanoparticles were prepared using the chemical coprecipitation technique where 2-aminoterephthalic acid (ATA) was used as a capping agent. The procedure involves the mixture of 1.17 g of  $\text{FeCl}_3 \cdot 6\text{H}_2\text{O}$ , 0.43 g of  $\text{FeCl}_2 \cdot 4\text{H}_2\text{O}$ , and 0.82 g of ATA with 22.5 ml of pure water in a 150 ml flask. The entire mixture was stirred using a magnetic stirrer with a flask on a hot plate, 60 °C for 1 h. The reaction process occurred under the flow of  $\text{N}_2$  gas to avoid thermal degradation. While stirring, 2.5 ml of  $\text{NH}_4\text{OH}$  mixed with water was added into the mixture. The pH range of the mixture was 10–11, and it was robustly stirred for another 1 h with the plate heated to a high temperature (80 °C). The nucleated iron oxide nanocomposite was left to cool to room temperature. The mixture was then magnetically separated and washed using ethanol and collected as ATA- $\text{Fe}_2\text{O}_3$ .

The homogeneous aqueous mixture of GO containing 0.1 mg ml<sup>-1</sup> was added to the ATA- $\text{Fe}_2\text{O}_3$  mixture and ultrasonicated in a sonicator bath at room temperature. The sonication process aims to give a uniform dispersion of the particles. The mixture was thereafter dried in a microwave and collected as the r-GO-ATA- $\text{Fe}_2\text{O}_3$  nanocomposite.

The structural studies of the synthesized composites were performed using a Rigaku Smartlab X-ray diffractometer (0.154 nm Cu  $K\alpha$  line). Raman spectra were measured using HORIBA scientific XploRA at 532 nm (~2.41 eV) LASER light excitation energy. The surface morphological structures were studied using JEOL JEM 2100. The Fe  $L_{III}$ ,  $11\bar{1}$ -edge, C  $K$ -edge, and O  $K$ -edge XANES measurements were performed at the Taiwan Light Source (TLS), Hsinchu, Taiwan. The core shells C 1s, O 1s, and Fe 2p were performed using a KRATOS-SUPRA spectrometer with monochromatic Al  $K\alpha$  radiation possessing excitation energy,  $h\nu = 1486.6$  eV, and base pressure  $1.2 \times 10^{-9}$  Torr at UNISA (Florida Science Campus). The ultraviolet photoelectron spectroscopy (UPS) spectra were obtained using He-I ( $h\nu = 21.22$  eV) and He-II ( $h\nu = 40$  eV) using the same KRATOS-SUPRA spectrometer. The electrical conductivity was studied using Keithley 6487 with voltage sweep ranging from -1 to 1 V. A SQUID-type magnetometer that has a sensitivity of  $<5 \times 10^{-8}$  emu was used for the M-H loop. All the measurements were performed at room temperature.

## III. RESULT AND DISCUSSION

TEM images of Fe-NPs and of r-GO-ATA- $\text{Fe}_2\text{O}_3$  nanocomposites are shown in Figs. 1(a) and 1(b), respectively. The morphology

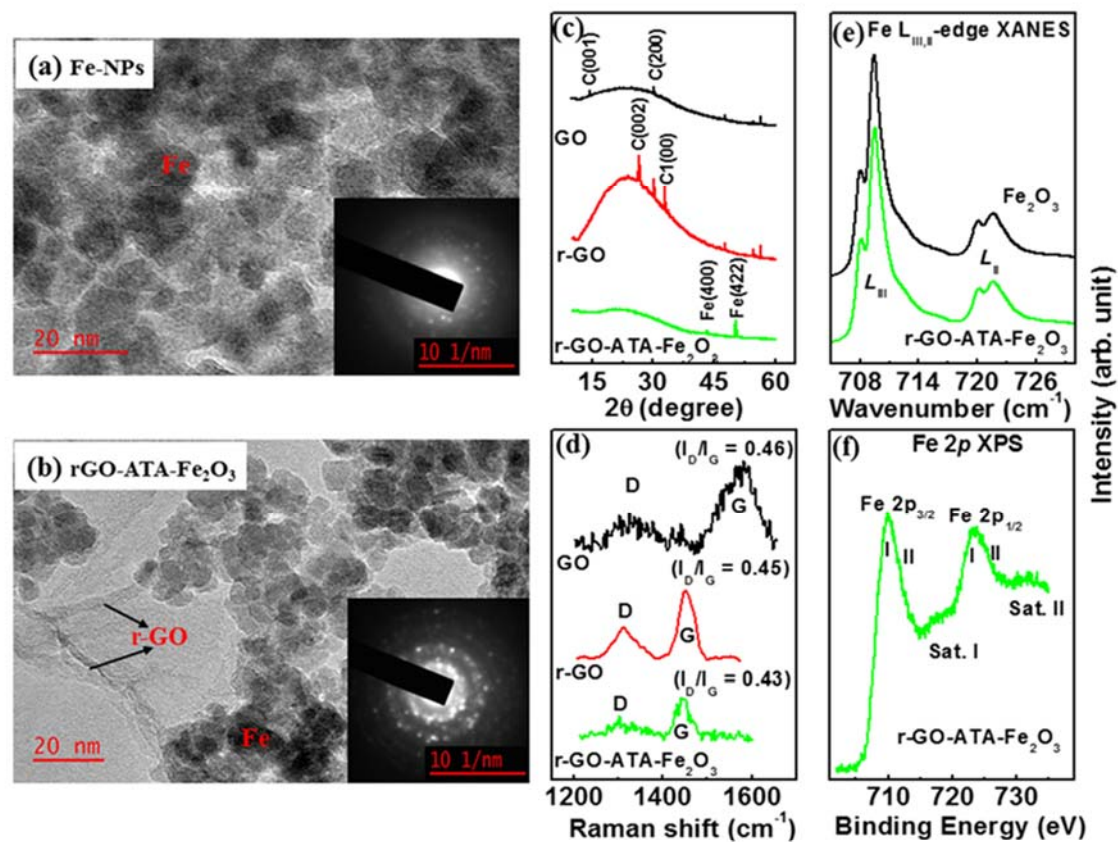


**FIG. 1.** Transmission electron microscopy of (a) Fe-NPs and (b) r-GO-ATA-Fe<sub>2</sub>O<sub>3</sub> nanocomposite. (c) X-ray diffraction and (d) Raman spectroscopy of GO, r-GO, and r-GO-ATA-Fe<sub>2</sub>O<sub>3</sub> nanocomposites. (e) Fe L<sub>III</sub>-edge X-ray absorption near edge structure (XANES) and (f) Fe 2p X-ray photoelectron spectroscopy of r-GO-ATA-Fe<sub>2</sub>O<sub>3</sub> nanocomposites.

indicates that Fe-NPs are completely dispersed in r-GO and have formed their iron oxide nanocomposites.<sup>23</sup> The images show spherical composites of the nanoscale range with an average size of Fe-NPs as ~8–10 nm. Images do not show the agglomeration of the composites but a homogeneous dispersibility of the r-GO-Fe<sub>2</sub>O<sub>3</sub> nanocomposites. The formation of r-GO-Fe<sub>2</sub>O<sub>3</sub> nanocomposites can be observed from Fig. 1(b) with different particles in the composites.

The XRD measurements for GO, r-GO, and r-GO-ATA-Fe<sub>2</sub>O<sub>3</sub> nanocomposites are shown in Fig. 1(c). The obtained structure of r-GO-ATA-Fe<sub>2</sub>O<sub>3</sub> is similar to the spinel phase of Fe<sub>3</sub>O<sub>4</sub> with JCPDS card no. 19-0629.<sup>24</sup> As expected, the XRD spectra confirm the amorphous nature of graphene oxide as indicated by the hump with the (002) peak. There is a significant decrease in the intensity of the peak when r-GO is attached to ATA-Fe<sub>2</sub>O<sub>3</sub>. The decrease in the intensity shows the formation of the r-GO-ATA-Fe<sub>2</sub>O<sub>3</sub>

nanocomposite. Fe (400) and Fe (422) peaks are consistent with Fe<sub>3</sub>O<sub>4</sub> as obtainable for iron oxide nanoparticles.<sup>25,26</sup>

Figure 1(d) shows the Raman spectra of GO, r-GO, and r-GO-ATA-Fe<sub>2</sub>O<sub>3</sub> nanocomposites. Two prominent peaks (D and G) are observed at ~1334 and ~1583 cm<sup>-1</sup>, respectively. The G peak arises from the degenerate (TO and LO) E<sub>2g</sub> phonon vibration modes at the Brillouin zone,<sup>23</sup> whereas the D peak is attributed to the induced defect. We have obtained the information about the structural defect from the I<sub>D</sub>/I<sub>G</sub> ratio using the “D”/“G” peak height. The I<sub>D</sub>/I<sub>G</sub> ratio is found to be reduced from 0.46 (GO) → 0.43 (r-GO-ATA-Fe<sub>2</sub>O<sub>3</sub> nanocomposites) that are given in Table I. A decrease in the ratio confirms the reduction of sp<sup>2</sup> clusters with an increase in sp<sup>3</sup> content. The downward shift of the D peak from 1334 cm<sup>-1</sup> (GO) → 1314 cm<sup>-1</sup> (r-GO) → 1313 cm<sup>-1</sup> (r-GO-ATA-Fe<sub>2</sub>O<sub>3</sub>) is also observed. This shift may be attributed to the recovery of a hexagonal carbon network.<sup>27,28</sup>

**TABLE I.** Elemental compositions/quantification (XPS),  $sp^2$  content (XANES),  $(I_D/I_G)$  ratio (Raman), work function ( $\Theta$ ), valence band maximum (VBM), saturation magnetization ( $M_s$ ), and coercivity ( $H_c$ ).

	C 1s (at. %)	O 1s (at. %)	Fe 2p (at. %)	C/O ratio	$sp^2$ content (a.u.)	$I_D/I_G$ ratio	$\Theta$ (eV)	VBM (eV)	$M_s$ @1.8 K (emu/g) $\times 10^{-3}$	$H_c$ (Oe)
GO	63.8	36.2	...	1.76	0.73	0.46	3.8	2.5	0.31	...
r-GO	72.0	28.0	...	2.57	0.39	0.45	...	...	0.15	...
r-GO-ATA-Fe <sub>2</sub> O <sub>3</sub>	61.0	34.0	5.0	1.79	0.28	0.43	3.67	2.7	0.93	11 @ 300 K 30 @ 40 K 58 @ 1.8 K

Figure 1(e) shows the Fe  $L_{III,II}$ -edge XANES spectrum of the r-GO-ATA-Fe<sub>2</sub>O<sub>3</sub> nanocomposite along with Fe<sub>2</sub>O<sub>3</sub> as a reference. The features of r-GO-ATA-Fe<sub>2</sub>O<sub>3</sub> nanocomposites spectrum are similar to the Fe<sub>2</sub>O<sub>3</sub> spectrum confirming the formation of an r-GO-Fe<sub>2</sub>O<sub>3</sub> composite. Two doublet types,  $L_{III}$  and  $L_{II}$  edges, are shown in the figure. These edges correspond to the transition of an electron from  $2p_{3/2}$  to  $2p_{1/2}$  energy levels, respectively.<sup>27,28</sup> The energy separation of peaks in the  $L_{3}$ -edge is  $\sim 1.4$  eV for r-GO-ATA-Fe<sub>2</sub>O<sub>3</sub> nanocomposites. The  $L_{III}$ -edge displays two peaks at  $\sim 708.2$  eV and  $\sim 709.6$  eV, and this pattern is the same for Fe<sup>2+</sup> and Fe<sup>3+</sup> although the relative intensity is very different. In the case of the reference, Fe<sub>2</sub>O<sub>3</sub>, this peak is  $\sim 0.2$  eV, lower than that of r-GO-ATA-Fe<sub>2</sub>O<sub>3</sub> nanocomposites. The  $L_{II}$ -edge also displays two peaks at  $\sim 720.2$  eV and at  $\sim 721.5$  eV. Both peaks in Fe  $L_{III}$ - and Fe  $L_{II}$ -absorption edges confirm the iron atoms in the metallic environment. We have estimated the intensity of both edges and compared them with that of the reference, Fe<sub>2</sub>O<sub>3</sub>, and found that the intensity of r-GO-ATA-Fe<sub>2</sub>O<sub>3</sub> nanocomposites is slightly lower indicating that the formation of r-GO-ATA-Fe<sub>2</sub>O<sub>3</sub> nanocomposites is by substitution of "Fe" with the carbon and/or oxygen atoms in the composite.<sup>29,30</sup>

Fe 2p core-level spectra for "r-GO-ATA-Fe<sub>2</sub>O<sub>3</sub>" nanocomposites are shown in Fig. 1(f). Fe  $2p_{3/2}$  and Fe  $2p_{1/2}$  peaks are observed in the figure. The binding energies for the Fe  $2p_{3/2}$  peak at  $\sim 709.6$  eV and at  $\sim 722.6$  eV for the Fe  $2p_{1/2}$  peak are found in the 2p core level with a satellite structure. These results agree with the reported values of Fe<sub>2</sub>O<sub>3</sub>.<sup>31</sup> Both Fe  $2p_{3/2}$  and Fe  $2p_{1/2}$  have a shoulder along with their main peaks. The binding energies of these two components, Fe<sup>2+</sup> and Fe<sup>3+</sup>, are 708.1 eV and 710.1 eV for Fe  $2p_{3/2}$ , whereas for Fe  $2p_{1/2}$  are 721.8 eV and 724.1 eV. These energies have been reported for "r-GO-ATA-Fe<sub>2</sub>O<sub>3</sub>" nanocomposites.<sup>32</sup> These components are marked I and II in Fig. 1(f). The main peaks were explained in terms of core-shell spin-orbit splitting of 13.2 eV,<sup>33</sup> and their each double-subpeaks shown in Fig. 1(f) has been observed before in transitional-metal carbides and they correspond to the usual ligand-field splitting ( $\approx 2.0$  eV).<sup>34-36</sup>

Figure 2 shows the normalized C K-edge and O K-edge X-ray absorption near edge structure (XANES) spectra of GO, r-GO, and r-GO-ATA-Fe<sub>2</sub>O<sub>3</sub> nanocomposites. The spectrum in Fig. 2 clearly shows the presence of states, unoccupied  $\pi^*$  ( $1s \rightarrow \pi^*$ ) at 2.85.2 eV and  $\sigma^*$  ( $1s \rightarrow \sigma^*$ ) at 291.0 eV, indicating that GO/r-GO/r-GO-ATA-Fe<sub>2</sub>O<sub>3</sub> nanocomposites still display the aromaticity of the original pristine graphene.<sup>37-39</sup> The normalized O K-edge XANES spectra also show these states, at  $\sim 531.0$  eV and  $\sim 541.8.0$  eV. These

states are assigned to  $1s \rightarrow \pi^*$  C=O and  $1s \rightarrow \sigma^*$  C-O/C=O, respectively.<sup>37-39</sup> It can be seen from Figs. 2(a) and 2(e) that the spectral features of both C K-edge and O K-edge for the nanocomposites are similar. The  $\pi^*$  regions are subtracted using Gaussian lines shown as the inset of Figs. 2(a) and 2(e) with dotted lines. We have estimated the  $\pi^*$  area ( $\pi^*/\sigma^*$  ratio) from C K-edge XANES spectra and found a change from 0.73 (0.98)  $\rightarrow$  0.39 (0.95)  $\rightarrow$  0.28 (0.88) of GO, r-GO, and r-GO-ATA-Fe<sub>2</sub>O<sub>3</sub> nanocomposites, respectively. This change indicates that the composites lose their  $sp^2$  content in the r-GO-ATA-Fe<sub>2</sub>O<sub>3</sub> nanocomposite structure. Similarly, in O K-edge XANES spectra, these values change from 0.91 (0.66)  $\rightarrow$  0.88 (0.64)  $\rightarrow$  0.92 (0.65) indicating that the oxide contents decrease in the r-GO-ATA-Fe<sub>2</sub>O<sub>3</sub> nanocomposite. Figures 2(b)-2(d) and 2(f)-2(h) show three peaks at  $\sim 283.2$  ( $\pm 0.1$ ) eV,  $\sim 284.5$  ( $\pm 0.1$ ) eV, and  $\sim 285.1$  eV for the C K-edge. Intensities of these peaks decrease showing a decrease in  $sp^2$ -hybridized carbon. In the O K-edge, two deconvoluted peaks arise at  $\sim 530.8$  eV and 532.0 eV, respectively, and their intensities change slightly indicating small deoxidation. Deconvoluted different parameters, viz., peak position (x), peak width ( $\Delta\omega$ ), and their intensity obtained from the C K-edge and O K-edge XANES spectra are tabulated in Table II.

Figures 3(a) and 3(e) show the C 1s and O 1s XPS spectra for GO, r-GO, and r-GO-ATA-Fe<sub>2</sub>O<sub>3</sub> nanocomposites, respectively. The composition and quantification of GO, r-GO, and r-GO-ATA-Fe<sub>2</sub>O<sub>3</sub> nanocomposites are tabulated in Table I. The spectral features of C 1s and O 1s of r-GO-ATA-Fe<sub>2</sub>O<sub>3</sub> nanocomposites are different from that of GO and r-GO. Spectral features of C 1s and O 1s for r-GO shift to lower energy as shown in Figs. 3(a) and 3(e). This shift indicates a change in their electronic/bonding structures. For a detailed study of their electronic and bonding structures, we have deconvoluted C1s and O 1s XPS spectra into four and three Gaussian lines as shown in Figs. 3(b)-3(d) and 3(f)-3(h), respectively. One additional Gaussian peak of O 1s spectrum for the r-GO-ATA-Fe<sub>2</sub>O<sub>3</sub> nanocomposite at 531.5 eV is assigned to oxygen double-bonded to carbon.<sup>38,39</sup> The origin of other peaks of C 1s spectrum for GO's are  $\sim 283.8$  eV, 285.7 eV, 286.1 eV, and 287.3 eV, respectively, labeled as I, II, III, and IV in the figure. These four peaks are assigned to  $sp^2$  C=C, hydroxyl/phenolic group, epoxy group, and  $>C=O$ , respectively.<sup>28,36,40,41</sup> In the case of r-GO, these peaks are shifted toward lower energy at  $\sim 281.5$  eV (pre- $sp^2$ -C),  $\sim 283.2$  eV ( $sp^2$ -C),  $\sim 284.2$  eV ( $sp^2$ -C), and  $\sim 285.5$  eV (C-O), respectively.<sup>28,36,40,41</sup> In the case of the r-GO-ATA-Fe<sub>2</sub>O<sub>3</sub> nanocomposite, the bond structure, Fe-C at  $\sim 282.8$  eV (peak-I), C-Fe and/or  $sp^2$ -C

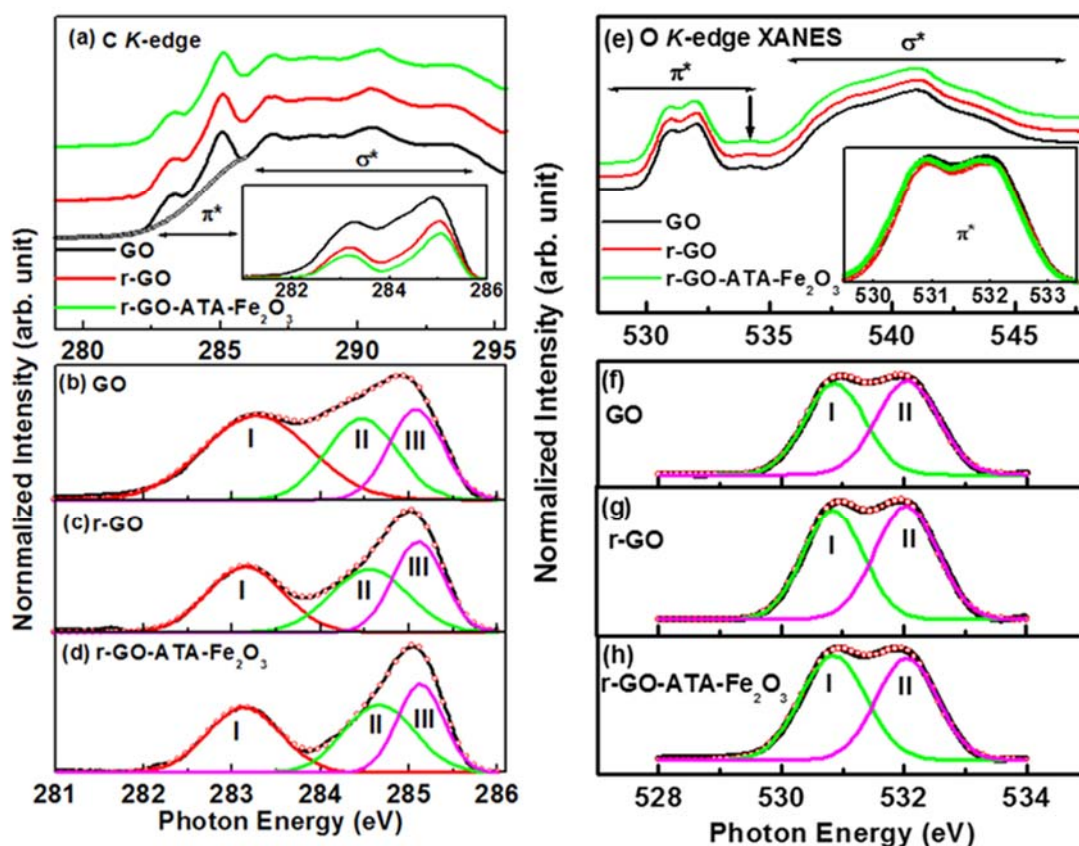


**FIG. 2.** (a) C K-edge and (e) O K-edge x-ray absorption near edge structure (XANES) spectroscopy of GO, r-GO, and r-GO-ATA-Fe<sub>2</sub>O<sub>3</sub> nanocomposites. The inset shows the  $\pi^*$  region of C K-edge and O K-edge XANES spectra. (b)–(d) C K-edge and (f)–(h) O K-edge XANES spectra deconvoluted into three and two Gaussian lines, respectively, of GO, r-GO and r-GO-ATA-Fe<sub>2</sub>O<sub>3</sub> nanocomposites.

at  $\sim 284.5$  eV (peak-II), epoxy group at  $\sim 286.3$  eV (peak-III), and  $>C=O$  at  $\sim 287.7$  eV (peak-IV) have been reported before.<sup>28,36,40,41</sup> The deconvoluted peaks of O 1s spectra for GO/r-GO (r-GO-ATA-Fe<sub>2</sub>O<sub>3</sub> nanocomposite) are 530.1/527.7 (527.5) eV

(peak-I), 531.3/529.1 (528.7) eV (peak-II), and 532.2/530.3 (530.2) eV (peak-III). The peak arising at  $\sim 530.2$  ( $\pm 0.1$ ) eV is associated with quinone groups. The peak at  $\sim 531$  eV is assigned to  $C=O$  (oxygen doubly bonded to aromatic carbon) whereas the peak at

**TABLE II.** Deconvoluted different parameters from C K-edge O K-edge XANES spectra.

	C K-edge XANES									O K-edge XANES					
	Peak-I			Peak-II			Peak-III			Peak-I			Peak-II		
	x (eV)	$\Delta\omega$ (eV)	Int. (a.u.)	x (eV)	$\Delta\omega$ (eV)	Int. (a.u.)	x (eV)	$\Delta\omega$ (eV)	Int. (a.u.)	x (eV)	$\Delta\omega$ (eV)	Int. (a.u.)	x (eV)	$\Delta\omega$ (eV)	Int. (a.u.)
GO	283.3	1.21	3.32	284.4	0.76	1.92	285.1	0.62	1.99	530.9	0.98	4.4	532.1	1.01	4.7
r-GO	283.1	0.85	1.32	284.5	0.88	1.29	285.1	0.57	1.23	530.8	0.97	4.2	532.0	1.02	4.5
r-GO-ATA-Fe <sub>2</sub> O <sub>3</sub>	283.1	0.83	0.96	284.7	0.80	0.97	285.1	0.52	0.83	530.8	1.06	4.7	532.0	0.99	4.3

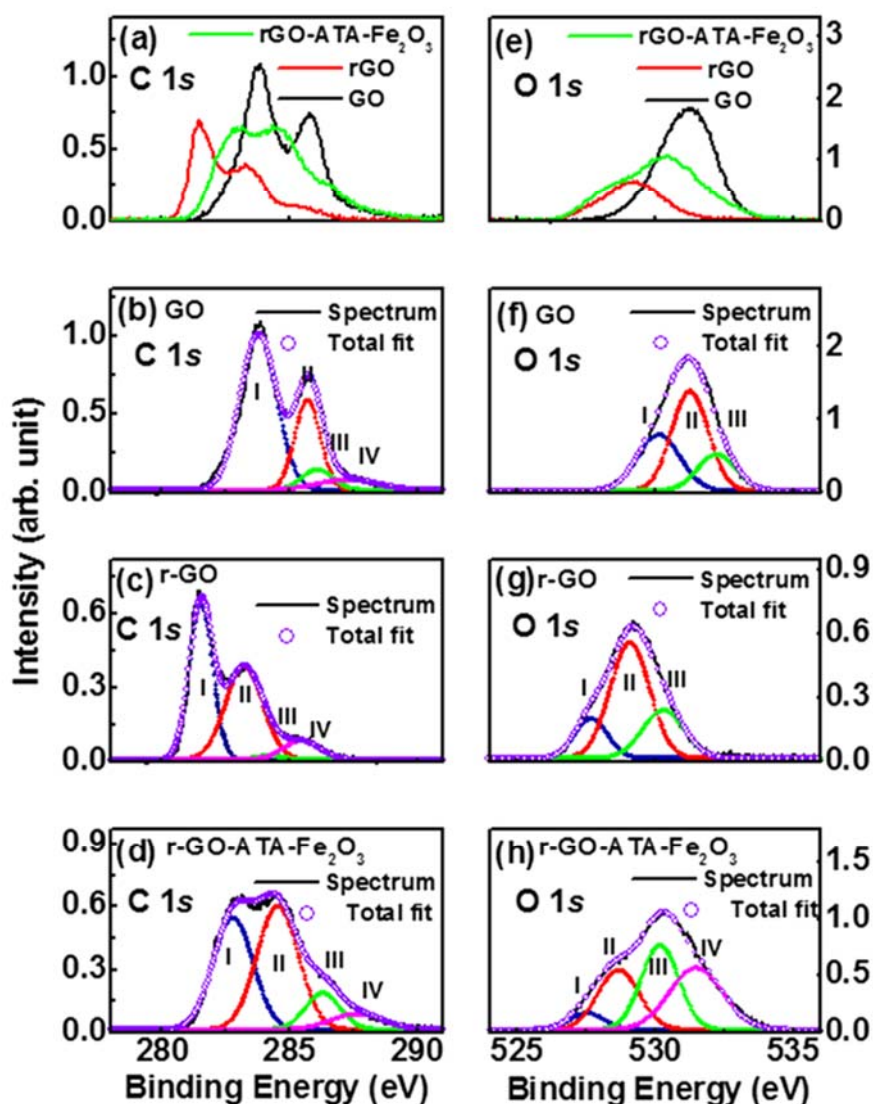


FIG. 3. (a) C 1s and (e) O 1s x-ray photoelectron emission spectroscopy (XPS) of GO, r-GO, and r-GO-ATA-Fe<sub>2</sub>O<sub>3</sub> nanocomposites. (b)–(d) C 1s and (f)–(h) O 1s XPS spectra deconvoluted into four and three Gaussian lines, respectively, of GO, r-GO, and r-GO-ATA-Fe<sub>2</sub>O<sub>3</sub> nanocomposites.

~532 eV is associated with C–O phenolic group (oxygen singly bonded to aliphatic carbon). The peak at ~527.6 ( $\pm 0.1$ ) eV is associated with carbon–oxygen and the peak at 528.7 eV is attributed to oxides of iron.<sup>41</sup> Deconvoluted different parameters, viz., peak position ( $x$ ), peak width ( $\Delta\omega$ ), and their intensity obtained

from C 1s and O 1s XPS spectra are tabulated in Table III. We have also found a different oxygen group with carbon/iron, like alkoxy, epoxy, O–H, C=C, C=O, and Fe–O, in GO, r-GO, and r-GO-ATA-Fe<sub>2</sub>O<sub>3</sub> composites from Fourier transform infrared spectroscopy as shown in Fig. S1 in the supplementary material.

TABLE III. Deconvoluted different parameters from C 1s and O 1s XPS and He-II UPS.

	Peak-I			Peak-II			Peak-III			Peak-IV		
	x (eV)	$\Delta\omega$ (eV)	Int. (a.u.)	x (eV)	$\Delta\omega$ (eV)	Int. (a.u.)	x (eV)	$\Delta\omega$ (eV)	Int. (a.u.)	x (eV)	$\Delta\omega$ (eV)	Int. (a.u.)
C 1s X-ray photoemission spectroscopy (XPS)												
GO	283.8	1.7	2.1	285.7	1.2	1.0	286.1	1.5	0.5	287.3	3.1	0.5
r-GO	281.5	1.1	0.9	283.2	1.7	0.8	284.2	1.6	0.2	285.5	1.8	0.3
r-GO-ATA-Fe <sub>2</sub> O <sub>3</sub>	282.8	1.8	1.3	284.5	1.9	1.4	286.3	1.7	0.6	287.6	2.7	0.4
O 1s X-ray photoemission spectroscopy (XPS)												
GO	530.1	1.9	1.8	531.3	1.6	2.6	532.2	1.7	1.2	...	...	...
r-GO	527.7	1.5	0.6	529.1	1.7	1.3	530.2	1.9	0.8	...	...	...
r-GO-ATA-Fe <sub>2</sub> O <sub>3</sub>	527.5	1.6	0.7	528.7	1.8	1.4	530.2	1.6	1.7	531.5	2.4	1.7
Ultraviolet photoemission spectroscopy (UPS), He-II ( $h\nu = 40.8$ eV excitation)												
GO	4.9	2.7	0.3	6.7	2.3	0.3	8.5	2.8	0.4	10.9	3.3	0.2
r-GO	7.2	2.4	0.1	9.1	3.5	0.4	11.2	1.7	0.1	13.0	1.5	0.1
r-GO-ATA-Fe <sub>2</sub> O <sub>3</sub>	4.7	3.4	0.2	7.4	3.6	0.4	10.2	3.0	0.2	11.8	2.9	0.1

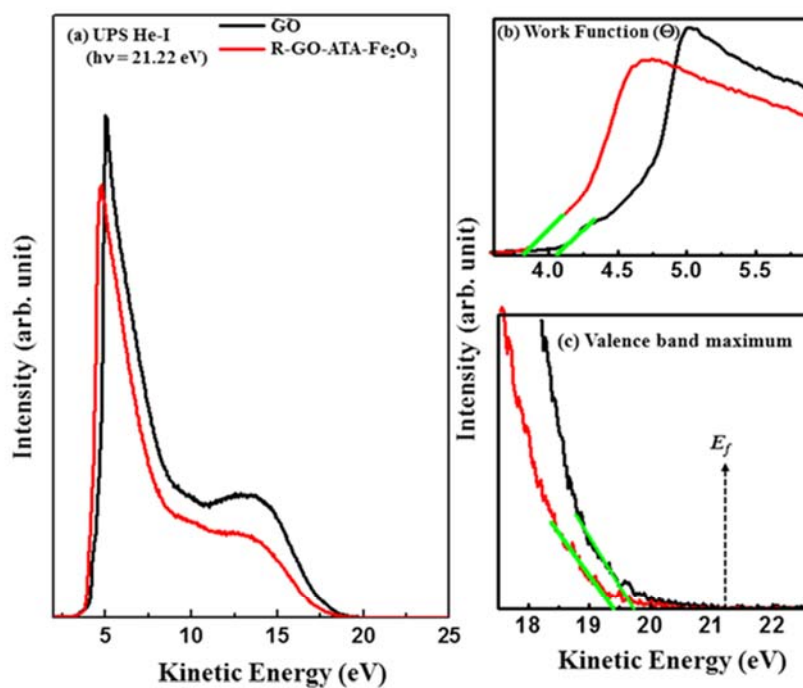


FIG. 4. (a) Ultraviolet photoemission spectroscopy (UPS) of (a) GO and r-GO-ATA-Fe<sub>2</sub>O<sub>3</sub> nanocomposites at an excited energy  $h\nu = 21.22$  eV (He-I). (b) Lower kinetic energy part of UPS for estimation of work function and (c) upper kinetic energy part of UPS for estimation of valence band maximum (VBM).

However, the spectral feature and peak shift of C 1s and O 1s XPS spectra for r-GO-ATA-Fe<sub>2</sub>O<sub>3</sub> nanocomposites indicate a change in the structural network of r-GO with Fe-NP atoms.<sup>39,42</sup>

To gain further insight into the effect for the r-GO-ATA-Fe<sub>2</sub>O<sub>3</sub> nanocomposite, we have studied the valence band density of states (DOS) near the Fermi level by carrying out UPS measurements at He-I ( $h\nu = 21.22$  eV) and He-II ( $h\nu = 40.81$  eV) radiation as shown in Figs. 4 and 5, respectively. The Ag thin film was used for the Fermi level edge ( $E_f$ ), appearing at  $\sim 21.22$  eV (not shown here), which is in excellent agreement with the excitation energy of the He-I line. It was reported from the first-principles calculations that changes in magnetic properties can be attributed to defect induction.<sup>43</sup> The created defect in a single atom of graphene related lattice causes a shift in the quasilocalized states at the Fermi level. The quasilocalized state lying at the Fermi level is the main contributor to the itinerant magnetism in graphene.<sup>43</sup> From Fig. 5, a shift of r-GO away from the density of states (DOS) indicates a decrease in the DOS of r-GO.<sup>44</sup> Then, DOS of r-GO-ATA-Fe<sub>2</sub>O<sub>3</sub> is

enhanced compared to r-GO, and it is confirmed by the increase of magnetization as shown in Figs. 6(e)–6(g). In this case, the decrease in DOS indicates a reduction in the  $sp^2$  C-C cluster with the formation of new bonds as indicated by XPS. The formation of the new bonds gives an increase in the magnetization that will be discussed in Figs. 6(e)–6(g). The energy difference between the valence band maximum (VBM) and the Fermi level ( $E_f - E_{VB}$ ) was then estimated from the intersection of the slope of each spectrum in an inset of Fig. 4(c) (VB edge) with the extrapolated background providing the valence band maximum (VBM) position of GO and r-GO-ATA-Fe<sub>2</sub>O<sub>3</sub> nanocomposites. The VBM position of GO and r-GO-ATA-Fe<sub>2</sub>O<sub>3</sub> nanocomposites is 1.8 eV and 2.5 eV, respectively, and are shown in the upper inset of Fig. 4(c). From the UPS He-I spectra, we also estimated the work function of GO and r-GO-ATA-Fe<sub>2</sub>O<sub>3</sub> nanocomposites following the same process as shown in Fig. 4(b). The work function of GO and r-GO-ATA-Fe<sub>2</sub>O<sub>3</sub> nanocomposites are 3.8 eV and 4.1 eV, respectively, that are given in Table I. The variation of the work function and valence band maximum are related to the dipole moment. For instance, the difference in work function (0.3 eV) implies a reduction in dipole moment, which has an impact on the charge redistribution. The charge redistribution gives rise to unpaired electrons (vacancies) which eventually influence the magnetization of r-GO-ATA-Fe<sub>2</sub>O<sub>3</sub> nanocomposites.<sup>45</sup>

The UPS spectra corresponding to the VB DOS of GO, r-GO, and r-GO-ATA-Fe<sub>2</sub>O<sub>3</sub> nanocomposites obtained at He-II radiation ( $\sim 40.81$  eV) are shown in Fig. 5. The overall photoemission intensity changes from 0.9 (GO)  $\rightarrow$  0.6 (r-GO)  $\rightarrow$  0.7 (r-GO-ATA-Fe<sub>2</sub>O<sub>3</sub>), and their Fermi edges shifted to 2.5 eV  $\rightarrow$  4.5 eV  $\rightarrow$  2.9 eV (GO  $\rightarrow$  r-GO  $\rightarrow$  r-GO-ATA-Fe<sub>2</sub>O<sub>3</sub> nanocomposites) revealing the insulating nature of the material. Different methods used to determine the Fermi level of a graphitic material have found it ranging from 2 eV to 12 eV showing characteristics of C 2p electrons. The binding energy ranging from 12 to 22 eV, on the other hand, corresponds to C 2s valence electrons, followed by the O 2s region at higher binding energy.<sup>46</sup> For a detailed study, we have deconvoluted the spectra into four Gaussian lines and restricted the binding energy range of 0–16 eV as shown in Figs. 5(b)–5(d). The deconvoluted Gaussian lines of GO/r-GO (r-GO-ATA-Fe<sub>2</sub>O<sub>3</sub> nanocomposite) are 4.9/7.3 (4.8) eV (peak-I), 6.7/9.1 (7.4) eV (peak-II), 8.5/11.1 (10.2) eV (peak-III), and 10.9/13.0 (11.8) eV (peak-IV), respectively. The different Gaussian peaks are assigned as the C-2p <sub>$\pi$</sub>  ( $4.9 \pm 0.1$  eV), 2p-( $\pi$ - $\sigma$ ) overlap state ( $7.0 \pm 0.3$  eV), C-2p <sub>$\sigma$</sub>  ( $8.8 \pm 0.3$  eV), C-2sp mixed state ( $11.4 \pm 0.4$  eV), and C-2s (13 eV). However, some researchers have reported that the peaks at  $\sim 13.25$  eV and at 11.78 eV are due to  $\sigma$  and  $\pi$  bonds arising from C=O and the O lone pair bonds, respectively.<sup>37–39,46,47</sup> Deconvoluted different parameters, viz., peak position (x), peak width ( $\Delta\omega$ ), and their intensity obtained from UPS spectra (He-II) are also tabulated in Table III.

The current–voltage (I–V) measurements were recorded at a sweeping voltage loop of 0 to +1 V and then from +1 to –1 V and then –1 to 0. The results are presented in different ways to understand the conduction mechanism of the composites. Figures 6(a) and 6(b) show the linear I–V loops, and Figs. 6(c) and 6(d) show the ln I–V loops of r-GO and r-GO-ATA-Fe<sub>2</sub>O<sub>3</sub> nanocomposites, respectively. Both r-GO and r-GO-ATA-Fe<sub>2</sub>O<sub>3</sub> nanocomposites

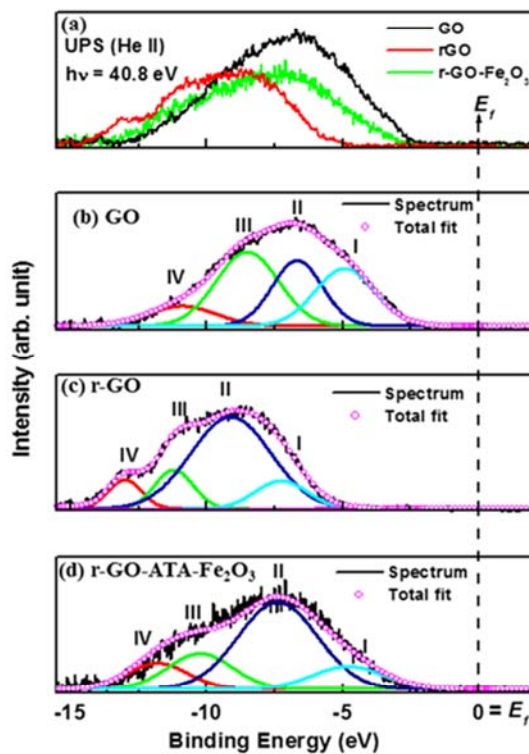


FIG. 5. (a) Ultraviolet photoemission spectroscopy (UPS) of GO, r-GO, and r-GO-ATA-Fe<sub>2</sub>O<sub>3</sub> nanocomposites. Deconvoluted into four Gaussian lines of (b) GO, (c) r-GO, and (d) r-GO-ATA-Fe<sub>2</sub>O<sub>3</sub> nanocomposites.

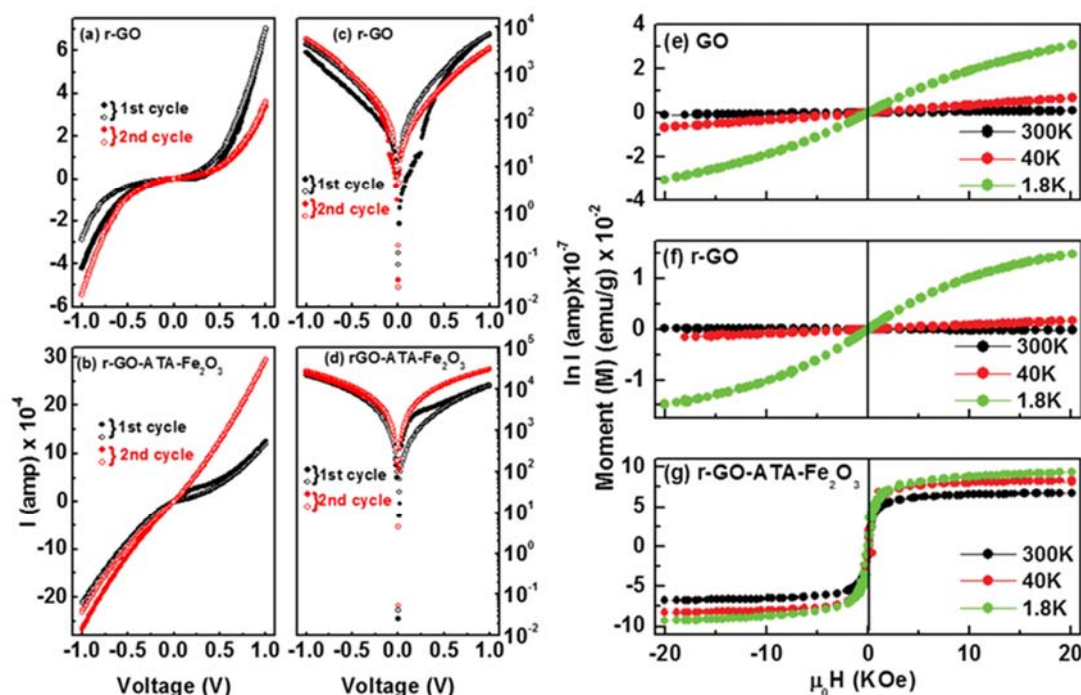


FIG. 6. Current ( $I$ )-voltage ( $V$ ) linear relationships of (a) r-GO and (b) r-GO-ATA-Fe<sub>2</sub>O<sub>3</sub> nanocomposites; log ( $I$ )- $V$  relationships of (c) r-GO and (d) r-GO-ATA-Fe<sub>2</sub>O<sub>3</sub> nanocomposites. Magnetization vs applied magnetic field at different temperature, viz., 300 K, 40 K, and 1.8 K of (e) GO, (f) r-GO, and (g) r-GO-ATA-Fe<sub>2</sub>O<sub>3</sub> nanocomposites.

show the semiconducting behaviors with r-GO-ATA-Fe<sub>2</sub>O<sub>3</sub> nanocomposites having higher conductivity. Two successive ( $I$ - $V$ ) cycle measurements show the presence of a very weak ferroelectric behavior. The semiconducting behaviors of r-GO originate from the polarization of adsorbed molecules and the defects that might be introduced in the GO sheet during the reduction process. The reduction in the conductivity of the first and second loops is attributed to the Coulomb blockade originating electron-hole recombination and electron tunneling resistance. The variation in the electrical conductivity proves the importance of tuning the relationship of conductivity and relative intra-extracellular fluid volumes in tissues of MRI applications.<sup>48,49</sup>

To correlate the electrical behavior with magnetic properties, we have measured the  $M$ - $H$  hysteresis loops of GO, r-GO, and r-GO-ATA-Fe<sub>2</sub>O<sub>3</sub> nanocomposites at the different temperature conditions, viz., 1.8 K, 40 K, and 300 K as shown in Figs. 6(e)-6(g). A slight dependence of magnetization on the field indicated a superparamagnetic behavior at 300 K. It is shown that the magnetization increases with a decrease in the measurement temperature due to the atomic spins that tend to get easily aligned at low temperature.<sup>50,51</sup> GO and r-GO nanocomposites show a weak

ferromagnetic behavior, whereas the r-GO-ATA-Fe<sub>2</sub>O<sub>3</sub> nanocomposite shows a superparamagnetic behavior. The values of saturation magnetization ( $M_s$ ) for r-GO-ATA-Fe<sub>2</sub>O<sub>3</sub> nanocomposites is  $\approx 0.68 \times 10^{-3}$  emu/g (300 K) and  $0.93 \times 10^{-3}$  emu/g (1.8 K) as tabulated in Table I. These values are smaller than that of the bulk Fe  $\approx 220$  emu/g. The value of  $M_s$  for the nanocomposites with graphene and Fe<sub>2</sub>O<sub>3</sub> contents is due to the Fe particle size and the loading of Fe<sub>2</sub>O<sub>3</sub> on the surface of graphene. Figures 1(a) and 1(b) reveals that the particle size of the naked Fe-loaded nanoparticles is similar indicating an inconsiderable effect of particle size on  $M_s$ . Thus, the value of  $M_s$  depends on the loading content of Fe nanoparticles. The quantification of Fe nanoparticles was 5 at. % that was estimated using XPS analysis and is given in Table I. Superparamagnetism makes magnetic nanoparticles to disperse easily in r-GO-ATA-Fe<sub>2</sub>O<sub>3</sub> nanocomposites as observed in the TEM image of Fig. 1(b) possessing negligible magnetic interactions between each other and avoid magnetic clustering. We have obtained the coercivity ( $H_c$ ) of r-GO-ATA-Fe<sub>2</sub>O<sub>3</sub> nanocomposites as  $\approx 11$  Oe (see Table I) and is higher than bulk Fe  $\approx 0.9$  Oe at the room temperature (300 K)<sup>51</sup> comparable with superparamagnetic behavior. The low coercivity observed in the r-GO-ATA-Fe<sub>2</sub>O<sub>3</sub>



nanocomposite signifies the characteristics of a soft magnet of SPIONs, which are a good candidate for MRI applications.<sup>52</sup> The origin of the magnetization may be attributed to the vacancies created by the hydroxyl/oxygen attached to the surface and basal plane of GO/r-GO.<sup>46</sup> The increase in the magnetization of r-GO-ATA-Fe<sub>2</sub>O<sub>3</sub> nanocomposites with respect to GO is a consequence of defect generation due to the functionalization.<sup>43</sup> The defect induced from functionalization increases the crystalline size from 8 nm (GO) to 10 nm (r-GO-ATA-Fe<sub>2</sub>O<sub>3</sub>) and decreases Raman I<sub>D</sub>/I<sub>G</sub> values 0.46 (GO) → 0.43 (r-GO-ATA-Fe<sub>2</sub>O<sub>3</sub>). This inevitably leads to the formation of new bonds (Fe—C, C—Fe, and N=C) as indicated by XPS. Superparamagnetic behavior has been reported previously in nanocomposites having a diameter range of 3–50 nm with a single domain magnetic particle.<sup>53</sup> The origin of the magnetization of r-GO-ATA-Fe<sub>2</sub>O<sub>3</sub> nanocomposites may be due to the contributions of Fe-NPs atoms' presence in Fe<sub>2</sub>O<sub>3</sub> as discussed above. Iron falls under 3d transition metals which are ferromagnetic by nature. The exchange of atoms between atoms of carbon/Fe could be the result of magnetism in r-GO-ATA-Fe<sub>2</sub>O<sub>3</sub> nanocomposites. This possibility of manipulating the superparamagnetic nanoparticles of the composites by applying a magnetic field is extremely important for applications in biological and biomedical fields, particularly for magnetic resonance imaging (MRI) applications.

#### IV. CONCLUSION

We have successfully synthesized GO, r-GO, and r-GO-ATA-Fe<sub>2</sub>O<sub>3</sub> nanocomposites through the wet chemical bottom up approach, where GsO/r-GO was functionalized with Fe<sub>2</sub>O<sub>3</sub> using 2-aminoterephthalic acid (ATA) as a capping/stabilizing agent. The electronic, structural, and bonding properties showed carbon, oxygen, and iron bonded with GO/r-GO structures. The appearance of the bonding between -O-C- and -C-O-Fe-O allows for the tuning of the electrical and magnetic properties of r-GO-ATA-Fe<sub>2</sub>O<sub>3</sub> nanocomposites. The electrical properties of r-GO were enhanced when functionalized with Fe<sub>2</sub>O<sub>3</sub> for the synthesis of r-GO-ATA-Fe<sub>2</sub>O<sub>3</sub> nanocomposites. The r-GO-ATA-Fe<sub>2</sub>O<sub>3</sub> nanocomposite shows a superparamagnetic behavior that could be useful for the contrast agent for the magnetic resonance imaging application.

#### SUPPLEMENTARY MATERIAL

See the [supplementary material](#) for FTIR spectra and details of GO, r-GO, and r-GO-ATA-Fe<sub>2</sub>O<sub>3</sub>.

#### ACKNOWLEDGMENTS

D.O.I., J.A.O., S.J.M., S.S., and S.C.R. gratefully acknowledge the financial support received from the National Research Foundation (NRF), South Africa (Grant Nos. 105292, PD-TWAS150813137166, and EQP13091742446). A.M.S. acknowledges financial assistance from SA-NRF (No. 93549) and from FRC and URC of UJ.

The authors declare no conflict of interest.

#### REFERENCES

- X. Zhou and F. Liang, "Application of graphene/graphene oxide in biomedicine and biotechnology," *Curr. Med. Chem.* **21**, 855–869 (2014).
- R. Romero-Aburto, T. N. Narayanan, Y. Nagaoka, T. Hasumura, T. M. Mitcham, T. Fukuda, P. J. Cox, R. R. Bouchar, T. Maekawa, D. S. Kumar, S. V. Torti, S. A. Mani, and P. M. Ajayan, "Fluorinated graphene oxide; a new multimodal material for biological applications," *Adv. Mater.* **25**, 5632–5637 (2013).
- O. V. Yazyev, "Emergence of magnetism in graphene materials and nanostructures," *Rep. Prog. Phys.* **73**, 056501 (2010).
- M. Stoneham, "The strange magnetism of oxides and carbons," *J. Phys. Condens. Matter* **22**, 074211 (2010).
- M. Rohrer, H. Bauer, J. Mintorovitch, M. Requardt, and H.-J. Weinmann, "Comparison of magnetic properties of MRI contrast media solutions at different magnetic field strengths," *Invest. Radiol.* **40**, 715–724 (2005).
- S. Laurent, D. Forge, M. Port, A. Roch, C. Robic, L. V. Elst, and R. N. Muller, "Magnetic iron oxide nanoparticles: Synthesis, stabilization, vectorization, physicochemical characterizations, and biological applications," *Chem. Rev.* **108**, 2064–2110 (2008).
- J. Mohapatra, A. Mitra, H. Tyagi, D. Bahadur, and M. Aslam, "Iron oxide nanorods as high-performance magnetic resonance imaging contrast agents," *Nanoscale* **7**, 9174–9184 (2015).
- J. Qin, S. Laurent, Y. S. Jo, A. Roch, M. Mikhaylova, Z. M. Bhujwalla, R. N. Muller, and M. Muhammed, "A high-performance magnetic resonance imaging T<sub>2</sub> contrast agent," *Adv. Mater.* **19**, 1874–1878 (2007).
- M. H. Levitt, *Spin Dynamics: Basics of Nuclear Magnetic Resonance*, 2nd ed. (John Wiley & Sons, 2008).
- C. Heyn, C. V. Bowen, B. K. Rutt, and P. J. Foster, "Detection threshold of single SPIO-labeled cells with FIESTA," *Magn. Reson. Med.* **53**, 312–320 (2005).
- E. Küstermann, U. Himmelreich, K. Kandal, T. Geelen, A. Ketkar, D. Wiederemann, C. Strecker, J. Esser, S. Arnhold, and M. Hoehn, "Efficient stem cell labeling for MRI studies," *Contrast Media Mol. Imaging* **3**, 27–37 (2008).
- J.-R. Jeong, S.-C. Shin, S.-J. Lee, and J.-D. Kim, "Magnetic properties of superparamagnetic  $\gamma$ -Fe<sub>2</sub>O<sub>3</sub> nanoparticles prepared by co-precipitation technique," *J. Magn. Magn. Mater.* **286**, 5–9 (2005).
- H. Ai, C. Flask, B. Weinberg, X. Shuai, M. D. Pagel, D. Farrell, J. Duerk, and J. Gao, "Magnetite-loaded polymeric micelles as ultrasensitive magnetic-resonance probes," *Adv. Mater.* **17**, 1949–1952 (2005).
- G. Liu, Z. Wang, J. Lu, C. Xia, F. Gao, Q. Gong, B. Song, X. Zhao, X. Shuai, X. Chen, H. Ai, and Z. Gu, "Low molecular weight alkyl-polycation wrapped magnetite nanoparticle clusters as MRI probes for stem cell labeling and in vivo imaging," *Biomaterials* **32**(2), 528–537 (2011).
- S. H. Yuk, K. S. Oh, S. H. Cho, B. S. Lee, S. Y. Kim, B.-K. Kwak, K. Kim, and I. C. Kwon, "Glycol chitosan/heparin immobilized iron oxide nanoparticles with a tumor-targeting characteristic for magnetic resonance imaging," *Biomacromolecules* **12**, 2335–2343 (2011).
- H. Wei, O. T. Bruns, M. G. Kaul, E. C. Hansen, M. Barch, A. Wiśniowska, O. Chen, Y. Chen, N. Li, and S. Okada, "Exceedingly small iron oxide nanoparticles as positive MRI contrast agents," *Proc. Natl. Acad. Sci. U.S.A.* **114**, 2325–2330 (2017).
- J. Park, E. Lee, N. Hwang, M. Kang, S. C. Kim, Y. Hwang, J. Park, H. Noh, J. Kim, and J. Park, "One-nanometer-scale size-controlled synthesis of monodisperse magnetic iron oxide nanoparticles," *Angew. Chemie Int. Ed. Engl.* **44**, 2872–2877 (2005).
- H.-P. Cong, J.-J. He, Y. Lu, and S.-H. Yu, "Water-soluble magnetic-functionalized reduced graphene oxide sheets: In situ synthesis and magnetic resonance imaging applications," *Small* **6**, 169–173 (2010).
- W. Chen, P. Yi, Y. Zhang, L. Zhang, Z. Deng, and Z. Zhang, "Composites of aminodextran-coated Fe<sub>3</sub>O<sub>4</sub> nanoparticles and graphene oxide for cellular magnetic resonance imaging," *ACS Appl. Mater. Interfaces* **3**, 4085–4091 (2011).
- G. Wang, G. Chen, Z. Wei, X. Dong, and M. Qi, "Multifunctional Fe<sub>3</sub>O<sub>4</sub>/graphene oxide nanocomposites for magnetic resonance imaging and drug delivery," *Mater. Chem. Phys.* **141**, 997–1004 (2013).

- <sup>21</sup>B. Ghosh, S. Sarma, M. Pontsho, and S. C. Ray, "Tuning of magnetic behaviour in nitrogenated graphene oxide functionalized with iron oxide," *Diam. Relat. Mater.* **89**, 35–42 (2018).
- <sup>22</sup>G. Kandasamy, S. Surendran, A. Chakrabarty, S. N. Kale, and D. Maity, "Facile synthesis of novel hydrophilic and carboxyl-amine functionalized superparamagnetic iron oxide nanoparticles for biomedical applications," *RSC Adv.* **6**, 99948–99959 (2016).
- <sup>23</sup>G. Bhattacharya, G. Kandasamy, N. Soin, R. K. Upadhyay, S. Deshmukh, D. Maity, J. McLaughlin, and S. S. Roy, "Novel  $\pi$ -conjugated iron oxide/reduced graphene oxide nanocomposites for high performance electrochemical supercapacitors," *RSC Adv.* **7**, 327–335 (2017).
- <sup>24</sup>S. J. Iyengar, M. Joy, C. K. Ghosh, S. Dey, R. K. Kotnala, and S. Ghosh, "Magnetic, x-ray and Mössbauer studies on magnetite/maghemite core-shell nanostructures fabricated through an aqueous route," *RSC Adv.* **4**, 64919–64929 (2014).
- <sup>25</sup>A. C. Ferrari and D. M. Basko, "Raman spectroscopy as a versatile tool for studying the properties of graphene," *Nat. Nanotechnol.* **8**, 235–246 (2013).
- <sup>26</sup>D. J. Wilson, N. P. Rhodes, and R. L. Williams, "Surface modification of a segmented polyetherurethane using a low-powered gas plasma and its influence on the activation of the coagulation system," *Biomaterials* **24**, 5069–5081 (2003).
- <sup>27</sup>D. C. Marcano, D. V. Kosynkin, J. M. Berlin, A. Sinitskii, Z. Sun, A. Slesarev, L. B. Alemany, W. Lu, and J. M. Tour, "Improved synthesis of graphene oxide," *ACS Nano* **4**, 4806–4814 (2010).
- <sup>28</sup>S. Stankovich, D. A. Dikin, R. D. Piner, K. A. Kohlhaas, A. Kleinhammes, Y. Jia, Y. Wu, S. T. Nguyen, and R. S. Ruoff, "Synthesis of graphene-based nanosheets via chemical reduction of exfoliated graphite oxide," *Carbon* **45**, 1558–1565 (2007).
- <sup>29</sup>F. M. F. de Groot, M. Groni, J. C. Fuggle, J. Ghijsen, G. A. Sawatzky, and H. Petersen, "Oxygen 1s x-ray-absorption edges of transition-metal oxides," *Phys. Rev. B* **40**, 5715–5723 (1989).
- <sup>30</sup>M. Pollak, M. Gautier, N. Thomat, S. Gota, W. C. Mackrodt, and V. R. Saunders, "An in-situ study of the surfaces phase transitions of  $\alpha$ -Fe<sub>2</sub>O<sub>3</sub> by x-ray absorption spectroscopy at the oxygen K-edge," *Nucl. Instr. Meth. Phys. Res. B* **97**, 383–386 (1995).
- <sup>31</sup>J. Lu, X. Jiao, D. Chen, and W. Li, "Solvothermal synthesis and characterization of Fe<sub>3</sub>O<sub>4</sub> and  $\gamma$ -Fe<sub>2</sub>O<sub>3</sub> nanoplates," *J. Phys. Chem. C* **113**, 4012–4017 (2009).
- <sup>32</sup>T. Fujii, F. M. F. de Groot, G. A. Sawatzky, F. C. Voegt, T. Hibma, and K. Okada, "In situ XPS analysis of various iron oxide films grown by NO<sub>2</sub>-assisted molecular-beam epitaxy," *Phys. Rev. B* **59**, 3195–3202 (1999).
- <sup>33</sup>A. Furlan, U. Jansson, J. Lu, L. Hultman, and M. Magnuson, "Structure and bonding in amorphous iron carbide thin films," *J. Phys. Condens. Matter* **27**, 045002 (2015).
- <sup>34</sup>M. Magnuson, M. Andersson, J. Lu, L. Hultman, and U. Jansson, "Electronic structure and chemical bonding of amorphous chromium carbide thin films," *J. Phys. Condens. Matter* **24**, 225004 (2012).
- <sup>35</sup>J. Schwan, S. Ulrich, V. Batori, H. Ehrhardt, and S. R. P. Silva, "Raman spectroscopy on amorphous carbon films," *J. Appl. Phys.* **80**, 440–447 (1996).
- <sup>36</sup>M. Magnuson, O. Wilhelmsson, J.-P. Palmquist, U. Jansson, M. Mattesini, S. Li, R. Ahuja, and O. Eriksson, "Electronic structure and chemical bonding in Ti<sub>2</sub>AlC investigated by soft x-ray emission spectroscopy," *Phys. Rev. B* **74**, 195108 (2006).
- <sup>37</sup>S. C. Ray, C. W. Pao, J. W. Chiou, H. M. Tsai, J. C. Jan, W. F. Pong, R. McCann, S. S. Roy, P. Papakonstantinou, and J. A. McLaughlin, *J. Appl. Phys.* **98**, 033708 (2005).
- <sup>38</sup>S. C. Ray, C. W. Pao, H. M. Tsai, J. W. Chiou, W. F. Pong, M. H. Tsai, T. I. T. Okpalugo, P. Papakonstantinou, and T. W. Pi, "Enhancement of sp<sup>3</sup>-bonding in high-bias-voltage grown diamond-like carbon thin films studied by x-ray absorption and photoemission spectroscopy," *J. Phys. Condens. Matter* **19**, 176204 (2007).
- <sup>39</sup>S. C. Ray, C. W. Pao, H. M. Tsai, B. Bose, J. W. Chiou, W. F. Pong, and D. DasGupta, "Orientation of graphitic planes during annealing of "dip deposited" amorphous carbon film: A carbon K-edge X-ray absorption near-edge study," *Carbon* **44**, 1982–1985 (2006).
- <sup>40</sup>L. Q. Xu, W. J. Yang, K.-G. Neoh, E.-T. Kang, and G. D. Fu, "Dopamine-induced reduction and functionalization of graphene oxide nanosheets," *Macromolecules* **43**, 8336–8339 (2010).
- <sup>41</sup>Z. Yang, T. Zhao, X. Huang, X. Chu, T. Tang, Y. Ju, Q. Wang, Y. Hou, and S. Gao, "Modulating the phases of iron carbide nanoparticles: From a perspective of interfering with the carbon penetration of Fe@Fe<sub>3</sub>O<sub>4</sub> by selectively adsorbed halide ions," *Chem. Sci.* **8**, 473–481 (2017).
- <sup>42</sup>A. Bianconi, S. B. M. Hagström, and R. Z. Bachrach, "Photoemission studies of graphite high-energy conduction-band and valence-band states using soft-x-ray synchrotron radiation excitation," *Phys. Rev. B* **16**, 5543–5548 (1977).
- <sup>43</sup>O. V. Yazyev and L. Helm, "Defect-induced magnetism in graphene," *Phys. Rev. B* **75**, 125408 (2007).
- <sup>44</sup>S. Sarma, S. C. Ray, and A. M. Strydom, "Electronic and magnetic properties of nitrogen functionalized graphene-oxide," *Diam. Relat. Mater.* **79**, 1–6 (2017).
- <sup>45</sup>S. Gabriel, R. W. Lau, and C. Gabriel, "The dielectric properties of biological tissues: III. Parametric models for the dielectric spectrum of tissues," *Phys. Med. Biol.* **41**, 2271 (1996).
- <sup>46</sup>G. Goncalves, P. A. A. P. Marques, C. M. Granadeiro, H. I. S. Nogueira, M. K. Singh, and J. Grácio, "Surface modification of graphene nanosheets with gold nanoparticles: The role of oxygen moieties at graphene surface on gold nucleation and growth," *Chem. Mater.* **21**, 4796–4802 (2009).
- <sup>47</sup>D. S. Sutar, G. Singh, and V. Divakar Botcha, "Electronic structure of graphene oxide and reduced graphene oxide monolayers," *Appl. Phys. Lett.* **101**, 103103 (2012).
- <sup>48</sup>X. Zhang, J. Liu, and B. He, "Magnetic-resonance-based electrical properties tomography: A review," *IEEE Rev. Biomed. Eng.* **7**, 87–96 (2014).
- <sup>49</sup>I. Carmeli, V. Skakalova, R. Naaman, and Z. Vager, "Magnetization of chiral monolayers of polypeptide: A possible source of magnetism in some biological membranes," *Angew. Chemie Int. Ed. Engl.* **41**, 761–764 (2002).
- <sup>50</sup>T. Tang, F. Liu, Y. Liu, X. Li, Q. Xu, Q. Feng, N. Tang, and Y. Du, "Identifying the magnetic properties of graphene oxide," *Appl. Phys. Lett.* **104**, 123104 (2014).
- <sup>51</sup>C. J. Cong, L. Liao, Q. Y. Liu, J. C. Li, and K. L. Zhang, "Effects of temperature on the ferromagnetism of Mn-doped ZnO nanoparticles and Mn-related Raman vibration," *Nanotechnology* **17**, 1520–1526 (2006).
- <sup>52</sup>S. Abdelbasir, A. E. Shalan, "Intriguing properties and applications of functional magnetic materials," in *Functional Materials* (IntechOpen, 2019).
- <sup>53</sup>R. M. Bozorth, *Ferromagnetism* (D. Van Nostrand Company Inc., New York, 1951), Chap. XII.

## Appendix 5

## ARTICLE IN PRESS

Materials Today: Proceedings xxx (xxxx) xxx



Contents lists available at ScienceDirect

## Materials Today: Proceedings

journal homepage: [www.elsevier.com/locate/matpr](http://www.elsevier.com/locate/matpr)Magnetic properties of graphene oxide functionalized with “Au” and “Fe<sub>2</sub>O<sub>3</sub>” nanoparticles: A comparative study

David O. Idisi, James A. Oke, Evan M. Benecha, Sabato J. Moloi, Sekhar C. Ray\*

Department of Physics, CSET, University of South Africa, Private Bag X6, Florida, 1710, Science Campus, Christiaan de Wet and Pioneer Avenue, Florida Park, Johannesburg, South Africa

## ARTICLE INFO

## Article history:

Received 25 January 2020  
Accepted 24 February 2020  
Available online xxxx

## Keywords:

r-GO  
r-GO: Au-NPs  
r-GO-Fe<sub>2</sub>O<sub>3</sub>  
DFT  
DOS

## ABSTRACT

Reduced graphene oxide (r-GO) nanocomposites are very useful for different applications such as magnetic storage media and bio-imaging/medical applications and recently have been found to be very useful in electronic and magnetic resonance imaging contrast agent where r-GO was functionalized with silica coated gold and iron oxide nanoparticles. The potential material for these different applications was established by experimental data where the microstructural, electronic, electrical and magnetic properties were studied. In the present study, we have compared the electronic and magnetic properties of these nanocomposites (r-GO: Au NPs & r-GO: Fe<sub>2</sub>O<sub>3</sub> NPs) using different experimental data. The data is verified with density functional theory (DFT) calculations to elucidate the relationship between the density of state (DOS) and their magnetic properties. Coupled with the experimental data, the DFT studies revealed that the magnetization enhancement of rGO: Au-NPs is mainly due to the nano-sized clusters with addition of Au 3d and O 2p orbital states as contributors; whereas that of r-GO: Fe<sub>2</sub>O<sub>3</sub> NPs is mainly due to Fe 2p, Fe 3d and O 2p orbital states as contributors.

© 2020 Elsevier Ltd. All rights reserved.

Selection and peer-review under responsibility of the scientific committee of the Third International Conference on Advanced Energy Materials.

## 1. Introduction

There has been an upward surge in graphene research owing to the potential application it offers. Graphene oxide (GO)/reduced graphene oxide (r-GO) as an alternative and derivative of pristine graphene has found application in various areas of science and technology such as biomedicine, optoelectronics, energy conversion etc. [1–3]. The tuning of the electronic properties of GO is essential for the modification of the electronic structure of zero-band gap of pristine graphene [4]. The zero-band gap of pristine graphene is a draw back for being used for electronic devices. One of the ways to modify the electronic structure and magnetic behavior of GO/r-GO is through covalent and non-covalent functionalization with metals [5].

Au and Fe have been found to be promising metals to functionalize GO/r-GO. Li et al. [6] explored r-GO: Au-NPs for supercapacitor applications where femto-laser writing technique was used. Huang et al. [7] controlled the size of Au and GO/r-GO for surface enhanced Raman scattering and catalytic activities. The

impact by Au atoms in the GO/r-GO matrix can cause a catalyst effect, leading to electronic perturbations in the composite. The catalytic process is attributed to electron-transfer between graphene-gold interactions. Zhengshan et al. [8] found that the electromagnetic (EM) absorption of the nanocomposites was enhanced after  $\alpha$ -Fe<sub>2</sub>O<sub>3</sub> nanocrystal was functionalized with GO. The enhanced EM absorption was attributed to the well-dispersed Fe<sub>2</sub>O<sub>3</sub> over r-GO. Zhang et al. [9] used  $\alpha$ -Fe<sub>2</sub>O<sub>3</sub>/r-GO nanocomposite for detection and removal of organic pollutant. The report of Zhang et al. showed the surface area of r-GO was enhanced when functionalized with  $\alpha$ -Fe<sub>2</sub>O<sub>3</sub> nanoparticles.

The mechanism of Au and Fe adsorption on GO/r-GO which are responsible for the enhanced properties can be attributed to the sites occupied by the introduced atoms in the carbon matrix [10]. The adsorbed atoms cannot be easily probed with experimental techniques. Although the sensitivity of spectroscopic probes can analyze data point, however, the site location of atoms especially for r-GO matrix cannot be easily accounted for. It is with this reason that theoretical studies on r-GO composite is essential in order to fully understand the effect of metals on the properties of the rGO composite. The studies would lead to understanding of charge distribution and absorption of Au and Fe on rGO matrix.

\* Corresponding author.

E-mail address: [Raysc@unisa.ac.za](mailto:Raysc@unisa.ac.za) (S.C. Ray).<https://doi.org/10.1016/j.matpr.2020.02.869>

2214-7853/© 2020 Elsevier Ltd. All rights reserved.

Selection and peer-review under responsibility of the scientific committee of the Third International Conference on Advanced Energy Materials.

Please cite this article as: D. O. Idisi, J. A. Oke, E. M. Benecha et al., Magnetic properties of graphene oxide functionalized with “Au” and “Fe<sub>2</sub>O<sub>3</sub>” nanoparticles: A comparative study, Materials Today: Proceedings, <https://doi.org/10.1016/j.matpr.2020.02.869>

The density functional theory (DFT) has been explored to understand the adsorption and electronic properties of carbon related materials. Xiaoxing et al. [11] studied experimentally the sensing capability of Au modified graphene for  $H_2S$  and  $SO_2$  gas. Afterwards, DFT was used to interpret the interaction between the gases and the surface of Au-modified graphene. Their density of state (DOS) and Mulliken population findings showed that there is a charge transfer between "Au" and graphene with van der Waals effect dominating the adsorption in graphene. Yunfang et al. [12] explored the interaction between graphene sheet and Fe-nanowires using molecular dynamic DFT calculations. A relative orientation between the Fe-nanowires and the graphene sheet was observed to have significant impact on the self-scrolling of the sheets. In all these studies, very less attention has been devoted to the impact of "Au" and "Fe" adsorption on graphene as it pertains to its magnetic behavior. Hence, theoretical studies is essential for clarity on the adsorptive behaviour of the rGO composite.

Our recent experimental studies [14,16] on the electronic and magnetic properties of GO/r-GO functionalized with "Au-NP" and "Fe<sub>2</sub>O<sub>3</sub>-NPs" showed a relationship between the DOS and their magnetic behaviors. Our results showed an enhancement of magnetization and the material potential for the device to be used for dielectric charge storage and magnetic resonance imaging contrast agent. In this present study, we have compared the effect of the electronic structure of Au and Fe<sub>2</sub>O<sub>3</sub>-NPs on the magnetic properties of rGO using DFT calculations to probe the relationship between the DOS and the magnetization. Additionally, the results of the partial density of state (PDOS) showed that O 2p, Au 3d and Fe 3d are additional contributors to the magnetization of the composites.

## 2. Experimental details

The GO was synthesized using the modified Hummer's method as previously reported in our work [13]. The obtained GO was chemically reduced using ammonia hydroxide (NH<sub>4</sub>OH) and separated into three parts for functionalization purposes. The obtained

r-GO was functionalized with silica coated Au-NPs. The silica coating of the Au-NPs allows easy branching of the Au clusters and attachment on r-GO [14]. The Fe<sub>2</sub>O<sub>3</sub> NPs was initially prepared using co-precipitation method [15]. Then Fe<sub>2</sub>O<sub>3</sub> NPs was capped with 2-aminoterephthalic acid for stabilization. The other part of r-GO was functionalized with the ATA-Fe<sub>2</sub>O<sub>3</sub>. The prepared r-GO, r-GO: Au-NP and r-GO: Fe<sub>2</sub>O<sub>3</sub> NPs are used for this present study. Details of the experimental procedures are given in our previous reports [14,16] and characterization techniques employed in the samples.

## 3. Theoretical calculations

The electronic and magnetic properties of r-GO, r-GO: Au-NP and r-GO: Fe<sub>2</sub>O<sub>3</sub> were explored using plane wave pseudopotential density functional theory calculation using the CASTEP [16] code. The r-GO is assumed to possess epoxide and hydroxyl groups, so graphene structure was constructed to include both C=O and C-OH as shown in later section. Full geometry optimization of the r-GO structure was carried out using a  $5 \times 5 \times 1$  supercell constructed from graphite ceramic crystal as proposed by the formalism of Moon et al. [17]. The Vanderbilt ultrasoft pseudopotentials [18] and the general gradient approximations (GGA) [19] of Perdew-Burke-Ernzenhof (PBE) were used for the estimation of core-level electron interactions and in-situ Coulomb interactions respectively, while optimization was carried out using  $5 \times 5 \times 1$  Monkhorst-Pack k-grid points and a plane wave cut-off energy of 600 eV.

## 4. Results and discussions

The morphology of r-GO, r-GO: Au-NP and r-GO: Fe<sub>2</sub>O<sub>3</sub>-NPs as indicated by scanning electron microscopy and energy dispersion X ray spectroscopy (EDX) are shown in Fig. 1(a)-(f). The sheets of r-GO exhibit flake-like structure which is consistent with thermally exfoliated GO/r-GO as previously reported [20]. The effect of functionalizing r-GO with Au-NP gives a change in the shape

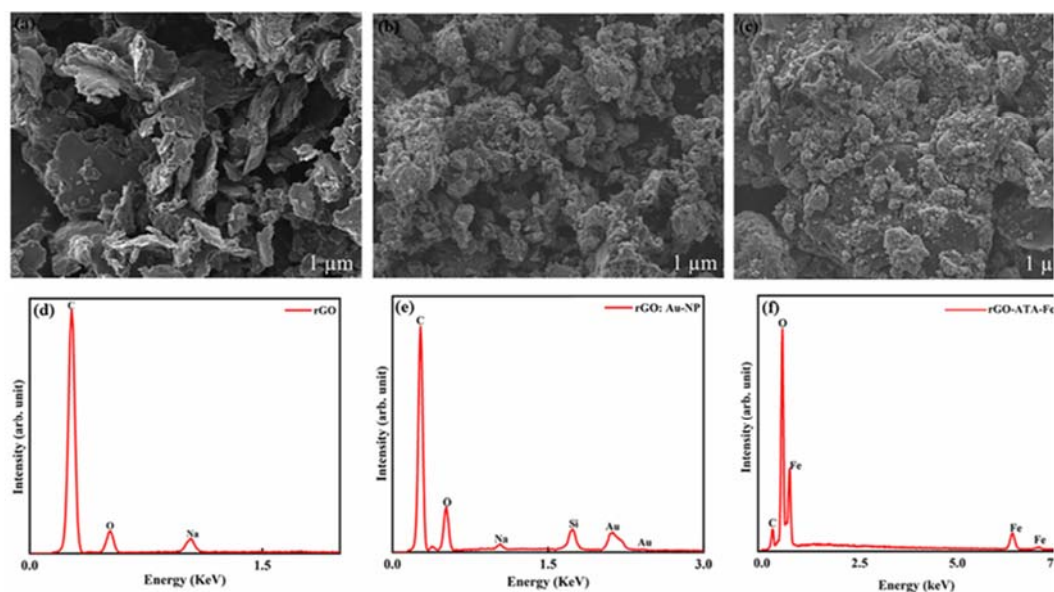


Fig. 1. Surface morphology scanning electron microscopy images of (a) r-GO, (b) r-GO: Au-NPs, (c) r-GO: Fe<sub>2</sub>O<sub>3</sub>; (d)-(f) EDX spectra of r-GO, r-GO: Au-NPs and r-GO: Fe<sub>2</sub>O<sub>3</sub>.

Please cite this article as: D. O. Idisi, J. A. Oke, E. M. Benecha et al., Magnetic properties of graphene oxide functionalized with "Au" and "Fe<sub>2</sub>O<sub>3</sub>" nanoparticles: A comparative study, Materials Today: Proceedings, <https://doi.org/10.1016/j.matpr.2020.02.869>

of the sheets as shown in Fig. 1(b). The r-GO: Au-NPs composite gives a cluster like features indicating the attachment of Au atoms on the surface of r-GO. The case of r-GO functionalization with Fe<sub>2</sub>O<sub>3</sub> gives granular clusters indicated possible agglomeration. The EDX spectra shown in Fig. 1(d)–(f) gives the composition of the composite. The observed Na and Si peaks indicate impurities from the residue of the reduction procedure and silicon wafer that was used for the SEM measurements respectively.

The transmission electron microscopy (TEM) images crystalline structures of r-GO, r-GO: Au-NP and r-GO: Fe<sub>2</sub>O<sub>3</sub>-NPs are shown in Fig. 2(a–c), respectively. A non-homogeneous dispersion of the particles is observed in most part of the particle distribution for r-GO and r-GO: Au-NP. This may be due to clustering of the particles and the nature of Au-attachment to the edge of r-GO. Based on the effect of the clustering, the estimation of particles sizes is impossible. However, weak agglomeration is also observed in the case of r-GO: Fe<sub>2</sub>O<sub>3</sub>-NPs with significant homogeneous dispersion of the particles where the size is estimated to be ≈10 nm. Fig. 2 (d) shows the XRD pattern of r-GO, r-GO: Au-NP and r-GO: Fe<sub>2</sub>O<sub>3</sub>-NP. The relevant peaks for r-GO and r-GO: Au-NP matches with JCPDS-PDF card No. 01-1172. For r-GO, the peak at  $2\theta \approx 26.2^\circ$  is associated with the (002) reflection plane [21]. The peaks for r-GO: Au-NP includes  $2\theta \approx 54.5^\circ$  and  $2\theta \approx 56.2^\circ$ , which are assigned to (420), and (511) reflective planes respectively [22]. The XRD pattern confirms the formation of the r-GO: Au-NP composite, which is a consequence of the FCC phase, exhibited by Au-atoms. In the case of r-GO: Fe<sub>2</sub>O<sub>3</sub>, two distinct peaks at  $2\theta \approx 43.2^\circ$  and  $2\theta \approx 50.3^\circ$  observed are assigned to the reflective planes of (4 0 0) and (4 2 2), respectively. Consequently, the r-GO: Fe<sub>2</sub>O<sub>3</sub> composite can be associated to the spinel phase exhibited by Fe<sub>3</sub>O<sub>4</sub>. Using the Scherrer equation, the crystalline size of r-GO and the composites were estimated to be in the range of ≈10–15 nm. The crystalline sizes are consistent with the range obtained from TEM images.

The core level Au 4f and Fe 2p x-ray photoelectron spectroscopy (XPS) are shown in Fig. 2(e) and (f) respectively; where core level doublet state with the degenerate features of Au 4f and Fe 2p are clearly observed. The binding energies of Au 4f and Fe 2p bands are influenced by the oxidation state of Au and Fe respectively. The Au 4f<sub>5/2</sub> and Au 4f<sub>7/2</sub> doublet state suggest the transition state of Au (0) (~84.6 eV) and Au (1) (~88.5 eV) of Au thiolate [23], suggesting the coexistence of Au (0) and Au (I) in both Au-NCs. How-

ever, upon composites with r-GO, the BE of both Au 4f<sub>5/2</sub> and Au 4f<sub>7/2</sub> doublet shifts towards higher values. Fig. 2(f) shows the binding energy for Fe 2p<sub>3/2</sub> peak at ~709.6 eV and at ~722.6 eV for Fe 2p<sub>1/2</sub> peak are found in 2p core level with the satellite structure. The Fe 2p<sub>3/2</sub> peak at ~709.6 eV is higher than Fe-metal (706.7 eV) and lower than Fe<sub>2</sub>O<sub>3</sub> (710.8 eV) indicating the formation of r-GO: Fe<sub>2</sub>O<sub>3</sub> nanocomposites.

The C 1s and O 1s core level XPS spectra for r-GO, r-GO: Au-NP and r-GO: Fe<sub>2</sub>O<sub>3</sub> are shown in Fig. 3(a–h). The C 1s spectra of r-GO: Au-NP and r-GO: Fe<sub>2</sub>O<sub>3</sub> have shifted to higher energy levels. The shift to higher binding energy implies energy transfers between the Au and Fe atoms to r-GO clusters. The C 1s and O 1s spectra are deconvoluted into four and three peaks respectively using Gaussian function. The peak indicated at ~284.8 eV is attributed to sp<sup>2</sup> C=C cluster, the peak arising at ~286.0 eV is assigned to O-H/O-C-O and 287.3 eV is attributed to O=C=O bonds [24,25]. The impact of Au-functionalization gives an additional peak with a slight shift in the peak position of the r-GO peaks. The peak at 283.7 eV can be attributed to C-Au bond that is mainly due to the weak attachment of Au atoms to carbon atoms [26]. Other peaks shifted slightly to higher binding energies: 284.4 → 285.4 eV (peak II), 286 → 286.3 eV (peak III) and 287.3 → 287.7 eV (peak IV). The impact of GO functionalization with Fe gives a significant shift in the peak positions with formation of new bonds. The peaks occurring at ~282.4 eV and ~282.8 eV are assigned to Fe-C and C-Fe, respectively. The peaks at ~284.5 eV and ~286 eV are attributed to sp<sup>2</sup> C-C and epoxy groups respectively [27,28]. The O 1s peak position of r-GO, 531.9 ± 1, 533.0 and 534.1 eV are assigned to C=O, C-O and C-OOH respectively [29]. The impact of Au and Fe leads to a shift in the peak positions of r-GO. Presumably, the peak shift is mainly attributed to energy transfer between GO and Au-Fe atoms. The energy transfer can be seen as chemical shift and are associated with electronegativity [30]. The relationship between the degree of oxidation in GO and electronegativity has been previously reported [31]. In this case, the impact of Au and Fe on GO functionalization leads to an increase in oxidation due to oxygen vacancies, which causes an increase in the electronegative functional groups. These defected electronegative functional groups are responsible for the shift in the observed XPS spectra.

Defect induced magnetization has enormous dependence on the DOS of the mobile electrons. These mobile electrons are responsible for the generation of the magnetic moment of r-GO [32]. The ultra-violet spectroscopy (UPS) He II (hν = 40.8 eV) enables the probing of the valence band state which clarifies the DOS of the nanocomposites. Fig. 3(i–j) gives the valence band photoelectron spectroscopic of r-GO, r-GO: Au-NP and r-GO: Fe<sub>2</sub>O<sub>3</sub> nanocomposites. The deconvoluted Gaussian peaks ~10.8 eV (peak I), ~8.6 eV (peak II), ~7.2 eV (peak III) and ~6.3 eV (peak IV) are assigned to 2s, 2sp mixed state, 2p<sub>π</sub> and 2π<sub>σ</sub> overlap state respectively. The impact of Au and Fe functionalization leads to shift in the peak position. In the case of r-GO: Au-NP, these peaks are shifted as: ~10.8 → 11.4 eV, ~8.6 → 9.7 eV, ~7.2 → 7.6 eV and ~6.3 → 5.9 eV respectively [33]. The shift to higher binding energies signifies an increase in the DOS. The increased DOS indicates a recovery of the carbon network in r-GO. The carbon network recovery can be attributed to the weak Au-attachment onto r-GO [34,35]. The carbon network recovery also implies the insignificance of oxygen moieties in the control of the band structure of r-GO. The effect of Fe functionalization gives an opposite shift in the peak positions of r-GO. These shifts are ~10.8 → 11.4 → 11.1 eV, ~8.62 → 9.7 → 9.2 eV, ~7.2 → 7.6 → 7.3 eV and ~6.3 → 5.9 → 5.6 eV). The downward shift in the peak positions signifies a decrease in the DOS of r-GO [36]. Presumably, there is a reduction in the sp<sup>2</sup> C-C network with formation of sp<sup>3</sup> C-C clusters for both nanocomposites. This observation is consistent with newly

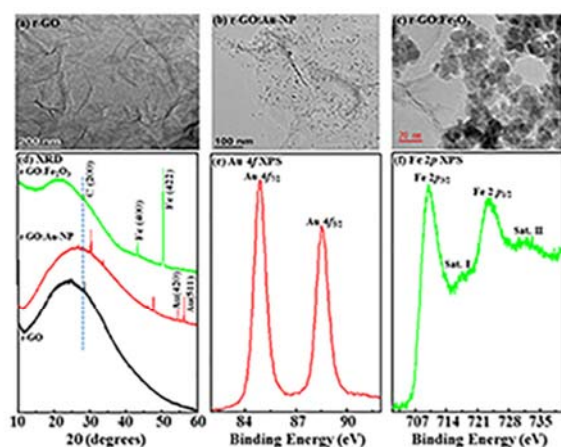


Fig. 2. Surface morphology transmission electron microscopy images of (a) r-GO, (b) r-GO: Au-NPs, (c) r-GO: Fe<sub>2</sub>O<sub>3</sub>; (d) XRD of r-GO, r-GO: Au-NPs and r-GO: Fe<sub>2</sub>O<sub>3</sub>; X ray photoelectron spectroscopy of (e) Au 4f and (f) Fe 2p.

## ARTICLE IN PRESS

4

D.O. Idisi et al./Materials Today: Proceedings xxx (xxxx) xxx

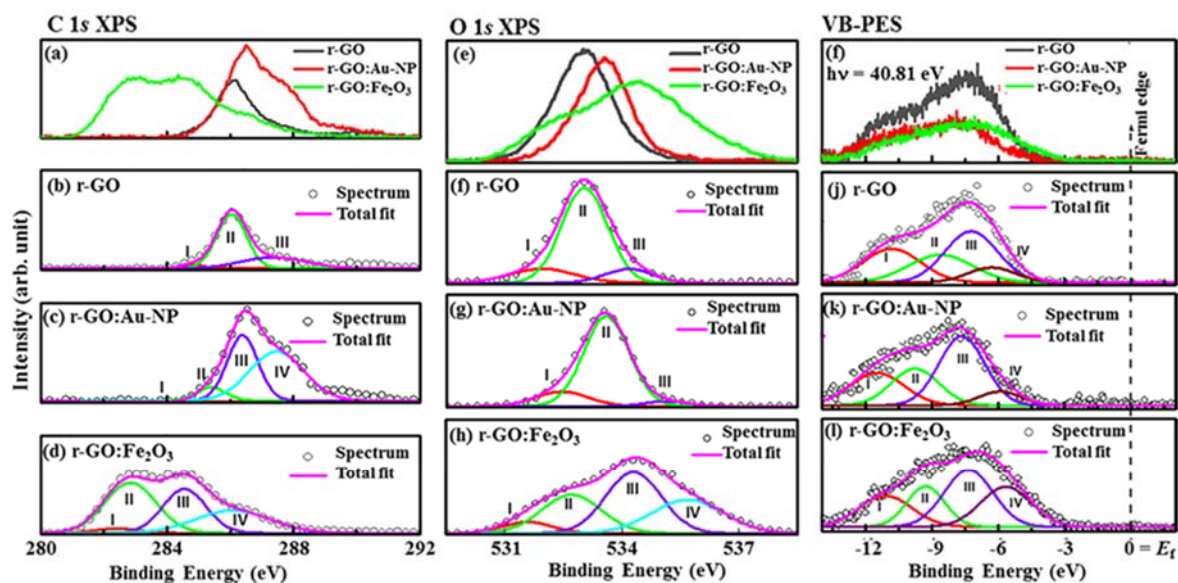


Fig. 3. X ray photoelectron spectroscopy of r-GO, r-GO: Au-NPs and r-GO:Fe<sub>2</sub>O<sub>3</sub> nanocomposites (a) C 1s and their deconvolution into different Gaussian lines (b-d); (e) O 1s and their deconvolution into different Gaussian lines (f-h); (i) Valence band photoemission spectroscopy and their deconvolution into different Gaussian lines (j-l).

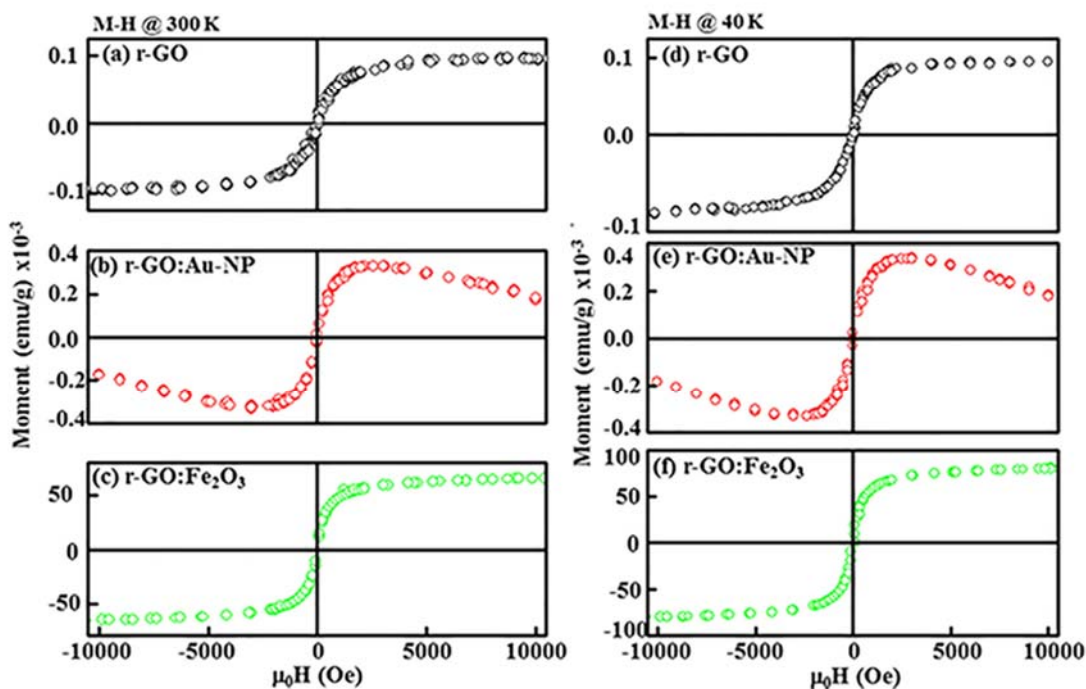


Fig. 4. M-H hysteresis loops of r-GO, r-GO: Au-NPs and r-GO: Fe<sub>2</sub>O<sub>3</sub> nanocomposites (a-c) Room temperature (300 K) and (d-f) Low temperature (40 K).

formed C-Fe and Fe-C bonds that was revealed in the C 1s spectra of XPS.

Fig. 4 (a-f) shows the M-H loop for r-GO, r-GO: Au-NP and r-GO: Fe<sub>2</sub>O<sub>3</sub> NP at room temperature (300 K) and low temperature (40 K). The weak coercivity and negligible remanence implies superparamagnetic properties which is a consequence of the particle size

being <50 nm. The main distinction is the improved magnetism with respect to r-GO. As observed, the saturation magnetization (Ms) of r-GO: Au-NP  $\sim 3 \times 10^{-4}$  (emu/g) is about three times of the magnetization of r-GO. The improved magnetization can be attributed to the defects induced by the C-Au bond as observed in XPS. Bulk Au is considered diamagnetic in nature however,

Please cite this article as: D. O. Idisi, J. A. Oke, E. M. Benecha et al., Magnetic properties of graphene oxide functionalized with "Au" and "Fe<sub>2</sub>O<sub>3</sub>" nanoparticles: A comparative study, Materials Today: Proceedings, <https://doi.org/10.1016/j.matpr.2020.02.869>

## ARTICLE IN PRESS

D.O. Idisi et al./Materials Today: Proceedings xxx (xxxx) xxx

5

recent reports have indicated a possible reorientation of the atomic spins when the size of Au particles are miniaturized [37,38]. The interaction of the miniaturized reoriented Au spins (diamagnetism  $\rightarrow$  ferromagnetism) with the carbon network enhances  $sp^3$  clusters which could be the reason for the enhanced magnetization. The impact of low temperature does not impair the magnetization of both r-GO and r-GO:Au-NP implying the electrons responsible for the magnetic moment are not affected by the temperature. In the case of r-GO:  $Fe_2O_3$ , more improvement in the magnetization of r-GO with  $M_s \sim 6.7 \times 10^{-2}$  emu/g is observed. The improvement can be attributed to the increased  $sp^3$  C-C clusters from the new defects of the C-Fe and Fe-C bonds. The attachment of Fe to carbon atoms is stronger in comparison to the weak attachment of Au atoms to the carbon network [39]. The enhancement of r-GO:  $Fe_2O_3$  is consistent with previously reported data [40], where the magnetization improvement was explained in terms of transition of  $Fe^{2+} \rightarrow Fe^{3+}$  states.

To further elucidate the relationship between DOS and the magnetization enhancement in r-GO nanocomposites, first principles DFT calculations were performed using a  $5 \times 5 \times 1$  supercell model proposed by Moon et al. [17]. The concentration of Au and Fe-O as indicated in the experimental results were considered accordingly. The DFT calculations did not consider possibility of experimentally obtained defect inhomogeneity such as dopant aggregation or simultaneous interstitial and edge site occupancy. The Au and Fe-O atoms were maintained at either the edge or interstitial sites in the r-GO lattice, as illustrated in Fig. 5(b-f). The different atomic lattice site configuration locations were considered in order to ascertain preferred sites for optimum magnetization. The calculated magnetization for r-GO was  $1.95 \mu_B$  whereas with the inclusion of Au in the edge site, the magnetization decreases to  $1.56 \mu_B$ . This magnetic reduction behavior can be attributed to the weak attachment of the C-Au bond [41] resulting from structural geometry relaxation. At the edge site the C-Au bond stretches by  $0.6 \text{ \AA}$  in comparison with C-C ( $1.41 \rightarrow 2.01 \text{ \AA}$ ), while at the interstitial site, the C-Au bond length reduces marginally ( $2.05 \rightarrow 2.01 \text{ \AA}$ ) which is consistent with our previous report [13].

An interesting observation is the slight decrease of the magnetization when the Au atoms are located interstitially, compared to the edge site ( $1.56 \mu_B \rightarrow 1.41 \mu_B$ ). The decrease in magnetization implies that interstitial site is not favorable for C-Au bond in terms of magnetization. Recent reports suggest Au atoms are better adsorbed at the edge of graphene [40], which could be the reason for the magnetization being slightly higher at the edge in comparison with interstitial site location. The contributions of O 2p as shown in Fig. 5(c) are less significant in comparison with Au 3d; however, the O-2p defects are attributed to the oxygen vacancies in r-GO [42].

In correlation with the experimental results, the magnetization of r-GO: Au-NP is greater than pristine r-GO. Based on this incoherence between the magnetization of the theoretical and experimental results, we hypothesize that the enhanced magnetization in the experimental result implies the dependence of magnetization of r-GO: Au composite on the cluster size and not necessary on the C-Au bonds interactions. Since the diamagnetic Au spins reorientate when the particle size is reduced [38], there is a possibility of exchange interaction between C, O and Au magnetic moments thereby leading to the enhanced magnetization as indicated in the experimental data.

A decrease in magnetization for rGO-Fe-O is observed for Fe atoms in the edge site of the r-GO lattice with a low magnetization of  $\sim 0.47 \mu_B$  in comparison with rGO ( $1.95 \mu_B$ ). The low magnetization of r-GO: Fe-O composites may be attributed to weak exchange interaction between C and Fe magnetic moment due to non-easy magnetization site of Fe atoms. Significant improvement in magnetization is observed when the Fe atoms are located interstitially ( $3.76 \mu_B$ ) in the carbon matrix. The behavior is consistent with previous reports where transition metals prefer hollow absorption in comparison with top positions [43,44]. Therefore, the interstitial site favors easy magnetization associated with Fe due to strong exchange interaction with C magnetic moments in comparison to edge site [45].

Fig. 5(d-g) shows the DOS of r-GO with Au and Fe-O adatoms at different defect location. The defect created by virtue of the

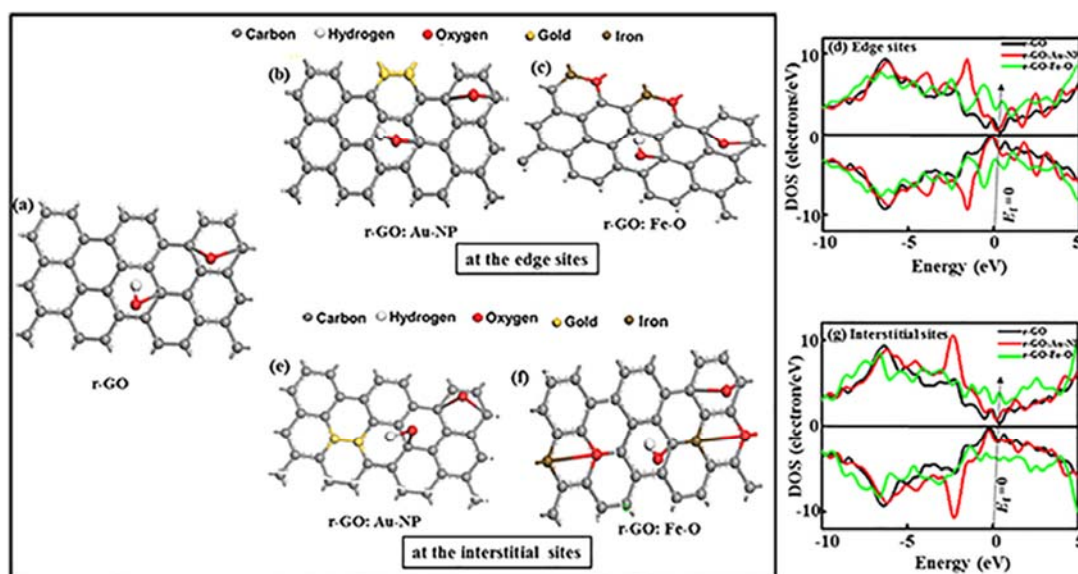


Fig. 5. Relaxed ball and stick illustration of (a) r-GO with C-O and C-OH defects, (b) r-GO: Au with defects located at the edge sites, (c) r-GO: Fe-O with defects located at the edge sites and their (d) total density of states at the edge sites. Relaxed ball and stick illustration of (e) r-GO with C-O and C-OH defects, (f) r-GO: Au with defects located at the interstitial sites, (g) r-GO: Fe-O with defects at the interstitial sites and their (d) total density of states at the interstitial sites.

Please cite this article as: D. O. Idisi, J. A. Oke, E. M. Benecha et al., Magnetic properties of graphene oxide functionalized with "Au" and " $Fe_2O_3$ " nanoparticles: A comparative study, Materials Today: Proceedings, <https://doi.org/10.1016/j.matpr.2020.02.869>

## ARTICLE IN PRESS

6

D.O. Idisi et al./Materials Today: Proceedings xxx (xxxx) xxx

atoms causes a shift away from the Fermi level. The impact of the defect position on the DOS is represented in Fig. 5(d–g) respectively. The shift in the energy level of rGO: Au composite is insignificant when either of the atoms are at the edge or at interstitial sites; although a slight increase in the DOS at the Fermi level is observed for interstitial defect site. rGO: Fe-O composite showed similar behaviour with a slight increase in the DOS at the Fermi level when the Fe-O atoms are located interstitially.

Fig. 6 shows the partial density of state (PDOS) of r-GO, r-GO: Au and r-GO: Fe-O indicating the contributions of the different core states to the total DOS. The contributions from C-2p and O-2p are much significant in comparison with C-2s and O-2s in the case of

r-GO. The C-2p and O-2p are attributed to the  $\pi$  and  $\sigma$  bond hybridization, which is consistent with pristine graphene [46]. The PDOS for Au 3d and Fe 3d are also indicated in Fig. 6(b–e). The magnetization of r-GO: Au can be attributed to contributions from O-2p and Au-3d. Although the experimental data indicates contributions from Au 4f doublet state, the exchange interaction between O 2p and Au 3d from DFT calculations gives another possibility for the magnetic enhancement of rGO: Au-NP. The case of r-GO: Fe-O shows significant contribution from 3d core state in comparison with Fe 2p (not shown in Fig. 6) which implies the impact of the exchange interaction between de-localized 3d and C-2p electrons leading to the enhanced magnetization [47]. The enhanced magne-

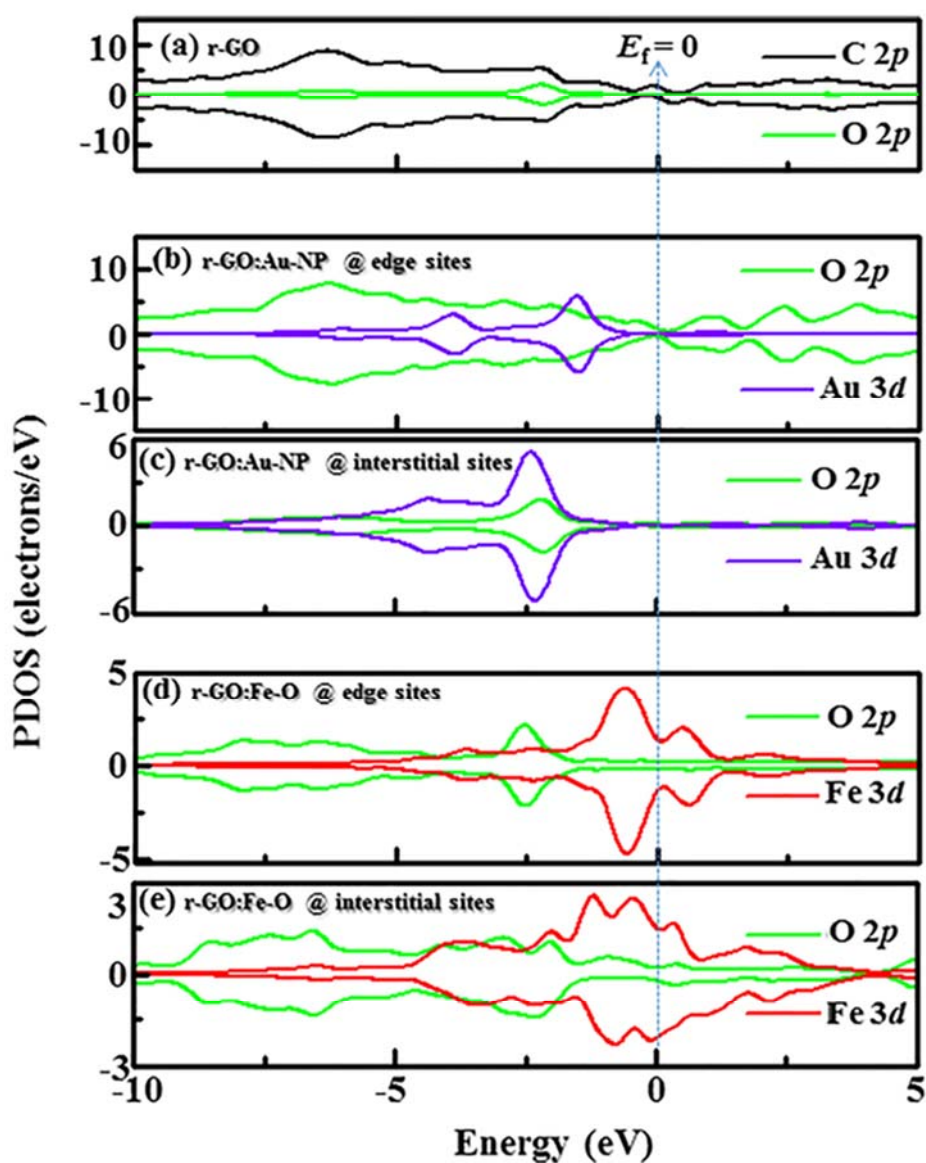


**Fig. 6.** Partial density of states (PDOS) showing contribution from C, Au, Fe and O orbitals in (a) r-GO, (b) r-GO: Au at edge sites, (c) r-GO: Au at interstitial sites, (d) r-GO: Fe-O at edge sites and (e) r-GO: Fe-O at interstitial sites. [Minimal contributing orbitals to the PDOS are C 2s, O 2s, Au 4s and Fe 2p (not shown)].

Please cite this article as: D. O. Idisi, J. A. Oke, E. M. Benecha et al., Magnetic properties of graphene oxide functionalized with "Au" and "Fe<sub>2</sub>O<sub>3</sub>" nanoparticles: A comparative study, Materials Today: Proceedings, <https://doi.org/10.1016/j.matpr.2020.02.869>



## ARTICLE IN PRESS

D.O. Idisi et al./Materials Today: Proceedings xxx (xxxx) xxx

7

tization from the experiment can also be attributed to the contributions from the C-2p, Fe-3d and Fe-2p exchange interactions.

### 5. Conclusion

We compared the electronic and magnetic properties of our previously reported work on r-GO: Au-NP and r-GO: Fe<sub>2</sub>O<sub>3</sub> nanocomposites using experimental results and DFT calculations. The XRD and TEM results showed cluster size for the composites are in the range ≈10–15 nm with weak agglomerations. The magnetization of r-GO was enhanced with the introduction of defects from Fe and Au atoms. The DFT calculations showed the enhanced magnetization of r-GO: Au-NP composites is mainly due to the nanosized clustered sized with additional contributions from O 2p and Au 3d orbital state whereas that of r-GO: Fe<sub>2</sub>O<sub>3</sub> is mainly attributed to the exchange interaction between C-2p, Fe-2p and Fe-3d orbital core states. The DFT calculations proffers the possibility of clarifying the contributors to the enhanced magnetization in GO/r-GO when functionalized with Au and Fe<sub>2</sub>O<sub>3</sub> nanoparticles.

### Declaration of Competing Interest

The authors declare that they have no known competing financial interests or personal relationships that could have appeared to influence the work reported in this paper.

### Acknowledgement

We appreciate the NRF (National Research Foundation) (Grant No. EQP13091742446) of South Africa for their financial support during the cost of this research.

### References

- [1] J. Zhao, L. Liu, F. Li, Graphene Oxide: Physics and Applications, Springer, 2015.
- [2] K. Yang, L. Feng, X. Shi, Z. Liu, Nano-graphene in biomedicine: theranostic applications, Chem. Soc. Rev. 42 (2013) 530–547.
- [3] G. Eda, M. Chhowalla, Chemically derived graphene oxide: towards large-area thin-film electronics and optoelectronics, Adv. Mater. 22 (2010) 2392–2415.
- [4] D.R. Dreyer, S. Park, C.W. Bielawski, R.S. Ruoff, The chemistry of graphene oxide, Chem. Soc. Rev. 39 (2010) 228–240.
- [5] S.P. Lonkar, Y.S. Deshmukh, A.A. Abdala, Recent advances in chemical modifications of graphene, Nano Res. 8 (2015) 1039–1074.
- [6] R.-Z. Li, R. Peng, K.D. Kihm, et al., High-rate in-plane micro-supercapacitors scribed onto photo paper using in situ femtosecond-reduced graphene oxide/Au nanoparticle microelectrodes, Energy Environ. Sci. 9 (2016) 1458–1467.
- [7] J. Huang, L. Zhang, B. Chen, et al., Nanocomposites of size-controlled gold nanoparticles and graphene oxide: formation and applications in SERS and catalysis, Nanoscale 2 (2010) 2733–2738.
- [8] Z. Tian, J. Dai, J. Li, et al., Tailored fabrication of  $\alpha$ -Fe<sub>2</sub>O<sub>3</sub> nanocrystals/reduced graphene oxide nanocomposites with excellent electromagnetic absorption property, J. Nanosci. Nanotechnol. 16 (2016) 12590–12601.
- [9] L. Zhang, Z. Bao, X. Yu, et al., Rational design of  $\alpha$ -Fe<sub>2</sub>O<sub>3</sub>/reduced graphene oxide composites: rapid detection and effective removal of organic pollutants, ACS Appl. Mater. Interfaces 8 (2016) 6431–6438.
- [10] S. Bhandary, O. Eriksson, B. Sanyal, Defect controlled magnetism in FeP/graphene/Ni (111), Sci. Rep. 3 (2013) 3405–3411.
- [11] X. Zhang, L. Yu, X. Wu, W. Hu, Experimental sensing and density functional theory study of H<sub>2</sub>S and SO<sub>2</sub> adsorption on Au-modified graphene, Adv. Sci. 2 (2015) 1500101–1500111.
- [12] Y. Li, H. Li, K. Zhang, K.M. Liew, The theoretical possibility of a graphene sheet spontaneously scrolling round an iron nanowire, Carbon N Y 50 (2012) 566–576.
- [13] D.O. Idisi, H. Ali, J.A. Oke, et al., Electronic, electrical and magnetic behaviours of reduced graphene-oxide functionalized with silica coated gold nanoparticles, Appl. Surf. Sci. 483 (2019) 106–113.
- [14] Y. Kobayashi, M.A. Correa-Duarte, L.M. Liz-Marzán, Sol–gel processing of silica-coated gold nanoparticles, Langmuir 17 (2001) 6375–6379.
- [15] D.O. Idisi, J.A. Oke, S. Sarma, et al., Tuning of electronic and magnetic properties of multifunctional r-GO-ATA-Fe<sub>2</sub>O<sub>3</sub>-composites for magnetic resonance imaging (MRI) contrast agent, J. Appl. Phys. 126 (2019) 35301–35312.
- [16] S.J. Clark, M.D. Segall, C.J. Pickard, et al., First principles methods using CASTEP, Zeitschrift für Krist. Mater. 220 (2005) 567–570.
- [17] H.S. Moon, J.H. Lee, S. Kwon, et al., Mechanisms of Na adsorption on graphene and graphene oxide: density functional theory approach, Carbon Lett. 16 (2015) 116–120.
- [18] K. Laasonen, R. Car, C. Lee, D. Vanderbilt, Implementation of ultrasoft pseudopotentials in ab initio molecular dynamics, Phys. Rev. B 43 (1991) 6796–6800.
- [19] B.N. Brahma, A.E. Merad, S. Dergal, Physical bowing parameters of ZnSxSe1-x ternary semiconductor from Ab initio study, J. Mater. Sci. Eng. A 3 (2013) 195–202.
- [20] S. Drewniak, R. Muzyka, A. Stolarczyk, T. Pustelny, M. Kotyczka-Morańska, M. Setkiewicz, Studies of reduced graphene oxide and graphite oxide in the aspect of their possible application in gas sensors, Sensors 16 (2016) 109–114.
- [21] L. Stobinski, B. Lesiak, A. Malolepszy, et al., Graphene oxide and reduced graphene oxide studied by the XRD, TEM and electron spectroscopy methods, J. Electron. Spectrosc. Relat. Phenomena 195 (2014) 145–154.
- [22] A. Sunatkar, S. Talwatkar, Y. Tamgadge, G. Muley, Synthesis, characterization and optical properties of L-arginine stabilized gold nanocolloids, Nanosci. Nanotechnol. 5 (2015) 30–35.
- [23] G. Pramanik, J. Humpolickova, J. Valenta, et al., Gold nanoclusters with bright near-infrared photoluminescence, Nanoscale 10 (2018) 3792–3798.
- [24] F. He, J. Fan, D. Ma, et al., The attachment of Fe<sub>3</sub>O<sub>4</sub> nanoparticles to graphene oxide by covalent bonding, Carbon N Y 48 (2010) 3139–3144.
- [25] D. Chen, H. Feng, J. Li, Graphene oxide: preparation, functionalization, and electrochemical applications, Chem. Rev. 112 (2012) 6027–6053.
- [26] J.R. Rani, J. Lim, J. Oh, et al., Substrate and buffer layer effect on the structural and optical properties of graphene oxide thin films, RSC Adv. 3 (2013) 5926–5936.
- [27] B. Ghosh, S. Sarma, M. Pontsho, S.C. Ray, Tuning of magnetic behaviour in nitrogenated graphene oxide functionalized with iron oxide, Diam. Relat. Mater. 89 (2018) 35–42.
- [28] Z. Yang, T. Zhao, X. Huang, et al., Modulating the phases of iron carbide nanoparticles: from a perspective of interfering with the carbon penetration of Fe@Fe<sub>3</sub>O<sub>4</sub> by selectively adsorbed halide ions, Chem. Sci. 8 (2017) 473–481.
- [29] S. Sotoma, K. Akagi, S. Hosokawa, et al., Comprehensive and quantitative analysis for controlling the physical/chemical states and particle properties of nanodiamonds for biological applications, RSC Adv. 5 (2015) 13818–13827.
- [30] A. Kaplan, Z. Yuan, J.D. Benck, et al., Current and future directions in electron transfer chemistry of graphene, Chem. Soc. Rev. 46 (2017) 4530–4571.
- [31] K. Krishnamoorthy, M. Veerapandian, K. Yun, S.-j. Kim, The chemical and structural analysis of graphene oxide with different degrees of oxidation, Carbon N Y 53 (2013) 38–49.
- [32] A. Brinkman, M. Huijben, M. Van Zalk, et al., Magnetic effects at the interface between non-magnetic oxides, Nat. Mater. 6 (2007) 493–498.
- [33] K.A. Mkhoyan, A.W. Contryman, J. Silcox, et al., Atomic and electronic structure of graphene-oxide, Nano Lett. 9 (2009) 1058–1063.
- [34] K. Jiang, A. Eitan, L.S. Schadler, et al., Selective attachment of gold nanoparticles to nitrogen-doped carbon nanotubes, Nano Lett. 41 (2003) 275–277.
- [35] L. Jiang, L. Gao, Modified carbon nanotubes: An effective way to selective attachment of gold nanoparticles, Carbon N Y 41 (2003) 2923.
- [36] D.S. Sutar, G. Singh, V. Divakar Botcha, Electronic structure of graphene oxide and reduced graphene oxide monolayers, Appl. Phys. Lett. 101 (2012) 103103–103109.
- [37] M. Agrachev, S. Antonello, T. Dainese, et al., Magnetic ordering in gold nanoclusters, ACS Omega 2 (2017) 2607–2617.
- [38] G.L. Nealon, B. Donnio, R. Greget, et al., Magnetism in gold nanoparticles, Nanoscale 4 (2012) 5244–5258.
- [39] N.A. Krans, N. Ahmad, D. Alloyeau, et al., Attachment of iron oxide nanoparticles to carbon nanofibers studied by in-situ liquid phase transmission electron microscopy, Micron 117 (2019) 40–46.
- [40] S. Majumder, M. Sardar, B. Satpati, et al., Magnetization enhancement of Fe<sub>3</sub>O<sub>4</sub> by attaching onto graphene oxide: an interfacial effect, J. Phys. Chem. C 122 (2018) 21356–21365.
- [41] M. Amft, S. Lebegue, O. Eriksson, N.V. Skorodumova, Adsorption of Cu, Ag, and Au atoms on graphene including van der Waals interactions, J. Phys. Condens. Matter. 23 (2011) 395001.
- [42] T.P. Kaloni, Y.C. Cheng, R. Faccio, U. Schwingenschlögl, Oxidation of monovacancies in graphene by oxygen molecules, J. Mater. Chem. 21 (2011) 18284–18288.
- [43] H. Valencia, A. Gil, G. Frapper, Trends in the adsorption of 3d transition metal atoms onto graphene and nanotube surfaces: a DFT study and molecular orbital analysis, J. Phys. Chem. C 114 (2010) 14141–14153.
- [44] M. Feyngenson, J.C. Bauer, Z. Gai, et al., Exchange bias effect in Au-Fe<sub>3</sub>O<sub>4</sub> dumbbell nanoparticles induced by the charge transfer from gold, Phys. Rev. B 92 (2015) 54416–54429.
- [45] S. Bhandary, O. Eriksson, B. Sanyal, Defect controlled magnetism in FeP/graphene/Ni (111), Sci. Rep. 3 (2013) 3405–3411.
- [46] L. Fritz, M. Vojta, The physics of Kondo impurities in graphene, Rep. Prog. Phys. 76 (2013) 32501–32516.
- [47] T. Eelbo, M. Waśniowska, P. Thakur, et al., Adatoms and clusters of 3 d transition metals on graphene: electronic and magnetic configurations, Phys. Rev. Lett. 110 (2013) 136804–136809.

Please cite this article as: D. O. Idisi, J. A. Oke, E. M. Benecha et al., Magnetic properties of graphene oxide functionalized with “Au” and “Fe<sub>2</sub>O<sub>3</sub>” nanoparticles: A comparative study, Materials Today: Proceedings, <https://doi.org/10.1016/j.matpr.2020.02.869>

## Appendix 6

Journal of Electron Spectroscopy and Related Phenomena 245 (2020) 147002



Contents lists available at ScienceDirect

Journal of Electron Spectroscopy and Related Phenomena

journal homepage: [www.elsevier.com/locate/elspec](http://www.elsevier.com/locate/elspec)Structural, electronic, and electrical behaviour of MWCNTs: TiO<sub>2</sub> (: SiO<sub>2</sub>) nanocompositesJames A. Oke<sup>a</sup>, David O. Idisi<sup>a</sup>, Sabata J. Moloji<sup>a</sup>, Sekhar C. Ray<sup>a,\*</sup>, K.H. Chen<sup>b</sup>, A. Ghosh<sup>b</sup>, A. Shelke<sup>b</sup>, W.F. Pong<sup>b,\*</sup><sup>a</sup> Department of Physics, CSET, University of South Africa, Private Bag X6, Florida, 1710, Science Campus, Christiaan de Wet and Pioneer Avenue, Florida Park, Johannesburg, South Africa<sup>b</sup> Department of Physics, Tamkang University, Tamsui 251, Taipei, Taiwan

## ARTICLE INFO

## Keywords:

TiO<sub>2</sub>  
SiO<sub>2</sub>  
MWCNTs  
NCs  
Raman spectroscopy  
XPS I-V technique

## ABSTRACT

We have functionalized multiwall carbon nanotubes (MWCNTs) with the composition of SiO<sub>2</sub> and TiO<sub>2</sub> (MWCNTs:TiO<sub>2</sub>:SiO<sub>2</sub>) at different Ti:Si stoichiometric ratios (Ti:Si ≈ 6:6 at% and ≈10:10 at%) using the hydrothermal process. The micro-structural, electronic and electrical properties of the unfunctionalized and functionalized MWCNTs were studied. Changes in surface morphology, degree of hybridization, crystallite structure and bonding structure due to functionalization were studied using field-emission scanning electron microscopy, Raman spectroscopy, x-ray diffraction, x-ray photoemission spectroscopy (XPS) and x-ray absorption near edge structure (XANES) spectroscopy techniques. Memristive and charge storage properties for MWCNTs:TiO<sub>2</sub>:SiO<sub>2</sub> nanocomposites (NCs) are more pronounced on NCs functionalised with high stoichiometric ratio (Ti:Si ≈ 10:10) due to the contribution of Ti<sup>3+</sup> and Si 2p core states as indicated by XPS and XANES results. The tunability of electrical conductivity is shown by an increase in the measured current and semiconducting I-V behaviour of the material as a result of high content of Ti-charge transfer. These observed changes in the electrical behaviour and electronic/bonding structure of the NCs indicate that the material could be useful for electrical/electronic applications and photocatalytic activity.

## 1. Introduction

Graphitic carbon nanomaterials such as fullerene, graphene, and carbon nanotubes (CNTs) have been of great research interest due to their excellent electrical conductivity, mechanical strength, and thermal properties [1]. These properties enable the materials to be useful for different applications such as electrochemical sensors, microelectronics, hydrogen storage, energy conversion devices, solar cells, and electromagnetic interference shielding [1–3]. Among these nanomaterials, CNTs have attracted enormous attention over the years, owing to the possibility of controlling their diameter, length, and morphology, which are parameters that have a large impact on tuning electronic and electrical behaviour of the material for several applications [4]. CNTs are cylindrical and hollow nanostructure with open or closed ends which are either in the form of single-walled (SW) or multi-walled (MW). SWCNT behaves as a metallic or semiconducting material with an energy gap ranging between 0.0 and 2.0 eV [5].

MWCNTs are composed of several coaxial SWCNTs. SWCNTs with

closed ends are known as fullerene and their limitations are that they can not be produced in large quantities. This shortfall leaves only MWCNTs more attractive than both graphene and fullerene. Regardless of their potential characteristics, the properties of MWCNTs need to be tuned for more and preferred applications. Several researchers have used heteroatoms such as nitrogen (N), boron (Br) [6] and silicon (Si) [7] and metal oxide like titanium-dioxide (TiO<sub>2</sub>), tin oxide (SnO<sub>2</sub>), zinc oxide (ZnO) and aluminum oxide (Al<sub>2</sub>O<sub>3</sub>) [8] to tailor properties of MWCNTs for applications in different fields. MWCNTs have also been utilized as a functionalizing agent in TiO<sub>2</sub>/SiO<sub>2</sub> matrix for photocatalytic application [9–11].

Our intention to introduce TiO<sub>2</sub> and SiO<sub>2</sub> in the lattice of MWCNTs due to exploiting the material stability for solution-based applications. As, it is known that MWCNTs are low-density material and are mostly conducting in nature because of their statistical probabilities and restrictions on the relative diameters of the individual tubes, and one of the shells, which makes them a zero-gap metal [5]. The effects of TiO<sub>2</sub> and SiO<sub>2</sub> as a bi-dopants on the lattice of MWCNTs have not been

\* Corresponding authors.

E-mail addresses: [Raysc@unisa.ac.za](mailto:Raysc@unisa.ac.za) (S.C. Ray), [wfpong@mail.tku.edu.tw](mailto:wfpong@mail.tku.edu.tw) (W.F. Pong).<https://doi.org/10.1016/j.elspec.2020.147002>

Received 14 May 2020; Received in revised form 12 September 2020; Accepted 29 September 2020

Available online 1 October 2020

0368-2048/© 2020 Elsevier B.V. All rights reserved.

explored nor understood. The choice of these bi-dopants is based on the possibility of Si atoms to act as a binding site for several molecules or atoms on the lattice of CNTs [12]. Si-atoms provide dangling bonds on CNTs surface through chemical absorption, influencing properties of CNTs for several applications [13]. TiO<sub>2</sub>, on the other hand, possesses a remarkable photocatalytic activity and the possibility of electron transfer in CNTs due to its high mobility of free electrons [14]. Meanwhile, memristive as a nonlinear circuit property is invaluable and it is applicable for electronic devices especially computer processors and memory. A recent review of TiO<sub>2</sub> [15] has explored the use in charge storage memristive applications using the ionic and other encouraging properties of TiO<sub>2</sub> material.

In our previous work, we studied the electrical and magnetic properties of MWCNTs:SiO<sub>2</sub>-NPs [16] and MWCNTs:TiO<sub>2</sub>-NPs [17] with different concentrations of Si (Si ≈ 1.5 & 5.75 at%) [16] and Ti (Ti ≈ 15 & 20 at%) [17] for various applications. The electrical conductivity of MWCNTs:SiO<sub>2</sub>-NPs was found to vary as a function of SiO<sub>2</sub> concentration, while that of MWCNTs:TiO<sub>2</sub>-NPs remained unchanged. An increase in electrical hysteresis loop was observed on MWCNTs:TiO<sub>2</sub>-NPs compared to MWCNTs. Based on their individual effects on properties of MWCNTs [16,17], TiO<sub>2</sub> and SiO<sub>2</sub> as a bi-dopant may improve the properties of the material for more applications. It is with this reason, we have functionalized MWCNTs with the composition of TiO<sub>2</sub> and SiO<sub>2</sub> at two different Ti:Si stoichiometric ratios (Ti:Si ≈ 6:6 at% and Ti:Si ≈ 10:10 at%) on the surface of MWCNTs using hydrothermal process. The present investigation is to establish the novelty of material properties for multidisciplinary applications like nanoelectronics, microelectronics, optoelectronics, and catalytic activities material-based devices. Focusing these applications, we have studied structural, electrical, and electronic behaviour of the prepared samples to establish and ascertain the feasibility of tuning the properties of MWCNTs by incorporating with the bi-dopant (Ti:Si) particularly for memristive and charge storage applications. To accomplish this goal, the properties of the prepared nano-composites materials were investigated using different experimental characterization techniques.

## 2. Experiments

### 2.1. Synthesis procedure

Ferrocene (C<sub>10</sub>H<sub>10</sub>Fe), acetylene (C<sub>2</sub>H<sub>2</sub>), toluene (C<sub>7</sub>H<sub>8</sub>), chloro(dimethyl) octadecylsilane, 1,3,5-trimethylbenzene, octadecylamine and TiO<sub>2</sub> were purchased from Sigma-Aldrich (Pty) Ltd. MWCNTs were synthesized using a spray pyrolysis procedure [16,18]. The process involves the use of ferrocene (Fe(C<sub>2</sub>H<sub>5</sub>)<sub>2</sub>) as catalyst and toluene (C<sub>7</sub>H<sub>8</sub>) as a carbon source to form a solution. Afterward, the solution was positioned in a quartz tube and then inserted into a hot-wall reactor of temperature 850 °C–900 °C. An argon flow was then introduced through the system until the growth of MWCNTs was completed (40 min). Moreover, acid treatment was used to purify the obtained MWCNTs. The solution of hydrochloric and nitric acid at ratio 1:1 was added to MWCNTs and stirred for 90 min. The mixture was then filtered to obtain pure MWCNTs.

Thermal decomposition techniques [16,19] was utilized to prepare Si-NPs. In this process, the solution of 1,3,5-trimethylbenzene and chloro(dimethyl) octadecylsilane in the presence of octadecylamine was placed in a quartz pipe in a vacuum condition and heated at a temperature of ~140 °C for 120 min. The mixture was left to air dry at room temperature to obtain Si-NPs. Silicon was oxidized upon exposure to air leading to the formation of SiO<sub>2</sub>. Hydrothermal technique [17,20] was adopted to obtain MWCNTs:TiO<sub>2</sub>:SiO<sub>2</sub> nanocomposites. MWCNTs (10 mg) were dispersed in water. TiO<sub>2</sub> and SiO<sub>2</sub> were added to MWCNTs suspension at two stoichiometric percentages (Ti:Si ≈ 6:6 at%) and (Ti:Si ≈ 10:10 at%). The solutions were sonicated for 30 min and stirred at 80 °C on a hot plate. Thereafter, we introduced an Ar flow through the suspension surface while the process of heating is still on to speed up the

water vaporization. Afterward, MWCNTs:TiO<sub>2</sub>:SiO<sub>2</sub> nanocomposites (NCs) were obtained in an oven at 100 °C after 15 h [21]. The synthesized powder samples were dissolved in methanol and dropped cast on a silicon wafer and then air-dried at room temperature for measurements and characterization. For each sample measurements were performed 2–3 times at different spots on the surface to ascertain the uniformity, validity and reliability of the acquired results.

### 2.2. Characterization

Different characterization techniques were used to study the morphology (field emission scanning electron microscopy (FE-SEM)), crystallite structure [X-ray diffractometer (XRD)], graphitization (Raman spectroscopy), local electronic structure [x-ray absorption near-edge spectroscopy (XANES)], chemical and bonding properties [x-ray photoelectron spectroscopy (XPS)] and electrical behaviour [current (I)-voltage (V) technique]. The morphology of the nanomaterials was studied utilizing FE-SEM JSM-7800 F supplied by JEOL Ltd. The crystallite structures were investigated using Smartlab X-ray diffraction with 0.154 nm Cu K $\alpha$  radiation line supplied by Rigaku. Raman spectra of the nanomaterials were studied using scientific XploRA of LASER light excitation energy of ~2.41 eV at 532 nm from HORIBA. The core shells which provide information about the electronic structure were examined utilizing KRATOS-SUPRA spectrometer with monochromatic Al K $\alpha$  radiation of pressure and excitation energy of  $1.2 \times 10^{-9}$  Torr and 1486.6 eV, respectively. The XANES spectra measurements of Ti L<sub>3,2</sub>-edge, Si L<sub>3,2</sub>-edge, C K-edge, and O K-edge were achieved using Taiwan Light Source (TLS) at NSRRRC (National Synchrotron Radiation Research Centre), Hsinchu, Taiwan. The electrical conductivity of the nanomaterials was studied by I–V measurements using Keithley 6487 with a voltage sweep from -1 to +1 V (-1 to 0 V, 0 to -1 V, +1 to 0 V, 0 to +1 V) in 3 cycles for each studied material. All characterizations were performed at room temperature. Silver paste was used to necessitate contacts between the sample and electrical test probes. The stability of the contact was confirmed by the continuity of the acquired I–V trends. Details of these experimental set-ups and characterization techniques can be found elsewhere [16,17].

## 3. Result and discussion

The FE-SEM images of TiO<sub>2</sub>, SiO<sub>2</sub>, MWCNTs, MWCNTs:Ti:Si (6:6 at%), and MWCNTs:Ti:Si (10:10 at%) NCs are presented in Figs. 1 (a–e), respectively. The images of TiO<sub>2</sub>, SiO<sub>2</sub>, and MWCNTs depict a typical spherical shape, balls clusters (50 nm–100 nm), and uniform tube-like profile, respectively. The image of MWCNTs:TiO<sub>2</sub>:SiO<sub>2</sub> shows that Si:Ti ≈ 6:6 at% is bounded to the surface of MWCNTs, indicating a good dispersion and prevention of Ti:Si clusters. The FE-SEM images of MWCNTs:TiO<sub>2</sub>:SiO<sub>2</sub> (Si:Ti ≈ 10:10 at%) display a uniform deposition with agglomeration on the surface of MWCNTs due to increased percentage of TiO<sub>2</sub> and SiO<sub>2</sub> on MWCNTs matrix [22]. These images indicate the growth of Ti on the surface of MWCNTs as confirmed by XRD results (shown later). This type of deposition on its surface might result in free electrons transfer of TiO<sub>2</sub> in the MWCNTs nanomaterials, hence enhancing the electrical properties of the NCs due to high electron mobility property of TiO<sub>2</sub>.

The crystal structures of the prepared NCs studied using XRD technique are displayed in Fig. 1 (f). XRD pattern of TiO<sub>2</sub> displays peaks at 2 $\theta$  25.3° (101), ~37.1° (103), ~37.9° (004), ~38.7° (112), ~48.1° (200), ~54.2° (105), ~55.3° (211) and ~62.9° (204) of anatase-phase [23]. The pattern of Si shows peaks at 7° (111) [24] and 22.9° (SiO<sub>2</sub>) [25] indicating that silicon was oxidized during the synthesis process. Two peaks at 2–26° (100) and ~44° (002) plane of graphitic carbon [25,26] are observed for MWCNTs. The deposition of Ti:Si ≈ 6:6 and Ti:Si ≈ 10:10 on the surface of MWCNTs results in anatase-phases as observed for TiO<sub>2</sub> and they also revealed rutile phases at 2 ~27.3° (110) and ~41.4° (111) [27,28]. MWCNTs: Ti:Si (6:6 at%) also shows a very less

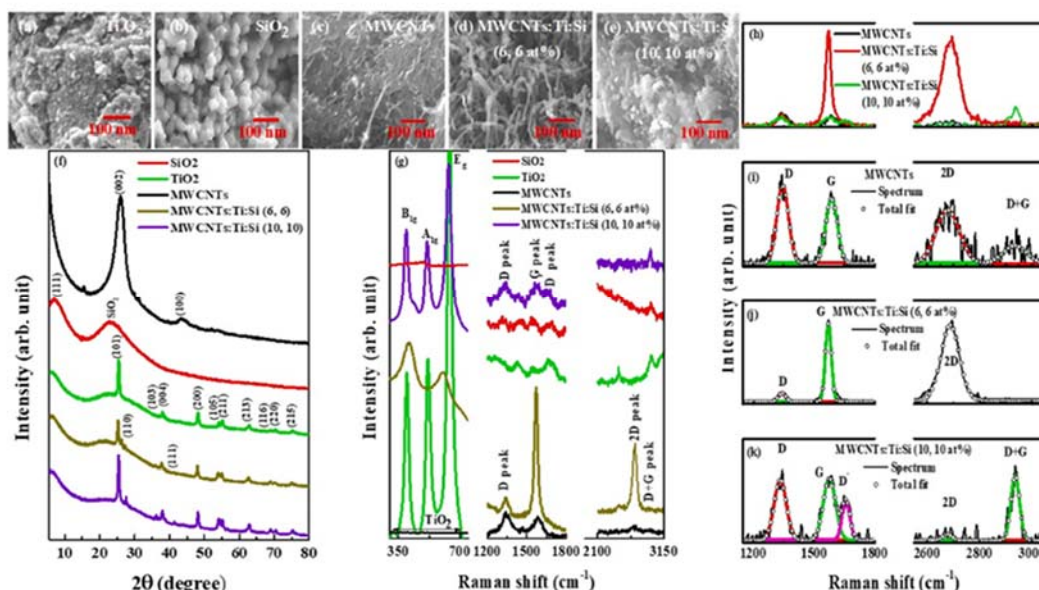


**Fig. 1.** (a), (b), (c), (d) and (e) Field emission scanning electron microscopy images (FE-SEM) of SiO<sub>2</sub>, TiO<sub>2</sub>, MWCNTs, MWCNTs:Ti:Si (Ti:Si ≈ 6:6 at%) and MWCNTs:Ti:Si (Ti:Si ≈ 10:10 at%) NCs, respectively; (f) and (g) X-ray diffraction spectra and Raman spectra of SiO<sub>2</sub>, TiO<sub>2</sub>, MWCNTs, MWCNTs:Ti:Si NCs (Ti:Si ≈ 6:6 at% and Ti:Si ≈ 10:10 at%), respectively; (h) First and second order Raman spectra of MWCNTs, MWCNTs:Ti:Si (Ti:Si ≈ 6:6 at%) and MWCNTs:Ti:Si (Ti:Si ≈ 10:10 at%) NCs; (i) (j) and (k) deconvolution of first and second order Raman spectra of MWCNTs, MWCNTs:Ti:Si (Ti:Si ≈ 6:6 at%) and MWCNTs:Ti:Si (Ti:Si ≈ 10:10 at%) NCs, respectively.

**Table 1**

Values of quantificational and compositional analysis from XPS, I<sub>D</sub>/I<sub>G</sub> ratio from Raman Spectra, and crystallite size from XRD.

	Quantificational and compositional analysis from XPS				(I <sub>D</sub> /I <sub>G</sub> ) ratio from Raman Spectra	Crystallite Size (nm) from XRD
	C at %	O at%	Si at%	Ti at%		
TiO <sub>2</sub>	–	65	–	35	–	18.10
SiO <sub>2</sub>	–	64	36	–	–	–
MWCNTs	98	02	–	–	1.18	–
MWCNTs:Ti:Si (6:6 at%)	59	29	6	6	0.16	19.09
MWCNTs:Ti:Si (10:10 at%)	27	53	10	10	0.97	19.27

intense (002) carbon peak which vanishes as Ti:Si content increases on MWCNTs matrix, indicating carbon atoms were gradually replaced by Ti atoms. This replacement is confirmed by an increase in the intensity of (101) plane of TiO<sub>2</sub>. Thus, Ti:Si has changed the structure of MWCNTs.

**Table 2**

Different parameters of D-peak, G-peak, D'-peak, 2D-peak and (D + G) peak, obtained from first and second order Raman spectra.

Samples	First-order Raman spectra									Second-order Raman spectra					
	D peak			G peak			D' peak			2D peak			D + G peak		
	x (cm <sup>-1</sup> )	Δω (cm <sup>-1</sup> )	Int. (a.u.)	x (cm <sup>-1</sup> )	Δω (cm <sup>-1</sup> )	Int. (a.u.)	x (cm <sup>-1</sup> )	Δω (cm <sup>-1</sup> )	Int. (a.u.)	x (cm <sup>-1</sup> )	Δω (cm <sup>-1</sup> )	Int. (a.u.)	x (cm <sup>-1</sup> )	Δω (cm <sup>-1</sup> )	Int. (a.u.)
MWCNTs	1345	68	18.17	1586	66	15.35	–	–	–	2678	104	4.19	2933	102	1.83
MWCNTs:Ti:Si (6:6 at%)	1342	43	21.90	1570	34	134.8	–	–	–	2687	83	61.7	–	–	–
MWCNTs:Ti:Si (10:10 at%)	1333	70	14.00	1575	71	14.42	1658	47	10	2677	44	2.53	2935	39	13.5

The Scherrer's equation ( $D = k\lambda/\beta\cos\theta$ ) [29] was used to obtain the crystallite size of TiO<sub>2</sub> in (101) plane of MWCNTs:Ti:Si (Ti:Si ≈ 6:6 at%) and MWCNTs:Ti:Si (Ti:Si ≈ 10:10 at%), where  $k$  is ~0.9,  $\lambda$  = 1.54 Å (wavelength of x-ray),  $\beta$  is full width at half maximum and  $\theta$  is the Bragg's angle. The crystallite sizes for TiO<sub>2</sub>, MWCNTs:Ti:Si (Ti:Si ≈ 6:6 at%) and MWCNTs:Ti:Si (Ti:Si ≈ 10:10 at%) were found to be 18.10, 19.09 and 19.27 nm, respectively. The observed increase in crystallite sizes indicates a growth of anatase TiO<sub>2</sub> on the wall of MWCNTs as confirmed by FE-SEM images (Table 1).

Raman spectroscopy technique was used to examine the degree of hybridization of MWCNTs and MWCNTs:Ti:Si NCs and the data is presented in Fig. 1 (g-k). Fig. 1 (g) shows three high intense peaks at ~398 (B<sub>1g</sub>), ~519 (A<sub>1g</sub>) and ~642 cm<sup>-1</sup> (E<sub>g</sub>) for TiO<sub>2</sub> anatase phase [30,31]. For SiO<sub>2</sub>, a first-order peak is observed at ~520 cm<sup>-1</sup> corresponding to Si/SiO<sub>2</sub> peak [32]. Raman spectra of MWCNTs consist of four main peaks at ~1345 (D peak) cm<sup>-1</sup>, ~1585 (G peak) cm<sup>-1</sup>, ~2664 (2D peak) cm<sup>-1</sup> and ~2912 (D + G peak) cm<sup>-1</sup> as expected for carbon and carbon-nanostructured materials [33]. The D and G peaks are an indication of disorder ( $sp^2$  hybridization) and ordered ( $sp^3$  hybridization) peaks, respectively in the carbon-based materials. The 2D peak is a signature of a second-order vibration process of D peak and the

J.A. Oke et al.

Journal of Electron Spectroscopy and Related Phenomena 245 (2020) 147002

occurrence of D + G peak is due to the D and G mode vibration process. These peaks were also observed on MWCNTs: Ti:Si NCs with additional peaks associated with the anatase phase of TiO<sub>2</sub> [30]. Si/SiO<sub>2</sub> peak was not observed because it could have been overlapped by TiO<sub>2</sub> peaks. In the case of MWCNTs: Ti:Si (10:10 at%), an additional D' peak is observed at 1658 cm<sup>-1</sup>, which is due to a slight shift and broadening of G band. The D' band is always inactive but becomes active due to defects (restriction of phonon) among the graphitic walls [21,34]. Moreover, these changes of MWCNTs are due to decoration of Ti:Si on the surface of MWCNTs. A slight shift and reduction in the intensity of B<sub>1g</sub>, A<sub>1g</sub>, and E<sub>g</sub> mode in MWCNTs: Ti:Si NCs Raman shift is possibly due to an increase in crystallite size of TiO<sub>2</sub> on the surface of MWCNTs [35]. To have an in-depth knowledge about the degree of hybridization, we have de-convoluted the Raman spectra of MWCNTs and MWCNTs: Ti:Si NCs with several Gaussian lines. From the de-convoluted Raman spectra, we were able to deduce parameters that are tabulated in Table 2. From Fig. 1(j), it was observed that the width of D and G bands got narrowed for Ti:Si (6:6 at%) deposition. Also, the intensity of D band decreases with an increase in the intensity of G band. These observations may be due to the longer isothermal exposure time rate of the nanocomposite, which aided the decrease in amorphous carbon in MWCNTs [35]. From Fig. 1(k), a slight broadening of G band with occurrence of D' band for Ti:Si (10:10 at%) deposition was observed, indicating a change in microstructural behaviors of these materials. The I<sub>D</sub>/I<sub>G</sub> ratios were calculated to be -1.18 for MWCNTs, -0.16 for Ti:Si (6:6 at%), and -0.97 for Ti:Si (10:10 at%) NCs. The observed variation of I<sub>D</sub>/I<sub>G</sub> ratio indicates a decrease in the sp<sup>2</sup> cluster and a reduction of defect density due to the replacement of carbon by Ti:Si atoms on the surface of MWCNTs. However, it is noted that the I<sub>D</sub>/I<sub>G</sub> ratio for Ti:Si (10:10 at%) is higher than (6:6 at%) for Ti:Si decorated MWCNTs-NCs implying that microstructural change has occurred in MWCNTs:(Ti:Si). This variation of the ratio with concentration is in consistent with XRD results discussed above (Table 3).

The XANES spectra in Fig. 2 (a-d) depict the C K-edge, O K-edge, Si L<sub>3,2</sub>-edge, and Ti L<sub>3,2</sub>-edge for TiO<sub>2</sub>, SiO<sub>2</sub>, MWCNTs, and MWCNTs: Ti:Si NCs. In each case, the inset shows magnified near-edge features, which were subtracted from the main near-edge spectra using the Gaussian line as the background, as shown in the dotted line in Fig. 2 (a-d). In C K-edge spectra, the binary features π\* and σ\* are located at approximately 286.2 eV (sp<sup>2</sup>) and 293.1 eV (sp<sup>3</sup>), respectively [26,36,37]. It was observed that the π\* region displays two features which are represented by an inset in Fig. 2 (a). The two features are located at -286.2 and -287.6 and are attributed to C-C and C-H bonds [38], respectively. From the inset, a gradual decrease in the intensities of the nanocomposites is observed indicating a defect in the graphitization of MWCNTs. The O K-edge for the MWCNTs and MWCNTs:Ti:Si presented in Fig. 2(b) shows π\* and σ\* structures. The π\* structure also displays two peaks at ~528.6 eV and ~530.1 eV which are assigned to the carboxylic (C=O) group [39]. These peaks shift slightly towards low photon energy for the NCs, signifying the reaction of C and O with Ti-Si in the lattice of MWCNTs. The σ\* bond located at 540 eV is assigned to the hydroxyl (C-OH) group [39] which is mostly due to interactions of C-H bonds. Two peaks at ~533.7 and ~535.1 eV are attributed to the physical absorption of oxygen between 530-536 eV region [40]. These two peaks are assigned to t<sub>2g</sub> and e<sub>g</sub> orbit separation of Ti 3d and Si 3d states [41,42]. The photon energies above 536 eV are signatures of oxygen 2p interaction with Ti 4sp and Si 3sp states [43]. The inset in Fig. 2 (b) also shows a similar trend in intensities as observed in C K-edge spectra, implying de-oxidation has occurred.

The Si L<sub>3,2</sub>-edge of SiO<sub>2</sub> and MWCNTs:Ti:Si NCs spectra are shown in Fig. 2 (c). Doublet orbital splitting (A and B) of SiO<sub>2</sub> is consistent with Si core states [44]. Taking structure A into consideration, binary peaks are confirmed at ~103.8 eV and ~105.0 eV with 1.2 eV apart, implying a poor resolute peak [45]. A change from silicon 2p → 3s derived states (i. e. core to anti-bonding states) induces a binary split of A, which is a spin-energy bi-edge [45]. The structure of B is due to the change from

**Table 3**  
Values obtained from the de-convolution of XPS spectra for C 1s, O 1s, Ti 2p, and Si 2p.

	C 1s			O 1s			Ti 2p			Si 2p		
	Peak I C=C	Peak II C=C/C-C/O	Peak III O=C=O	Peak I Ti-O-Ti/Ti-O-H	Peak II C-O/C=O/Ti-O-Si	Peak III C-O/Si-O	Peak I Si-C/Si-C-O	Peak II Si-C/Si-C-O	Peak III Si-O	Peak I Ti <sup>3+</sup> -2p <sub>3/2</sub>	Peak II Ti <sup>4+</sup> -2p <sub>1/2</sub>	Peak III Ti <sup>4+</sup> -2p <sub>3/2</sub>
	x (eV)	x (eV)	x (eV)	x (eV)	x (eV)	x (eV)	x (eV)	x (eV)	x (eV)	x (eV)	x (eV)	x (eV)
MWCNTs	283.5	284.3	290.0	528.6	530.5	531.9	100.6	101.1	101.6	457.3	459.2	457.1
MWCNTs:Ti:Si (6:6 at%)	284.6	285.7	290.0	528.6	530.6	532.4	102.1	103.6	104.6	457.1	459.2	457.1
MWCNTs:Ti:Si (10:10 at%)	284.6	286.3	290.0	528.3	530.2	532.0	101.7	103.3	104.8	457.1	459.2	457.1
TiO <sub>2</sub>	-	-	10,967	-	-	-	-	-	-	-	-	-
SiO <sub>2</sub>	-	-	10,967	-	-	-	-	-	-	-	-	-
MWCNTs:Ti:Si (6:6 at%)	457.3	459.2	477	102.1	103.6	104.6	103.6	104.6	104.6	457.3	459.2	457.1
MWCNTs:Ti:Si (10:10 at%)	457.1	459.2	710	101.7	103.3	104.8	103.3	104.8	104.8	457.1	459.2	457.1

4

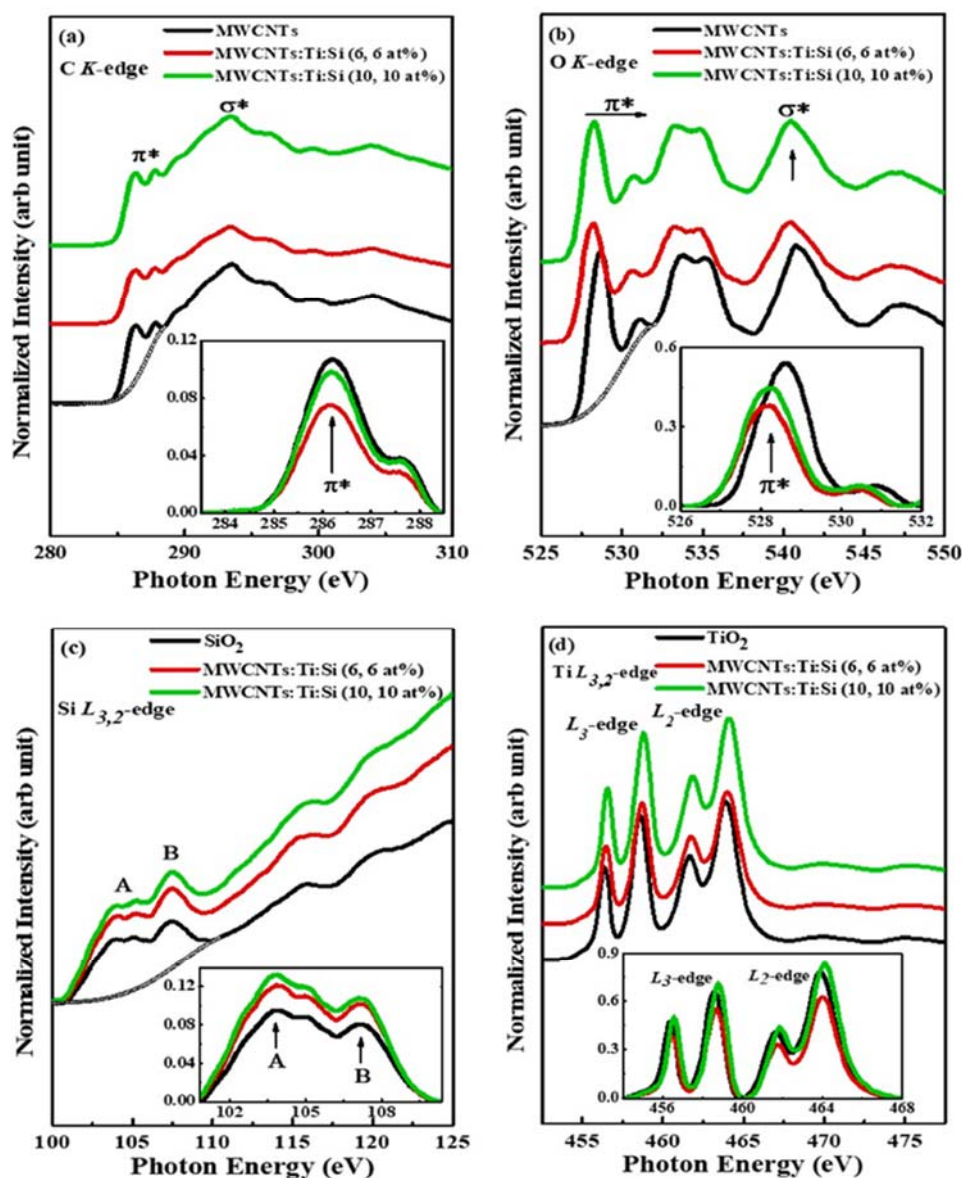


Fig. 2. X-ray absorption near edge structure (XANES) spectroscopy of  $\text{SiO}_2$ ,  $\text{TiO}_2$ , MWCNTs, MWCNTs:Ti:Si (Ti:Si  $\approx$  6:6 at%) and MWCNTs:Ti:Si (Ti:Si  $\approx$  10:10 at%) NCs (a) C K-edge, (b) O K-edge, (c) Si- $L_{3,2}$ -edge and (d) Ti- $L_{3,2}$ -edge.

silicon  $2p \rightarrow 3p$  which is related to  $3s$  states from oxygen  $2p$  hybridized orbitals [45]. A broadening region above B structure corresponds to the silicon  $2p \rightarrow 3d$  transition [43]. In reference to the inset in Fig. 2 (c), it is observed that there is a variation in the intensity of MWCNTs:Ti:Si NCs implying that Si has contributed to a change in the electronic structure of MWCNTs. The Ti  $L_{3,2}$ -edge spectra of  $\text{TiO}_2$  and MWCNTs:Ti:Si NCs are depicted in Fig. 2 (d). The spectra show a complex structure of  $L_3$ -edge and  $L_2$ -edge regions that occur because of crystal field effect and atomic contact [46]. The  $L_3$ -edge and  $L_2$ -edge regions correspond to oxygen  $2p_{3/2}$  and  $2p_{1/2}$  titanium  $3d$  bands, respectively. The effect of the crystal field has divided titanium  $3d$  band into two bands ( $t_{2g}$  and  $e_g$ ) which brings about the binary features observed in  $L_3$ -edge and  $L_2$ -edge regions

as shown in the figure. These features are located at approximately 456.3 eV, 458.5 eV, and 461.6 eV, 463.9 eV, which are assigned to  $t_{2g}$  and  $e_g$  bands [46], respectively. The inset in Fig. 2(d) shows a variation in the intensities of  $\text{TiO}_2$  and MWCNTs:Ti:Si NCs spectra, implying oxygen and/or carbon substitution/ attachment by Ti atom.

XPS technique was used in probing the electronic structure and bonding properties of  $\text{TiO}_2$ ,  $\text{SiO}_2$ , MWCNTs, and MWCNTs:Ti:Si NCs. Fig. 3 (a–d) displays the comparison of C 1s, O 1s, Ti 2p, and Si 2p XPS spectra for each material and their composition and quantification parameters are presented in Table 1. The variation in the intensities of C 1s, O 1s, Ti 2p, and Si 2p spectra for  $\text{TiO}_2$ ,  $\text{SiO}_2$ , MWCNTs, and MWCNTs:Ti:Si NCs shown in the figure, confirms the functionalization of MWCNTs

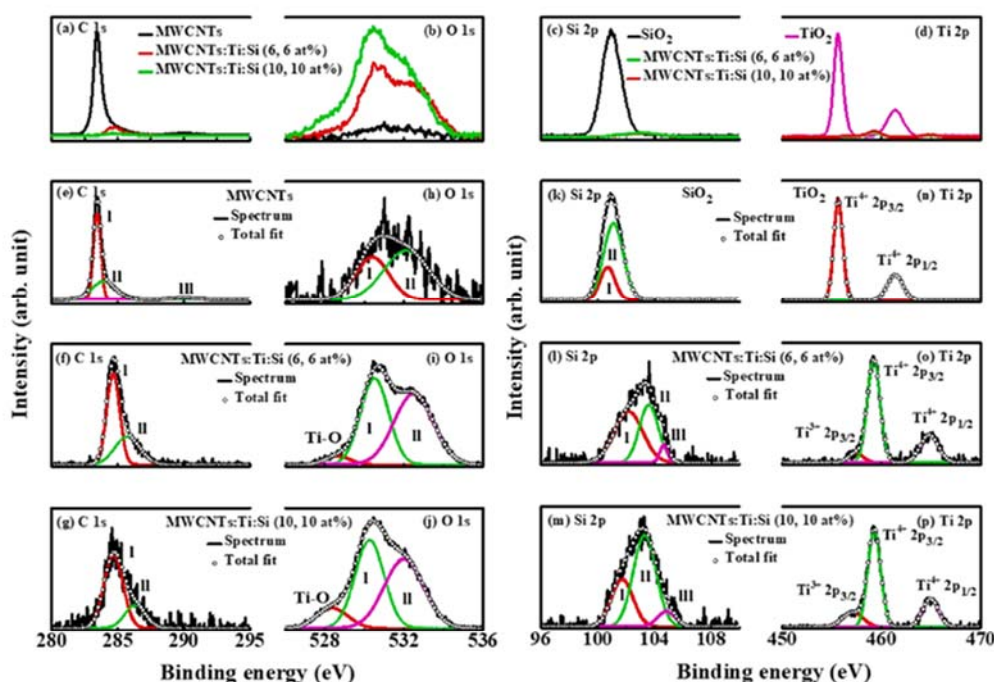


Fig. 3. (a) C 1s, (b) O 1s, (c) Si 2p and (d) Ti 2p x-ray photoelectron spectroscopy (XPS) of  $\text{TiO}_2$ ,  $\text{SiO}_2$ , MWCNTs, MWCNTs:Ti:Si (Ti:Si  $\approx$  6:6 at%) and MWCNTs:Ti:Si (Ti:Si  $\approx$  10:10 at%) NCs; (e-g) and (h-j) Deconvolution of C 1s and O 1s XPS spectra, respectively for MWCNTs, MWCNTs:Ti:Si (Ti:Si  $\approx$  6:6 at%) and MWCNTs:Ti:Si (Ti:Si  $\approx$  10:10 at%) NCs; (k-m) Si 2p spectra of  $\text{SiO}_2$ , MWCNTs:Ti:Si (Ti:Si  $\approx$  6:6 at%) and MWCNTs:Ti:Si (Ti:Si  $\approx$  10:10 at%) NCs; (n-p) Ti 2p spectra of  $\text{TiO}_2$ , MWCNTs:Ti:Si (Ti:Si  $\approx$  6:6 at%) and MWCNTs:Ti:Si (Ti:Si  $\approx$  10:10 at%) NCs.

and oxidation of Ti and Si nanoparticles. The C 1s, O 1s, Ti 2p, and Si 2p XPS spectra were de-convoluted into several Gaussian lines and are presented in Fig. 3 (e-p). The C 1s of MWCNTs were de-convoluted using Gaussian lines into three peaks at  $\sim 283.5/\sim 284.0$  and  $\sim 290.0$  eV corresponding to C-graphite/ $\text{C}=\text{C}$  ( $sp^2$ ) and  $\text{O}=\text{C}-\text{O}$  or  $\pi-\pi^*$  bonding [47, 48], respectively. These peaks (C-graphite/ $\text{C}=\text{C}$  ( $sp^2$ )) shifted to  $\sim 284.6/\sim 285.7$  eV for MWCNTs:Ti:Si (6:6 at%) and  $\sim 284.7/\sim 286.3$  eV for MWCNTs:Ti:Si (10:10 at%) indicating a structural change due to the introduction of Ti:Si on MWCNT matrix. The O 1s XPS spectra are depicted in Fig. 3 (h-j) and were de-convoluted using Gaussian lines into two and three peaks for MWCNTs and MWCNTs:Ti:Si NCs, respectively. From the O 1s of MWCNTs, peaks are located at  $\sim 530.4$  eV and  $\sim 532.1$  eV which are signatures of  $\text{C}=\text{O}$  and  $\text{C}-\text{O}$  [48], respectively. These peaks shifted to  $\sim 528.6/\sim 530.5$  for MWCNTs:Ti:Si (6:6 at%) and  $\sim 528.3/\sim 530.2$  for MWCNTs:Ti:Si (10:10 at%) which are the signatures of hydroxyl and oxygen ( $\text{Ti}-\text{O}-\text{Ti}/\text{Ti}-\text{O}-\text{H}/\text{C}=\text{O}/\text{Ti}-\text{O}-\text{Si}$ ) groups [10,49], respectively. These bonds indicate that  $\text{SiO}_2$  did not bond into the matrix of  $\text{TiO}_2$  but was connected to  $\text{TiO}_2$  through Ti-O-Si chemical bonding. The peaks at  $\sim 532.4$  eV and  $\sim 532.0$  eV for NCs confirm the presence of the Si-O-Si bond [10,49]. The Si 2p XPS spectrum in Fig. 3 (k-m) displays two peaks for  $\text{SiO}_2$  and three peaks for MWCNTs:Ti:Si NCs. The peaks were located at  $\sim 100.6$  eV and  $\sim 101.1$  eV corresponding to Si-Si bond and these peaks shift towards high binding energy at  $\sim 102.1$ ,  $\sim 103.6$  and  $\sim 101.7$ ,  $\sim 103.3$  eV for MWCNTs:Ti:Si (6:6 at%) and MWCNTs:Ti:Si (10:10 at%), which are signatures of Si-C-O/Si-C [50, 51], respectively. The peaks at  $\sim 104.6$  eV and  $\sim 104.8$  eV correspond to Si-O bonding [52]. This shift indicates that Si has an impact on the bonding and electronic system of MWCNTs. Fig. 3 (n-p) represents the core level of Ti 2p and its peaks were de-convoluted into two and three peaks for  $\text{TiO}_2$  and MWCNTs:Ti:Si NCs, respectively. For Ti 2p XPS spectrum, peaks are located at  $\sim 455.6$  eV ( $\text{Ti}^{4+} 2p_{3/2}$ ) and  $\sim 461.3$  eV

( $\text{Ti}^{4+} 2p_{1/2}$ ) with a spin energy splitting of  $\sim 5.7$  eV, indicating the presence of  $\text{Ti}^{4+}$  state [5]. These peaks shift towards high binding energy with an appearance of a new peak at  $\sim 457.3$  eV and  $\sim 457.1$  eV for MWCNTs:Ti:Si (6:6 at%) and MWCNTs:Ti:Si (10:10 at%) NCs, respectively. The blue shift in their energies signified that Ti is deposited on MWCNTs at a different region to that of pristine  $\text{TiO}_2$  [53,54] and the occurrence of the new peak indicates that  $\text{Ti}^{3+}$  state is also present [5, 53]. It is obvious that Ti:Si led to the observed  $\text{Ti}^{3+}$  in MWCNTs:Ti:Si NCs and  $\text{Ti}^{3+}$  can form radicals when reacting with  $\text{O}_2$  [55]. Previous review reporting on the photocatalytic mechanism of  $\text{TiO}_2$  established the generation of electron-hole pair in the surface of the material when exposed to light. The electron-hole pair generation is attributed to a short penetration depth from radical formation due to oxidizing agents [55,56].

The I-V plots and hysteresis loops for  $\text{TiO}_2$ ,  $\text{SiO}_2$ , MWCNTs, MWCNTs:Ti:Si (6:6 at%), and MWCNTs:Ti:Si (10:10 at%) are displayed in Fig. 4. For all samples the trends are solid (continuous) indicating a stable contact between the samples and the probes. It can be seen from Fig. 4, that the measured current for  $\text{SiO}_2$  is lower than that of other samples indicating an insulating behaviour of the material. In comparison to other plots, the I-V trends obtained from MWCNTs are relatively ohmic indicating a well-known conducting behaviour of the material [5]. The trends, however, changes from conducting to semiconducting behaviour as Ti:Si is introduced on the surface of MWCNTs. As observed in Figs. 4 (d) & 4(e), the semiconducting behaviour of the material after the introduction of Ti:Si can be explained by switching properties at  $\pm 0.5$  V. This switching property originates from switching sites that are embedded in  $\text{SiO}_2$  and nanogap region that are associated with Si-Si bonds. This encouraging switching properties of  $\text{SiO}_2$  was reported in detail by Yao et al [57]. The observed increase in the measured current indicates that the conductivity of the material increases with an

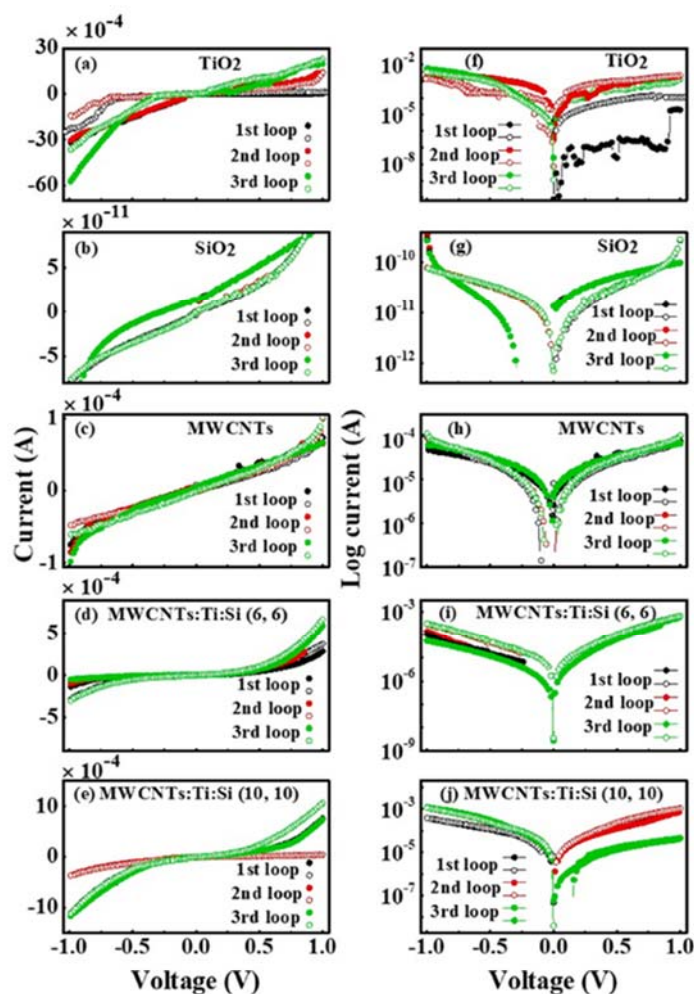


Fig. 4. (a-e) and (f-j) linear and log current-voltage (I-V) measurement, respectively of  $\text{SiO}_2$ ,  $\text{TiO}_2$ , MWCNTs, MWCNTs:Ti:Si (Ti:Si  $\approx$  6:6 at%) and MWCNTs:Ti:Si (Ti:Si  $\approx$  10:10 at%) NCs [Three cycles measurements of linear and log I-V].

increases in an introduced Ti:Si content. A high conductivity is associated to an increase in the concentration of mobile electrons due to Ti:Si content on the lattice of MWCNTs [58]. An increase in the conductivity of the material with an increase in the concentration of the introduced  $\text{TiO}_2$  on the surface of MWCNTs was reported before [17]. Based on the results presented then [17] and the ones presented here, it can be safely concluded that the introduction of  $\text{SiO}_2$  with  $\text{TiO}_2$  on the surface of MWCNTs increases the electrical conductivity of MWCNTs:Ti:Si-NCs. In addition to the tunability of the material conductivity for various applications, this work also indicates that properties can be tuned to make the more suitable for electronic switching devices.

The results presented in Fig. 4 also show the functionalised MWCNTs are promising for memristive and charge storage material-based devices. Possibilities of the material to be suitable for these applications is based on the observed hysteresis I-V loop in the figure. Based on a low measured current for  $\text{SiO}_2$  and ohmic I-V of MWCNTs it was safely assumed that the experimental set-up would result in a reliable data and three loops would be enough to establish and study the memristive and charge storage behaviour of our samples. The previous review on the memristive capability of  $\text{TiO}_2$  [15] established its ionic bonding

structure which is associated with  $\text{Ti}^{3+}$  and  $\text{O}^-$ . Apparently, oxygen vacancies can easily translate ionically thereby leading to an auto-doping phase behaviour. The constituent oxygen ions can cause an anodic attachment. The ionic translation and anodic attachment are consistent with previously reported ReRAM properties [59]. Furthermore, the observed insulating properties of  $\text{SiO}_2$  are useful for the fabrication of memory devices. The previous report by Yao et al. [57] on  $\text{SiO}_2$  showed encouraging resistive switching and memories. The fourth circuit-states, which is associated with memristors depends on the rate of change of magnetic flux and charges. Since both flux and charges are dependent on current and voltage, I-V characteristics can be used to study memristive behaviour of the material [60]. Moreover, reports have indicated memristive characters when an I-V trend is either non-zero or zero origin crossing [61,62]. As described in the review by Sun et al. [63], the non-zero and zero-crossing point structures signify capacitance and memristive states which are attributes of a memristor. Although, pristine MWCNT gives conducting electrical features, however, the inclusion of Ti:Si leads to a semiconducting behaviour with an apparent hysteresis loop that is associated with charge storage behaviour. Presumably, the formation of MWCNTs:Ti:Si leads to an



attachment of ionic  $Ti^{3+}$  and Si-Si bonds which could be a major factor in the observed charge storage behaviour which is comparable with memristive features that were previously reported [63]. From the above results, we suggest that the NCs will be a potential candidate for ferroelectric devices too due to the observed hysteresis loops. The stability of the material for these applications has confirmed by more loops elsewhere [63]. Furthermore, the oxygen vacancies that are created by  $O^-$  can also lead to the formation of oxidizing radicals which could be useful for photocatalytic applications [64].

The agglomeration observed on the surface of MWCNTs:Ti:Si from FE-SEM image indicates a growth of Ti on MWCNTs surface and it is consistent with XRD and Raman results. The observed growth of Ti was confirmed by XRD due to the calculated increase in the crystallite sizes of Ti in the nanocomposites. This increase in crystallite size also corresponds to the decrease in the  $I_D/I_G$  ratios of the nanocomposites. The  $I_D/I_G$  ratios calculated from Raman spectra of the nanocomposites decreases for Ti:Si  $\approx 10:10$  at% and further decrease for Ti:Si  $\approx 6:6$  at% when compared to that of MWCNTs. These observed decreases are in agreement with XANES and XPS data. The XPS C 1s spectra for nanocomposites show a positive shift to that of pristine MWCNTs. The XANES C K-edge spectra show a steady decrease in the intensities of  $\pi^*$  ( $C-sp^2$ ) with the concentration of the bi-dopant in comparison with MWCNTs, corresponding to the steady decrease in the  $I_D/I_G$  ratios of the nanocomposites. This observation signifies a reduction in the  $sp^2$  clusters of MWCNTs with a corresponding increase in  $sp^3$  clusters. The electrical conductivity of the nanocomposites increases for Ti:Si  $\approx 6:6$  at% and further increase for Ti:Si  $\approx 10:10$  at% with a considerable hysteresis loop that is associated with charge storage behaviour. As observed from the XANES spectra, the intensities of O K-edge showed the same trend as C K-edge. This observation translates to a reduction in oxygen (O) vacancies as inversely reported in a previous study [65]. The reduction in O vacancy may be responsible for an increase in the concentration of the mobile electrons resulting in an increase in electrical conductivity of the nanocomposites [59].

#### 4. Conclusion

$TiO_2$ ,  $SiO_2$ , MWCNTs, and MWCNTs:Ti:Si nanocomposites have been synthesized and characterized by the use of different techniques. Their structural, electronic, and electrical behaviour have been studied. The FE-SEM image shows good dispersion and agglomeration of Ti:Si on the surface of MWCNTs due to the introduction and variation of Ti:Si content on the MWCNTs matrix. It was observed from Raman that the introduction of Ti:Si results in a decrease in the  $sp^2$  cluster in MWCNTs, which is consistent with the decrease in the intensities of XANES C K-edge, making in MWCNTs rich of  $sp^3$  cluster. The I-V behaviour of MWCNTs changes from conducting to semiconducting behaviour due to the inclusion of  $SiO_2$  and  $TiO_2$  on its surface. The transformed structure also displays an increasing electrical conductivity due to higher content Ti in the MWCNTs. The inclusion of  $TiO_2$  and  $SiO_2$  NPs in MWCNTs reveals the possibility of tuning the electronic/electrical behaviour of MWCNTs. By virtue of the charge storage properties induced onto MWCNT by ionic  $Ti^{3+}$ , Si-Si, and  $O^-$  bonds, the NCs could find applications in memristive devices and photocatalytic activity.

#### Declaration of Competing Interest

The authors affirm no conflict of interest.

#### Acknowledgment

We appreciate the National Research Foundation (NRF) of South Africa for its financial support (Grant Nos. 88070 and 105292).

#### References

- [1] A. Kumar, K. Kumar, P.K. Ghosh, K. L. Yadav, MWCNT/ $TiO_2$  hybrid nanofiller toward high-performance epoxy composite, *Ultrason. Sonochem.* 41 (2018) 37–46.
- [2] R.H. Baughman, A.A. Zakhidov, W.A. De Heer, Carbon nanotubes — the route toward application, *Science* 297 (2012) 787–792.
- [3] W. Bauhofer, J.Z. Kovacs, A review and analysis of electrical percolation in carbon nanotube-polymer composites, *Compos. Sci. Technol.* 69 (2009) 1486–1498.
- [4] M. Daenen, R.D. De Fouw, B. Hamers, P.G. Janssen, K. Schouteden, M.A. Veld, The wondrous world of carbon nanotubes, *Eindhoven Uni. Technol* (2003) 1–35.
- [5] M. Božić, V. Vivod, R. Vogrinčić, I. Ban, G. Jakša, S. Hribnik, D. Fakin, V. Kokol, Enhanced catalytic activity of the surface-modified  $TiO_2$ -MWCNT nanocomposites under visible light, *J. Coll. Interf. Sci.* 465 (2016) 93–105.
- [6] J.J. Adjizian, R. Leghrib, A.A. Koos, I. Suarez-Martinez, A. Crossley, P. Wagner, N. Grobert, E. Llobet, C.P. Ewels, Boron- and nitrogen-doped multi-wall carbon nanotubes for gas detection, *Carbon* 66 (2014) 662–673.
- [7] R.J. Baierle, S.B. Fagan, R. Mota, A.J. da Silva, A. Fazzio, Electronic and structural properties of silicon-doped carbon nanotubes, *Phys. Rev. B* 64 (2001) 854131–854134.
- [8] V.V. Bolotov, V.E. Kan, E.V. Knyazev, N.A. Davletkildecv, S.N. Nesov, I. V. Ponomareva, D.V. Sokolov, P.M. Koruseenko, Formation of the N-MWCNT/ $TiO_x$  nanocomposite structure using magnetron method for gas sensing application, *AIP Conf. Proc.* 1876 (2017), 020063.
- [9] B. Czech, W. Buda, S. Pasieczna-Patkowska, P. Oleszczuk, MWCNT- $TiO_2$ - $SiO_2$  nanocomposites possessing the photocatalytic activity in UVA and UVC, *Appl Catal B Environ* 162 (2015) 564–572.
- [10] B. Czech, W. Buda, Photocatalytic treatment of pharmaceutical wastewater using new multiwall-carbon nanotubes/ $TiO_2$ / $SiO_2$  nanocomposites, *Environ. Res.* 137 (2015) 176–184.
- [11] B. Czech, K. Tyszczyk-Rotko, Visible-light-driven photocatalytic removal of acetaminophen from water using a novel MWCNT- $TiO_2$ - $SiO_2$  photocatalysts, *Sep. Purif. Technol.* 206 (2018) 343–355.
- [12] C. Song, Y. Xia, M. Zhao, X. Liu, F. Li, B. Huang, H. Zhang, B. Zhang, Functionalization of silicon-doped single walled carbon nanotubes at the doping site: an ab initio study, *Phys Letts A* 358 (2006) 166–170.
- [13] C. Gao, Z. Guo, J.H. Liu, X.J. Huang, The new age of carbon nanotubes: an updated review of functionalized carbon nanotubes in electrochemical sensors, *Nanoscale* 4 (2012) 1948–1963.
- [14] D.C. Hurum, K.A. Gray, T. Rajh, M.C. Thurnauer, Recombination pathways in the degussa P25 formulation of  $TiO_2$ : surface versus lattice mechanisms, *J. Phys. Chem. B* 109 (2005) 977–980.
- [15] E. Gale,  $TiO_2$ -based memristors and ReRAM: materials, mechanisms and models (a review), *Semicond. Sci. Technol.* 29 (2014), 104004.
- [16] J.A. Oke, D.O. Idisi, S. Sarma, S.J. Moloi, S.C. Ray, K.H. Chen, A. Ghosh, A. Shelke, W.F. Pong, Electronic, electrical, and magnetic behavioral change of  $SiO_2$ -NP-decorated MWCNTs, *ACS Omega* 4 (2019) 14589–14598.
- [17] J.A. Oke, D.O. Idisi, S. Sarma, S.J. Moloi, S.C. Ray, K.H. Chen, A. Ghosh, A. Shelke, S.-H. Hsieh, W.F. Pong, Tuning of electronic and electrical behaviour of MWCNTs- $TiO_2$  nano-composites, *Diam. Relat. Mater.* 100 (2019), 107570.
- [18] V. Vatanpour, S.S. Madaeni, R. Moradian, S. Zinadini, B. Astinchap, Fabrication and characterization of novel antifouling nanofiltration membrane prepared from oxidized multiwalled carbon nanotube/polyethersulfone nanocomposite, *J. Memb. Sci.* 375 (2011) 284–294.
- [19] P. Das, A. Saha, A.R. Maity, S.C. Ray, N.R. Jana, Silicon nanoparticle based fluorescent biological label via low temperature thermal degradation of chloroalkylsilane, *Nanoscale* 5 (2013) 5732–5737.
- [20] H. Yin, Y. Wada, T. Kitamura, S. Kambe, S. Murasawa, H. Mori, T. Sakata, S. Yanagida, Hydrothermal synthesis of nanosized anatase and ruffe  $TiO_2$  using amorphous phase  $TiO_2$ , *J. Mater. Chem.* 11 (2001) 1694–1703.
- [21] D. Chaudhary, N. Khare, V.D. Vankar, Ag nanoparticles loaded  $TiO_2$ /MWCNT ternary nanocomposite: a visible-light-driven photocatalyst with enhanced photocatalytic performance and stability, *Ceram. Internat* 42 (2016) 15861–15867.
- [22] D.O. Idisi, H. Ali, J.A. Oke, S. Sarma, S.J. Moloi, S.C. Ray, H.T. Wang, N.R. Jana, W. F. Pong, A.M. Strydom, Electronic, electrical and magnetic behaviours of reduced graphene-oxide functionalized with silica coated gold nanoparticles, *Appl. Surf. Sci.* 483 (2019) 106–113.
- [23] A. Jitianu, T. Cacciaguerra, R. Benoit, S. Delpeux, F. Béguin, S. Bonnamy, Synthesis and characterization of carbon nanotubes- $TiO_2$  nanocomposites, *Carbon* 42 (2004) 1147–1151.
- [24] R. Casati, N.M. Hamidi, M. Coduri, V. Tirelli, M. Vedani, Effects of platform pre-heating and thermal-treatment strategies on properties of alsi10mg alloy processed by selective laser melting, *Metals* 8 (2018) 954.
- [25] Y. Chen, N. Du, H. Zhang, D. Yang, Facile synthesis of uniform MWCNT@Si nanocomposites as high-performance anode materials for lithium-ion batteries, *J. Alloys. Compd.* 62 (2015) 966–972.
- [26] V.B. Koli, A.G. Dhodamani, A.V. Raut, N.D. Thorat, S.H. Pawar, S.D. Delekar, Visible light photo-induced antibacterial activity of  $TiO_2$ -MWCNTs nanocomposites with varying the contents of MWCNTs, *J. Photochem. Photobiol. A: Chem.* 328 (2016) 50–58.
- [27] N.D. Abazović, M.I. Čomor, M.D. Dramićanin, D.J. Jovanović, S.P. Ahrenkiel, J. M. Nedeljković, Photoluminescence of anatase and rutile  $TiO_2$  particles, *J. Phys. Chem. B* 110 (2006) 25366–25370.
- [28] Y.S. Hu, L. Kienle, Y.G. Guo, J. Maier, High lithium electroactivity of nanometer-sized rutile  $TiO_2$ , *Adv Mater* 18 (2006) 1421–1426.

J.A. Oke et al.

Journal of Electron Spectroscopy and Related Phenomena 245 (2020) 147002

- [29] L.A. Ardila, D.N. Travessa, Core/shell structure of TiO<sub>2</sub>-coated MWCNTs for thermal protection for high-temperature processing of metal matrix composites, *Adv. Mater. Sci. Eng. Int. J.* (2018) 1–11.
- [30] J. Yu, T. Ma, S. Liu, Enhanced photocatalytic activity of mesoporous TiO<sub>2</sub> aggregates by embedding carbon nanotubes as electron-transfer channel, *Phys. Chem. Chem. Phys.* 13 (2011) 3491–3501.
- [31] J. Yu, J. Fan, B. Cheng, Dye-sensitized solar cells based on anatase TiO<sub>2</sub> hollow spheres/carbon nanotube composite films, *J Power Sour* 196 (2011) 7891–7898.
- [32] V. Senoz, A. Armigliato, I. De Wolf, G. Carnevale, R. Balboni, S. Frabboni, A. Benedetti, Strain determination in silicon microstructures by combined convergent beam electron diffraction, process simulation, and micro-Raman spectroscopy, *J. Appl. Phys.* 94 (2003) 5574–5583.
- [33] S.C. Ray, S.K. Bhunia, A. Saha, N.R. Jana, Electric and ferro-electric behaviour of polymer-coated graphene-oxide thin film, *Phys. Procedia* 46 (2013) 62–70.
- [34] S. Osswald, M. Havel, Y. Gogotsi, Monitoring oxidation of multiwalled carbon nanotubes by Raman spectroscopy, *J. Raman Spectrosc.* 38 (2007) 728–736.
- [35] S.D. Delekar, A.G. Dhodamani, K. More, T.D. Dongale, R.K. Kamat, S.F. Acquah, N. S. Dalal, D.K. Panda, Structural and optical properties of nanocrystalline TiO<sub>2</sub> with multiwalled carbon nanotubes and its photovoltaic studies using ru(ii) sensitizers, *ACS Omega* 3 (2018) 2743–2756.
- [36] C.W. Pao, S.C. Ray, H.M. Tsai, Y.S. Chen, H.C. Chen, I.N. Lin, W.F. Pong, J. W. Chiou, M.H. Tsai, N.G. Shang, P. Papakonstantinou, Change of structural behaviors of organo-silane exposed graphene nanoflakes, *J Phys Chem C* 114 (2010) 8161–8166.
- [37] S.C. Ray, C.W. Pao, H.M. Tsai, J.W. Chiou, W.F. Pong, C.W. Chen, M.H. Tsai, P. Papakonstantinou, L.C. Chen, K.H. Chen, A comparative study of the electronic structures of oxygen- and chlorine-treated nitrogenated carbon nanotubes by x-ray absorption and scanning photoelectron microscopy, *Appl. Phys. Lett.* 91 (2007) 3–5.
- [38] A. Kuznetsova, I. Popova, J.T. Yates, M.J. Bronikowski, C.B. Huffman, J. Liu, R. E. Smalley, H.H. Hwu, J.G. Chen, Oxygen-containing functional groups on single-wall carbon nanotubes: NEXAFS and vibrational spectroscopic studies, *J. Am. Chem. Soc.* 123 (2001) 10699–10704.
- [39] S. Banerjee, T. Hemraj-Benny, M. Balasubramanian, D.A. Fischer, J.A. Misewich, S. S. Wong, Ozonized single-walled carbon nanotubes investigated using NEXAFS spectroscopy, *Chem. Commun. (Camb.)* 10 (2004) 772–773.
- [40] S.C. Ray, C.W. Pao, H.M. Tsai, H.C. Chen, Y.S. Chen, S.L. Wu, D.C. Ling, I.N. Lin, W. F. Pong, S. Gupta, High-temperature annealing effects on multiwalled carbon nanotubes: electronic structure, field emission and magnetic behaviors, *J. Nanosci. Nanotechnol.* 9 (2009) 6799–6805.
- [41] M. Magnuson, M. Mattesini, S. Li, C. Höglund, M. Beckers, L. Hultman, O. Eriksson, Bonding mechanism in the nitrides Ti<sub>2</sub>AlN and TiN: an experimental and theoretical investigation, *Phys. Rev. B* 76 (2007) 1–9.
- [42] Z.Y. Wu, F. Jollet, F. Seifert, Electronic structure analysis of  $\alpha$ -SiO<sub>2</sub> via x-ray absorption near-edge structure at the Si K, L<sub>2,3</sub> and O K edges, *J. Phys. Condens. Matter* 10 (1998) 8083–8092.
- [43] M.W. Gaultois, A.P. Grosvenor, XANES and XPS investigations of (TiO<sub>2</sub>)<sub>x</sub>(SiO<sub>2</sub>)<sub>1-x</sub>: the contribution of final-state relaxation to shifts in absorption and binding energies, *J. Mater. Chem.* 21 (2011) 1829–1836.
- [44] L.L. Lev, D.V. Averyanov, A.M. Tokmachev, F. Bisti, V.A. Rogalev, V.N. Strocov, V. Storchak, Band structure of the EuO/Si interface: justification for silicon spintronics, *J. Mater. Chem. C Mater. Opt. Electron. Devices* 5 (2017) 192–200.
- [45] S.D. Mo, W.Y. Ching, X-ray absorption near-edge structure in alpha-quartz and stishovite: ab initio calculation with core-hole interaction, *Appl. Phys. Lett.* 78 (2001) 3809–3811.
- [46] F.M. De Groot, M.O. Figueiredo, M.J. Basto, M. Abbate, H. Petersen, J.C. Fuggle, 2 p X-ray absorption of titanium in minerals, *Phys. Chem. Miner.* 19 (1992) 140–147.
- [47] D. Su, C.L. Teoh, A. Samanta, N.Y. Kang, S.J. Park, Y.T. Chang, The development of a highly photostable and chemically stable zwitterionic near-infrared dye for imaging applications, *Chem. Commun. (Camb.)* 51 (2015) 3989–3992.
- [48] T.I. Okpalugo, P. Papakonstantinou, H. Murphy, J. McLaughlin, N.M. Brown, High resolution XPS characterization of chemical functionalised MWCNTs and SWCNTs, *Carbon* 43 (2005) 153–161.
- [49] H. Zhang, X. Luo, J. Xu, B. Xiang, D. Yu, Synthesis of TiO<sub>2</sub>/SiO<sub>2</sub> core/shell nanocable arrays, *J Phy Chem B* 108 (2004) 14866–14869.
- [50] M. Pedio, F. Borgatti, A. Giglia, N. Mahne, S. Nannarone, S. Giovannini, C. Cepek, E. Magnano, G. Bertoni, E. Spiller, M. Sancrotti, Annealing temperature dependence of C<sub>60</sub> on silicon surfaces bond evolution and fragmentation as detected by NEXAFS, *Phys Scripta* (2005) 695.
- [51] H.X. Deng, S.H. Wei, S.S. Li, J. Li, A. Walsh, Electronic origin of the conductivity imbalance between covalent and ionic amorphous semiconductors, *Phys. Rev. B* 87 (2013) 1–5.
- [52] S.C. Ray, D.K. Mishra, A.M. Strydom, P. Papakonstantinou, Magnetic behavioural change of silane exposed graphene nanoflakes, *J. Appl. Phys.* 118 (2015), 115303.
- [53] B.S. Huang, H.H. Tseng, M.Y. Wey, Comparison of visible-light-driven routes of anion-doped TiO<sub>2</sub> and composite photocatalyst, *Ceram Soc of Japan* 117 (2009) 753–758.
- [54] X. Zhou, X. Ge, R. Tang, T. Chen, G. Wang, Preparation and catalytic property of modified multi-walled carbon nanotube-supported TiO<sub>2</sub> for the transesterification of dimethyl carbonate with phenol, *Chinese J of Catal* 35 (2014) 481–489.
- [55] L.B. Xiong, L. Li, Y. Bo, Y. Ying, Ti<sup>3+</sup> in the surface of titanium dioxide: generation, properties and photocatalytic application, *J. Nanomater.* (2012) 1–13.
- [56] K. Szot, W. Speier, G. Bihlmayer, R. Waser, Switching the electrical resistance of individual dislocations in single-crystalline SrTiO<sub>3</sub>, *Nat. Mater.* 5 (2006) 312–320.
- [57] J. Yao, Z. Sun, L. Zhong, D. Natelson, J.M. Tour, Resistive switches and memories from silicon oxide, *Nano Lett.* 10 (2010) 4105–4110.
- [58] J. Schneider, M. Matsuoka, M. Takeuchi, J. Zhang, Y. Horiuchi, M. Anpo, D. W. Bahnemann, Understanding TiO<sub>2</sub> photocatalysis: mechanisms and materials, *Chem. Rev.* 114 (2014) 9919–9986.
- [59] Z. Shuai, L. Wang, Q. Li, Evaluation of charge mobility in organic materials: from localized to delocalized descriptions at a first-principles level, *Adv. Mater.* 23 (2011) 1145–1153.
- [60] L. Chua, Memristor-the missing circuit element, *IEEE Trans. Circuit Theory* 18 (1971) 507–519.
- [61] S. Menzel, M. Waters, A. Marchewka, U. Böttger, R. Dittmann, R. Waser, Origin of the ultra-nonlinear switching kinetics in oxide-based resistive switches, *Adv. Funct. Mater.* 21 (2011) 4487–4492.
- [62] H. Abunahla, M. Abi Jaoude, I.A. Omar, B. Mohammad, M. Al-Qutayri, Resistive switching in sol-gel derived microscale memristors, *IEEE 59th International Midwest Symposium on Circuits and Systems (MWSCAS)* (2016) 1–4.
- [63] B. Sun, M. Xiao, G. Zhou, Z. Ren, Y.N. Zhou, Y.A. Wu, Non-zero-crossing current-voltage hysteresis behavior in memristive system, *Mater Today Adv* 6 (2020), 100056.
- [64] B. Ghosh, S.C. Ray, M. Pontsho, S. Sarma, D.K. Mishra, Y.F. Wang, W.F. Pong, A. M. Strydom, Defect induced room temperature ferromagnetism in single crystal, poly-crystal, and nanorod ZnO: a comparative study, *J. Appl. Phys.* 123 (2018), 161507.